LAWRENCE
LIVERMORE
NATIONAL
LABORATORY

LLNL-TH-645412

BIOPHYSICAL ANALYSIS OF BACTERIAL AND VIRAL SYSTEMS: A SHOCK TUBE STUDY OF BIO-AEROSOLS AND A CORRELATED AFM/NANOSIMS INVESTIGATION OF VACCINIA VIRUS

S. D. Gates

October 29, 2013

Disclaimer

This work performed under the auspices of the U.S. Department of Energy by Lawrence Livermore National Laboratory under Contract DE-AC52-07NA27344.

BIOPHYSICAL ANALYSIS OF BACTERIAL AND VIRAL SYSTEMS: A SHOCK TUBE STUDY OF BIO-AEROSOLS AND A CORRELATED AFM/NANOSIMS INVESTIGATION OF VACCINIA VIRUS

A DISSERTATION
SUBMITTED TO THE DEPARTMENT OF MECHANICAL ENGINEERING
AND THE COMMITTEE ON GRADUATE STUDIES
OF STANFORD UNIVERSITY
IN PARTIAL FULFILLMENT OF THE REQUIREMENTS
FOR THE DEGREE OF
DOCTOR OF PHILOSOPHY

Sean Damien Gates
May 2013

I certify that I have read this dissertation and that, in my opinion, it is fully adequate in scope and quality as a dissertation for the degree of Doctor of Philosophy.

Professor Ronald K. Hanson, Principal Advisor

I certify that I have read this dissertation and that, in my opinion, it is fully adequate in scope and quality as a dissertation for the degree of Doctor of Philosophy.

Professor Ellen Kuhl

I certify that I have read this dissertation and that, in my opinion, it is fully adequate in scope and quality as a dissertation for the degree of Doctor of Philosophy.

Dr. Alexander J. Malkin

Approved for the Stanford University Committee on Graduate Studies.

THIS PAGE IS INTENTIONALLY LEFT BLANK

Abstract

The work presented herein is concerned with the development of biophysical methodology designed to address pertinent questions regarding the behavior and structure of select pathogenic agents. Two distinct studies are documented: a shock tube analysis of endospore-laden bio-aerosols and a correlated AFM/NanoSIMS study of the structure of vaccinia virus.

An experimental method was formulated to analyze the biological and morphological response of endospores to gas dynamic shock waves. A novel laser diagnostic system was implemented to provide time resolved data concerning the structural decomposition of endospores in shock-heated flows. In addition, an ex situ methodology combining viability analysis, flow cytometry and scanning electron microscopy was employed to both assess the biological response of the endospore to the shock event, as well as to provide complementary data regarding the structural state of the treated endospore. This methodology was implemented to model the shock wave induced response of a variety of *Bacillus* endospores. The results are subsequently synthesized into a theoretical framework to be employed in modeling the interaction of endospore-laden bio-aerosols with blast waves.

An analytical method combining atomic force microscopy (AFM) and nanometer-scale secondary ion mass spectrometry (NanoSIMS) was developed to examine the spatial localization and depth distribution of specific biological elements in viral systems. This methodology was implemented to analyze the distribution of ^{13}C labeled fatty acids as well as ^{15}N labeled thymidine in individual nanometer sized vaccinia viral particles. Based upon the ^{13}C and ^{15}N signals, three-dimensional depth-resolved data regarding the architecture and localization of the virion lipid membrane and the nucleoprotein complex

was generated. In addition, this methodology was employed to provide direct correlation of architectural and chemical data for isolated sub-viral structures. The technique and results presented herein represent a novel tool for the structural and chemical study of both intact viral particles as well as specifically targeted sub-viral elements.

Acknowledgements

First and foremost, I would like to express my sincerest gratitude to my advisor, Professor Ronald Hanson, for his guidance and encouragement during the course of this research. I would also like to thank him for allowing me the freedom to explore scientific questions of interest and develop as an independent researcher. My sincere thanks also goes to Dr. Jay Jeffries who was an instrumental part of the research I conducted at Stanford. I would also like to express my appreciation to the other members of the Hanson group for their valuable insight into matters both of research and of life.

Additionally, I am grateful to both Dr. Alex Malkin and Dr. Peter Weber at Lawrence Livermore National Laboratory for allowing me the opportunity to broaden my scientific horizons. This work was performed under the auspices of the U.S. Department of Energy by Lawrence Livermore National Laboratory under Contract DE-AC52-07NA27344. This work was supported by the Lawrence Livermore National Laboratory through Laboratory Directed Research and Development Grant 11-ERD-027.

I would not have embarked upon this journey if not for my parents who instilled within me a fondness for creative endeavors. And last, but not least, to my wife Alia, whose love and encouragement has made it all possible.

THIS PAGE IS INTENTIONALLY LEFT BLANK

Table of Contents

List of Figures

Chapter 1 Introduction

1.1 Background and Motivation

The understanding and modeling of heterogeneously constructed biological systems is increasingly dependent upon the ability to utilize physical measurement methodology to complement biochemical, genetic and molecular biology techniques. Furthermore, due to the current international climate and the prevailing concern regarding the deliberate release of pathogenic agents, a renewed emphasis has been placed upon the development of experimental methods to address unresolved issues regarding the structure, behavior and biological constitution of such agents. The work presented herein focuses upon the development and implementation of novel biophysical interrogation schemes designed to:

1. Model the biological and morphological response of aerosolized *Bacillus* endospores to gas dynamic shock waves
2. Investigate the architectural construction and structure-function relationship of vaccinia virus

The impetus behind the examination of the first topic was predicated upon the desire to model the response of *Bacillus anthracis*, the etiologic agent of anthrax, to a blast wave in a natural environment. The latter issue, concerning the interrogation of vaccinia, was undertaken in order to provide three-dimensional structural and chemical data to aid in the development of anti-viral therapies for the smallpox virus; vaccinia being the laboratory model and live vaccine for smallpox.

Due to the somewhat disparate nature of the experimental work, the current manuscript is divided into two distinct parts. The first section details experiments focused upon the study of the interaction of bio-aerosols and gas dynamic shock waves. The latter section is concerned with the implementation of a correlated atomic force microscopy (AFM)/nanometer-scale secondary ion mass spectrometry (NanoSIMS) methodology to model both the spatial distribution of viral constituents as well as the large-scale architecture of the vaccinia viral particle.

1.2 Shock tube study of endospore laden bio-aerosols

A novel shock tube methodology was developed in order to generate experimental data concerning the response of aerosolized endospores to blast waves. Two methods of interrogation were designed to monitor the bio-aerosol/shock wave interaction: an in situ interrogation scheme consisting of a multitude of laser diagnostics as well as ex situ evaluation techniques including viability analysis, flow cytometry and scanning electron microscopy (SEM). The former method was implemented to provide time resolved data concerning both the morphological state of the endospore during the shock wave event as well as the variation of pertinent flow variables. The latter method was designed to assess the loss of biological functionality of the endospore after exposure to the shock wave. In addition, the ex situ methodology enabled the examination of the structural integrity of the endospore, thus complementing the time-resolved measurements generated through the implementation of the laser diagnostic system.

This methodology was employed to generate data for a range of *Bacillus* endospores including *B. subtilis* as well as *B. thuringiensis*; the latter species bearing a close phenotypical and genotypical correspondence to *B. anthracis*. In addition, shock tube experiments were conducted in inert and oxidative test environments utilizing a variety of test times. A conceptual framework was subsequently developed and employed to predict the morphological and biological response of endospores exposed to shock heated flows.

1.3 Correlated AFM/NanoSIMS study of vaccinia virus

Novel biophysical methodology was developed to investigate the architectural arrangement and structural composition of the vaccinia virion. A two-pronged approach was implemented, in which physical imaging using AFM was combined with chemical imaging using NanoSIMS, in order to elucidate the constitution and spatial distribution of specific viral structures.

This methodology was employed to examine the distribution of the lipid membranes and the nucleoprotein complex within intact viral particles. Identification of specific macromolecular assemblages was done through the incorporation of ^{13}C and ^{15}N isotopic labels within the viral lipid membrane and DNA, respectively. Quantitative depth resolved maps detailing the distribution of the isotopic tags were subsequently generated, thereby enabling the construction of architectural models of the vaccinia viral particle. In addition, the possibility of NanoSIMS analysis of enzymatically and chemically isolated nucleoprotein structures is addressed.

Part I: Shock tube study of bio-aerosols

Chapter 2 Bio-aerosol/shock wave interaction

2.1 The endospore and shock heated flows: an introduction

During periods of environmental stress certain Gram-positive bacteria, such as *Bacillus* and *Clostridium*, can revert to a dormant, metabolically inactive state through the process of endosporulation[1,2]. This transformation results in the production of a bacterial structure, the endospore, which is able to survive without nutrients and is highly resistant to stress mechanisms such as ultraviolet radiation, desiccation, elevated temperatures and chemical disinfectants[3-7]. The ability of the endospore to resist a multitude of stress mechanisms can be attributed to its unique structural and biochemical composition. Specifically, the multi-tiered structural constitution of the endospore consists of a coat resistant to lysozyme, a peptidoglycan cortex layer and a core wall encasing the DNA[8]. The bacterial genome itself is enclosed within chromatin-like proteins, termed α/β-type SASPs, that protect the DNA from ultraviolet radiation and elevated temperatures[9,10]. In addition, the presence of dipicolinic acid within the core is thought to stabilize the DNA and may aid in the resistance of the endospore to heat and oxidizing agents[11]. When environmental conditions are more favorable the endospore will revert back to the metabolically active vegetative state allowing for cellular division.

While a multitude of previous studies have focused upon the resistance of endospores to specific stress mechanisms, minimal experimental data exists concerning the morphological and biological response of endospores exposed to a dynamic physical process. Of particular interest is the examination of the interaction of aerosolized endospores with blast waves in a natural environment. In order to model this physical

event a laboratory methodology was developed utilizing a gas dynamic shock tube. Typically employed in the study of chemical physics[12,13], the shock tube was, in the present work, modified to expose endospore-laden bio-aerosols to shock waves.

In addition, an array of interrogation methods was developed to monitor the shock wave induced morphological and biological response of the endospore. In situ laser diagnostics were employed to provide both time-resolved data concerning the rate of structural decomposition of the endospore as well as to monitor the variation of the temperature during the shock wave process. Specifically, laser absorption and scattering signals from an ultraviolet (266 nm) and visible (665 nm) laser were coupled with spectroscopic models to examine the morphological state of the endospore in the post-shock environment. Furthermore, near infrared lasers were employed in a two-line thermometry technique designed to provide temperature measurements with 50 μs resolution. While the aforementioned laser diagnostic system provided pertinent information regarding the structural integrity of the endospore during the shock wave process, the generation of quantitative information regarding the reduction in biological functionality from such interrogation methods was precluded. Consequently, the in situ methodology was complemented with a variety of ex situ characterization techniques designed to assess the biological effect of the bio-aerosol/shock wave interaction. Endospore samples exposed to the shock event were extracted from the shock tube and examined with three interrogation methods: viability analysis, flow cytometry and scanning electron microscopy. The former two techniques were combined to provide a quantitative assessment of the loss of endospore biological functionality as a result of shock wave exposure. In addition, a fluorescent DNA binding dye, propidium iodide, was added to analyzed endospore samples; subsequent examination with flow cytometry provided ex situ data concerning the morphological state of the endospore to complement those generated with the laser diagnostic system. Physical imaging and qualitative assessment of the endospores was performed with the third ex situ characterization technique, scanning electron microscopy.

A description of the experimental apparatus as well as theoretical considerations regarding the modeling of the bio-aerosol/shock wave interaction is first presented. The

subsequent chapter details the design and formulation of the in situ and ex situ methodology, with more emphasis placed on the latter. Results obtained from the implementation of the interrogation methodology are then described; the response of a variety of *Bacillus* endospore species exposed to distinct environmental conditions is presented culminating in the characterization of *B. thuringiensis*, the laboratory model for *B. anthracis*. Based upon the results, a framework characterizing the structural and biological response of aerosolized endospores to gas dynamic shock waves is formulated.

2.2 Stanford aerosol shock tube and bio-aerosols

The Stanford Aerosol Shock Tube (SAST) facility[14] provides a laboratory environment to expose aerosols to shock waves of controlled strength. While past shock tube studies have focused upon the analysis of combustion systems and reaction kinetics[15,16], the experiments detailed herein demonstrate the application of this method to aerosolized bacterial endospores. To facilitate our study the shock tube was equipped with a multitude of laser diagnostics to provide time-resolved in situ monitoring of the shock wave/bio-aerosol interaction as well as instruments for the production and extraction of the aerosolized endospores.

The SAST is a gas dynamic device consisting of a driver section and a driven section separated with a diaphragm; the driven region is further divided into an upstream section and a test section. As illustrated in Figure 2-1, the upstream section is filled with argon bath gas and the test section, sealed with a sliding gate valve to limit diffusive transport of the bio-aerosol, is filled with a mixture of argon bath gas and aerosol produced by a Collison nebulizer from an aqueous particle suspension.

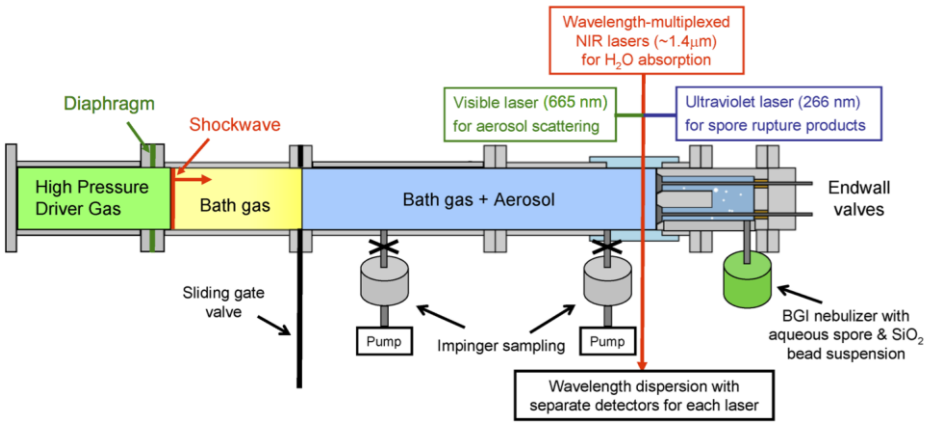

Figure 2-1: Schematic of the driven section of the Stanford AST facility configured for shock heating endospore-laden aerosols. Three in situ laser diagnostics monitor the shock-heated gas/aerosol, while pre- and post-shock samples are taken with gas dynamic impingers for ex situ analysis. (Not drawn to scale).

After the two driven sections are loaded, the gate valve is opened, and the driver section is pressurized with helium driver gas. The resulting pressure differential between the driven and the driver section causes the diaphragm to rupture, initiating the formation of a set of compression and expansion waves. The wave pattern generated by this event is illustrated in the x - t diagram in Figure 2-2; the horizontal axis represents the position along the shock tube and the vertical axis represents the time coordinate with diaphragm rupture occurring at $t = 0$. Initially, the right running compression wave exists in a non-equilibrium configuration characterized by a distribution of velocities. This nonlinear wave speed results in the steepening of the wave front and the rapid formation of a shock wave: a narrow fluid structure whose passage induces an effectively instantaneous change in flow variables[17]. In addition, diaphragm rupture generates a left running rarefaction wave, which, in contrast to the compression wave, becomes more diffuse as it propagates, resulting in the formation of an expansion fan[17]. The contact surface is a third fluid structure formed by the diaphragm rupture and represents the boundary between the driver and driven gas.

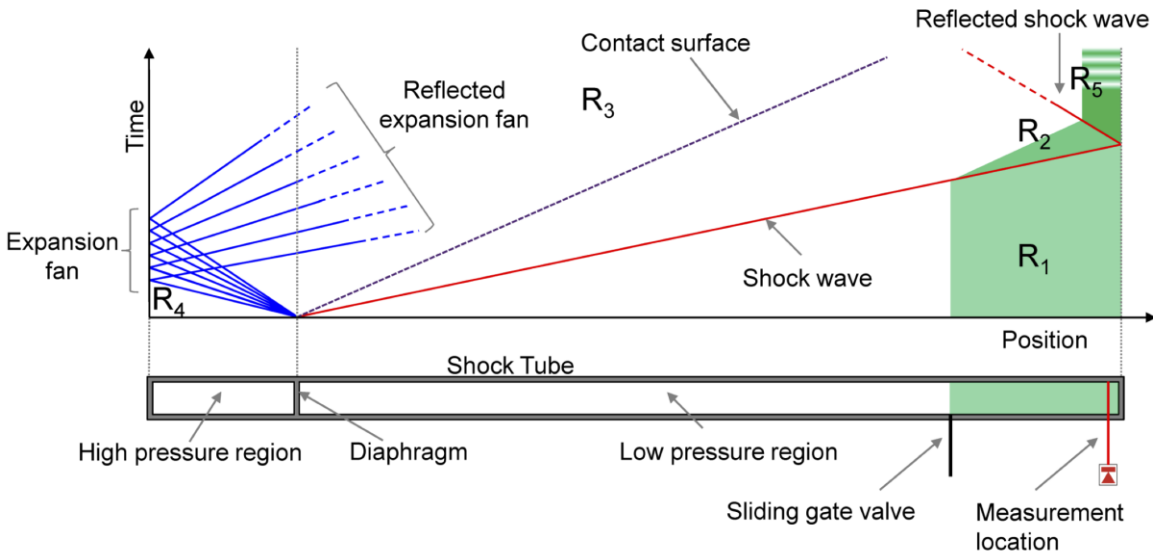

Figure 2-2: Wave pattern generated by the diaphragm rupture in the SAST. Region 1 is the pre-shock arrival gas state. When the shock wave arrives, a step change in pressure and temperature occurs (Region 2). The passage of the reflected shock wave once again compresses and heats the gas (Region 5) producing a stagnant flow region of high temperature and pressure.

Our interest lies in the interaction of the shock wave with the endospore-laden bio-aerosol in the test section of the shock tube. As illustrated in Figure 2-2, three distinct regions characterize this interaction. Region 1 (R_1) is the unperturbed state prior to the arrival of the incident shock wave; Region 2 (R_2) and Region 5 (R_5) are the fluid states after the arrival of the incident and reflected shock waves, respectively. When the incident shock arrives at the measurement station, the pre-shock gas/aerosol mixture at initial temperature (T_1) and pressure (P_1) is abruptly heated, compressed and accelerated. The acceleration forces induce the fragmentation of the larger droplets while the hot gas evaporates the solvent from the bio-aerosol. The shock wave is then reflected by the endwall and subsequently heats and compresses the gas/aerosol mixture a second time to the final test temperature and pressure T_5 and P_5, respectively. In addition, the flow is stagnated in Region 5, providing a steady state high temperature and pressure region for the duration of the test time. Under these conditions the possibility of endospore

morphological breakdown exists. For the majority of the experiments the test conditions persist for 2-3 ms, being limited by the eventual interaction of the reflected expansion fan with the reflected shock wave. The temperature and pressure then decay in approximately 50 ms through a variety of expansion processes to room temperature and a resting pressure above atmospheric[18]. Temperatures behind the reflected shock wave and outside of the boundary layer are highly uniform and vary isentropically with pressure[19]. The time evolution of the gas temperature and pressure observed at the laser diagnostic port 5 cm from the endwall is detailed in Figure 2-3.

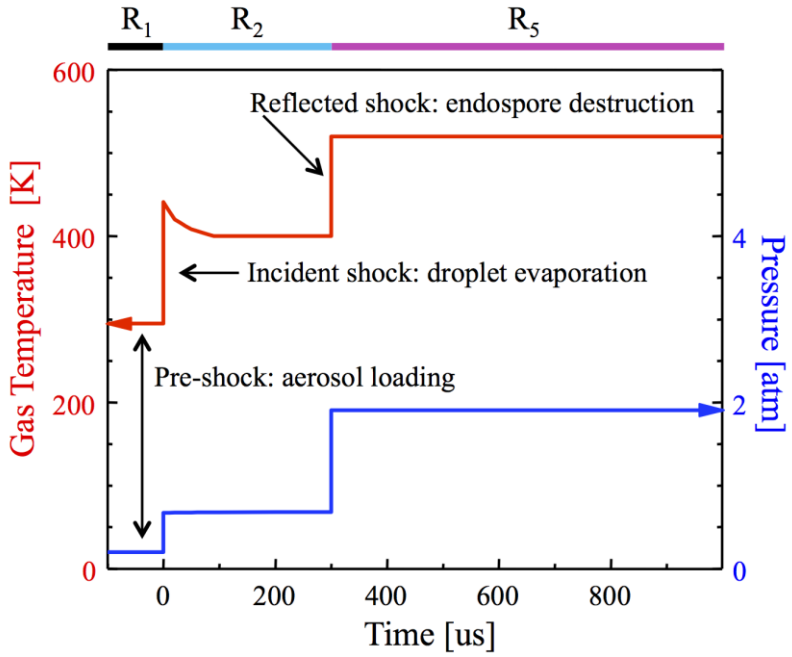

Figure 2-3: Theoretical time evolution of shock heating of gas observed at the measurement location of Figure 2-1. The step change in gas temperature and pressure from the incident shock (Region 1 to 2) and from the reflected shock (Region 2 to 5) are observed. The decrease in temperature in Region 2 is due to droplet evaporation. Uniform test conditions persist for 2 to 3 ms until a variety of processes result in the decay to room temperature and an elevated resting pressure.

Due to the heterogeneous nature of the bio-aerosol employed in our study quantification of the temperature and pressure in Region 2 and 5 is inherently more complicated than in pure gas phase shock wave experiments. In traditional shock tube

combustion studies the incident and reflected shock waves propagate into a gaseous medium; this interaction has been well studied and the subsequent change in flow variables is accurately modeled with the shock jump equations[17]. The interaction of a shock wave with a heterogeneous medium composed of multiple phases, as is the case with the particle-droplet laden gas mixture employed in our study, cannot be characterized as readily. However, a qualitative assessment of the physical processes generated during the shock wave event and the implementation of modeling schemes and laser diagnostic measurement tools enable us to accurately determine the flow variables of interest.

From a qualitative perspective the shock wave event can be modeled as a process composed of two regimes: the incident wave encountering an evaporating fluid droplet gas mixture and the reflected wave propagating into a dusty gas. Initially, the interaction of the incident shock wave with the bio-aerosol results in the rapid heating and acceleration of the gas phase; thereafter, larger liquid droplets fragment and are accelerated to the velocity of the carrier gas. During this process two physical phenomena of particular interest occur: heat transfer from the gas phase to the particle-laden droplets and solvent evaporation. These processes result in a Region 2 temperature reduction as seen in Figure 2-3. By the end of Region 2 evaporation is complete and the bio-aerosol consists of particles in a fully gaseous medium. Therefore, the reflected shock wave encounters a mixture of perfect gas and solid particulates. Due to the fact that the particles in the bio-aerosol flow environment are large with respect to molecular dimensions the thickness of the shock wave is negligible in comparison to the distance required for momentum and thermal equilibrium to be established[20]. Consequently, the interaction of a normal shock wave with a particle-gas mixture may be accurately modeled as a gas dynamic shock followed by a relaxation zone where equilibrium is established between the two phases. An extensive theoretical development concerning the equations governing the temporal and spatial structure of this relaxation zone is presented in Marble[20]. For our purposes, however, we are mainly focused upon the rate of heat transfer between the two phases and the characteristic time for the particles to equilibrate with the heated gas. As will be explored further in a subsequent chapter, the biological

impact of the bio-aerosol/shock wave interaction is modeled as a phenomenon solely dependent upon the post-shock temperature values; consequently, determining whether the endospore particle reaches thermal equilibrium with the gas is critical for the accurate correlation of temperature and viability reduction. Following Marble[20], the thermal equilibration time, defined as the time required for the temperature difference between a particle and the gas to be reduced to e^{-1} of its original value, is formulated below:

$$\tau_T = \frac{1}{3}\mathrm{Pr}\left(\frac{c_s}{c_p}\right)\left(\frac{\rho_s}{\rho}\right)\frac{\sigma^2}{\upsilon}, \quad (1)$$

where $\mathrm{Pr} = c_p\mu/k$ is the fluid Prandtl number, c_s, ρ_s and c_p, ρ are the specific heat and density of the solid and fluid, respectively, υ is the kinematic viscosity and σ is the radius of the particle. The parameter predominately governing the magnitude of the thermal equilibration time is the square of the particle radius ($\sigma^2 \sim 10^{-12}$ m). Therefore, employing characteristic values for the particle and fluid specific heats and densities[20,21], Equation 1 indicates that the thermal equilibration time is at least an order of magnitude faster than the experimental test time. Consequently, measuring the gas temperature during the shock wave process is strongly indicative of the internal temperature of the entrained endospore particle.

While the aforementioned considerations provide a qualitative model for the bio-aerosol/shock wave interaction quantitative evaluation of the time dependent flow variables, such as temperature, requires the implementation of measurement and computational techniques. As previously stated, the physical complexities associated with the bio-aerosol/shock wave interaction limit the implementation of the shock jump equations for calculating pertinent flow variables in Regions 2 and 5. Two techniques were therefore employed to mitigate this issue: the monitoring of temperature through laser diagnostic techniques and the utilization, where applicable, of the computer code AEROFROSH for the calculation of gas shock conditions in the aerosol-laden flow. Further discussion of these methods will be conducted in subsequent sections.

2.3 Experimental procedure and considerations: Bio-aerosol generation, shock tube loading and endospore sampling

Endospore suspensions were cultivated using a large-scale broth method, details of which can be found in Appendix AI. The endospore-laden aqueous aerosol was produced from the particle suspension through the employment of a commercial gas dynamic nebulizer (6-jet Collison type, BGI Inc.). This technique utilizes a flowing gas to aspirate the suspension into a sonic velocity gas jet. During this process the induced shear forces cause the formation of particle - enveloped droplets. Reduction in droplet size is subsequently accomplished through the impaction of the jet with the interior of the suspension container. Characterization of the droplet size distribution produced by the nebulizer indicated that the mass median diameter was 2.2 μm with a standard deviation of 1.4. Considering the size of the endospores this data demonstrates that the large majority of droplets contained one or two bacterial particles. Furthermore, for reasons that will be made clear in a subsequent chapter, one-micron mono-dispersed silica (SiO_2) beads were added to the endospore suspension prior to nebulization. This specific particle was chosen both for its ability to remain structurally intact at high temperatures and for its ability to follow the fluid flow in a manner analogous to that of the endospores. The former consideration was validated through the exposure of aerosolized silica beads to high temperature shock waves while the latter was quantitatively assessed by examining the Stokes number (Sk). The Stokes number is a non - dimensional parameter that describes a particle's motion in a fluid; it is the ratio of the particle relaxation time (τ) to the hydrodynamic time and is expressed as follows[22]:

$$Sk = \frac{\tau V}{D}$$

where τ is as previously defined, V is the fluid velocity and D is a characteristic dimension of an object obstructing the flow. The quotient V/D has dimensions of inverse time and is the quantity previously referred to as hydrodynamic time. τ, the particle

relaxation time, is the time response of a particle to changes in the aggregate fluid motion, caused, for example, by obstacles in the flow. This quantity is formed as follows:

$$\tau = \frac{d_p^2 \, \rho_p}{18\mu}$$

where d_p and ρ_p are the particle's diameter and density, respectively and μ is dynamic viscosity of the surrounding fluid. Consequently, for the silica bead particles to follow the trajectory of the endospores during the loading and shock wave process, the two particles' diameter and density should be quantitatively similar. Therefore, one-micron beads were chosen as the tracer particle and the material, silica, was selected for its ability to remain undamaged over the range of post shock temperatures as well as for its endospore comparable density value.

In addition to the aforementioned considerations, an investigation into the pertinent optical properties of the silica beads was performed. As will be discussed in further detail in Chapter 3, quantification of the extent of endospore viability reduction required the identification and enumeration of the particles in the test suspensions. To this end the samples were interrogated with a multitude of lasers and the subsequent particulate scattering signals were detected. Particle differentiation, identification and enumeration were then based upon the ratio of forward to side scatter signals. Implementation of this methodology, however, required that the silica beads exhibit a substantially different scattering ratio than the endospores. Experiments conducted to assess the feasibility of the SiO_2 particle regarding this constraint indicated that a measurable difference existed between the scattering signals of the endospores and the silica beads. Further elaboration concerning this method of data analysis is detailed in Chapter 3.

After nebulization the particle-laden aerosol was introduced into the evacuated sealed test section of the SAST through poppet valves in the endwall as illustrated in Figure 2-1. In addition, the arrangement of the valves was optimized to enhance turbulent mixing in an attempt to maximize the uniformity of the aerosol mixture in the test section. The issue of aerosol uniformity is critical to the fidelity of the in situ laser diagnostic measurements. As detailed in Chapter 3, the laser techniques implemented for

the monitoring of temperature and endospore morphological integrity yield a path-averaged quantity. Consequently, embedded in our in situ measurement construct is the implicit assumption of a spatially uniform aerosol medium along the laser line of sight. Due to the heterogeneous nature of the bio-aerosol employed in our study we conducted an independent investigation to establish the level of aerosol uniformity in the shock tube. Laser scattering measurements conducted with the 665 nm laser were performed to confirm that the axial and vertical concentration gradients in the test section were sufficiently small. These experiments yielded concentration variations of approximately 10%. Therefore, while non-uniformities were present in the environment, the results indicated that our loading technique was sufficiently reliable for accurate path averaged laser measurements. Additional experiments were conducted to assess the density of loading as well as the water mole fraction of the aerosol. Laser scattering and absorption data indicated that the spore density of the two-phase bio-aerosol in the test section was on the order of 10^6 spores/cm^3 with a water mole fraction of between 3 and 7 percent[23].

Endospore samples for ex situ analysis were vacuum extracted with a commercial (Ace Glass Inc.) gas dynamic liquid impinger from the sealed bio-aerosol test section of the SAST before and after the shock event. The flow of aerosol through the impinger is directed onto a 10 ml pool of sterilized and filtered water. Any particulate in the flow impacts the water and is captured, while the carrier gas is extracted to vacuum. Two impingers were attached to the test region of the SAST as illustrated in Figure 2-1. After the sealed test region of the shock tube had been filled to a specified pressure with the nebulizer, a small (~10% of loading pressure) pre-shock sample was collected with the up-stream impinger. The gate valve was subsequently opened and the shock event and the laser diagnostic system initiated. After the shock wave event the gate valve was closed to confine the shock - heated bio-aerosol. The down-stream impinger was then implemented to collect a post-shock sample from the resealed test section at the conclusion of the experiment. Thereafter all sampling equipment was sterilized with an All American model 75X electric pressure steam autoclave and the shock tube was sterilized with high temperature shocks in pure oxygen. The collected aqueous endospore suspension in the impingers was then analyzed with three different ex situ methods detailed in Chapter 3.

The analysis of the morphological and biological effect produced by the aerosolization and sampling procedure was of prime importance in assessing the suitability of these techniques. If the production and sampling of the aerosol was detrimental to the structural integrity or biological viability of the bacterial endospore one would be unable to accurately decouple the endospore damage incurred as a result of nebulization and sampling with that incurred as a result of shock wave exposure. Initially, generation and sampling of the bio-aerosol was attempted with a sonic nebulizer and a vacuum filtering method, respectively. This nebulization procedure, however, resulted in a significant drop in endospore viability. Furthermore, the extraction of a sufficient quantity of shock treated endospores from the filtering matrix was prohibitively difficult. The aforementioned gas dynamic nebulizer and liquid impinger method was then adopted and experiments were developed to verify its suitability. To this end we initiated a series of tests whereby the full experimental procedure was performed save for the shock wave event; endospore samples were thereafter taken from the nebulizer and extracted from the shock tube with the two impingers. Utilizing the ex-situ techniques described in detail in Chapter 3 we were able to assess the viability and morphological integrity of each of the endospore suspensions as well as an untreated sample. These experiments indicated an intact, uncompromised endospore structure with no decrease in viability as compared to the untreated sample. Therefore, all of the damage incurred by the endospore during the experiment could be confidently attributed to the interaction with the shock wave.

Chapter 3 Methods of Inquiry

Characterization of the morphological and biological response of endospores exposed to gas dynamic shock waves required the development of in situ and ex situ interrogation methodology. A novel in situ laser diagnostic scheme was employed to provide time-resolved data concerning the bio-aerosol/shock wave interaction. In addition, the modeling of the biological response of the endospore required the formulation of ex situ interrogation schemes including viability analysis, flow cytometry and scanning electron microscopy.

3.1 In situ analysis

The interaction of endospore-laden bio-aerosols with gas dynamic shock waves is a highly dynamic event that generates a multitude of complex physical and biological processes on a microsecond time scale. Quantitatively assessing the temporal evolution of this interaction is crucial for the construction of accurate modeling and predictive schemes. Numerous studies have utilized laser absorption measurements to monitor the temporal variation of specific species during shock tube combustion experiments[24,25]. In the present context, a novel time-resolved laser diagnostic method employing direct absorption spectroscopy was developed to analyze the bio-aerosol/shock wave interaction. Consisting of a four-laser system, the in situ optical diagnostic technique was implemented to monitor experimental parameters and the real time extent of endospore morphological breakdown during exposure to shock-heated flows. Specifically, we employed a two line wavelength-multiplexed near infrared (NIR) laser absorption

technique to measure temperature and species mole fraction as well as a combination of visible and ultraviolet lasers to monitor the shock wave induced breakdown of endospore morphology and the release of ultraviolet (UV) active biomolecules.

3.1.1 In situ laser diagnostic experimental setup and methodology

Laser absorption and scattering techniques were developed to provide time-resolved measurements of bio-aerosols in shock-heated flows. The dynamic morphological response of the endospores was monitored with laser extinction measurements at two wavelengths, one in the visible (665 nm) and one in the ultraviolet range (266 nm). In addition, two telecommunications-grade fiber coupled diode lasers, tuned to two water vapor transitions in the NIR at 1343.3 and 1391.7 nm, were employed in a two-line thermometry temperature measurement technique.

The ultraviolet laser light at 266 nm was produced by BBO second-harmonic generation from a Coherent Verdi Nd: YVO4 5 watt source. The visible light near 665 nm was produced by a single mode Hitachi HL6501MG laser diode. The 266 and 665 nm continuous wave laser beams, of initial intensity I_o, were subsequently combined onto a common optical path and passed through the SAST at a window location 2 cm from the endwall. Furthermore, a double pass optical configuration was implemented to increase the signal to noise ratio. The transmitted laser light, of intensity I, was thereafter collected and wavelength dispersed onto separate detectors. In addition, the two multiplexed NIR fiber coupled lasers were single passed through the SAST 5 cm from the endwall and, as with the aforementioned visible and ultraviolet lasers, were wavelength dispersed, through the use of a grating, onto separate detectors. The laser diagnostic configuration is shown in Figure 3-1.

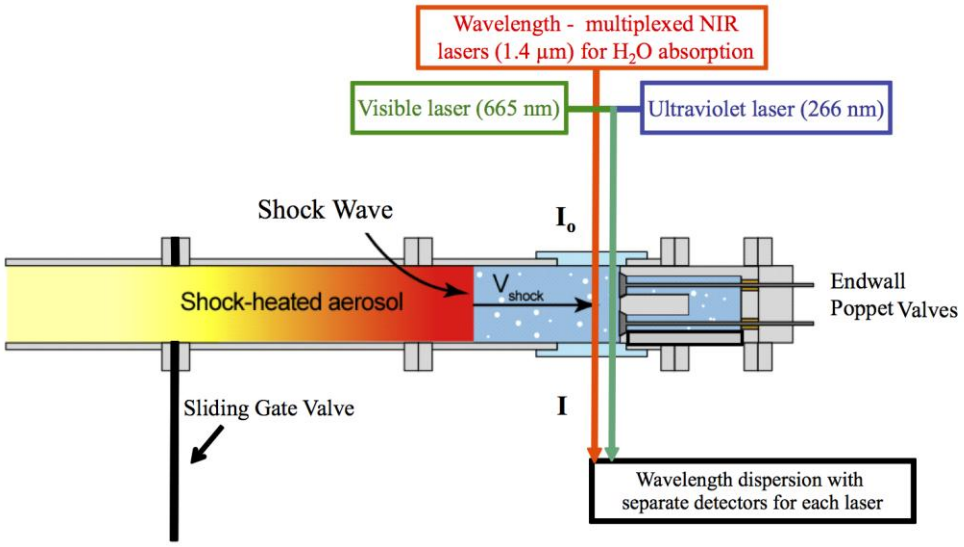

Figure 3-1: Diagram of the Stanford AST illustrating the in situ laser diagnostic experimental configuration. The UV and visible lasers were combined onto a common optical path 2 cm from the endwall. The NIR fiber coupled lasers were passed through the shock tube 5 cm from the endwall. Wavelength dispersion was employed to direct each laser onto a separate detector.

Quantitative interpretation of the time varying laser signals required the development and implementation of spectroscopic models. To this end the Beer-Lambert law was employed in the two forms shown below:

$$\left(\frac{I}{I_o}\right)_v = exp(-k_v L) \quad (2)$$

$$\left(\frac{I}{I_o}\right)_v = exp(-\sigma_v n L) \quad (3)$$

Within the framework of the temperature laser diagnostic we were concerned with two water absorption features, therefore, Equation 2, relating the ratio of incident and transmitted laser intensities to the transition specific spectral absorption coefficient, k_v, and laser path length, L, was employed. Further details regarding this methodology can be found in Appendix AII and in McCartt et al.[23].

The direct absorption laser diagnostic developed for the time-resolved monitoring of endospore morphology did not entail the quantification of a specific transition feature. Therefore, an alternative form of Beer's Law, Equation 3, relating the ratio of incident and transmitted laser intensities to the absorption cross section at frequency v (σ_v), the particle number density (n) and the laser path length, L, was implemented for signal analysis. Due to the heterogeneous nature of the bio-aerosol a modified version of Equation 3 was required for an accurate interpretation of the resonant and non-resonant laser signals; the development and implementation of this model is detailed in a subsequent section.

3.1.2 Wavelength-multiplexed NIR laser absorption temperature measurements

Traditionally, shock tube experiments have focused upon the dynamic heating and compressing of gas phase mixtures. In this regime shock wave velocity measurements can be used to generate accurate values for the flow variables in Region 2 and Region 5. In the present context, however, the bio-aerosol introduced into the shock tube test section was of a heterogeneous composition; specifically, liquid enveloped particulates and carrier gas. As previously detailed, the passage of the shock wave induces rapid evaporation of the liquid aerosol in Region 2, resulting in a substantial drop in gas temperature and inhibiting accurate shock wave speed based temperature measurements. In order to mitigate this issue a water vapor laser absorption technique was implemented. The aforementioned diode lasers were tuned using a temperature controller to two water vapor transitions near 1343.3 and 1391.7 nm[26]. These specific transitions were chosen for two reasons: the relative isolation of each absorption feature and the wide spread in the lower state energy value for the two transitions: 1790 cm^{-1} for the transition at 1343.3 nm and 1045 cm^{-1} for the transition at 1391.7 nm. The former consideration was important for the prevention of interference from absorption feature overlap at elevated pressures, while the latter enabled measurements over a wide range of temperature values[23]. In addition, due to the presence of water vapor in the ambient environment the optical instrumentation was enclosed in a nitrogen purge environment. During the experiment the

two lasers were scanned in wavelength over their respective absorption feature, providing integrated line strengths for each transition and hence, temperature measurements, every 50 μs. To provide an accurate assessment of the post shock temperature during the test time the initial transient region was neglected and the measured values were averaged after temperature stabilization had occurred. A theoretical background of this methodology is given in Appendix AII.

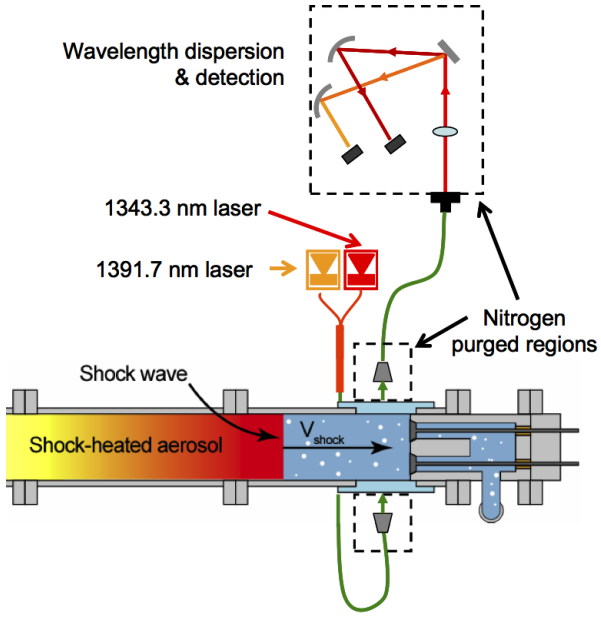

Figure 3-2: Configuration of the NIR laser absorption system for temperature measurements. The fiber-coupled lasers were passed through the shock tube 5 cm from the endwall and wavelength dispersed onto separate detectors. The indicated regions were nitrogen purged to eliminate absorption from water vapor in the ambient environment.

The direct measurement of T_5 using this diagnostic was precluded for shocks with pressure values greater than approximately 5 atm in Region 5. At sufficiently high pressures the absorption features begin to broaden and the ability to establish a baseline for the construction of the Voigt profile used in the temperature calculation becomes increasingly difficult. This problem was mitigated, however, through the utilization of AEROFROSH, a computational scheme previously developed in our group, which allows for the calculation of temperature and gas composition in regions 1, 2 and 5 based upon

the measured shock wave speed and the water absorption measurements[27]. Specifically, AERFROSH accounts for changes in the bulk fluid properties in Regions 1 and 2 due to the presence of the liquid phase; additionally, the decrease in the gas phase temperature caused by droplet evaporation in Region 2 is modeled. An inherent assumption of the AEROFROSH computation, however, is that complete droplet evaporation occurs in Region 2. To determine if this criterion was satisfied over the range of our experimental conditions we initiated a series of tests utilizing aerosolized water droplets and the non-resonant 665 nm laser. Complete droplet evaporation in Region 2 was assessed by examining the scattering signal from the 665 nm laser; an extinction value of zero in Region 2 would indicate complete droplet evaporation. Our experiments confirmed the evaporation process was complete in Region 2 for the conditions of interest, thereby validating the implementation of AEROFROSH for the calculation of post-shock conditions.

3.1.3 In situ diagnostics for monitoring of endospore morphology

Two continuous wave lasers at 665 nm and 266 nm were employed to monitor the structural and biological response of endospore laden bio-aerosols to gas dynamic shock waves. The visible laser at 665 nm is scattered by particulates in the flow while the ultraviolet 266 nm laser is both scattered and absorbed by UV active biochemicals. Therefore, the 665 nm signal provides time resolved information regarding the morphological state of the endospore while the 266 nm signal monitors the presence of bio-chemicals released into the flow.

In order to interpret the two laser signals and model their relation to the time evolution of the structural and biological state of the endospore, a modified Beer's Law following Equation 3 was developed[23]:

$$\left(\frac{I}{I_o}\right)_{665\,nm} = e^{-\alpha_{665\,nm}} = e^{-L\left(n_{SiO_2}\cdot\sigma_{SiO_2} + n_{Intact\,Spores}\cdot\sigma_{Intact\,Spores}\right)_{665\,nm}} \quad (4)$$

$$\left(\frac{I}{I_o}\right)_{266\,nm} = e^{-\alpha_{266\,nm}} = e^{-L\left(n_{SiO_2}\cdot\sigma_{SiO_2} + n_{Intact\,Spores}\cdot\sigma_{Intact\,Spores} + n_{Destroyed\,Spores}\cdot\sigma_{Aromatics}\right)_{266\,nm}} \quad (5)$$

The former equation models the visible laser extinction, α_{665nm}, attributed solely to scattering due to laser interaction with the SiO_2 beads and intact endospores in the flow. Once again following Equation 3, n_i and σ_i are the number density and the 665 nm scattering cross section of particle i, respectively. High temperature measurements conducted with bio-aerosols consisting purely of endospores indicated that there is no 665 nm absorption by biological compounds or the products of endospore pyrolysis. Consequently, the visbile cross section coefficient for destroyed endospores was neglected. Additionally, the SiO_2 bead morphology remains unchanged over the range of test conditions and, therefore, the silica bead cross section coefficient was assumed to be constant. Consequently, attenuation of the 665 nm beam can be attributed solely to scatter from the silica beads and the intact endsopores. The variation in the 665 nm transmitted signal, then, provides a time evolution of the morphological state of the endospore.

The latter equation, Equation 5, models the ultraviolet laser extinction, α_{266nm}, attributed to particulate scattering and absorption by UV active biochemicals. The essential characteristic of Equation 5 begins to manifest itself only in the high temperature regime where significant endospore morphological breakdown and rupture occur. The rapid structural damage experienced by the endospore behind the reflected shock wave results in the release of UV absorbing biochemicals into the environment[28,29]. This UV absorbing lysate, predominately composed of dipicolinic acid (DPA), deoxyribonucleic acid (DNA) and proteins, will quickly pyrolyze into stable aromatic products such as pyridine, purine and pyrimidine[30]. In the present context we have modeled the aggregate absorption of all UV active molecules released from a single destroyed endospore by a single cross section coefficient ($\sigma_{Aromatics}$). The presence of these UV active aromatics in the flow indicate the onset of endospore rupture. In addition, the variation of the UV laser absorption signal during the shock wave process provides pertinent information regarding the temporal evolution of endospore morphological breakdown. The temporal variation in the 266 nm transmitted signal, then, provides a time resolved measurement of the release of internal endospore constituents and complements the 665 nm data concerning the post shock morphological state of the endospore.

In order to implement the above equations, values for the absorption and scattering cross section coefficients need to be established. Details regarding this procedure can be found in McCartt et al.[23]. In addition, a more thorough account of this methodology can be found in Appendix AIII.

3.2 Ex situ analysis

As detailed in Chapter 2, each experiment resulted in the production of two particle laden suspensions: a pre-shock sample extracted from the shock tube prior to testing and a post-shock sample extracted after shock wave exposure. These two samples were subsequently subjected to ex situ analysis which served to complement the in situ laser diagnostic data as well as extend our knowledge of the biological response of endospores to shock heated flows. We employed three methods of ex situ analysis: flow cytometry for particle enumeration and morphological interrogation, agar plating for quantitative determination of endospore viability and scanning electron microscopy for qualitative assessment of endospore structural integrity.

3.2.1 Flow cytometry

Flow cytometry, a laser based technique for enumerating and assessing physical properties of microscopic particles, has been employed extensively in the biological sciences to analyze cellular apoptosis[31], division[32] and DNA content[33]. Within the present context, flow cytometry was employed to evaluate both the quantity of particles within the pre-and post-shock samples as well as the structural integrity of the shock treated endospores. During flow cytometry analysis a hydrodynamically focused stream of the endospore suspension is directed into the optical path of a set of lasers resulting in the scattering and/or absorption and re-emission of the laser light. A PMT detector in line with the laser records the forward scatter signal and a series of PMT detectors arranged perpendicular to the beam record the side scatter signal. Furthermore, the addition of a selective fluorescent chemical tag to the suspension results in laser excitation and the subsequent reemission of light at a longer wavelength than the excitation source. The

reemitted light is detected and, in the present context, provides additional information regarding the morphological state of the fluorescently tagged particle. Flow cytometry measurements were conducted at the Stanford Shared FACS Facility (SSFF).

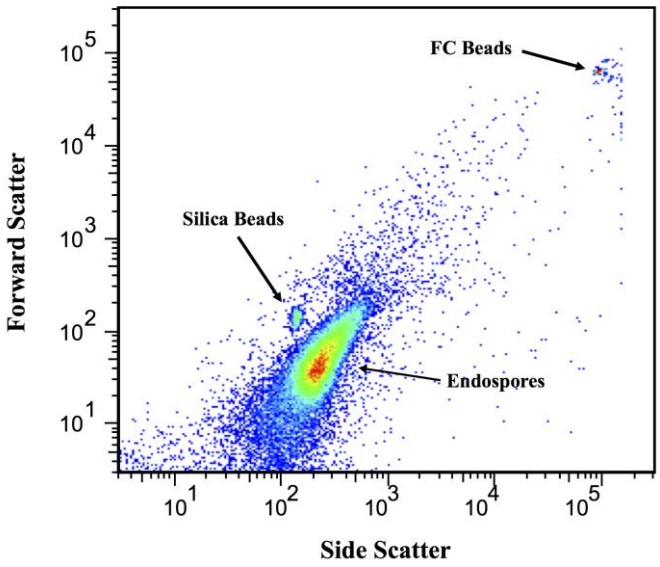

Figure 3-3: Typical flow cytometry data of endospore suspension indicating forward versus side scatter signals. The three distinct particle groups are clearly differentiated.

Flow cytometry data was employed to enumerate the particles in the pre- and post-shock samples as well as quantify the extent of shock wave induced endospore morphological breakdown through the inclusion of a deoxyribonucleic acid binding dye, propidium iodide. A four-laser BD Biosciences, model LSR II with laser excitation at 405, 488, 532 and 635 nm was employed in the current study. The analyzed samples were composed of three distinct particle groups: silica beads, endospores and flow cytometry beads. The latter group was added to the suspension after post-shock collection and served as a calibration tool to quantify the interrogated suspension volume. The flow cytometry bead suspension was prepared by the staff of the SSFF to a concentration of 10^9/ml. Data analysis was conducted using FlowJo commercial flow cytometry software. Particle differentiation and enumeration was obtained by examining the forward and side scatter signals; optical scattering signals being a function of the particle size, morphology

and the material refractive index. Based upon differences in these properties each particle set in the suspension occupied a distinct region in an optical scatter plot. A typical flow cytometry data set is shown in Figure 3-3. The three particle groups are clearly differentiated, allowing for unambiguous identification and enumeration. The wide spread in scatter values for the endospore group can be attributed to the natural variability in size and shape as well as the specific particle orientation at the time of laser exposure.

In addition to producing particle counts, flow cytometry was utilized to interrogate shock wave induced endospore morphological deterioration. To this end a deoxyribonucleic acid (DNA) fluorescent dye, propidium iodide (PI), was added to each sample prior to flow cytometry analysis. PI is, to a large extent, a membrane impermeant and has been employed as a live/dead assay for cellular population studies[31,34]. In the present context, however, the inclusion of propidium iodide fluorescent dye in the samples was used for the interrogation of intact but morphologically damaged endospores. Propidium iodide is a fluorescent agent that binds to DNA by intercalating between the base pairs[35]. There is no binding sequence preference and under normal conditions a PI molecule will bind to DNA once every five bases. Binding of the dye molecule to nucleic acids results in an approximately 25-fold increase in the fluorescence signal; in addition, the fluorescence excitation and emission maximum are shifted 40 nm to the red and 15 nm to the blue, respectively[35]. Excitation of propidium iodide is optimized at wavelengths between 450 and 500 nm; the laser at 488 nm was therefore utilized as the excitation source in our study. Excited PI electrons returning to the ground state generate the fluorescence emission at wavelengths between 550 – 750 nm[35]. The magnitude of the detected fluorescence signal provides an indication of the amount of DNA bound propidium iodide and is, therefore, correlated to the extent of endospore morphological deterioration. The data generated from the PI fluorescence signals, then, was utilized to corroborate and expand upon the 665 nm laser data monitoring the evolution of endospore structural decomposition.

While propidium iodide will preferentially bind to nucleic acids it has been suggested that reagents of this type will also bind to the proteinaceous endospore coat, the peptidoglycan cortex[6] and an insoluble shell below the proteinaceous coat termed a

rind[36]. Due to these considerations, an unambiguous interpretation of the specific biological components that were fluorescently labeled was precluded to some degree. What was important for our purposes, however, was the relative increase in fluorescent label incorporation as a result of shock wave exposure. All of the components identified as potential label binding agents, save for the proteinaceous coat, are interior to the endospore structure. Heightened endospore morphological deterioration would necessarily expose more structures amendable to fluorescent dye incorporation, including the nucleic acid laden core region. Therefore, by examining the relative fluorescent change between pre- and post-shock samples a qualitative and, to a certain degree, quantitative assessment of the extent of endospore morphological damage can be ascertained.

3.2.2 Viability analysis

Viability analysis of endospore suspensions was conducted at SRI International. 100 μl samples from a series of dilutions of the pre-shock and post-shock samples collected from the impingers were plated on nutrient agar (NA) plates for viable counts. After overnight incubation at 29 °C the colonies were counted. The plates then continued to incubate at room temperature for another 48 hours to insure colony count stabilization. For all experiments an inoculum control was tested. Furthermore, each sample was plated five times, at five dilutions, to produce a statistical distribution of viability results. The exposure of viable endospores to a nutrient environment induces germination and the subsequent formation of a bacterial colony. Viable counts were subsequently given units of CFU (colony forming unit) per ml of suspension. An inherent assumption in the assessment of the number of CFUs is that a given colony was formed by a single germinating endospore. Therefore, care was taken to plate the sample suspensions in an even manner to prevent the formation of dense areas of concentrated colonies on the agar plate.

Due to the variability in experimental conditions, specifically, loading pressures, the viable counts alone do not provide sufficient data to accurately quantify the extent of endospore deactivation. Each sample was therefore normalized by the pre-shock flow

cytometry particle count and a derived quantify, the viable fraction, was constructed. Viable fraction (V_f) is defined as the fraction of the initially viable spores that remain viable after shock-exposure. For experiments with T_5 less than some nominal value the endospore morphology remains largely unaltered and endospores in the collected samples can be directly counted by flow cytometry. For these shock treatments the viable fraction is given by:

$$V_f = \frac{S_p}{(S_{FC} * P_v)} \qquad (6)$$

S_P is the number of viable spores per ml in the post-shock sample measured by plating, S_{FC} is the number of intact spores per ml in the post-shock sample determined by flow cytometer and P_v is the fraction of viable spores in the pre-shock sample (typically 80-95%). For T_5 greater than an established nominal value the morphology for a significant number of spores is significantly degraded and the collected spores cannot be accurately assessed through flow cytometry. Consequently, within this temperature regime the employment of Equation 6 for the quantification of the viable fraction was precluded. This issue was mitigated through the addition of the aforementioned mono-dispersed one-micron SiO_2 beads. As previously detailed these particles remain undamaged over the full range of T_5 and are added to the spore suspension at a known spore-silica bead ratio (R). The viable fraction for the higher temperature shock experiments is then given by:

$$V_f = \frac{S_p}{(Si_{FC} * R * P_v)} \qquad (7)$$

We are able, therefore, to deduce the number of shock treated spores from the flow cytometry count of the silica beads (Si_{FC}) and the known spore-silica bead ratio (R). The viable fraction can then be determined as per Equation 7. For experiments with low and moderate values of T_5 Equation 7 can also be employed. The consistent agreement between viable fraction values calculated from Equation 6 and Equation 7 in the low and moderate temperature regime provides the basis for the sole employment of Equation 7 for viable fraction calculation in the high temperature regime.

3.2.3 Scanning electron microscopy (SEM)

Scanning electron microscopy micrographs were used to qualitatively characterize the morphology of shock-treated and untreated spores. An example of a SEM micrograph depicting an untreated endospore suspension is shown in Figure 3-4. Assessment of the SEM images provided significant information regarding the onset of endospore morphological breakdown and complemented the scattering and absorption signals from the laser diagnostic system. Details regarding the scanning electron microscope methodology and experimental parameters can be found in Appendix AIV.

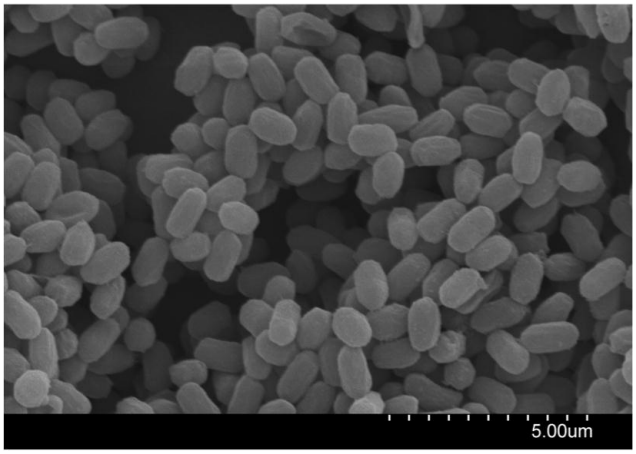

Figure 3-4: SEM micrograph of a pre-shock endospore suspension.

Chapter 4 Endospore response to gas dynamic shock waves

Utilizing the procedures and assessment methods detailed above, a series of bio-aerosol experiments were conducted to determine the dynamic biological and physical response of endospores exposed to shock-heated flows. As previously detailed, the passage of the incident and reflected shock waves generate an effectively instantaneous increase in the temperature and pressure of the environment. In addition, the flow undergoes rapid acceleration during this event. Inherent in our experimental construct is the coupling of these three potential damage mechanisms. In an attempt to isolate and attribute the effective contribution of each physical parameter to the measured reduction in endospore structural and biological viability, each potential damage mechanism was examined. Within the experimental framework employed for these studies, however, the systematic decoupling of acceleration, temperature and pressure effects was prohibitively difficult. A multitude of other studies examining the effects of isolated stress mechanisms were therefore employed to provide quantitative bounds for endospore survivability. Specifically, a study conducted implementing impactor schemes and bacterial cells has shown that extremely large accelerations ($\sim 10^{12}$ m/s^2), far exceeding those predicted in our experiments ($\sim 10^{8}$ m/s^2), are required to induce substantial reduction in biological viability[37]. Therefore, acceleration forces and their accompanying mechanical stresses were considered to lend a negligible contribution to endospore breakdown and loss of viability. Furthermore, it is well established that endospores are largely insusceptible to morphological breakdown and viability reduction at pressures less than 1000 atm[38,39]; two orders of magnitude greater than our experimental pressure range of interest.

Considering the aforementioned conclusions, then, the measured reduction in the endospore structural integrity and biological viability was solely attributed to the step change in temperature associated with the passage of the reflected shock wave. Consequently, the viable fraction as quantified through the aforementioned ex situ analysis techniques was plotted versus the measured post shock temperature (T_5).

A variety of endospore species and test conditions were employed in the current study, with experiments developing towards the implementation of architecturally complex endospores in a simulated air environment. Pertinent results from each experiment will first be detailed, followed, thereafter, by the development of an interpretive qualitative framework for modeling the interaction of bio-aerosols with gas dynamic shock waves in a natural environment. While emphasis is placed upon the results obtained from the ex situ methodology, complementary and relevant data obtained from the in situ diagnostics will also be employed to help elucidate the endospore response to gas dynamic shock waves.

4.1 Bacillus atrophaeus

Bacillus atrophaeus endospores were tested in an inert bath gas environment for the initial set of experiments. The data set generated detailing the variation of the viable fraction as a function of post-shock temperature is shown in Figure 4-1. Error bars indicate one standard deviation based upon the viable counts. Readily apparent is the rapid decrease in viable fraction with increasing temperature. This behavior, corresponding to a roughly linear trend on a semi-log plot, is indicative of endospore response to stress catalysts and has been observed in other studies[3]. As will be further analyzed in subsequent sections morphological deterioration is not initiated until elevated temperatures. Consequently, at low to moderate temperatures direct endospore enumeration with flow cytometry is possible. In this temperature regime then, the viable fraction value can be calculated with both Equation 6 and 7. Good agreement is noted between the indirect viable fraction calculation conducted with the silica beads (triangles) and those done with direct endospore counts (circles). At temperatures greater than

approximately 700 K, however, enumeration of the endospore count by flow cytometry is precluded due to structural deterioration of the particle. Consequently, quantification of the viable fraction within this region was done solely with Equation 7. In addition to the experiments detailed in Figure 4-1, a test conducted with a post- shock temperature of 1018 K yielded a viable fraction value of zero, providing an upper temperature bound for endospore viability in this environment.

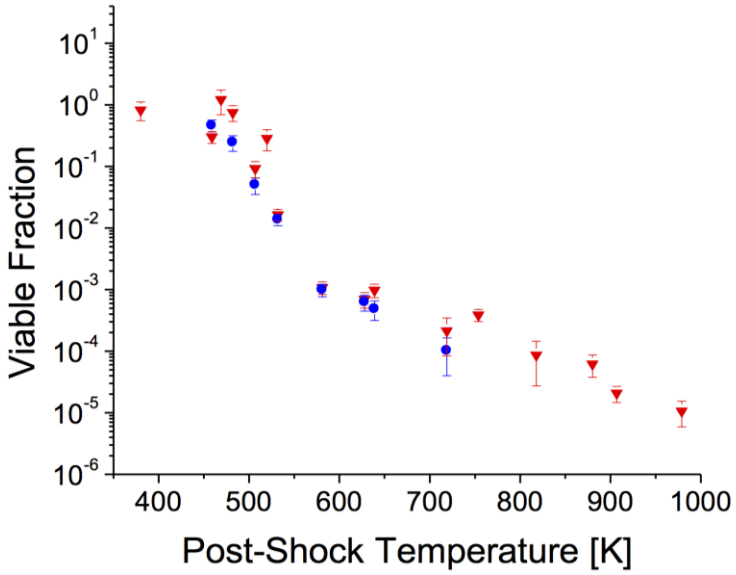

Figure 4-1: Viable fraction as a function of post-shock temperature for *B. atrophaeus*. Circles are data points calculated using direct flow cytometer spore counts. Triangles are data points calculated using silica bead flow cytometer counts. The data displays a roughly linear trend on a semi-log plot.

Further insight into the endospore structural and biological response to shock wave exposure can be gained by examining the change in the flow cytometer fluorescence signal as a function of post-shock temperature. For illustrative purposes the direct flow cytometer data is shown with the corresponding fluorescence signal distribution. Figure 4-2 illustrates flow cytometer results for a pre- (A) and post-shock (B) sample for $T_5 \sim 520$ K. The relatively large fluorescence scatter of endospores seen in the pre-shock sample can be attributed to the nonspecific incorporation of the PI dye previously addressed. For the purposes of our analysis we are interested in examining the

relative change in fluorescence signal levels between the two samples. A qualitative assessment of the flow cytometry images indicates that the pre- and post-shock samples display endospore regions at relatively consistent levels of fluorescence, indicating low levels of endospore morphological deterioration. Furthermore, the histograms demonstrate a moderate increase in fluorescence levels, confirming the qualitative assessment. Variation in histogram counts can be attributed to the experiment specific loading conditions and impinger sampling time.

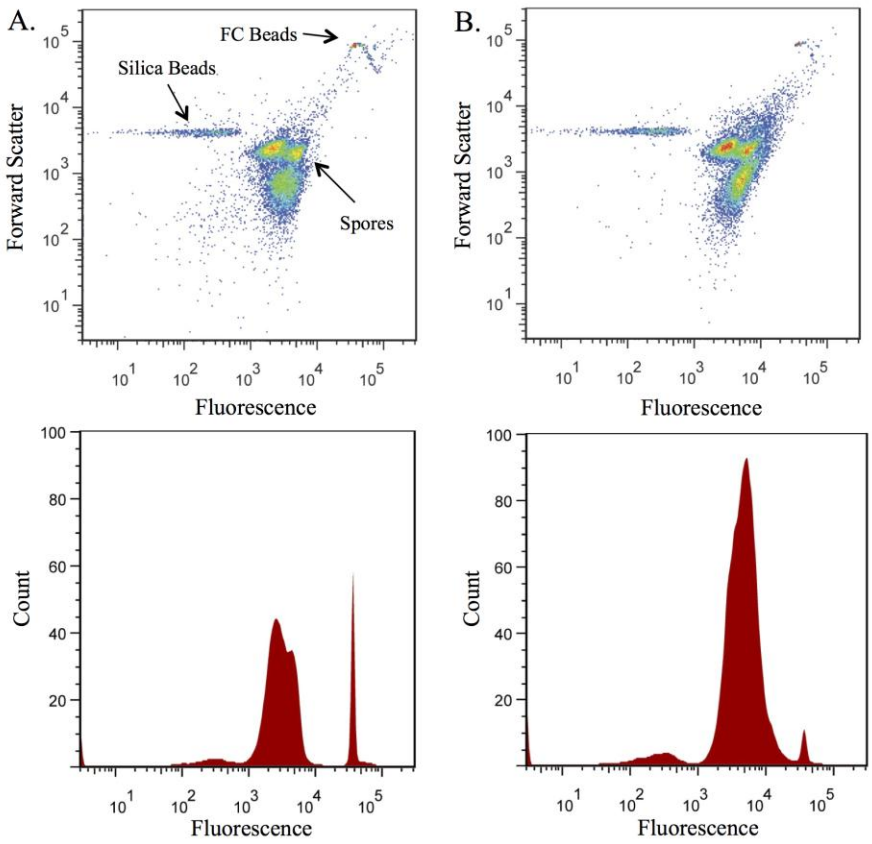

Figure 4-2: Flow cytometry fluorescence data for a *B. atrophaeus* pre- (A) and post-shock (B) sample. The post-shock temperature was approximately 520 K. A slight shift in the fluorescence signal in the post-shock sample indicates minimal levels of morphological damage.

Analysis of post-shock samples from higher temperature experiments indicate increased morphological damage and, consequently, higher fluorescence signals. Figures

4-3C and D illustrate flow cytometry data from two post-shock samples with a T_5 of 605 K and 675 K, respectively. The corresponding pre-shock samples displayed a quantitatively analogous distribution of fluorescence signal as that shown in Figure 4-2A. In Figure 4-3C we begin to see the formation of a secondary histogram spike at a fluorescence signal level of approximately 10^4, indicating increased levels of PI binding and the onset of extensive morphological deterioration. The progression of the structural decomposition process can be seen by examining the data shown in Figure 4-3D; the minor fluorescence feature near 10^4 seen in Figure 4-3C has now become a dominant feature in the plot.

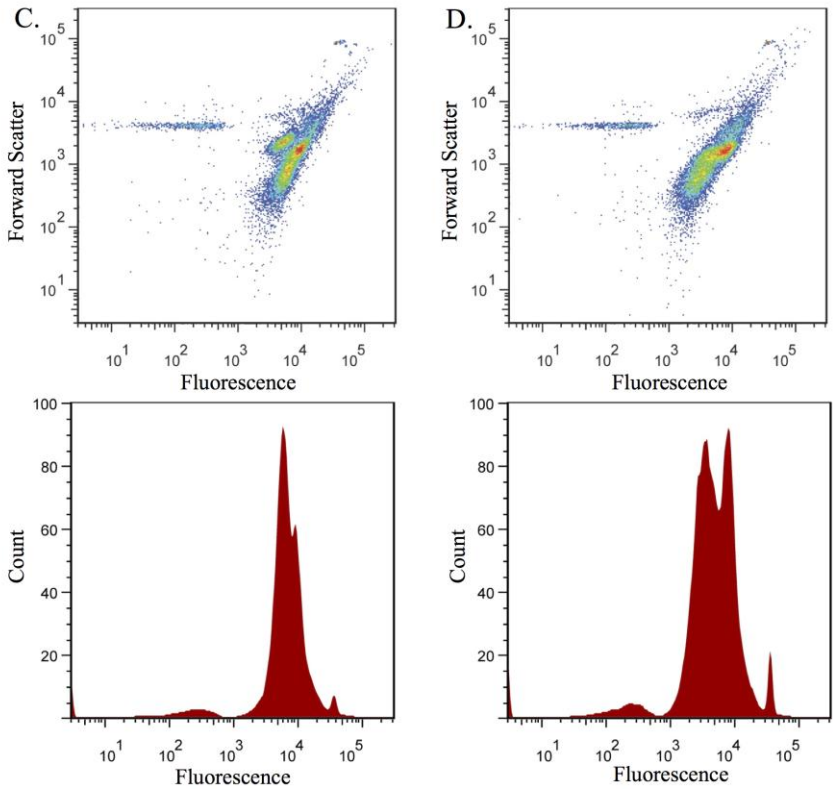

Figure 4-3: Flow cytometry fluorescence data for *B. atrophaeus* exposed to shock waves with a post-shock temperature of 605 K (C) and 675 K (D). The increase in fluorescence signal can be attributed to the decrease of endospore morphological integrity and the exposure of endospore constituents, including the DNA, susceptible to propidium iodide binding.

The increased fluorescence levels may be caused by a multitude of morphological damage mechanisms. Endospore interaction with the shock wave may have induced the deterioration of the proteinaceous coat and subsequently increased the exposure of the rind or spore cortex to the dye molecules. Additionally, the impermeability of the inner membranes may have been compromised leading to the introduction of the PI dye directly into the endospore core resulting in substantial staining of the nucleic acids. In all likelihood both of these potential damage mechanisms are interrelated and exist to varying degrees in the post shock samples. Whatever the biological components being affected it is apparent that at low and moderate temperatures where the endospores remain intact after shock exposure, this trend of increased morphological deterioration as T_5 increases is a characteristic phenomenon.

In order to gain a unified perspective of the shock wave induced damage to the endospore particle, the viable fraction data is presented in conjunction with both the flow cytometer measurements concerning the incorporation of PI dye as well as the 665 nm laser scattering data. Figure 4-4 details the combination of these three measurement techniques. The viable fraction (triangles) values from Figure 4-1 were converted to percentages and are plotted on a linear scale. In addition, the percentage of intact endospores obtained from the 665 nm laser data is plotted (circles). The most prominent characteristic of Figure 4-4 is the large discrepancy between the structural integrity and biological viability of the endospore in the 500-750 K post-shock temperature regime. Viable fraction levels are near zero at post-shock temperatures above 500 K. The visible laser diagnostic, however, maintained a high level of extinction indicating little to no endospore breakup below 750 K. These data suggest that for temperature treatment between 500 and 750 K, the majority of endospores remain intact but are no longer viable. This indicates a mechanism of endospore inactivation that does not significantly alter the endospores' overall morphological structure. Temperatures above this regime lead to the rapid breakdown of endospore morphology, as determined with flow cytometry and confirmed by both visible laser scattering and UV laser absorption of lysate material. While the morphological structure of the endospore may be largely undamaged in the post-shock temperature range of 500 to 750 K, the increased PI dye

uptake demonstrated at a T_5 value of approximately 520 K indicates the presence of endospores whose structural integrity has been compromised.

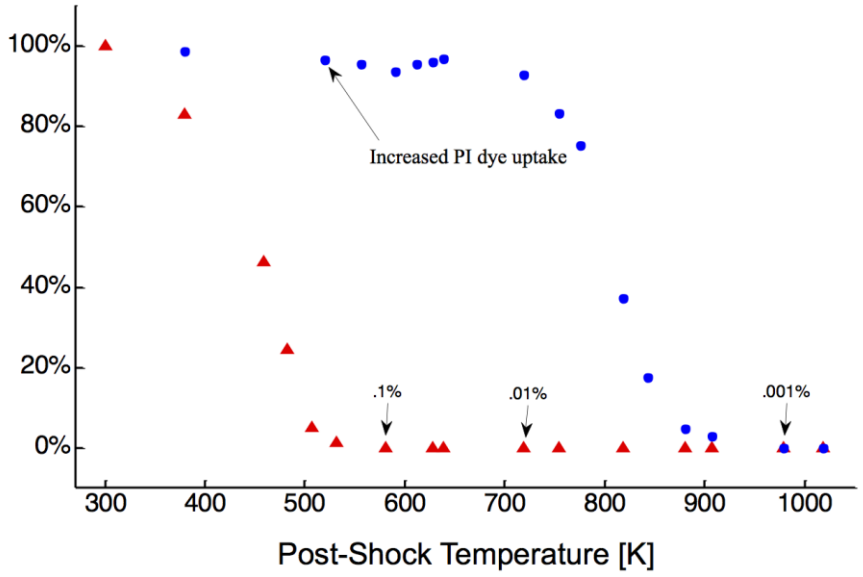

Figure 4-4: Viable fraction and intact endospore percentage as a function of post-shock temperature. Circles represent the percentage of intact endospores as assessed by the 665 nm scattering signal. Triangles indicate the percentage of viable endospores. There exists a substantial reduction in endospore viability before the onset of large-scale structural decomposition.

4.2 Bacillus subtilis and oxidative environments

In response to the results from the first set of *B. atrophaeus* data detailed above, we developed a set of experiments to:

1) Replicate the previous data utilizing a structurally similar endospore strain.
2) Implement the first steps in elucidating the mechanism of deactivation for morphologically intact endospores.
3) Extend the gas composition to oxidative agents as a step towards replicating a natural environment.

To this end, we obtained, from Dr. Peter Setlow at the University of Connecticut, a new endospore species, *B. subtilis* PS533. Performing experiments with an additional endospore species allowed us to determine if the rate of viability reduction as a function of post-shock temperature is species specific or could be more broadly applied to a class of endospores with similar structural composition. In addition to sharing a similar architectural structure with the previous tested species, *B. subtilis* PS533 has been extensively studied and a breadth of mutants lacking specific proteins and biological components have been generated[5]. The established knowledge linking gene-to-gene product would enable us to selectively test endospores deficient in a variety of structural components as well as biological pathways. Through these tests the specific biological mechanism being disrupted prior to morphological breakdown may be identified. The initial step, however, required the satisfaction of our first objective: method validation and result reproducibility. These experiments also served to characterize the *B. subtilis* wild type response, establishing a baseline for possible future genetic experiments. Along with the aforementioned experiments employing the *B. subtilis* strain, tests were performed with *B. atrophaeus* in an oxidative gas environment. An air stimulant driver bath gas consisting of 21% oxygen in argon was employed to determine if the presence of an oxidizing gas would increase the loss of viability and/or rate of morphological deterioration.

The *B. subtilis* strain experiments along with the air stimulant driver bath gas tests resulted in the viable fraction plot in Figure 4-5. An additional *B. atrophaeus* data set produced from experiments conducted in an inert gas environment is plotted for comparative purposes. The data sets clearly indicate a consistent behavior between the two strains. Therefore, it is reasonable to hypothesize that wild type endospores of related species sharing similar structural compositions would exhibit a consistent characteristic relation between viable fraction and post-shock temperature. In addition, the coherent behavioral response of *B. atrophaeus* to inert and oxidative gas environments indicates that the loss of endospore viability and morphological breakdown may primarily be a temperature/time dependent phenomenon. These hypotheses are furthered reinforced by examining the flow cytometer results.

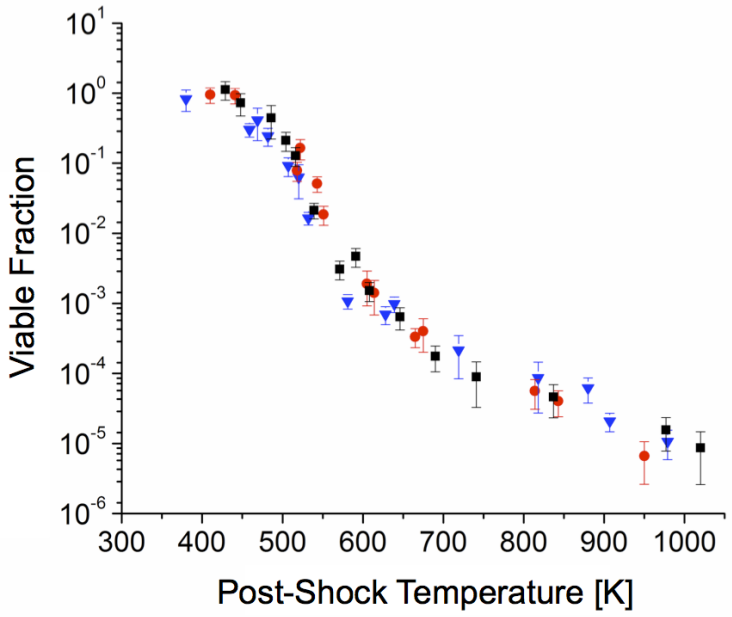

Figure 4-5: Viable fraction plotted versus post-shock temperature (T_5) for a test time of 2.5 ms. Triangle: *B. atrophaeus* inert gas environment. Circle: *B. subtilis* inert gas environment. Square: *B. atrophaeus* oxidative environment.

B. atrophaeus exposed to an oxidative shock environment exhibited quantitatively similar levels of morphological deterioration as those produced in the *B. atrophaeus* inert gas experiments. A representative sequence of flow cytometry data for *B. atrophaeus* exposed to an oxidative shock is shown in Figure 4-6. Data from a test with a T_5 of 450 K demonstrates the relatively consistent fluorescence levels for the pre-and post-shock samples, indicating low levels of endospore morphological deterioration. Post-shock samples from the 580 and 650 K tests, however, indicate the onset of increased morphological damage and the corresponding higher fluorescence signals. The progressive increase in fluorescence levels closely follows those shown in Figures 4-2 and 4-3. In addition, the 665 nm laser scattering data corroborates the aforementioned observations; the rate of endospore morphological decay in inert and oxidative environments is quantitatively similar[40]. Consequently, both the loss in endospore viability and the rate of morphological damage are characteristics not dependent upon the presence of an oxidizing agent in the flow.

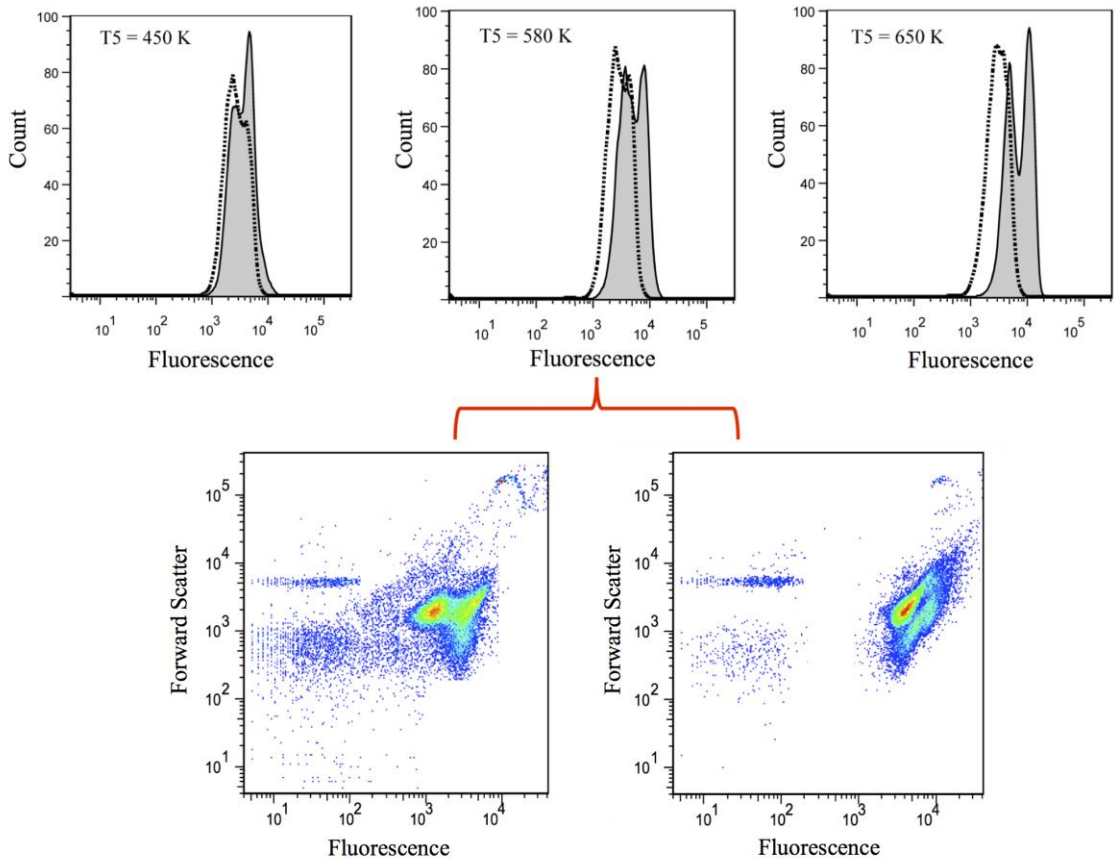

Figure 4-6: Sequence of flow cytometry fluorescence histograms for a *B. atrophaeus* aerosol exposed to post-shock temperatures of 450, 580 and 650 K in an oxidative environment. The raw data used to generate the histogram for the 580 K shock is also shown. The rate of morphological decomposition in this environment closely paralles that seen for *B. atrophaeus* in an inert gas environment.

4.3 Biological interpretation of laser time histories

The 266 and 665 nm laser measurements provide time-resolved data concerning the dynamics of the bio-aerosol/shock wave interaction. Specifically, this methodology enables in situ monitoring of the initiation and progression of endospore morphological deterioration and rupture behind the reflected shock wave. It is instructive, then, to examine and interpret the laser time histories within the context of the corresponding SEM micrographs. To this end, the time resolved laser signals are coupled with a

qualitative analysis of the structural integrity of the post-shock endospore samples as assessed by scanning electron microscopy.

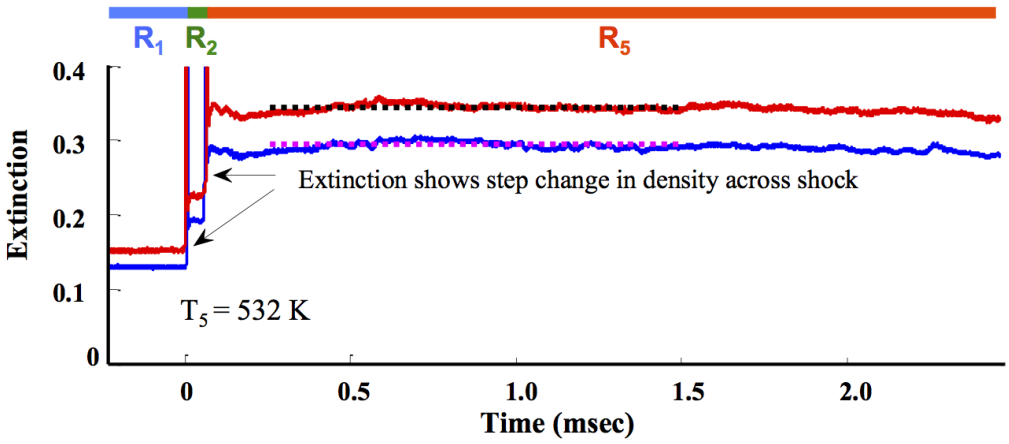

Figure 4-7: 266 nm (blue) and 665 nm (red) laser time histories for a bio-aerosol/shock wave experiment resulting in a post-shock temperature of 532 K. The consistent level of 665 nm extinction in Region 5 indicates the lack of substantial endospore morphological decomposition.

The time evolution of the 266 nm (blue) and 665 nm (red) laser extinction signals during an experiment resulting in a test temperature of 532 K is shown in Figure 4-7. The three distinct regions - R_1, R_2, R_5 - are as previously defined. The discontinuous nature of the signal during the arrival of the incident and reflected shock wave, termed Schlieren spikes, is a result of beam steering due to high - density gradients. Furthermore, the elevated level of extinction between R_1 and R_2 is the result of the rise in density from the passage of the incident shock wave, the rise between R_2 and R_5 similarly results from the reflected shock wave. The dashed lines in Figure 4-7 indicate the expected levels of extinction based upon the calculated density levels from the shock jump equations. As previously mentioned, a T_5 value of 532 K would not result in morphological breakdown or endospore rupture. Consequently, both the 266 and 665 nm laser signal maintain stable extinction levels for the duration of the test time. To gain a qualitative understanding of the endospore structural response to the shock wave, a sample of the post-shock suspension was examined with the SEM. A typical image is shown in Figure 4-8. The

endospores are intact and a comparison with Figure 3-4 demonstrates that effectively no discernible morphological damage has been incurred as a result of the shock wave interaction.

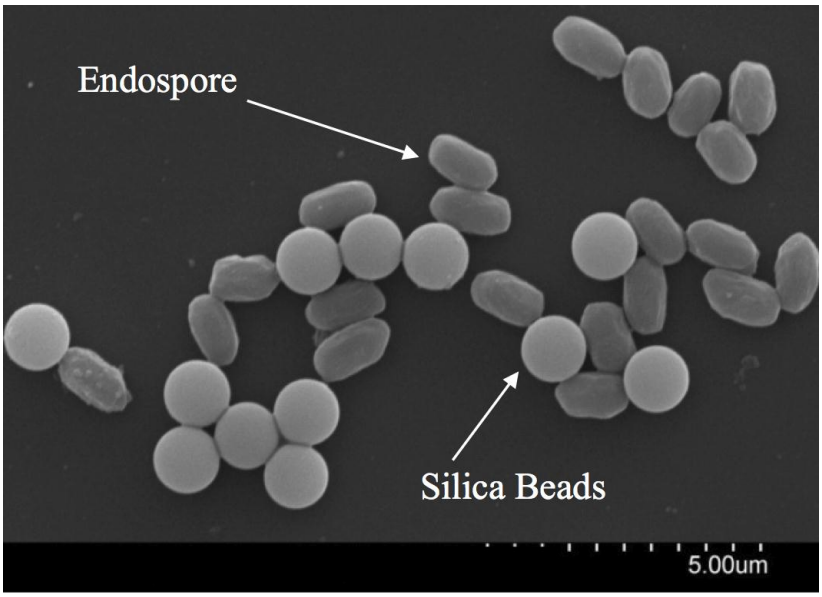

Figure 4-8: Scanning electron microscope image of a post-shock sample (T_5 = 532) corresponding to the laser data shown in Figure 4-7. The endospores are structurally intact, corroborating the 266 nm and 665 nm laser signals.

At progressively higher post-shock temperatures, however, the breakdown of endospores and the release of lysate behind the reflected shock wave become apparent. Figure 4-9A details the laser time histories for a T_5 of 843 K. The steady decrease in the 665 nm laser indicates the morphological degradation of the endospore while the sustained level of the 266 nm laser provides evidence of the release of UV active bio-chemicals into the flow. As detailed in Chapter 3 the UV laser extinction is due to a combination of particulate scattering and lysate absorption. In the high temperature regime, then, the long time 266 nm signal displays the interplay between extinction reduction due to particle breakdown and extinction increase due to the release of UV active lysate. Extension of the experiments to higher temperatures, Figure 4-9B, results in a more rapid decrease in the 665 nm signal due to the increased rate of endospore structural decomposition. This characteristic behavior provides significant details

regarding the decay rate of endospores behind shock waves and is further explored in McCartt et al.[23]. The sustained extinction level for the 266 nm laser is, once again, indicative of the presence of UV absorbing molecules released upon endospore rupture. Furthermore, the stabilization of the 665 nm extinction signal to a non-zero value is attributed to the scattering from the silica beads.

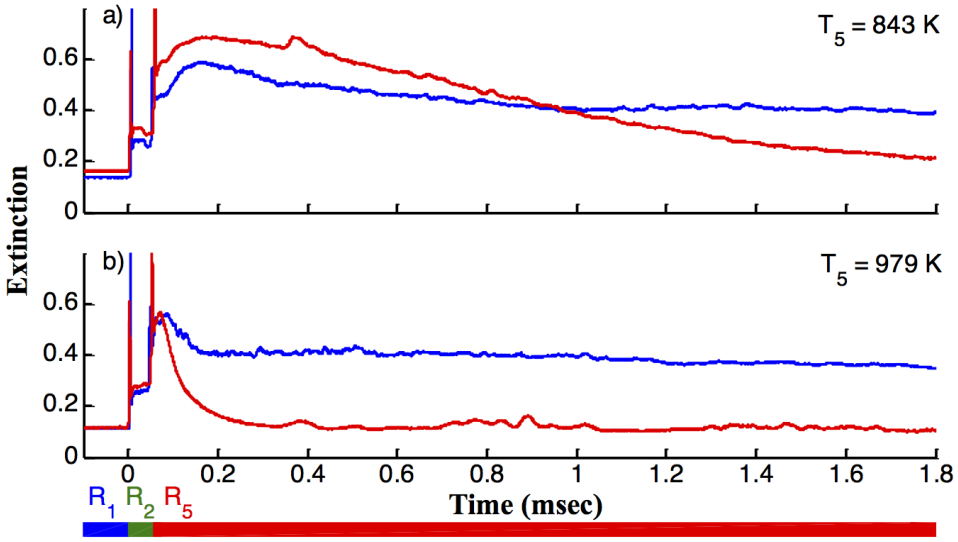

Figure 4-9: Extinction (α_i) as a function of time for the 266 nm and 665 nm lasers. The decreasing extinction at 665 nm is indicative of endospore breakdown behind the reflected shock wave. The rate of endospore decomposition is more rapid at higher post-shock temperatures. The sustained extinction levels at 266 nm are attributed to UV absorption by pyrolyzed endospore biochemicals.

Complementing the high temperature laser diagnostic data are additional SEM images illustrating the process of endospore morphological breakdown. An example micrograph is shown in Figure 4-10A from a post-shock sample with a T_5 of 830 K, correspondingly closely to the temperature in Figure 4-9A. The spherical silica beads as well as a number of endospores are visible. In addition, the presence of an additional bulk substance is apparent; these structures are presumably composed of the products of endospore deterioration including the UV active nucleic and dipicolinic acids. No such conglomerations were observed in samples treated in the low to moderate temperature

regime (~500-750 K) where substantial endospore breakdown is precluded. Furthermore, referencing Figure 4-4, approximately 20 percent of endospores will retain their morphological integrity at this temperature, corroborating the observation of a number of intact but structurally compromised endospores in the image. The SEM images from high temperature experiments also corroborate our flow cytometer data indicating that the silica beads remain undamaged in the high temperature regime. Micrograph images produced from post-shock suspensions with T_5 near 1000 K show only silica beads and endospore decomposition products. As demonstrated in Figure 4-10B, large aggregations of lysate material are seen after centrifugation of high temperature post shock samples. This observation corroborates the laser time history shown in Figure 4-9B indicating complete endospore morphological decompostion and the release of UV active lysate. Furthermore, no intact endospores were observed in SEM images of post-shock samples within the high temperature regime (~ 900 K and above). A more detailed analysis of the laser time histories can be found in McCartt et al.[23].

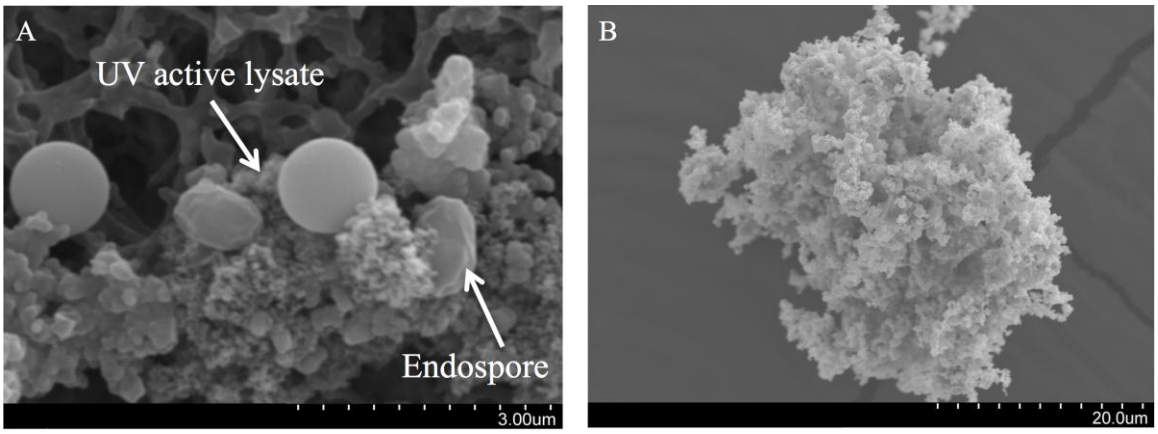

Figure 4-10: SEM micrographs of post-shock samples with a T_5 of approximately 830 K (A) and 1000 K (B). These samples correspond closely to the laser data shown in Figure 4-9. At the lower temperature lysate material as well as intact endospores are readily apparent. The background substrate seen in image A is the filtering matrix used during sample preparation. At the elevated temperature no endospores were observed, only conglomerations of UV active lysate. These observations corroborate the 266 nm and 665 nm laser time histories in Figure 4-9.

4.4 Effects of extended test time

An additional set of experiments was undertaken to determine the endospore response to extended exposure to the elevated post-shock temperature T_5. All of the experiments previously detailed had sustained post-shock temperatures for 2-3 ms, after which a variety of expansion processes led to a rapid temperature decay[18]. By implementing tailored nitrogen/helium driver gas mixtures and an extended driver section, we were able to delay the onset of temperature decay by approximately 40 ms. Utilizing this technique enabled us to expose the bio-aerosol to the elevated post-shock temperatures for a substantially longer time period. The *B. atrophaeus* viability results for this experiment are detailed in Figure 4-11 along with a short test time data set for comparison. The data sets are consistent for post-shock temperatures below approximately 600 K. As has been previously noted this temperature regime induces a rapid drop in viability without significant morphological deterioration. The correspondence between the data sets over this specific temperature range suggests that the viability reducing mechanism acts over a short time scale (2-3 ms). Significant deviation, however, is noted at the moderate temperature levels between 600 and 700 K. The long test time data continues to follow the low temperature trend (solid line) while the short test time results (dashed lines) demonstrate a decreased rate of viability loss. Specifically, the viable fraction value for the long test time experiment with a T_5 of approximately 650 K would correspond to a short test time viable fraction value at a temperature near 900 K. While discrepancies exist between viability levels in this temperature regime, flow cytometry analysis and 665 nm laser data from both the short and extended test time experiments indicate consistent levels of morphological damage. With extended test time experiments in the moderate temperature regime, then, viable fractions quantitatively similar to short test time data sets are achieved at significantly lower temperatures and without the onset of severe structural breakdown.

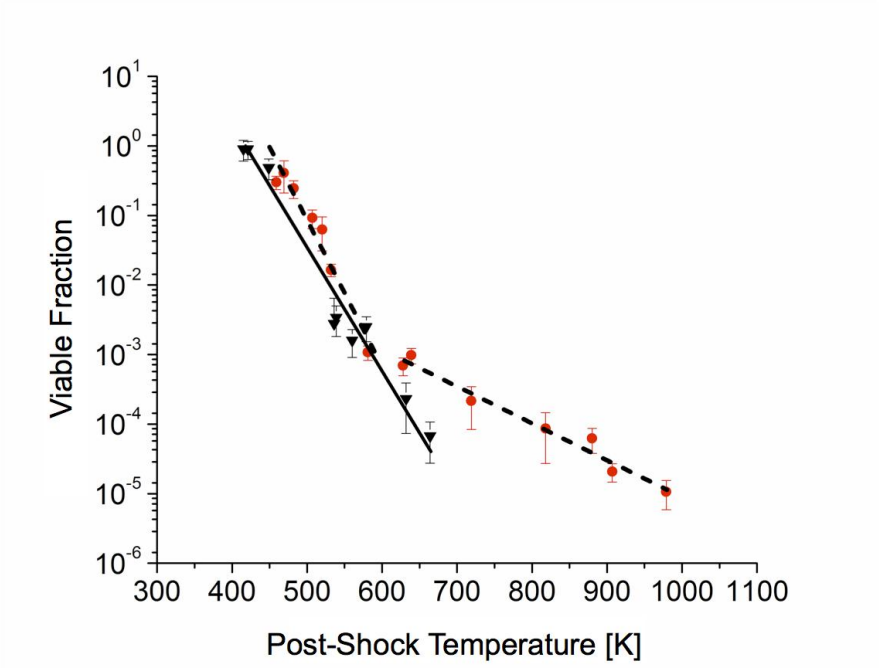

Figure 4-11: Viability results: *B. atrophaeus* argon shock test time variation. Circles: Short test time (~2.5 ms). Triangles: Long test time (~ 45 ms). For long test times in the moderate temperature regime, significantly lower levels of endospore viability were observed. The rate of endospore morphological decomposition was, however, comparable to the levels observed during the short test time experiments.

4.5 Bacillus thuringiensis

A series of experiments employing *B. thuringiensis* – Al Hakam endospores was initiated in order to examine the response of a more architecturally complex endospore species to gas dynamic shock waves. These experiments were designed to serve a twofold purpose; the first being to determine if the rate of endospore viability reduction and morphological breakdown as a function of post-shock temperature was a feature largely independent of physical constitution. In addition, these experiments were implemented to model the response of *B. anthracis* to shock heated flows; *B. thuringiensis* being the laboratory model for *B. anthracis*[41,42]. Compared to the previous species studied, *B. thuringiensis* endospores are larger, possess a thin cell coat and exhibit an architectural

network composed of a crystalline hexagonal honeycomb mesh encased in a flexible exosporium[43]. The BT endospores were obtained from Dr. Tony Buhr at the Naval Surface Warfare Center – Dahlgren and were grown using the sporulation protocol detailed in Appendix AV.

As previously detailed, the shock wave bio-aerosol interaction was monitored with in situ optical diagnostics, and the pre- and post-shock *B. thuringiensis* endospore suspensions were subjected to ex situ examination including viability and flow cytometer quantification as well as scanning electron microscopy analysis. Images of pre- and post-shock samples generated with the SEM are shown in Figure 4-12. A nebulized pre-shock sample extracted from the shock tube through the gas dynamic impinger is shown in the first image. The exosporium and overall structure of the endospore remained intact and uncompromised. Furthermore, viability analysis indicated no reduction in BT colony counts as a result of the nebulization and sampling procedure. The morphological effect of exposure to a shock wave generating a post-shock temperature of 500 K is demonstrated in image B. As was found in previous studies, the endospores within post-shock samples of low temperature experiments exhibited virtually no morphological deterioration. In addition, intact exosporiums are clearly visible. With increased post-shock temperatures, however, the onset of structural deterioration is observed. Image C illustrates the effect of endospore exposure to a post-shock temperature of 630 K. While the overall structure of the endospore remains intact the exosporium is absent and prominent morphological changes have become apparent.

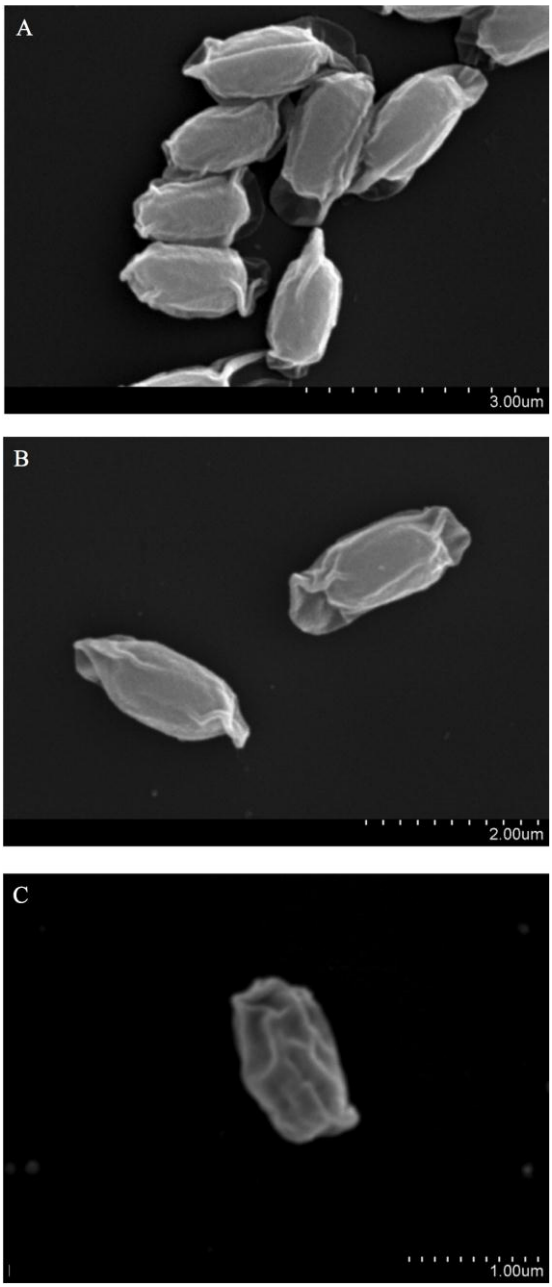

Figure 4-12: SEM micrographs of *B. thuringiensis* endospores. Image A is of a pre-shock sample. The nebulization and sampling procedure were shown to not adversely affect the exosporium. Post-shock samples from experiments with a T_5 of 500 K (B) and 630 K (C) are shown. The presence of the exosporium in image B is readily apparent. Endospore structural changes are observed in image C, including the lack of an exosporium and apparent surface morphological deterioration.

Viability analysis of pre- and post-shock samples was performed in order to elucidate the biological response of *B. thuringiensis*-Al Hakam to shock heated flows. Figure 4-13 details *B. thuringiensis* viability results along with data from previous *B. atrophaeus* and *B. subtilis* tests in an inert gas environment. The data sets indicate an analogous trend in viability reduction between the three species. While the previously presented data has demonstrated the consistent reduction in biological functionality of wild type endospores of related species sharing similar structural compositions, the data illustrated in Figure 4-13 indicates that this characteristic viability response can be applied to species with significantly different physical constitutions. This hypothesis is further reinforced by examining the in situ optical measurements.

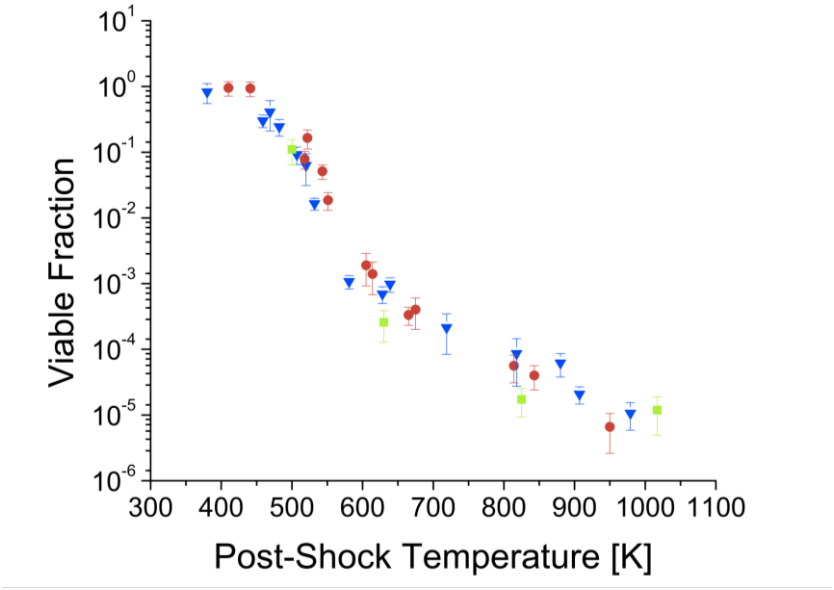

Figure 4-13: Viable fraction plotted versus post-reflected shock temperature (T_5) for a test time of 2.5 ms. Triangle: *B. atrophaeus*. Circle: *B. subtilis*. Square: *B. thuringiensis* Al Hakam. *B. thuringiensis* displays a quantitatively similar reduction in viability as compared to the two other tested species. The disparate structural constitution of the analyzed species does not appear to contribute significantly to shock wave resistance.

The in situ optical diagnostics detailed in Chapter 3 were employed to monitor the real time response of *B. thuringiensis*-Al Hakam endospores to shock heating. Pertinent data regarding the structural integrity of the endospore was extracted from the long time

665 nm extinction signal level. Specifically, the fraction of intact endospores as a function of post-shock temperature (T_5) was quantified and is shown in Figure 4-14.

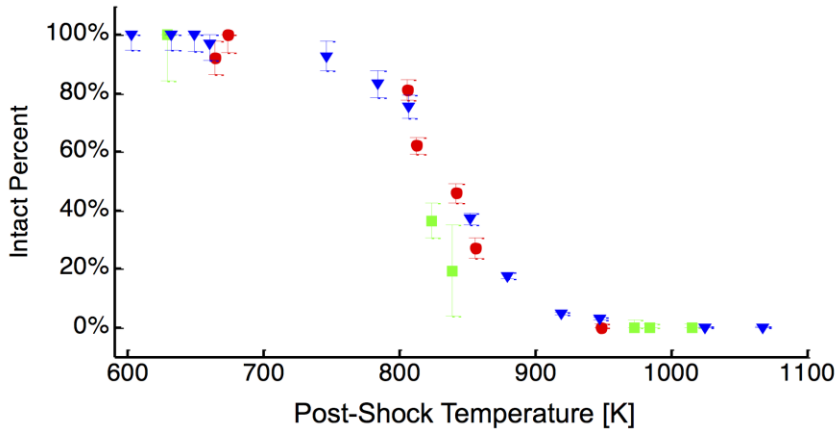

Figure 4-14: Percentage of endospores morphology that remain intact after the high temperature Region 5 test time plotted versus post-reflected shock temperature (T_5). Triangle: *B. atrophaeus*. Circle: *B. subtilis*. Square: *B. thuringiensis*-Al Hakam. The data indicates a similar rate of structural decomposition across all species considered.

Similar to the structural response of *B. atrophaeus* and *B. subtilis* endospores, *B. thuringiensis* exhibited a rapid rate of structural decomposition between 700 and 900 K. For all species, negligible morphological damage was incurred for tests with T_5 below 700 K, while complete morphological deterioration was observed for experiments with T_5 greater than 900 K. Consequently, the ex situ and in situ results indicate that the *B. thuringiensis*-Al Hakam response to gas dynamic heating is quantitatively similar to previously tested species.

While the viability and structural decomposition kinetics of the *B. thuringiensis* species exhibited an analogous trend with the other analyzed species, noticeable discrepancies existed between the 266 nm time histories. As previously detailed, the 266 nm laser light is absorbed by UV active bio-chemicals released upon endospore rupture. In comparison to the latter two species, the long time 266 nm extinction signal for high temperature shocks with *B. thuringiensis* endospores exhibited a substantial reduction[44].

While the 266 nm laser response would seem to indicate the absence of ruptured endospores, the 665 nm signal and the corresponding derived intact percentage quantity depicted in Figure 4-14 precluded this possibility. Consequently, these data indicate a lack of UV active bio-chemicals in the *B. thuringiensis* endospore. It is, however, well established that differing growth conditions and environments can lead to large discrepancies in the chemical constitution of endospores[45]. Therefore, it is a distinct possibility that the disparate chemical signature of this specific species can be attributed to its unique growth environment. While the amount of released UV active chemicals deviated markedly from the previously tested strains, the shock wave induced biological and morphological breakdown rates between the three species were quantitatively consistent.

Chapter 5 Conclusion and future work

5.1 Conclusion

Results of the experiments detailed above enabled us to formulate a conceptual framework for interpreting and predicting the response of endospore-laden bio-aerosols exposed to gas dynamic shock waves. Quantitative analysis of both the shock-heated endospore viability and the structural breakdown rates performed on the *B. subtilis*, *B. atrophaeus* and *B. thuringiensis*-Al Hakam yielded consistent results. In addition, experiments conducted in inert and oxidative gas environments were comparable. Consequently, an interpretive framework for modeling the endospore response to shock heated flows in a variety of environments was formulated. The three-tiered framework consists of the following damage levels:

1. Weak shocks (T_5 < 500 K) cause minimal morphological damage to the endospores and a significant fraction of the collected post-shock endospores remain viable.
2. Moderate shocks (500 K < T_5 < 750 K) cause a rapid rate of decline in viability and a corresponding but significantly slower rate of severe endospore morphological breakdown.
3. Strong shocks (T_5 > 750 K) cause a near complete loss of viability and the majority of endospores experience rapid morphological deterioration coupled with the release of UV active lysate.

The existence of a rate differential between the loss of viability and morphological breakdown indicates that essential biological mechanisms are being disrupted prior to the onset of major endospore structural damage. The majority of endospore viability loss most likely results from temperature induced protein denaturation, resulting in the disruption of pathways critical for germination and outgrowth. Consequently, a four-log reduction in viable fraction was observed before the onset of significant morphological damage. The data presented herein indicates that this framework applies to bio-aerosol shock heating experiments satisfying the following criteria:

1) Bio-aerosol composed of endospores structurally similar to either *B. atrophaeus* or *B. thuringiensis*
2) Test conducted in an inert or oxidative gas environment
3) Test conducted with short test times (> 10 ms)

Bio-aerosols exposed to test times of approximately 45 ms, produced results that deviate from the previous experiments but are still consistent with the aforementioned framework. In comparison to the long test time experiments, quantitatively similar viability levels can only be achieved during short test time tests at significantly higher temperatures and accompanied by severe structural deterioration. For extended test-time experiments, then, a slight modification to the second stage of the endospore damage framework is warranted: the rate differential between loss of viability and severe endospore morphological breakdown is significantly increased. The vast majority of viability loss precedes extensive morphological breakdown caused by substantial coat protein denaturation at elevated temperatures.

The totality of the results reinforces our hypothesis that loss of endospore viability is largely a temperature/time dependent phenomenon induced by protein denaturation and the subsequent disruption of biochemical pathways essential for germination and outgrowth. While the reduction in viability is a function of temperature and duration of exposure, the morphological state of the endospore after interaction with the shock-heated flow appears to be solely correlated to the post-shock temperature.

5.2 Future work

In order to extend the methodology presented in the present work, two specific areas of future study have been identified. The first concerns the determination of the specific endospore components or processes that are being disrupted by the shock wave process. Specifically, it would be informative to examine the deactivation mechanism responsible for the rapid decline in viability in the post-shock temperature regime between 500 and 750 K. As previously addressed, a substantial majority of endospores remain structurally intact in this temperature range. Consequently, the loss of biological functionality is due to the disruption of the endospore reactivation mechanism. In order to address this issue experiments conducted with mutant endospores lacking specific proteins involved in the process of activation, germination and outgrowth would be instructive. The foundation of this process has been laid in the current work with the characterization of wild-type *B. subtilis*. Subsequent experiments employing mutant endospores could then be conducted to determine the variation in viability results within the moderate temperature regime. A similar methodology can also be employed to examine both the specific proteins responsible for the endospore resistance to morphological decomposition as well as the biological constituents responsible for the UV absorption at high post-shock temperatures.

The second area of future work involves the method of bio-aerosol introduction into the shock tube. The application of a second generation aerosol shock tube employing a plug flow technique[46] would enable the loading of a more spatially uniform and higher density bio-aerosol into the test section. Experiments conducted with a dense homogeneously distributed bio-aerosol would enable the generation of more accurate laser measurements and improve the characterization of the bio-aerosol/shock wave interaction.

Part II: Correlated AFM/ NanoSIMS study of vaccinia virus

Chapter 6 Biophysical analysis of vaccinia virus: an introduction

Vaccinia virus, a member of the *Poxviridae* family, is a large heterogeneous human virus that is used as a live vaccine for smallpox. Due to its unique assembly pathway and replication cycle, involving the construction of an array of sub-viral structures in a process that is unparalleled in virology, vaccinia virus has been the subject of intense investigation and remains the laboratory model for Poxvirus studies[1]. Vaccinia has been extensively employed as a cloning and expression vector for the introduction of foreign DNA into cells[2]. Furthermore, live recombinant vaccinia strains have been effectively utilized to express immunizing antigens for a multitude of viruses[3,4,5]. Due to recent concerns regarding the deliberate release of smallpox, however, a renewed emphasis has been placed upon the modeling of virus pathogenesis, virus-cell interactions and the employment of vaccinia as a platform for the development of antiviral therapies[6]. The achievement of these objectives requires a more detailed understanding of the physical structure of the vaccinia viral particle, specifically, the localization and arrangement of the virion lipoprotein membrane and nucleoprotein complex.

Modeling of the distribution and localization of lipoprotein membranes in vaccinia virus is critical for understanding the mechanisms and processes of viral morphogenesis and cell infection. Lipoprotein membranes enable viral fusion with the plasma membrane or endocytic vesicles of uninfected cells following macropinocytosis; consequently, this viral structure plays an instrumental role in the propagation of the infection[7,8]. Numerous studies have postulated the existence of two membranes in intracellular mature vaccinia virions (IMV); an outer one enveloping the virion and an

inner membrane around the viral core[9,10,11]. More recent research, however, has indicated the presence of a single outermost membrane[12]. The ambiguity regarding the distribution of the lipoprotein membranes within vaccinia virions hinders the development and implementation of effective preventative strategies focused upon viral entry into uninfected cells.

While the development of models detailing the architectural arrangement of lipoprotein membranes within the virion is critical for understanding virus-cell interactions, a more important issue for the development of anti-viral drugs is the large scale arrangement and protein-nucleic acid relationship of the viral genome. Unlike other animal DNA viruses, the 200 kb Poxvirus genome is replicated and transcribed within the interphase cytoplasm[1]. This characteristic of the Poxvirus replication cycle, and the unique regulatory mechanisms that it necessarily entails, provides opportunities for fundamental studies regarding host-pathogen interactions and, ultimately, the development of antiviral drugs that specifically target the process of viral genome expression[6]. The realization of these ambitions, however, requires a more fundamental understanding of the assembly and structure-function relationship of the vaccinia virion, specifically, the architectural arrangement of the viral genome within the nucleoprotein complex. This assemblage, contained within the virion core, is a structure composed of the double stranded DNA genome and associated proteins[13]. Poxviruses contain no apparent helical or icosahedral nucleocapsid and the general architectural assembly of the nucleoprotein complex within the core, along with the protein/nucleic acid arrangement within the complex itself, remains unresolved.

Conventional structural biology techniques, including X-ray crystallography and NMR, have fundamental limitations for the characterization of large asymmetric viruses. Consequently, structural details regarding the architecture of vaccinia have been derived, to a large extent, from conventional and cryo-electron microscopy (EM) studies.[10,11,14,15,16] Due to the vaccinia virion's large size, heterogeneity and absence of symmetric elements, however, conventional three-dimensional EM image reconstruction is prohibitively difficult[17]. In an attempt to mitigate these issues recent analyses have employed in situ atomic force microscopy (AFM) for the interrogation of vaccinia

structure[18,19]. These studies have contributed pertinent structural information regarding viral surface topology and architecture with minimal sample preparation. In addition, chemical and enzymatic agents have been employed to systematically digest the virion to reveal internal structures for AFM imaging. One of the most recent vaccinia structural studies implemented a combination of cryo-microscopy and electron tomographic reconstruction to resolve the structure of the virion to 4-6 nm[9]. While these methods have produced a wealth of information regarding the large scale architecture of vaccinia few structural features remain unambiguous; these are limited to the presence of a proteinaceous core containing the genome and viral enzymes, as well as the presence of proteinaceous lateral bodies, surface tubular elements and an exterior membrane. The distribution of the lipoprotein membrane and the detailed architecture of the nucleoprotein complex within the core remain unclear. The prevailing architectural model of the former, based upon EM studies, is of a single lipoprotein membrane surrounding the viral particle. AFM studies of the latter, namely, the nucleoprotein complex, indicate an assembly consisting of a hierarchical tubular structure 30-40 nm in diameter displaying a helical substructure[11,19]. Additional data suggests that subsequent treatment with protease reduces this assemblage to 16 nm fibers, presumably a conglomeration of proteins and viral DNA[19].

Due to the lack of well-resolved structural models for the lipoprotein membrane and nucleoprotein complex the application of additional physical measurement techniques is warranted. Detailed herein are experiments conducted implementing atomic force microscopy and nanometer-scale secondary ion mass spectrometry (NanoSIMS) to physically image and chemically depth profile isotopically labeled vaccinia virus for the determination of nucleoprotein and lipoprotein membrane localization and architecture.

Atomic force microscopy studies utilizing high-resolution physical imaging were initially implemented to characterize intact wild type intracellular mature vaccinia virions. Chemical and enzymatic digestion was subsequently employed to model sub-viral architecture and produce isolated nucleoprotein structures; high-resolution physical imaging of these structures is detailed. The majority of this section, however, is predominantly concerned with describing the development of novel NanoSIMS

methodology for depth resolved chemical imaging of nanometer scale viral systems as well as presenting the results obtained from its implementation. Experimental results detailing both the incorporation of molecule specific isotopic labels into individual viral particles as well as the subsequent construction of depth resolved isotope maps are reported. Specifically, ^{13}C labeled fatty acids and ^{15}N labeled thymidine nucleosides were incorporated into BSC-40 cells employed for virus growth; subsequent cellular inoculation with vaccinia virus resulted in the production of isotopically labeled virions. NanoSIMS imaging was thereafter employed to map the depth distribution of the ^{13}C and ^{15}N signal and, consequently, the localization of the virion lipoprotein membrane and nucleoprotein complex, respectively. The isotopic depth profiles are subsequently compared to prevailing structural models of vaccinia virus. In addition, we report results concerning AFM/NanoSIMS analysis of isolated nucleoprotein complexes extracted from chemically and enzymatically treated virions. These experiments demonstrate the possibility of directly correlating structure, composition and function at the level of sub-viral structures. Furthermore, this methodology represents a novel imaging platform for the nano-scale analysis of complex biological assemblies.

Chapter 7 Structure of vaccinia as visualized by atomic force microscopy

Atomic force microscopy has been extensively employed for the in situ imaging of a variety of viral particles[18-20]. This interrogation method preserves the three-dimensionality of biological specimens and allows for direct visualization of topographical features on the specimen surface. Furthermore, the exposure of intact virions to chemical and enzymatic treatment results in the systematic degradation of the viral particle and, consequently, the possibility of high resolution imaging of internal sub-viral structures[20]. In addition, AFM, being a single particle analysis method, does not require the presence of a homogeneous sample; population based structural information can be as readily ascertained as can individual features from a single viral particle. These characteristics make AFM a highly useful tool for the structural investigation of large asymmetric viruses such as vaccinia. In this study, ex situ atomic force microscopy was employed to visualize and model the architecture of intact intracellular mature vaccinia virions (IMV) as well as chemically and enzymatically derived viral sub-structures. Furthermore, systematic evaluation of the viral degradation pathway was conducted; analysis of this process is crucial for the construction of accurate virion morphogenesis models.

Intact, dehydrated IMV virions adsorbed from suspension in Tris-HCl to glass substrates were imaged ex situ by AFM (see Appendix BI). The virion dimensions, approximately 330 x 260 nm (lateral) by 125 nm (height), and general surface topographical features were consistent with those reported in earlier studies[18,19]. In

addition, the vast majority of viral particles displayed the characteristic rectangular shape. Due to the inherent heterogeneity and pleomorphic nature of vaccinia viral particles, however, surface characteristics assumed a multitude of forms. The most prominently observed surface composition consisted of surface tubular elements (STEs), alternatively referred to as surface fibrous elements (SFEs)[18]. These proteinaceous structures appeared to form a dense network upon the virion surface lacking any specific orientation or large-scale architectural arrangement. Previous studies implementing AFM imaging of hydrated virions demonstrated evidence, not of surface tubular elements, but of protrusions composed of 6 nm diameter subunits; assemblies which would correspond to globular proteins with a molecular mass of approximately 120 to 150 kDa[19]. The membrane proteins encoded by the vaccinia virus genome are of significantly lower molecular mass than the observed structures, consequently, it has been speculated that these surface features represent protein oligomers[19]. Upon dehydration, anisotropic drying presumably results in the collapse of the proteinaceous features into the aforementioned surface tubular elements. The presence of the underlying lateral body (LB) was also observed as a pronounced surface protrusion in numerous dehydrated virions. The function and composition of the LB structure is ambiguous; it appears, however, to be a proteinaceous anchoring mechanism involved in membrane protein attachment[18]. In general, the vaccinia virion's external surface appeared consistent with that of various cell structures sharing similar structural composition, namely, an array of membrane proteins embedded within a lipid bilayer.

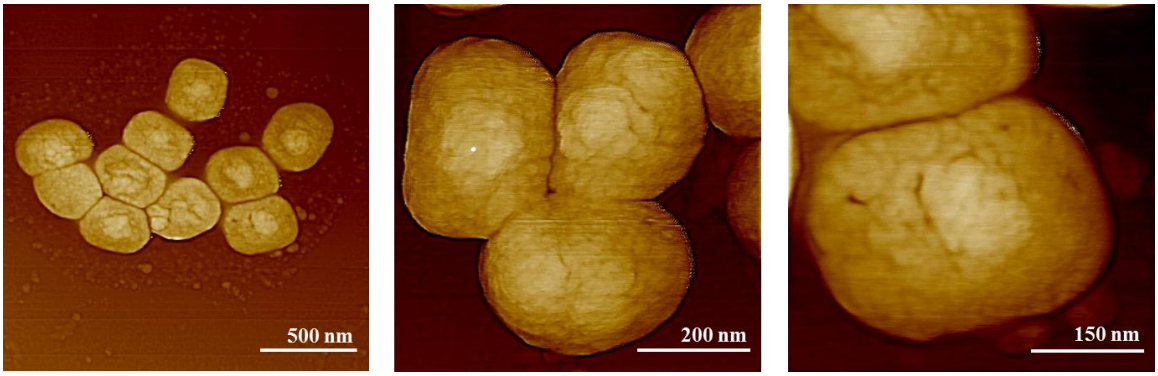

Figure 7-1: AFM images of intact vaccinia viral particles.

Viral particles were frequently found to be aggregated in large three-dimensional arrangements. These conglomerations precluded the accurate virion specific monitoring of structural changes induced by exposure of the sample to chemical and enzymatic agents. In all samples, however, regions of isolated single virions were also found, allowing for the unambiguous identification and attribution of structural degradation effects generated by exposure to the reducing agents. In addition, AFM assessment of the untreated viral samples (see Appendix BII) indicated a substrate largely devoid of cellular assemblies or sub-viral components from partially degraded viral particles. Consequently, the structures and sub-viral assemblages visualized after exposure to chemical and enzymatic reagents could be reliably ascribed to vaccinia virion degradation products. Before detailing the results of the virion degradation experiments it should be emphasized that for a given chemical and enzymatic treatment a multitude of viral decomposition states were observed. This phenomenon is presumably due to the inherent heterogeneity of individual virions within the viral sample. In addition, it is possible that nonequivalent sample exposure to the reagent treatment may have contributed to the variation observed. Consequently, elucidation of the virion degradation pathway is modeled not as a discrete well-defined progression but as a continuous highly variable process dependent upon the individual viral sample as well as the area visualized.

Internal viral structures and macromolecular assemblages were generated by controlled virion degradation with combinations of nonionic detergent, disulfide reducing agents and protease and were subsequently visualized by AFM (see Appendix BII). The first stage of viral particle reduction required the removal of the lipoprotein membrane. A combination of nonionic detergent (.5% NP40) and protein disulfide reducing agents (50 mM DTT), coupled with one-hour incubation at 37 ºC was employed to this end. The resulting particles, termed viral cores (Figure 7-2), displayed a surface composed of a protein shell referred to in the literature as the palisade layer[13]. The core surface displayed a structurally asymmetric architecture punctuated by holes and channels. It has been speculated that these pore-like structures may play an integral role in the extrusion process of mRNA into the cytoplasm of infected cells[21,22]. Quantitative evaluation of the core dimensions indicated an approximate 15-20% reduction in each dimension due to

the loss of the lipoprotein membrane. These features are consistent with that observed in previous studies[19].

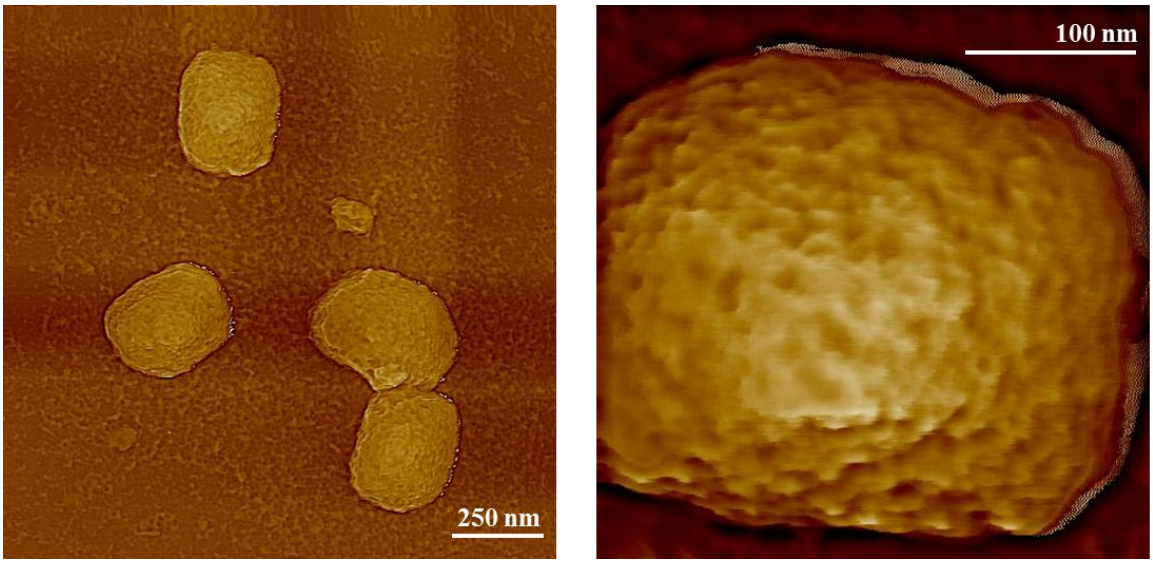

Figure 7-2: AFM images of vaccinia cores produced after treatment of IMV virions with nonionic detergent and reducing agents. The core particle is lacking the exterior lipid membrane present in the intact virions shown in Figure 7-1.

Further degradation of the virion was induced by exposure of virion cores to varying levels of proteinase K. Viral particles exposed to 0.2 mg/ml proteinase K treatment for two hours at 37 ºC displayed significant core wall deterioration resulting in the appearance of proteinaceous appendages extending from the virion surface (Figure 7-3A). In addition, viral particles were seen to exhibit a multitude of different structural configurations and sizes. This phenomenon is presumably caused by the breakdown of surface protein elements resulting in the release of physical constraints dictating the proportions and rectangular contour of the virion. Further proteinase K treatment (.5 mg/ml; 1 hr. 37 ºC) led to particle rupture and the release of extensive networks of, what was hypothesized to be, the nucleoprotein complex (Figure 7-3B,C). Severe morphological breakdown of the core wall was readily apparent in the majority of particles. In addition, the release of the internal nucleic acid/protein structure resulted in the collapse of the core superstructure into round configurations (Figure 7-3B,C,D).

These structures, presumably the remnants of the proteinaceous core wall, were approximately 10 – 50 nm in height and quickly degraded upon further exposure to proteinase K treatment (.5 mg/ml; 2 hrs. 37 ºC), leaving behind isolated tubular networks of, what appeared to be, nucleic acid/protein complexes.

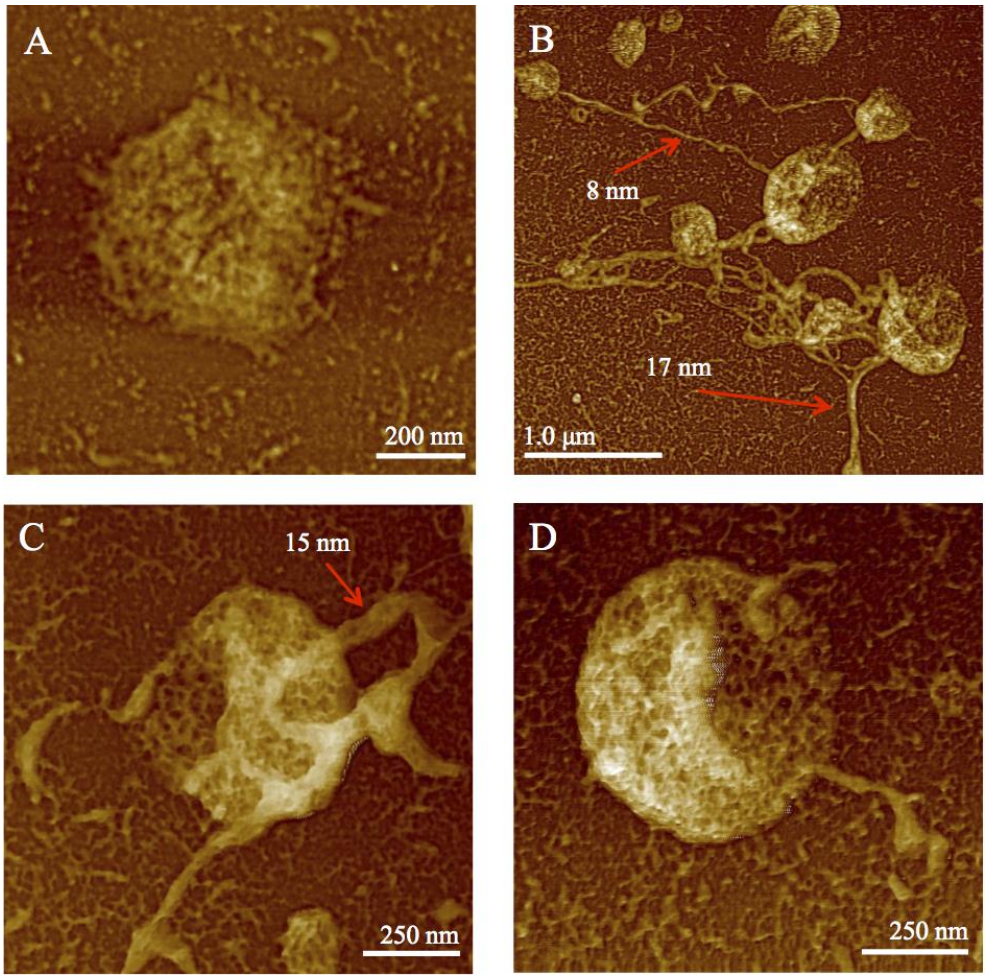

Figure 7-3: Degradation pathway of the vaccinia virion. Viral cores were exposed to various levels of proteinase K treatment, resulting in the structural decomposition of the core wall and the release of tubular networks (A-D). These elements are believed to be composed of proteinaceous and nuclear material.

The AFM imaging of viral tubular networks supports EM data indicating the presence of such assemblages condensed within the core[10,11,23]. Individual tubular

elements ranged in diameter from approximately 10 – 30 nm. A previous AFM study noted that the surface topology of these structures consisted of helically arranged protein subunits with a pitch of approximately 16 nm[19]. While no evidence of this architectural arrangement was observed in the current study, evidence of large protein oligomers associated with the structures was apparent (Figure 7-4B,C). These proteinaceous units may be consistent with the subnucleoid structures previously observed[24,25]. The subnucleoids were determined to be composed of proteins and supercoiled DNA complexed into spherical aggregates 30-60 nm in diameter. These structures were suggestive of the viral genome – protein assemblage existing in an architectural arrangement similar to that of the nucleosome. The tubular networks shown in Figure 7-4A,B, then, may be the result of the unraveling of this nucleosome-like structure. An alternative architectural theory postulates that the viral DNA is encased within the protein structures; the proteinaceous assemblages themselves then comprise a hierarchy of tubular elements condensed within the core[19]. While these theories may differ upon the structural relationship between the nuclear and proteinaceous material, both imply a compositional arrangement in which the viral genome is closely linked with the tubular networks shown in Figure 7-4A and B.

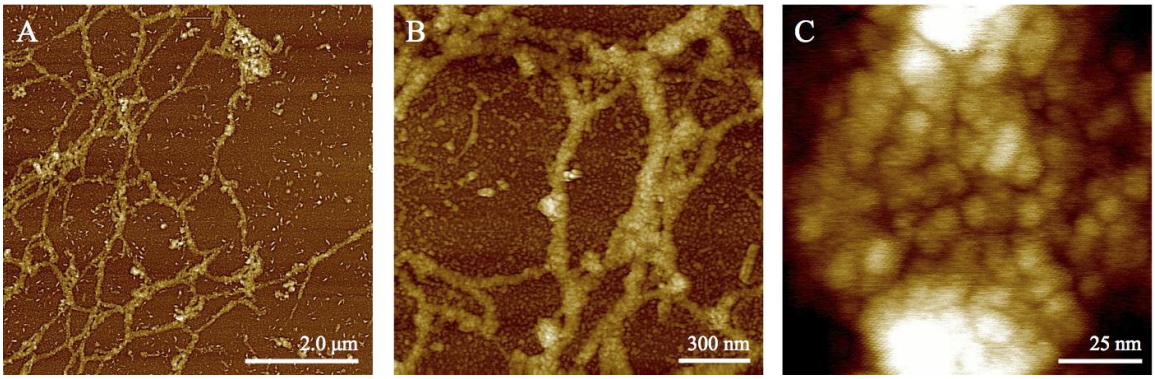

Figure 7-4: High-resolution AFM images of the nucleoprotein complex (A-C). Structure heights ranged between approximately 10 and 30 nm. The nodules observed in image C are presumably protein oligomers.

To address this issue, experiments were initiated whereby the presumed nucleoprotein networks were exposed to DNase, a nuclease enzyme that induces the

hydrolytic cleavage of DNA phosphodiester bonds (see Appendix BII). Viral samples were treated with 1.8 U/µl DNase and incubated for 1.5 hr. at 37 ºC. The results are displayed in Figure 7-5; images on the left (A,C) are of untreated samples and those on the right (B,D) are of the same areas after exposure to the aforementioned DNase treatment. As is readily apparent, extensive structural degradation of the proteinaceous networks was incurred as a result of DNase exposure; structure height was reduced by approximately 45%. Consequently, the viral DNA was shown to be an integral component of the tubular structures generated by proteinase K treatment of virion cores. The large-scale orientation and arrangement of the nucleoprotein complex within the virion core, whether it be reminiscent of a nucleosome-like assemblage or more accurately modeled as a hierarchical complex of tubule structures, remains unresolved.

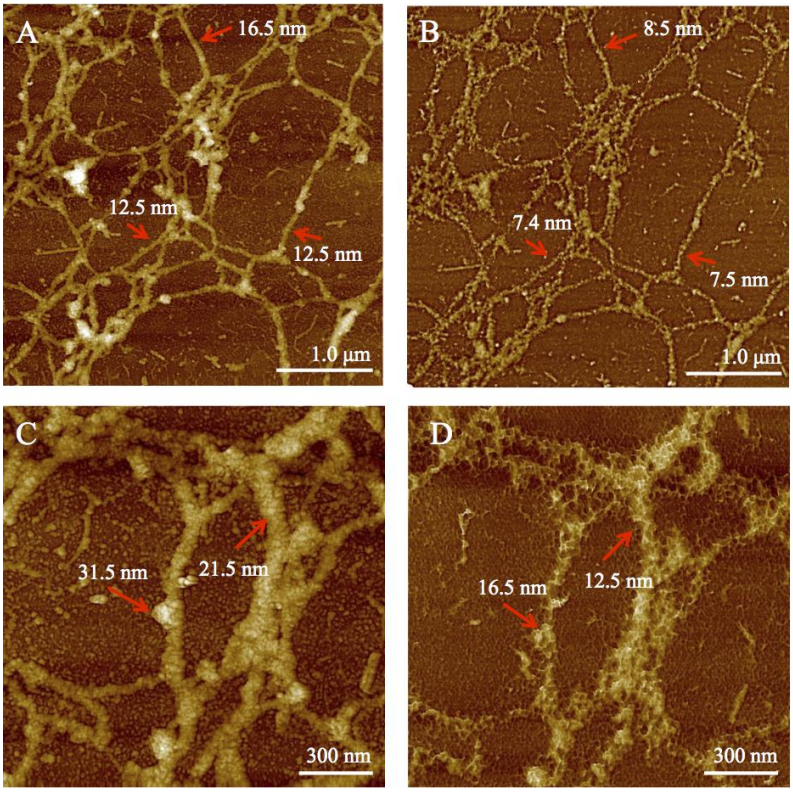

Figure 7-5: AFM images of nucleoprotein complexes exposed to DNase. The original networks, shown on the left, were treated with a nuclease enzyme for a specified duration and then re-imaged. The extensive structural degradation observed in the images on the right indicates that the viral genome is associated with the network structures.

A critical issue regarding vaccinia virion construction is the arrangement of the nucleoprotein complex within the virion core as well as the specific structural relationship between the complex's constituents. Previous studies have forwarded the interpretation that the viral genome may be topologically restrained by coiling; indicating the possibility that the viral DNA may be under superhelical stress[19]. The presence of a virus-encoded topoisomerase as well as studies indicating that the gene encoding this enzyme is essential for virus growth may provide support for the aforementioned hypothesis[26,27,28]. By contrast, other studies have found evidence that the packaged genome is only moderately packed within the virion core and may not be extensively associated with proteins[18]. While no indication of superhelically stressed DNA was observed in the current study, the DNase experiments provide substantial evidence supporting the assertion that the viral genome is extensively complexed with proteinaceous structures. The higher order arrangement of the nucleoprotein complex within the core remains, however, ambiguous. Nevertheless, based upon the viral morphogenesis process, it is evident that an arrangement amendable to the transcription of early genes is required. Furthermore, the viral genome would presumably be configured in such a way as to facilitate the systematic exposure of genes necessary for transcriptional activity.

The AFM data presented herein are consistent with the vaccinia virus structural model forwarded in previous studies. For illustrative purposes a three-dimensional schematic of the vaccinia virion, constructed by Prof. Condit's group at the University of Florida, is detailed in Figure 7-6. The virion linear DNA genome appears to be encased within, or extensively associated with, a multitude of proteins. The resulting nucleoprotein structures appear tubular in nature and may exhibit a higher order packing structure reminiscent of a nucleosome assemblage or a hierarchy of tubular substructures; these elements are shown in white in Figure 7-6. The nucleoprotein assemblies are approximately 50 nm in diameter and are condensed within a proteinaceous core structure whose wall is roughly 25 nm thick (blue/green elements). The virion core is associated with two satellite domains, termed lateral bodies (red elements). A highly cross-linked protein coat may surround the resulting assembly. The outer surface of the viral particle

is composed of a 15 nm thick lipid bilayer complexed with transmembrane proteins (yellow/brown elements). The aforementioned dimensions are based upon cryo electron tomography and cryo-EM studies of hydrated virions[9,29]. As was previously noted, all experiments presented herein were conducted with dehydrated virions; the dehydration process results in an approximate 50% reduction in virion height.

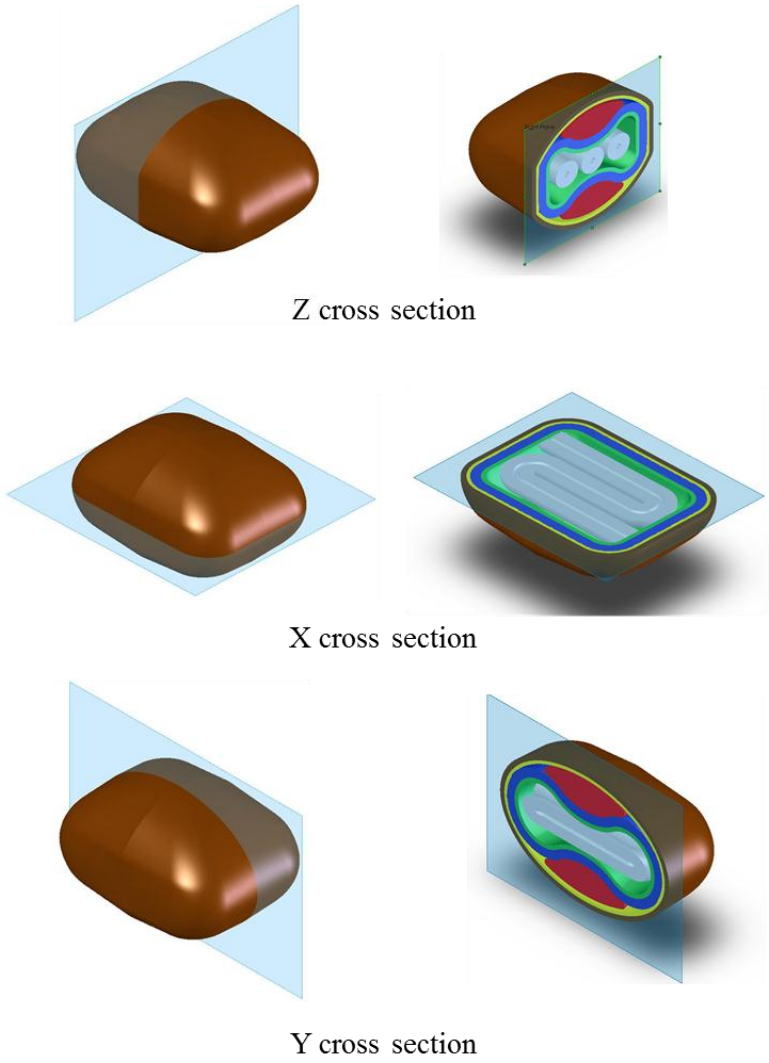

Figure 7-6: Model of the architectural structure of the vaccinia virion. The exterior lipid membrane is shown in yellow and brown. Proteinaceous elements including the lateral bodies (red) and the core wall (blue/green) are shown. The virion genome complexed with proteins is encased within the core and is shown in white.

Chapter 8 NanoSIMS: instrumentation and the physics of secondary ion generation and emission

Structural characterization techniques in the biological sciences have provided both architectural models for fundamental cellular constituents as well as insights into the kinetics of biological processes. Through the application of X-ray crystallography and nuclear magnetic resonance methods, the three - dimensional structure of a multitude of proteins and complex macromolecular assemblies, including the ribosome, have been resolved to the angstrom level. These techniques, however, provide highly refined structural information on the length scale of up to approximately 10 nm. To model the dynamic interactions and structural assemblies on a longer length scale the implementation of new interrogation methods is necessary. The application of secondary ion mass spectrometry (SIMS) to biological systems can provide pertinent information regarding the organization and composition of the analyzed sample at the lateral length scale of 50 nm to several microns[30]. This method, then, has the potential to fill the void between the atomic level resolution structures obtained from X-ray crystallography and NMR and the large-scale biological structures visualized with light microscopy.

8.1 Nanometer scale secondary ion mass spectrometry

The application of SIMS analysis to biological systems is far from being a mature field; the majority of published results concern the development of experimental methodology and capability demonstration. Numerous studies have focused upon the use

of isotopic analysis to elucidate metabolic pathways in microbial colonies[31,32,33,34]. As was demonstrated by Orphan et al., SIMS analysis can provide an experimental platform to directly monitor metabolic processes in naturally occurring heterogeneous microbial assemblages[35]. In addition, numerous isotopic tracer studies have been conducted to analyze cellular transport mechanisms[36], nitrogen fixation in animal cells[37] as well as rates of protein renewal in kidney cells[38]. Further studies have implemented SIMS to examine the construction and lateral distribution of lipids and membrane proteins in biological membranes[39]. In addition, quantitative three-dimensional elemental distribution data for eukaryotic cells[40] as well as micron sized *Bacillus* endospores[41] has been obtained with SIMS analysis. The studies presented herein demonstrate the extension of this capability to nanometer scale viral systems whose complete physiochemical composition and structure has eluded conventional analysis techniques.

SIMS analysis combines the unambiguous identification of biological molecules based upon their mass with three-dimensional spatial information. The SIMS method is predicated upon the generation of secondary ions through the bombardment of the interrogated sample with a high-energy primary ion beam. In the present study a NanoSIMS 50 instrument (CAMECA Instruments) was operated in the dynamic SIMS mode[42]. The dynamic mode of analysis exposes the sample, kept under high vacuum (10^{-10} torr.) to a continuous primary ion beam that is systematically scanned across the surface. This process results in the controlled erosion of the sample and the generation of neutral atoms and molecules as well as positive and negative ions. These ions, ejected into the gas phase, are detected with a magnetic sector mass spectrometer and provide depth resolved compositional information and enable the chemical imaging of complex, heterogeneously constructed biological samples. In addition, the simultaneous detection of distinct species-specific secondary ion counts allows for quantitative spatial measurements concerning the distribution and localization of multiple chemical species within the sample.

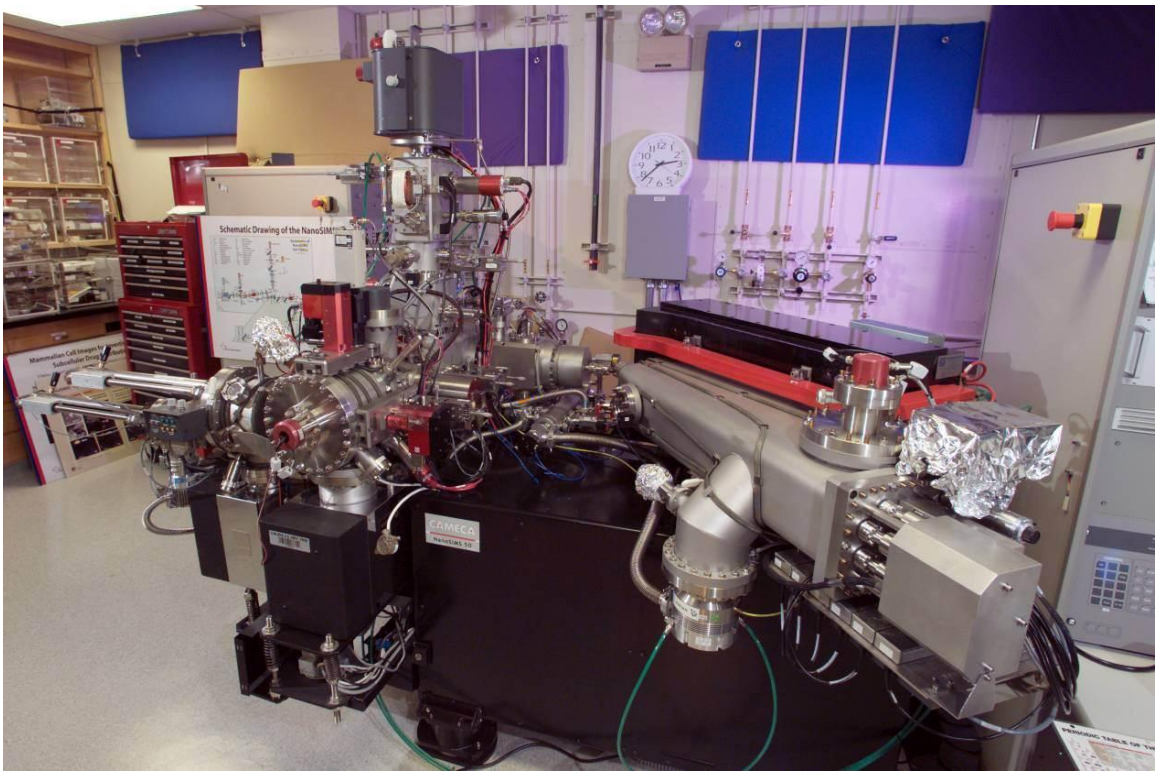

Figure 8-1: The NanoSIMS 50 instrument at Lawrence Livermore National Laboratory.

The NanoSIMS instrument employs either a cesium or oxygen primary ion beam to generate electronegative or electropositive secondary ions, respectively. The implantation of the reactive primary ions into the biological sample increases the probability of ionization of the ejected molecular fragments; this process being essential for species detection with the magnetic mass spectrometer. Figure 8-2 details a schematic of the NanoSIMS instrument employed in the current study. All results reported herein were obtained utilizing a 16 keV cesium primary beam. In addition to providing higher lateral resolution than the oxygen beam, the positively ionized cesium atoms lower the surface work function of the sample and significantly increase the yield of the electronegative diatom of interest, namely, $^{12}C^{14}N^-$ and isotopic variations thereof[43].

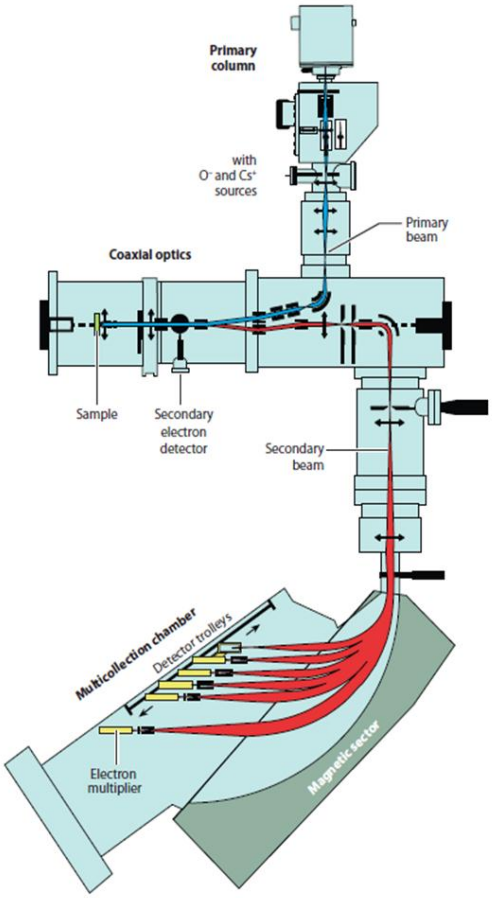

Figure 8-2: Schematic of the NanoSIMS 50. The primary oxygen or cesium ion beam impacts the interrogated sample and generates secondary ions that are separated by mass in the mass spectrometer. Simultaneous detection of multiple pre-selected species is done by electron multipliers. Figure reproduced from Ref. 30.

Generation of the primary ions in the NanoSIMS is achieved by bringing cesium vapor into contact with a high temperature tungsten plate[42]. An electric field is subsequently applied to the plate enabling the extraction and acceleration of the ionized cesium atoms. The primary ions transverse a multitude of optics and are focused into a coherent beam, impacting the sample at a right angle. The subsequently ejected secondary ions are directed onto a collinear path with the primary beam. This coaxial optical arrangement, enabling the formation of the common propagation path for the primary and secondary ion beams, places the main focusing optics in close proximity and

normal to the sample. This configuration reduces the beam spot size, mitigates focusing aberrations and, consequently, greatly enhances the lateral resolution of the measurement[42,44]. The generated secondary ion beam traverses a multitude of additional focusing optics and transfer lenses and the ionized species are separated in energy in the electrostatic sector. Specific ion trajectories are subsequently modified by the magnetic field based upon the individual mass to charge ratio of the charged particle. Ion detection is then completed in the multi-collection chamber with the use of electron multipliers. Throughout this process the topological information regarding the location of ion emission is retained, thereby providing the ability to localize and quantify the distribution of chemical species in the sample.

The NanoSIMS instrument allows for the simultaneous detection of up to seven preselected species. In addition, secondary electrons generated from the sample are detected, providing the possibility of physical imaging. Due to the dynamics of the ion bombardment process the ejected ions are generally atomic or diatomic in nature; the possibility exists, however, of the generation of larger molecular fragments. The majority of the ejected secondary ions consist of the former categories and, in general, an inverse relationship between mass and prevalence is noted. The ability to distinguish between molecular secondary ions of similar mass, essential for the accurate quantification of species counts, is characterized by the instrument's mass resolving power ($M/\Delta M$). This quantity is defined as the nominal mass of the species of interest divided by the mass difference of an adjacent species. An additional parameter of interest is the instrument sensitivity, a quantity dependent upon the ionization rate of the molecule of interest as well as the overall transmission of the system; the latter quantity being defined as the ratio of ions detected to ions formed. The NanoSIMS instrument is equipped with an energy window at the entrance slit to the mass spectrometer thereby enabling high transmission at high mass resolution. Full transmission is realized at a mass resolution of approximately 2000 $M/\Delta M$[30]. Significantly increased mass resolution, however, can be achieved at reduced transmission. Therefore, ions such as $^{13}C^{14}N^-$ (27.0064 amu) can be readily distinguished from $^{12}C^{15}N^-$ (27.001 amu). The NanoSIMS, then, is capable of producing quantitative compositional information on the nanometer length scale due to

the coupling of high lateral resolution with both enhanced detection sensitivity and mass specificity.

In addition to the aforementioned considerations, the generation of quantitatively reliable mass spectrometric imaging data on the nanometer scale of an individual viral particle requires a highly focused incident ion beam. Traditional SIMS instruments utilizing time-of-flight mass spectrometers typically employ liquid metal (Au_n^+, Bi_n^+) or cluster projectiles (C_{60}^+) as ion sources. The lateral resolution of these polyatomic ion beams, on the order of hundreds of nanometers, prohibits their use for the interrogation of viral samples. The NanoSIMS instrument, equipped with the aforementioned monatomic Cs^+ incident ion beam capable of being focused to a spot size of 50 nm, provides the necessary lateral resolution for individual virion analysis. In addition, the NanoSIMS has approximately ten times higher sensitivity at high mass resolving power than conventional time of flight SIMS (TOF-SIMS) techniques; a necessary feature considering the size of the interrogated sample volume and the correspondingly low secondary ion counts. The utilization of a monatomic incident ion beam, while providing the lateral resolution necessary for nanometer scale interrogation, introduces measurement complications that need to be addressed.

The bombardment of a biological specimen with a high-energy primary ion beam is an inherently destructive process resulting in the progressive erosion of the sample and the generation of secondary neutral and charged species. Upon impact the incident ion energy is deposited both on the surface and at depth. The degree to which the energy deposition process extends into the interior of the sample is a function of the characteristics of the ion beam as well as the physical properties of the material analyzed. The transfer of energy to the subsurface initiates a collision cascade whereby relatively low energy recoil atoms induce the ejection of secondary species from the sample surface. Species transport and ejection from subsurface regions is limited by the small diameter of the monatomic ion impact crater. Consequently, the majority of emitted ions are generated from the atoms in the uppermost two or three atomic layers of the momentary sputtered surface[45]. The generation of secondary ions in this manner results in the breaking of molecular bonds and the accumulation of subsurface damage, both

mechanisms being detrimental for quantitative molecular depth profiling. Attempts to mitigate these problems have resulted in the employment of the aforementioned cluster projectiles; the impact of a cluster ion induces a collective motion of the material near the impact zone, increasing the likelihood of the ejection of large mass fragments indicative of specific biological compounds[46]. In addition, the lack of incident cluster ion depth penetration reduces the amount of subsurface damage and depth mixing. As previously specified, however, the lack of lateral resolution with such techniques inhibits their use for nanometer scale viral systems.

Surface bombardment with a monatomic ion beam, then, causes the breaking of molecular bonds and the subsequent ejection of small molecular fragments lacking specificity regarding their structure of origin. The resulting atomic and diatomic secondary ions would, in and of themselves, yield little information regarding the chemical and structural composition of a viral particle. Consequently, the identification and localization of subsurface structures with NanoSIMS requires the incorporation of stable isotopic labels. The molecule specific isotopic tags are used to quantify and map the localization of the labeled structures throughout the virion depth; isotopic signal variation being correlated to the distribution of the labeled component under investigation. This methodology, then, allows for the possibility of nanometer scale differentiation of sub-viral structures and the generation of parallel quantitative mass imaging depth profiles.

As previously detailed, an additional measurement complication concerns the onset of sample mixing during ion bombardment. This physical phenomenon necessarily complicates depth profile interpretation. A quantitative study of this issue was conducted by Ghosal et al.[41] using a model multilayer substrate composed of alternating silicon/carbon layers 25.02 and 2.78 nm thick, respectively. Quantitative estimates concerning the depth resolution possible with the NanoSIMS instrument were based upon the increase in apparent interface thickness due to the sputtering process; the thickness of the interface was defined as the depth interval necessary for the secondary ion counts to fall from 84 to 16% of maximums. Based upon the $^{12}C_2^-$ peak, the depth resolution was approximately 3 nm for the front interface and 10.5 nm for the rear. The reduced

resolution at the rear interface can be attributed to the accumulation of sputter-induced mixing effects[41]. These results indicate that the ability to resolve features deteriorates with sputtered depth. In addition, due to sputtering-induced perturbations and mixing, sub-surface structures may appear to extend for a greater depth than is accurate.

8.2 The physics of sputtering and ion emission

Secondary ion mass spectrometry is an analytical technique enabling the systematic structural and compositional interrogation of a material. Sample characteristics are determined by the mass, and in some cases, energy analysis of charged particles emitted from the surface; the emission process being induced by the bombardment of the sample with a primary ion beam. In order to accurately interpret the detected secondary ion species counts and distributions it is necessary to understand the physical mechanisms responsible for the sputtering process and ion emission.

The theory most successful in quantitatively modeling the sputtering process over a wide range of experimental conditions is the linear collision cascade framework developed by Sigmund[47,48]. In this model the momentum and energy transfer of the primary ions to the surface is conceptualized as a series of cascades of energetic binary collisions. The energy deposition process is governed by nuclear collisions modeled as elastic and the energy loss per unit depth is ascertained through the assumption of a Thomas-Fermi or Born-Mayer interaction potential[49]. This process induces the development of collisional cascades within the bombarded sample consisting not only of collisions between the primary ions and the target atoms but also those between recoil and stationary target atoms. The sputtering of atomic and molecular species from the target surface and near-surface region is a consequence of the transference of energy and momentum, through binary collisions, to a surface atom or molecule. If the target surface particle acquires enough energy to overcome the surface binding forces it is emitted as a neutral or ionized atom or molecule. While the vast majority of sputtered particles are emitted as neutrals, the implantation of reactive species such as the aforementioned Cs^+ and O^- primary ions significantly increase the yield of ionized target particles.

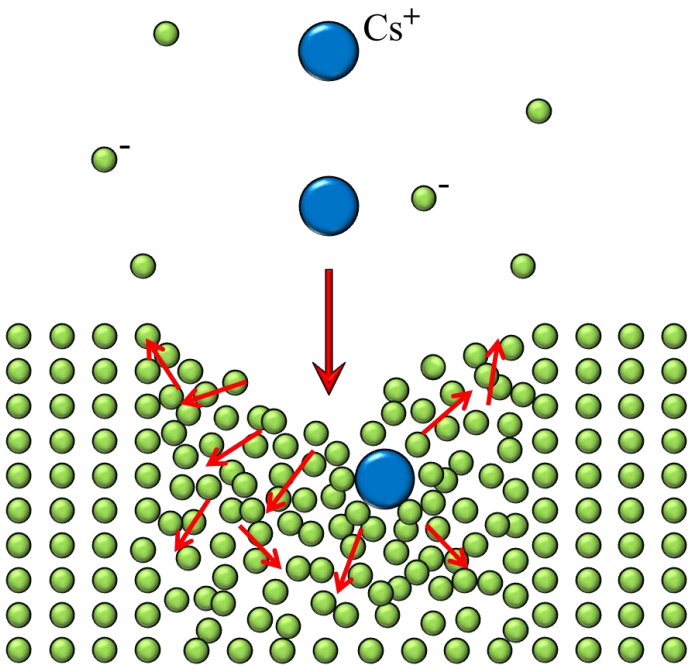

Figure 8-3: The impact of the primary ion with the surface induces the formation of a collision cascade within the interrogated sample. Sputtering results from the transference of energy and momentum to a surface atom. If the magnitude of the energy and momentum transfer is larger than the surface binding force of the solid the atom is emitted as a neutral or ionic species.

An alternative energy deposition process governs the interaction of heavy, high-energy incident ions. Specifically, collisions between heavy particles can induce the transfer of energy to bound electrons in the interrogated material. Such collisions are, therefore, modeled as inelastic and the evaluation of the electronic stopping power is generally based upon the theory developed by Lindhard and can be shown to be proportional to the square root of the energy of the impinging particle[50]. Within this regime the quantitative predictions of the linear cascade model begin to deviate substantially from experimental results. At high energy densities the sputtering process induces the formation of nonlinear collision cascades[49]. These cascades are characterized by the interaction of atoms set in motion by distinct ion impact events. The thermal spike model has been extensively employed to characterize this regime with models assuming

elastic and inelastic collisions[51,52]. This theory replaces the collisional cascade framework with a thermodynamic interpretation of the ion impact event. The effect of the impact is therefore modeled as an abrupt temperature rise within an infinitesimal cylindrical volume surrounding the ion trajectory through the solid. Post impact temperature distributions are modeled with the one-dimensional heat conduction equation. Sputtering is thereby assumed to be the result of particle flux from the transiently heated surface and is proportional to an activation term, $\exp\left(-\frac{U}{kT}\right)$, dependent upon the surface binding energy U, the Boltzmann constant k and the spike temperature T[53]. Discrepancies between the standard thermal spike theory and molecular dynamic (MD) simulations of the sputtering process prompted the development of two-dimensional models including mass and momentum transfer within the spike[54]. This framework entails the direct integration of the two-dimensional equations of fluid dynamics within the cylindrical spike geometry. It was shown that the transport of mass and momentum were an integral component of the sputtering process. In addition, the energy deposition process was demonstrated to be more akin to a detonation event than to a thermal diffusive process.

For the experimental conditions detailed herein, the linear cascade framework formulated by Sigmund[47] is most applicable. The quantitative aspects of the linear collision cascade model are predicated upon the calculation of the temporal and spatial evolution of the following function:

$$G(x, \boldsymbol{v}_o, \boldsymbol{v}, t) d^3 v_o dx$$

Assuming the motion of an initial atom with velocity **v**, the above function details the average number of atoms in motion at time t within a differential layer (x, dx) with velocity ($\mathbf{v}_o$, d^3v_o). Assuming an isotropic, homogeneous media, the evolution of the collision cascade phenomenon is governed by the equations of transport theory. Consequently, the function $G(x,\mathbf{v}_o,\mathbf{v},t)$ will satisfy the Boltzmann's equation:

$$-\frac{1}{v}\frac{\partial}{\partial t}\,G(x,\boldsymbol{v}_o,\boldsymbol{v},t)-\eta\frac{\partial}{\partial x}\,G(x,\boldsymbol{v}_o,\boldsymbol{v},t)$$
$$=N\int d\sigma\,[\,G(x,\boldsymbol{v}_o,\boldsymbol{v},t)-G(x,\boldsymbol{v}_o,\boldsymbol{v}',t)-G(x,\boldsymbol{v}_o,\boldsymbol{v}'',t)]$$

where v is the magnitude of the velocity vector $\mathbf{v}$, N is the density of target atoms, dσ is the differential cross section, $\mathbf{v}'$ is the velocity of the scattered particle, $\mathbf{v}''$ is the velocity of the recoiling atom and η is defined as v_x/v. For the present purposes we are interested in determining the material properties that govern the rate of sputtering. This quantity is closely related to the following function:

$$F(x,\boldsymbol{v}_o,\boldsymbol{v})=\int_0^\infty G(x,\boldsymbol{v}_o,\boldsymbol{v})\,dt$$

$F(x,\mathbf{v}_o,\mathbf{v})\,|v_{ox}|\,d^3v_o$ is, then, the number of atoms passing through the plane x with a velocity ($\mathbf{v}_o$, d^3v_o) during the collision cascade. The sputtering yield (atoms ejected/Cs ion) can then be formulated as follows:

$$H(x,\boldsymbol{v})=\int d^3v_o|v_{ox}|\,F(x,\boldsymbol{v}_o,\boldsymbol{v})$$

Utilizing the above relations and converting to energy variables, an integrodifferential Boltzmann type equation for the sputtering yield can be formed:

$$-\delta(x)\eta\varphi(-\eta)\varphi(E-U_s(\eta))-\eta\frac{\partial}{\partial x}\,H(x,E,\eta)$$
$$=N\int d\sigma\,[H(x,E,\eta)-H(x,E',\eta')-H(x,E'',\eta'')] \qquad (1)$$

where E', η', E'' and η'' are the energies and directional cosines of the scattered and recoiling atom, respectively. The term $\delta(x)\eta\varphi(-\eta)\varphi\big(E-U_s(\eta)\big)$ is a source term where

$$\varphi(\xi) = 1, \text{ for } \xi > 0$$
$$\varphi(\xi) = 0, \text{ for } \xi < 0$$

E is the incident ion energy and U_s is the surface binding energy of the target. Equation 1 was solved by Sigmund under the assumption of a well-developed collision cascade in a monatomic infinite medium. The solution is formulated as follows:

$$H(E) = \Lambda F_D(E) \quad (2)$$

where

$$\Lambda = \frac{.042}{NU_s}$$

$F_D(E)$ is the deposited energy at the surface:

$$F_D(E) = \alpha\left(\frac{M_2}{M_1}\right) N S_n(E)$$

α is a function of the incident ion mass (M_1) and target atom mass (M_2) and $S_n(E)$ is the nuclear stopping cross section, other variables are as previously defined. Based upon extensive experimental data, Equation 2 has been modified to the following semi-empirical form[55]:

$$H(E) = .042\frac{Q(Z_2)\alpha^*\left(\frac{M_2}{M_1}\right)}{U_s}\frac{S_n(E)}{1 + \Gamma k_e \epsilon^{0.3}}\left[1 - \sqrt{\frac{E_{th}}{E}}\right]^s \quad (3)$$

A number of empirical parameters have been introduced (Q, α^*, Γ) whose formulation can be found in Yamamura and Tawara[55]. The physically meaningful modifications to the original equation proposed by Sigmund include the incorporation of a Lindhard electronic stopping power term ($k_e\epsilon^{0.3}$) as well as a term accounting for the sputter yield

dependence upon the ratio of the primary ion energy (E) and the sputtering threshold energy (E_{th}).

The other important physical mechanism involved in secondary ion mass spectrometry is the process of ionization. In order for the sputtered atoms and molecular fragments to be detected with the mass spectrometer they need to have been ionized during the sputtering event. Early investigations focusing upon this matter noted the strong enhancement of negative ion emission at sputtered sites consisting of alkali metal atoms[56]. As a result, studies focused upon the monitoring of electronegative species generally employ cesium primary ion sources for sputtering. The near-surface region of the sample is thereby embedded with a reactive species, increasing the probability of secondary ion ejection during the sputtering process. The energy threshold of ion formation depends, in part, on the difference between the surface work function and the electron affinity of the species. Therefore, numerous ionization theories are constructed upon the model that the implantation of Cs^+ lowers the surface work function of the sample. Theoretical descriptions of the ion emission process predict an exponential dependence of the probability of ionization (P) on the species-specific electron affinity (A) and the work function (φ):

$$P^- \propto \exp\left[-\frac{(\varphi - A)}{\varepsilon}\right]$$

the additional parameter, ε, is related to the outward velocity of the sputtered particle[57]. Consequently, the probability of electronegative ion formation increases with the use of a work function reducing reactive species such as Cs^+. This phenomenon is especially critical for the current study due to the small volume of sputtered material. That being said, however, the vast majority (~ 98%) of particles remain neutral upon emission. A more detailed analysis of this process, as well as a review of additional theories regarding the ionization event, can be found in Williams[58].

Chapter 9 Development of NanoSIMS methodology for the analysis of vaccinia virus

The implementation of NanoSIMS analysis for the study of individual vaccinia virions required the development of novel experimental methodology. An orthogonal imaging approach was developed combining atomic force microscopy with NanoSIMS analysis. AFM was employed to produce physical images of the vaccinia viral particles as well as to assess the physical impact of the ion beam/virion interaction. This technique was subsequently utilized to construct a quantitative model of the systematic erosion of the viral particle during NanoSIMS interrogation. Theoretical considerations regarding the observed sputter rate phenomenon and its correlation to the dynamic process of ion bombardment are also formulated.

9.1 AFM mapping for NanoSIMS analysis

Prior to NanoSIMS interrogation (see Appendix BIII), viral samples were mapped utilizing atomic force microscopy to provide high - resolution information regarding virion surface topology and architecture as well as to locate areas suitable for analysis. Figure 9-1 illustrates a sequence of AFM images - a large scan for mapping and subsequently smaller scans for viral morphological characterization - and a corresponding $^{14}N^{12}C^-$ chemical image generated with the NanoSIMS. The NanoSIMS image displays the summed quantity of species counts registered at each pixel during the scan time. Sample areas composed of viral monolayers or isolated individual particles were

perferred for analysis; these regions enabled unambiguous correspondence between NanoSIMS species counts and their structure of origin. In addition, areas lacking host cell debris were required. The presence of potentially isotopically labeled cellular structures located in the analyzed region would complicate both the attribution of species counts as well as the construction of chemical depth profiles. As previously noted, the NanoSIMS instrument has the capability for large – scale sample imaging through the detection of secondary electrons; therefore, virion conglomerations, such as those shown in Figure 9-1A, can be found with the NanoSIMS and used as fiducial points to locate smaller monolayer regions (Figure 9-1B,C) suitable for interrogation. The analysis of intact virions entailed the employment of this methodology to provide sample mapping and qualitative assessment of virion surface morphology.

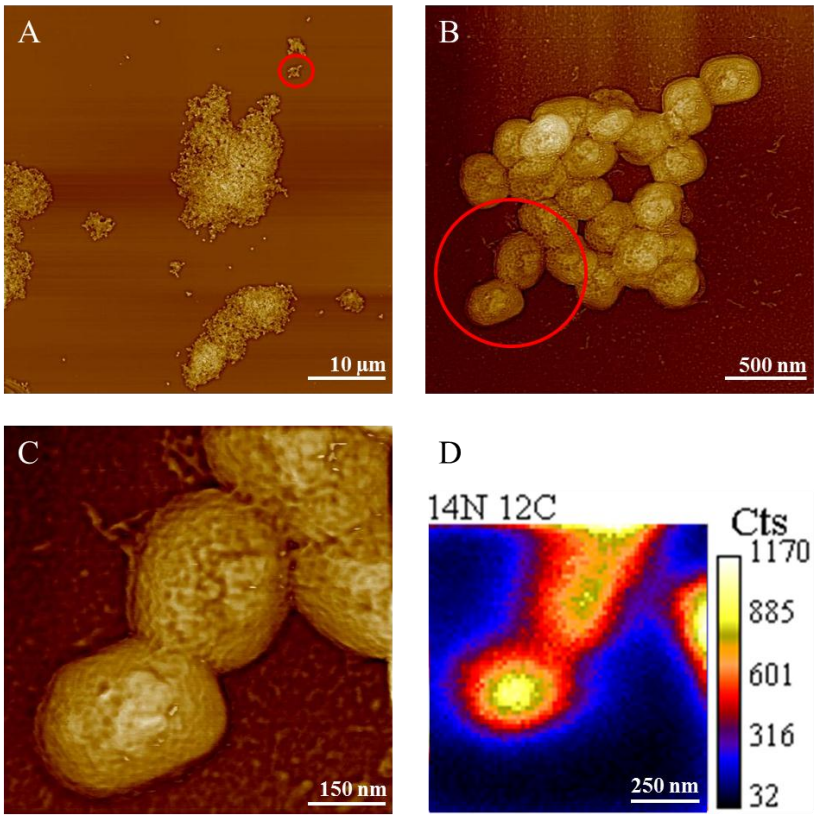

Figure 9-1: Correlated AFM/NanoSIMS analysis of vaccinia virus. The regions of the AFM images framed in red correspond to the area imaged in the subsequent frame. Image D is a NanoSIMS chemical image of the region shown in image C. Image D depicts the lateral distribution of the $^{14}N^{12}C^-$ species within the analyzed virions.

9.2 Viral particle erosion: model development

In order to implement secondary ion mass spectrometry to produce accurate structural models of individual vaccinia virions, the process of particle erosion through induced sputtering required quantification and validation.

9.2.1 Quantitative depth profiling

As previously addressed, the SIMS method utilizes a primary ion beam to cyclically scan the viral sample, thereby inducing the emission of secondary ions and systematically eroding the virions under investigation. Species counts were subsequently recorded as a function of the number of scan cycles. Therefore, for each scan cycle the ion counts for the five pre-selected species of interest were recorded. Chemical images were subsequently constructed detailing the number of species-specific ion counts registered at each pixel. Figure 9-2 details AFM generated viral images and the corresponding $^{14}N^{12}C^-$ counts during progressive stages (cycles 1, 15, 25 and 39) of NanoSIMS analysis. The effects of the erosion process on the quantity of the $^{14}N^{12}C^-$ species counts is readily apparent; an order of magnitude reduction in ion counts, from $3.2*10^5$ for cycle 1 to $4.8*10^4$ for cycle 39, was measured. In addition, the cycle dependent distribution of $^{14}N^{12}C^-$ counts indicates an erosive process simultaneously occurring in all three dimensions.

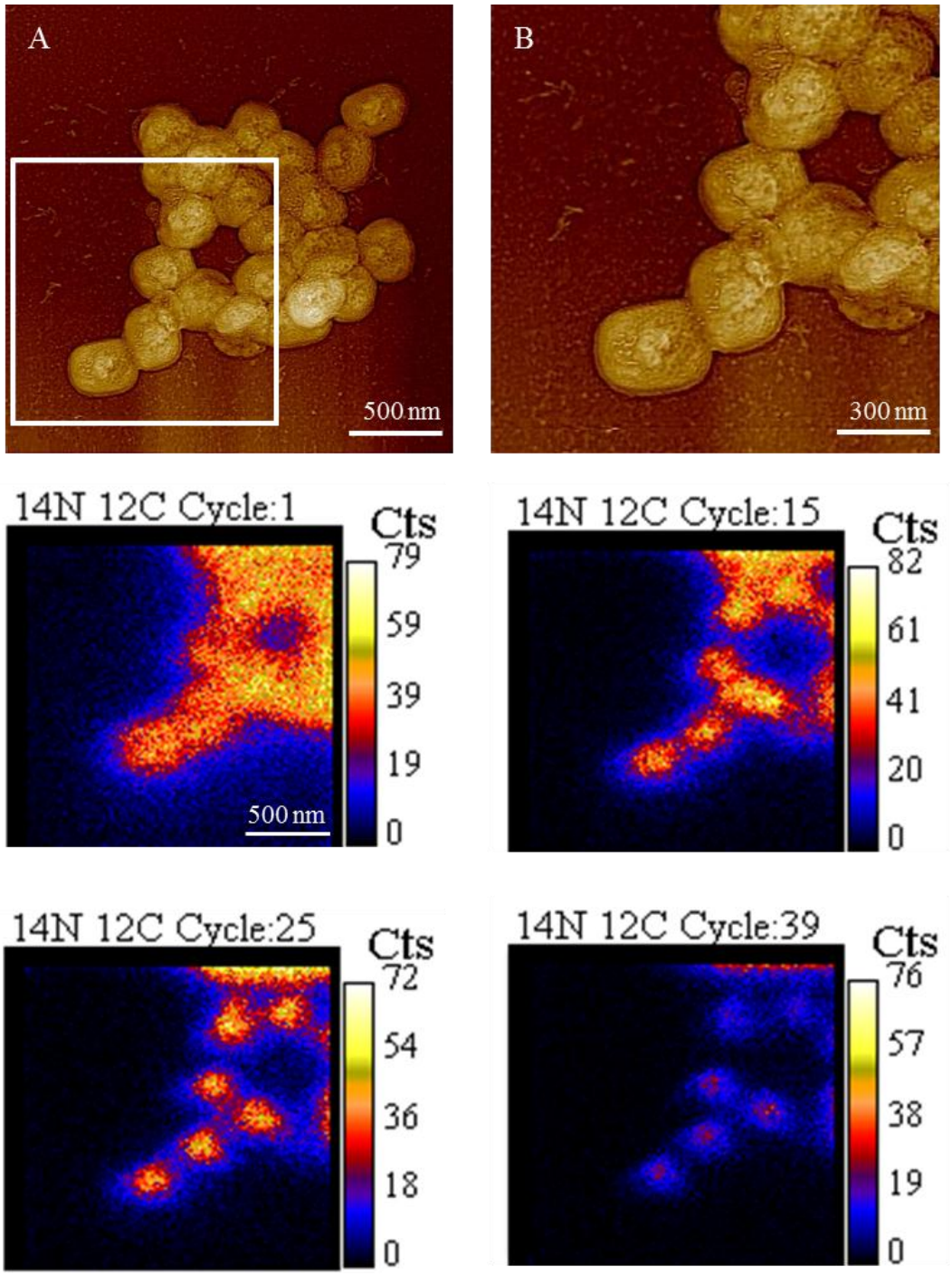

Figure 9-2: Correlated AFM and NanoSIMS image of vaccinia virions. The AFM image B corresponds to the region in image A framed by the white square. The sequence of NanoSIMS images details the distribution of the $^{14}N^{12}C^-$ species counts during the analysis time. The decrease in species counts as a function of cycle number is a result of material erosion through induced sputtering.

To generate physically relevant information regarding the depth distribution of the species of interest, namely, the isotopic tag, it is necessary to convert the number of scan cycles to viral particle depth utilizing a virion sputter rate. This quantity is a function of the implanted cesium ion density and is, therefore, proportional to the incident beam current (*I*), exposure time (*t*) as well as a volume metric. The latter is formed through the product of the raster area (*A*) and eroded virion depth (*d*). The sputter rate (ξ) is then constructed as follows:

$$\xi \left[\frac{nm * \mu m^2}{pA * sec}\right] = \frac{d * A}{I * t} \quad (4)$$

Initially, the average sputter rate was modeled as a material constant independent of beam current or raster scan area. In order to assess the validity of this assumption the average vaccinia virion sputter rate was measured for a range of beam currents at a specified raster area. Initially, the particle was considered completely sputtered at a time *t* when the $^{12}C_2^-$ counts fell to 30% of their maximum value; a method consistent with that employed in other studies[41]. In addition, an average virion height of 125 nm was used for the depth parameter, *d*, and all scans were performed with a raster size of 100 μm^2. Experiments performed over a range of primary beam currents (0.8-2.98 pA) consistently produced average sputter rates of approximately 2.30 nm*μm^2/pA*sec. Studies were subsequently implemented to examine the sensitivity of the average sputter rate to changes in the raster area. Experiments performed with a beam current of 2.46 pA and raster areas of 6.25 μm^2 and 100 μm^2 yielded average sputter rates of 2.15 and 2.26 nm*μm^2/pA*sec, respectively. A second set of scans, conducted utilizing a .78 pA beam and equivalent raster areas as the first, produced consistent average sputter rates as well. Large rate discrepancies were noted, however, when disparate values of voltage were applied to the L1 incident beam-focusing lens. The sensitivity of the sputter rate to this parameter can be attributed to the relationship between cesium beam divergence and L1 voltage. As would be expected, the level of incident ion beam divergence is inversely proportional to the observed sputter rate. These results indicate that while the average

virion sputter rate is a variable parameter dependent upon the incident ion beam divergence it closely follows Equation 4 over a wide range of beam currents and raster areas. Consequently, quantitative evaluation of depth resolved data regarding the distribution of isotopic labels within viral particles requires the application of a consistent voltage value for the ion optics over the range of experimental conditions.

This methodology, while providing a means to quantitatively map the depth distribution and localization of specific chemical species in the viral sample is predicated upon the assumption of planar erosion. As was demonstrated in Figure 9-2, however, the physical process of particle degradation under ion bombardment results in simultaneous size reduction in all three dimensions. Therefore, the modeling of the ion counts from each cycle as having been generated from successively parallel cross sections is not entirely accurate; ions will also have originated from regions of unequal depth, especially around the virion periphery. The majority of secondary ions, however, will be produced from the surface plane of the virion perpendicular to the incident ion beam.

In addition, this model assumes that the sputter rate is independent of the depth of erosion; it provides sputter rate values averaged over the full analysis time and, therefore, neglects the possibility of a dynamic rate dependent upon the progression of the sputtering process. The validity of this assumption is predominately governed by two factors: the generation of an equilibrium sputtering regime and the inherent biological heterogeneity of the virion. The former consideration, concerning equilibrium sputtering, is dictated, in part, by the establishment of a threshold concentration of cesium ions implanted within the sample. As previously mentioned, the cesium ions induce a reduction in the surface work function, thereby increasing the probability of the ejection of ionized species. Therefore, the establishment of equilibrium secondary ion sputtering conditions requires the accumulation of cesium ions within the sample; a necessarily time dependent process that alters the material composition of the sputtered particle. Prior to this, non-equilibrium conditions, exhibiting substantially different sputtering rates, are possible. In addition, the assumption of a depth independent sputter rate inherently requires modeling the sputtering characteristics of disparate biological macromolecular assemblages as essentially equivalent. The outer lipid membrane, protein core wall and

nucleic acid complexes within the core are considered, then, to sputter at equivalent rates. Consequently, while the aggregate sputtering rate for the entire virion may assume one value, sub-regions of the viral particle could potentially sputter at substantially different rates.

A depth varying sputter rate would complicate the interpretation of the NanoSIMS data and the construction of the chemical depth profiles. To test the validity of the single sputter rate model a series of experiments were initiated whereby the sputtering process was halted after a specified analysis time corresponding to a theoretical sputtered depth. Depths of 8, 25 and 80 nm as well as 160 nm were chosen to ensure penetration and complete sputtering of the biological components of interest; 8 nm for the lipid membrane, 25 nm for penetration of the protein structure of the core wall, 80 nm for complete sputtering of the protein layer and penetration of the nucleoprotein complex and 160 nm to ensure complete viral particle sputtering. These erosion depths correspond to sputter times of 104, 333, 1021 and 2070 seconds, respectively. Therefore, if the assumption of a depth independent uniform sputter rate were a valid model, post analysis AFM height measurements would be consistent with those calculated using Equation 4. Additionally, these experiments provided an opportunity to qualitatively examine the changes in the virion structure as a result of the cesium ion bombardment. Quantitative assessment of the reduction in the virion's lateral dimensions was also conducted to complement the height measurements and provide pertinent information regarding the evolution of the viral sputtering process.

Sample areas were imaged with atomic force microscopy before and after NanoSIMS analysis to assess the physical and morphological changes in the viral particle produced by the cesium ion interaction. An AFM imaged area is shown in Figure 9-3 along with the same region (Figure 9-3B) after 333 sec. of NanoSIMS analysis with a 2.98 pA cesium ion beam; the 10 μm by 10 μm-scanned area is framed in red. Due to the small change in silica substrate height (~ 1 nm) between the scanned and non-scanned areas, AFM height images proved inadequate for demonstrating the surface effects resulting from ion beam exposure. Consequently, Figures 9-3A,B were generated using phase mode post processing, whereby non-topographic changes in surface characteristics

are detected by monitoring variations in the cantilever phase oscillation during scanning. Additionally, the corresponding secondary electron and $^{14}N^{12}C^-$ counts from one analysis cycle of the scanned region are shown.

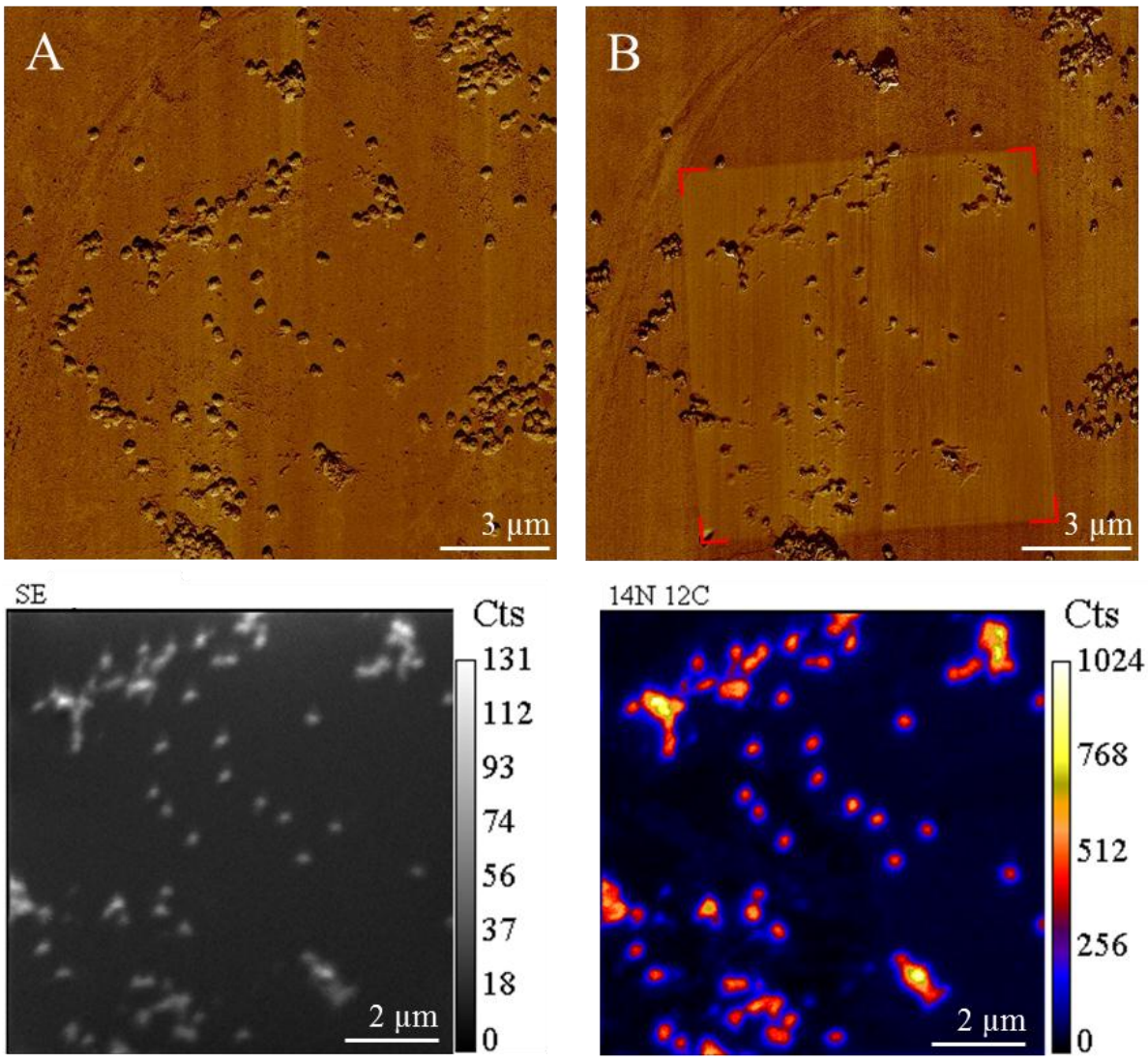

Figure 9-3: AFM image A and B illustrate a region of the viral sample before and after exposure to a 2.98 pA cesium ion beam for a duration of 333 seconds, respectively. The 10 µm x 10 µm-analyzed region is framed in red in image B. The corresponding NanoSIMS generated secondary electron image as well as a $^{14}N^{12}C^-$ chemical image of the interrogated region are shown.

High-resolution AFM imaging was subsequently implemented in the region of interest to assess the morphological and dimensional changes induced in individual viral particles by ion beam exposure. A 360 nm AFM scan of a single virion pre- and post-analysis is shown in Figure 9-4. Measurements indicated that the sputtering process resulted in an approximately 60 percent reduction in virion height coupled with a fivefold reduction in particle volume. Furthermore, the surface topology of the analyzed virion appeared relatively smooth, precluding the possibility of internal structure and sub-viral component identification. The lack of discernible morphological features is presumably the result of the mixing process generated by the penetration of the cesium ions into the virion.

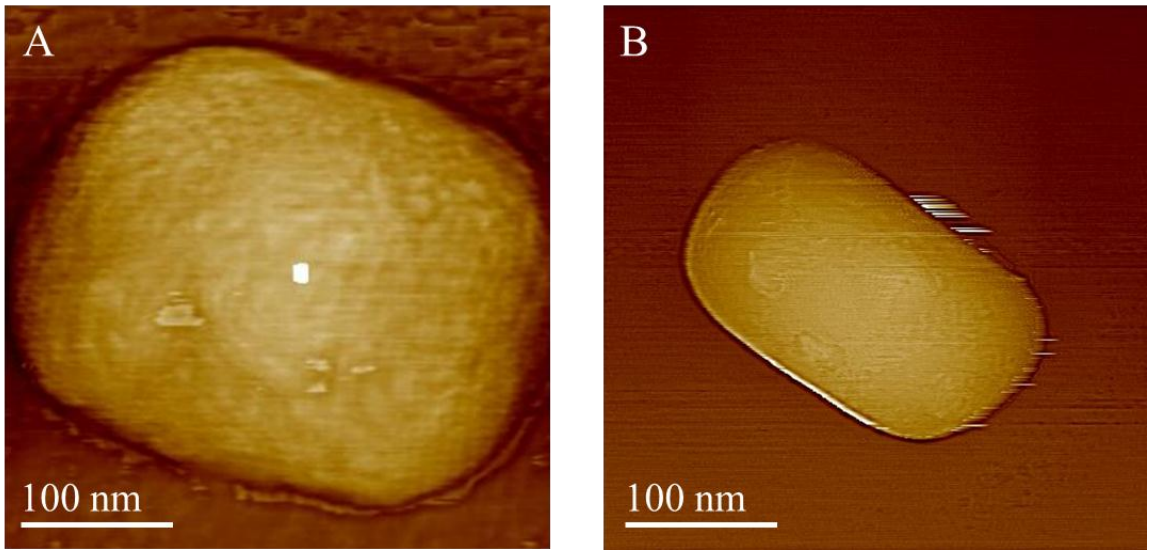

Figure 9-4: AFM images of a viral particle before NanoSIMS analysis (A) and after (B). The viral particle was within a 100 μm^2 region exposed to a 2.98 pA cesium ion beam for a time duration of 333 seconds.

Additional areas were analyzed with NanoSIMS for time durations of up to 2070 seconds. Post-analysis virion heights were again quantified with atomic force microscopy and are shown in Figure 9-5; each data point represents an average of between five and ten individual viral particles. Readily apparent from the figure is the lack of a continuous linear relationship between virion height and sputter time; instead, the presence of two distinct sputtering regions is noted. The first region (I), displaying an extremely rapid

erosive process, is characteristic of very short exposure times, while the second (II) is indicative of a substantially slower erosion process. Consequently, modeling the viral particle sputter rate as independent of depth is not a valid assumption. Further analysis of Figure 9-5 indicates that the physical mechanism responsible for the depth varying sputter rate is not the heterogeneous constitution of the virion but the sputtering process itself. The first measured data point, corresponding to a theoretical sputtered depth of approximately 8 nm, indicates an approximately 75 nm reduction in virion height. Therefore, the lipid membrane and protein core wall structure have been completely sputtered through and the viral nucleoprotein complex has, based upon the current vaccinia architectural model, been penetrated. The three discrete biological components of the virion have, then, been at least partially sputtered in region I. The area of Figure 9-5 designated region II would necessarily entail the sputtering of the remaining virion, consisting of the same three biological components, namely, the nucleic acid, protein and lipid. As a result, the large sputter rate discrepancy between region I and II cannot be attributed to the heterogeneous composition of the virion. While some variation in the sputtering characteristics of the aforementioned constituents is presumably present, it is clear that an additional physical phenomenon is responsible for the time varying sputter rate.

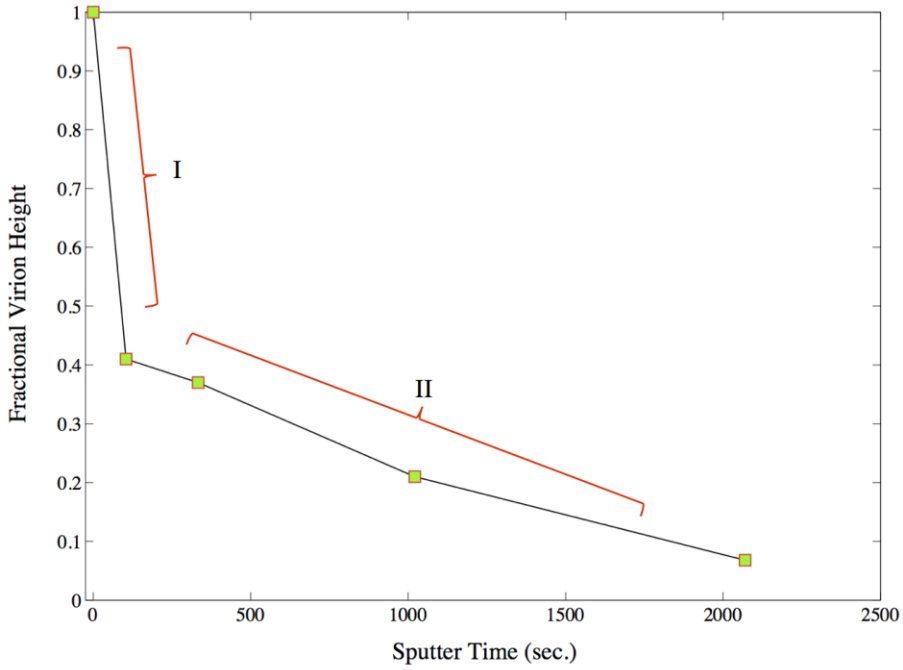

Figure 9-5: Viral particle height variation as a function of sputter time for a 2.98 pA cesium primary beam. The data is segregated into two distinct regions: an initial regime displaying a rapid non-equilibrium sputter rate (I) and an equilibrium sputter rate region indicative of long exposure times (II).

In an attempt to further elucidate the dynamics of the sputtering process a series of experiments was implemented utilizing a range of primary ion beam currents. These experiments focused upon the non-equilibrium/equilibrium sputtering transition as well as the long time sputtering process in the equilibrium region. The same procedure as previously outlined was employed to replicate the data in Figure 9.5 for the following beam currents: 1.4 and 0.8 pA. Furthermore, an additional short time data point was measured for the 2.98 pA curve. The results, including a subplot focused upon the non-equilibrium region, are shown in Figure 9-6. In addition, the predicted time of full viral particle erosion based upon the NanoSIMS $^{12}C_2^-$ counts are shown for each curve (gray circle). A qualitative assessment of Figure 9-6 indicates that the characteristic demarcation of the data into two distinct regions is present over the full range of primary ion beam currents. In addition, the transition between the two regions was consistently

measured to be at a depth of roughly 70 nm. This approximate depth was reached after a sputter time of 104 sec. with the 2.98 pA beam and 208 and 416 sec. employing the 1.4 and 0.8 pA beam, respectively. As would be expected from Equation 4, a reduction in the beam current by a factor of two results in a corresponding increase in the time required to sputter to an equivalent depth. Further validation of Equation 4 can be derived from examining the predicted time of complete viral particle erosion. Extrapolation of the data for each curve provides full erosion sputter times of 2580, 4900 and 9400 sec. for the 2.98, 1.4 and 0.8 pA beam, respectively; these times being separated, approximately, by a factor of two. Additionally, the region displayed in the subplot provides data concerning the dynamic process within the non-equilibrium sputtering regime. Transitory changes in the rate of sputtering in this region not readily apparent in the full figure are clearly discernible in the subplot.

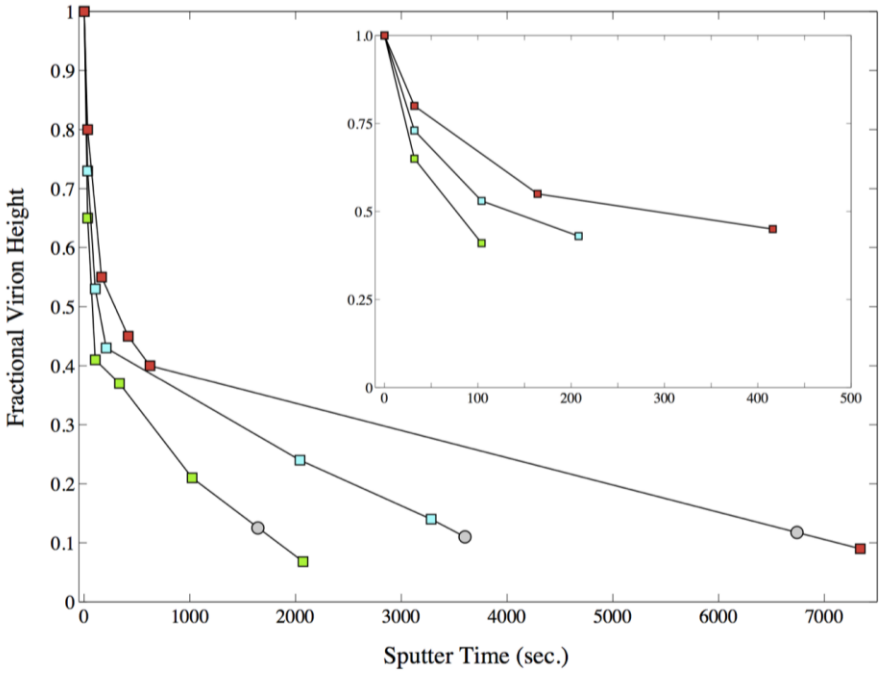

Figure 9-6: Viral particle height variation as a function of sputter time for three primary ion beam currents: 0.8 pA (red), 1.4 pA (blue) and 2.98 pA (green). In addition, the predicted time of full viral particle erosion based upon the NanoSIMS $^{12}C_2^-$ counts are shown for each curve (gray circle). The embedded subplot focuses on the initial 500 seconds of sputter time.

For our present purposes, namely, the construction of accurate isotopic depth profiles, quantification of the variation of the sputter rate as a function of time is required. A model of the time varying sputter rate is therefore constructed from the data in Figure 9-6 and Equation 4; the resulting relationship for the three beam currents (0.8 pA (red), 1.4 pA (blue) and 2.98 pA (green)) is displayed in Figure 9-7.

Due to the discrete nature of the NanoSIMS data acquisition process, the calculated sputter rate values, shown as red points for the 0.8 pA curve in Figure 9-7, are averaged quantities over the time frame of interest. Consequently, for modeling purposes the averaged sputter rate values are placed at a sputter time corresponding to one half of the total analysis time. The sputter rate data is well fit by curves of the form:

$$\xi(t) = \alpha + \beta \exp(-\varphi t) \qquad (5)$$

with α being the equilibrium sputter rate (~.7 nm*μm^2/pA*sec) and β the initial instantaneous sputter rate (~100 nm*μm^2/pA*sec). The variable φ is a fit constant dependent upon the experimental parameters and dictates the rate at which equilibrium sputtering conditions are established; analysis of a 100 μm^2 raster area with a 0.8 pA incident beam corresponds to a φ value of approximately .011. The relation displayed in Equation 5 allows for the generation of sputter rate curves for a range of experimental conditions. For example, the 1.4 pA curve in Figure 9-7 is well modeled by setting φ(1.4 pA) = δ φ(0.8 pA) with the value of δ being the ratio of primary beam currents (i.e. 1.75). Similar scaling arguments can be employed to generate sputter rate curves corresponding to the raster area of interest. In addition, this methodology enables the generation of depth resolved data based upon the time varying sputter rate. Systematic quantification of the depth of erosion, d, at time t, can be readily ascertained through the following expression:

$$d = \frac{I}{A}\int_0^t \xi(t)dt \qquad (6)$$

Evaluation of the integral in Equation 6 enables the construction of particle depth profiles and, consequently, provides a quantitative method for determining the distribution and localization of molecule specific isotopic labels within individual virions.

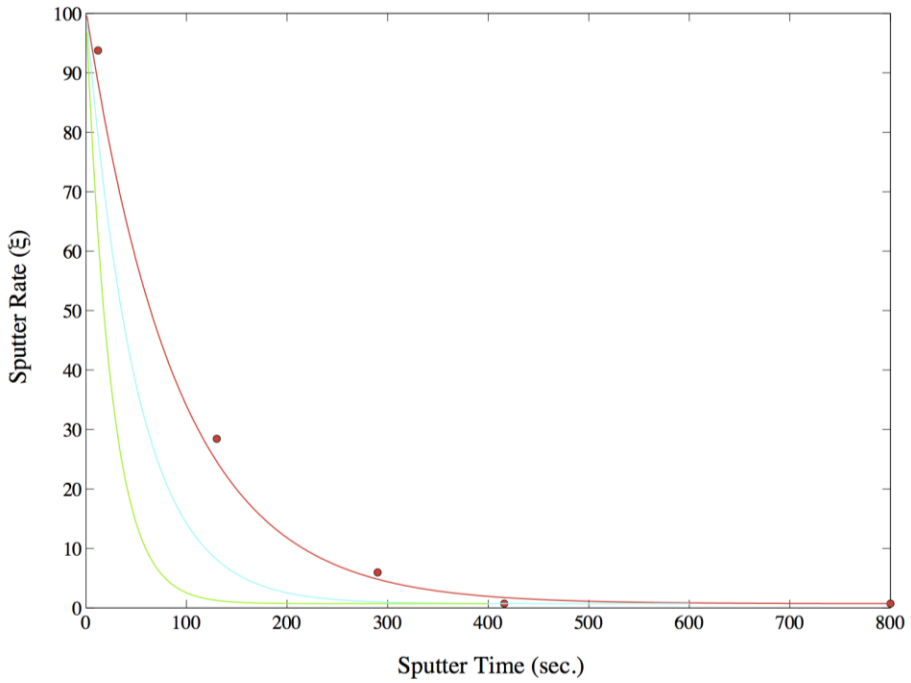

Figure 9-7: Viral particle sputter rate as a function of sputter time for three cesium ion beam currents: 0.8 pA (red), 1.4 pA (blue), 2.98 pA (green).

Development of the non-equilibrium sputter rate model necessitates a modification to the interpretation of NanoSIMS based calculations of sputter rates. As previously noted, virion sputter rates were initially calculated based upon the $^{12}C_2^-$ species counts; viral particles were considered completely sputtered when the $^{12}C_2^-$ counts had been reduced to 30% of maximum. The time (t') at which this criterion was met for each primary ion beam current is shown in Figure 9-6 (gray circle). While it was known that complete virion erosion was generally not achieved at this sputter time, the greatly diminished volume of sputtered material and corresponding low secondary ions counts resulted in large data variation and uncertainties beyond this threshold. The development of the non-equilibrium sputter rate model necessarily entails a modification to this methodology to ensure accurate construction of depth profiles; this process is illustrated

in Figure 9-8 for the 2.98 pA beam data series (green squares). Based upon the analysis conditions and data shown in Figure 9-6, the $^{12}C_2^-$ counts had been reduced to 30% of maximum after 50 scan cycles or a sputter time of 1643 seconds. The constant sputter rate model coupled with this criterion is shown in Figure 9-8. As can be readily discerned from the plot, there exists a considerable difference between the calculated time of complete erosion based upon the $^{12}C_2^-$ counts and the corresponding measured virion height at this time (~ 12.5 nm). Therefore, not only does the time invariant sputter rate model fail to accurately capture the initial transitory period of non-equilibrium sputtering but it also overestimates the viral particle sputter rate by approximately 30%.

As previously noted, the secondary ion counts are sufficiently reduced for analysis times greater than t' to preclude the possibility of obtaining accurate depth resolved compositional information. Consequently, the $^{12}C_2^-$ count criterion is still employed, but as an alternative to assuming complete virion erosion at this sputter time, the non-equilibrium model is utilized to determine the corresponding viral particle height. Constructed depth profiles, then, do not extend to the full depth of the particle (~125 nm) but to an analysis condition specific depth based upon the $^{12}C_2^-$ counts; for the example shown in Figure 9-8 a depth profile of approximately 110 nm could be generated. Further discussion and implementation of this methodology is provided in the chapters concerning depth profiling of the ^{13}C and ^{15}N labeled virions.

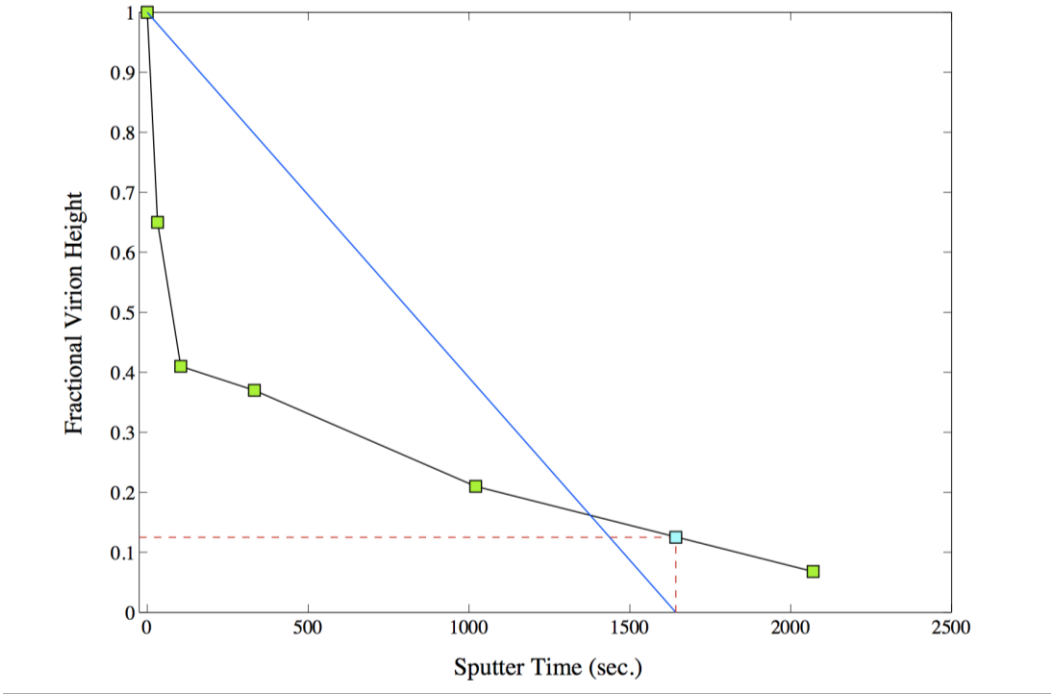

Figure 9-8: Viral particle height variation (blue) as predicted by the constant sputter rate model and as measured with AFM measurements of virions exposed to a 2.98 pA cesium ion beam for various time durations (green). Not only does the constant sputter rate model fail to capture the dynamics of the initial non-equilibrium region but it also predicts a full erosion time significantly shorter than AFM measurements indicate.

9.2.2 Viral particle erosion under gallium bombardment

Further investigation into the non-equilibrium sputtering phenomenon was undertaken to ensure that the time dependent sputter rate was a universal feature of the physical system and not an anomalous characteristic of the experimental protocol. Specifically, we wanted to address the issue of employing cesium, a reactive species, as the primary ion beam. As previously detailed, a reactive primary species was employed to increase the probability of ionization of the sputtered material. Our concern, then, revolved around the possible oxidation of the cesium within the viral particle when the NanoSIMS analyzed sample was removed from high vacuum for post-sputtering AFM analysis. We speculated that the observed high initial rate of sputtering may be a result of oxidation induced material decomposition. In order to examine this hypothesis a series of

sputtering experiments was conducted utilizing a focused ion beam (FIB) microscope. The FIB instrument employs a non-reactive gallium beam and is coupled with a high-resolution scanning electron microscope to provide in-situ measurements of interrogated regions.

Experiments were therefore implemented to characterize the viral particle sputtering response to a non-reactive incident ion beam. Initially, an in situ measurement of an intact as well as sputtered virion was performed using the scanning electron microscope. While providing an indication of the sputtering pattern, highly accurate height measurements can not be obtained in this manner. Therefore, regions of the viral sample were analyzed for discrete time durations and the post-sputtering particle heights were subsequently quantified with atomic force microscopy. In order to replicate as closely as possible the sputtering data generated with the NanoSIMS, the incident gallium beam was set to an energy of 16 keV and a current of 3.4 pA. However, due to the disparate nature of the interrogating species, specifically the approximate factor of two mass difference between gallium and cesium, quantitative agreement between the two data sets was not necessarily expected. The main issue that was to be addressed in this series of experiments was whether both physical systems manifested the same qualitative behavior, namely, the presence of a time dependent erosion rate exhibiting two distinct sputtering regimes.

In situ height measurements were performed on two viral particles: an intact non-sputtered virion as well as a virion within a 100 μm^2 sample region exposed to the 16 keV gallium beam for a duration of 360 seconds. The intact virion measurement would provide a baseline value to compare to viral particle dimensions generated with the atomic force microscope. Quantification of particle heights was done through the analysis of consecutive SEM images generated during the systematic cross sectioning of the virion. A layer of platinum was deposited through chemical vapor deposition upon the particle in order to shield the virion from material erosion during the cross sectioning procedure. The process of FIB assisted chemical vapor deposition is predicated upon the ion beam induced decomposition of a precursor gas, in the present case $C_5H_5Pt(CH_3)_3$, that has been allowed to chemisorb onto the sample[59]. Interaction with the gallium ion

beam initiates the decomposition of the gas into volatile and non-volatile components, the latter of which remains on the sample surface as a deposited aggregation of platinum. The metallic coating, then, acts as a sacrificial layer protecting the viral particle from uncontrolled degradation during the cross-sectioning procedure. Due to the deposition of platinum, however, measurement of the original dimensions of the sputtered virion was precluded. Figure 9-9 details SEM generated images illustrating the cross-sectioning process. The deposited platinum, configured as a rectangular structure covering the viral particle, can be readily discerned in the images.

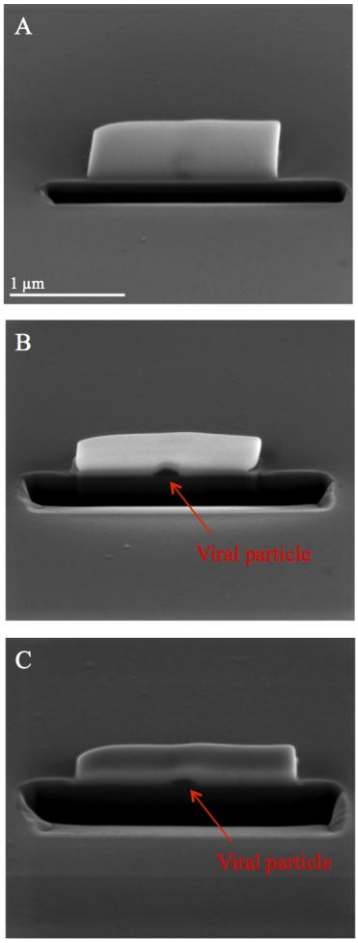

Figure 9-9: Sequence of SEM images during FIB cross sectioning of vaccinia virus for height determination. Platinum was deposited over the viral particle to protect against virion erosion during the cross-sectioning procedure (Image A). Image B depicts a cross section of an intact virion; image C shows a cross section of a virion previously exposed to a 16 keV gallium beam for 360 sec.

The focused gallium ion beam was subsequently scanned over the region, resulting in the systematic planar erosion of the platinum/viral particle assemblage. Parenthetically, the ion interaction with the silicon substrate results in surface damage and the formation of a distinct channel evident in the three images. The progression of the sectioning procedure can be perceived by examining Figures 9-9A, B. Figure 9-9A is an SEM image generated shortly after inception of the scan and before the virion embedded within the platinum structure has been exposed to the ion beam. Figure 9-9B is the fifth section image generated during the scan; the non-sputtered viral particle is now clearly discernible allowing for quantification of the height dimension. The sectioning process was continued until the virion was consumed and the SEM section images were analyzed to record the maximum particle height. For the virion shown in Figure 9-9B a height dimension of 117 nm was observed. While this measurement technique is somewhat subjective, the observed value is consistent with the particle heights generated with the AFM; an average vaccinia virion height value between 120-125 nm was consistently measured with the latter method.

The sectioning methodology was subsequently implemented to measure the height of a viral particle after exposure to the gallium beam for 360 seconds. After completion of the 10 μm x 10 μm erosion scan, the platinum layer was deposited upon the virion of interest and the sectioning procedure was initiated. The SEM image displaying the virion cross section with the largest height dimension is shown in Figure 9-9C. Quantification of the particle height indicated a value of approximately 54 nm. As previously stated, the initial dimensions of the specific virion under consideration are not known, however, it is clear that a substantial reduction in the particle height resulted from the gallium bombardment. Assuming that the particle was of average initial dimensions, the data indicate that over half of the virion height was removed during the scan. This significant dimensional reduction corroborates the data shown in Figure 9-6. In addition, these data support the presence of an initial sputtering regime characterized by a rapid rate of material erosion.

In order to generate more accurate height measurements, sample regions composed of individual viral particles were scanned with the non-reactive gallium beam

and the resulting dimensional change was quantified with atomic force microscopy. Three distinct 10 μm x 10 μm regions were scanned with the 3.4 pA gallium beam for time durations of 60, 360 and 900 seconds.

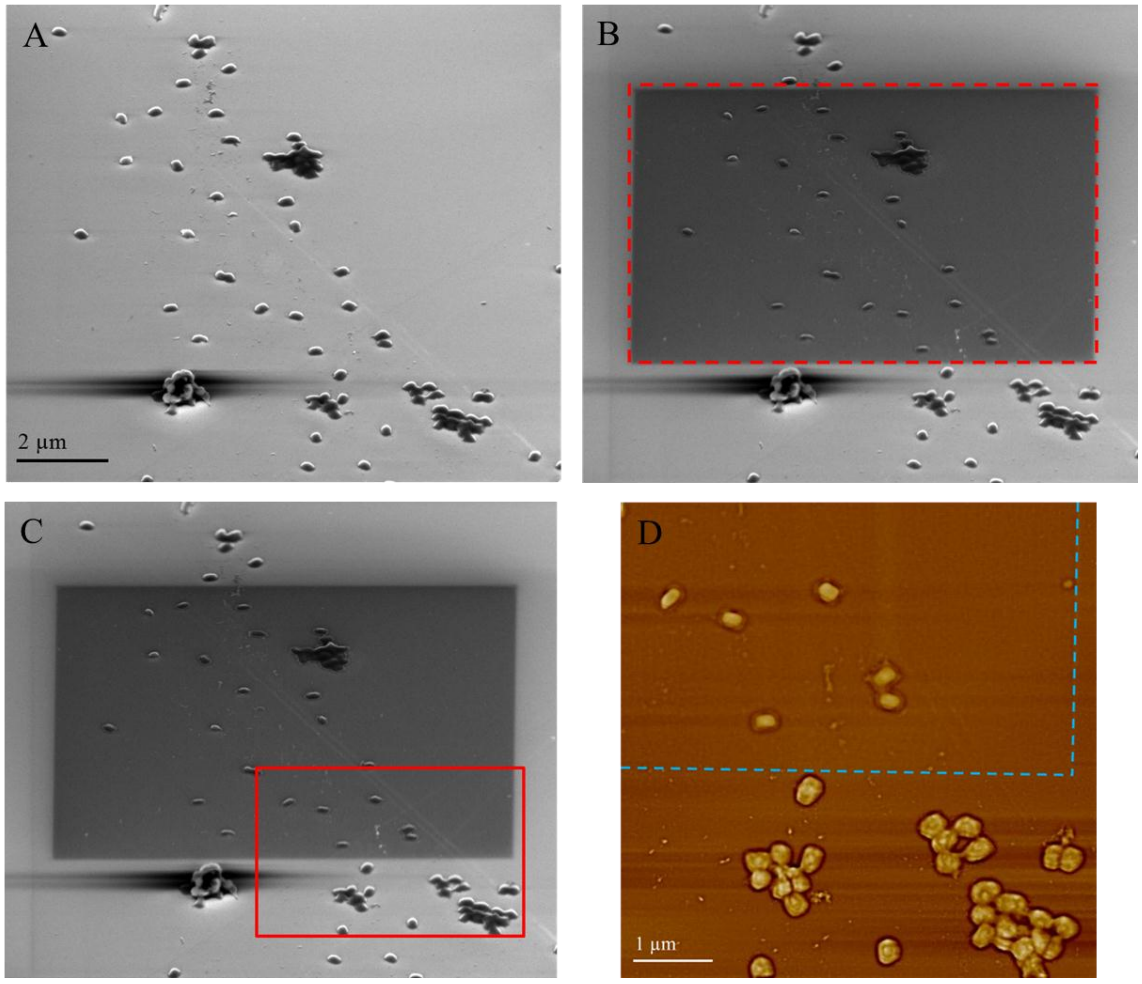

Figure 9-10: FIB analysis of a vaccinia viral sample. Image A and B are SEM images of the viral region before and after interrogation with a 3.4 pA gallium beam for 360 seconds, respectively. The analyzed region is shown framed in red in image B. Image D is an AFM image of the sample region framed in red in image C. The blue line in image D demarcates the region exposed to the beam (top) from the area outside of the analyzed area (bottom).

Figure 9-10A, B detail SEM generated images of a viral sample region prior to exposure to the gallium beam as well as the corresponding region after 360 seconds of analysis, respectively. The scanned region is framed in red in Figure 9-10B. Due to the

arrangement of the FIB instrument, specifically the 52 degree tilt of the sample substrate with respect to the secondary electron detectors, the scanned region appears distorted and non-symmetric. The analyzed region is, however, a 10 μm x 10 μm square. As previously stated, the analyzed regions were imaged with atomic force microscopy; an AFM image (Figure 9-10D) of the area demarcated by the red rectangle in Figure 9-10C is shown. Furthermore, the region exposed to the gallium beam is framed in blue in the AFM image. Readily apparent is the substantial size differential between the viral particles exposed to the beam and those outside of the analysis region. AFM measurements indicated an approximate 60% reduction in particle height as a result of the sputtering process.

The imaging and dimension quantification procedure was repeated for the two additional scanned regions. A sequence of AFM images (400 nm x 400 nm) illustrating the progressive erosion of a typical viral particle under gallium bombardment is shown in Figure 9-11. The first image 9-11A is of an intact non-sputtered virion, the following three depict typical viral particles after exposure to the ion beam for 60 (9-11B), 360 (9-11C) and 900 (9-11D) seconds. The substantial amount of material reduction clearly discernible between image 9-11A and B is indicative of the rapid, transitory sputtering regime observed in the NanoSIMS cesium experiments. Furthermore, the lack of significant particle degradation between image 9-11B and C is suggestive of a considerable reduction in the sputter rate and the establishment of the equilibrium-sputtering regime. The sustained erosion of the viral particles under equilibrium conditions can be seen in the progressive degradation of the virions in images 9-11B through D. AFM generated height profiles for the series of images in Figure 9-11 can be found in Appendix BIV.

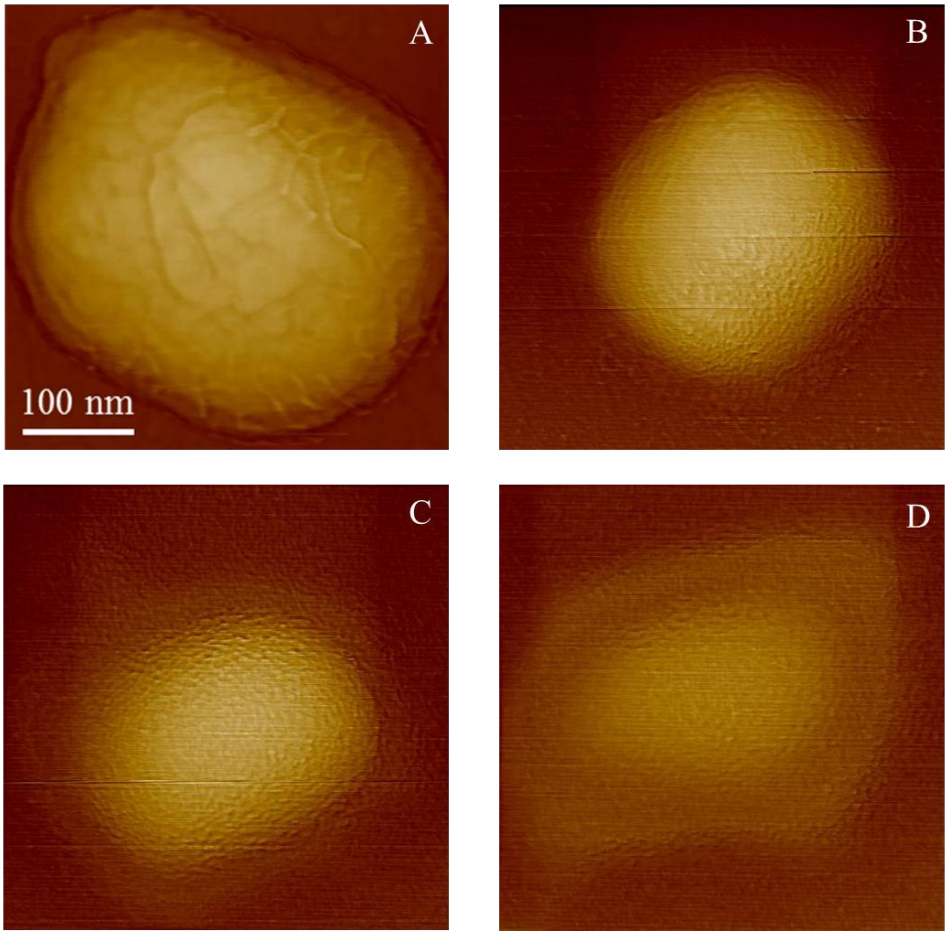

Figure 9-11: Viral particle erosion under gallium bombardment. AFM images of an intact viral particle (A) as well as particles within a 100 μm^2 region exposed to a 3.4 pA gallium beam for 60 (B), 360 (C) and 900 (D) sec.

Quantitative height measurements were obtained with the atomic force microscope and the results are shown as the blue data points in Figure 9-12. For comparison purposes the 2.98 pA cesium data is replicated and shown as the red data points. In addition to displaying the same qualitative characteristics, the two data sets exhibit quantitatively similar values over the full range of analysis times. Clearly discernible in the gallium data is the presence of the characteristic sputter rate variation; an initial non-equilibrium process rapidly stabilizing into a sputtering regime dominated by equilibrium conditions. These experiments corroborate the results generated with the

NanoSIMS and the reactive cesium beam. The demarcation of the sputter rate into two distinct regimes, then, appears to be a characteristic of the physical system itself and not an experimental artifact associated with a reactive incident beam.

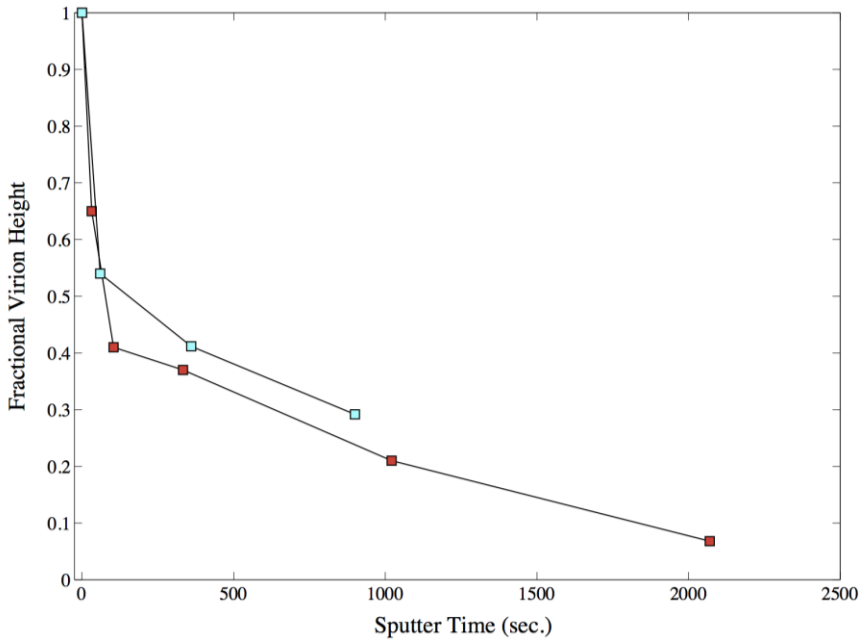

Figure 9-12: Viral particle height variation as a function of sputter time for a 2.98 pA cesium beam (red) and a 3.4 pA gallium beam (blue).

A similar set of experiments employing chemically fixed vaccinia virions was also conducted. The fixation process (see Appendix BII) terminates any biochemical processes and generates covalent chemical bonds between proteinaceous material within the virion. These experiments were designed to both address the issue of material decomposition under ion bombardment as well as to validate the non-equilibrium sputter rate model. The results, shown in Appendix BV, corroborate the previous data and provide further support for the time dependent sputter rate model.

9.3 Sputter rate variation: proposed physical attribution

The approximate two orders of magnitude reduction in the sputter rate, measured between the non-equilibrium and equilibrium-sputtering regime, is a phenomenon not previously documented. While the physical mechanism responsible for this rate variation is ambiguous, the dynamic process of cesium implantation and accumulation within the viral particle appears to play an instrumental role. A theoretical description of this process is first detailed and the numerical results generated from its implementation are subsequently compared to the experimental sputtering data. The results are then coupled with Monte Carlo simulations to model the anticipated change in viral particle sputtering characteristics due to cesium atom implantation. In addition, alternative theories, including sputter rate variation due to the breaking of molecular bonds within the viral particle, as well as ion beam induced plastic deformation of the virus, are explored from a qualitative perspective.

9.3.1 Dynamic cesium implantation

Ion bombardment results not only in the systematic erosion of the interrogated specimen, but it also induces a substantial material transformation due to the implantation of cesium atoms. During the initial stage of the sputtering process the concentration of embedded cesium atoms is time dependent and, therefore, exists at some non-equilibrium level. As the sputter time increases, however, an equilibrium regime is entered in which the concentration of cesium remains relatively constant and the process of secondary ion emission is stable. This steady state saturation value occurs when the momentary sputter front has reached the original cesium ion implantation front, or at a depth of approximately $2R_p$, where the variable R_p represents the average projected range of the implanted ions[60]. A theoretical treatment of this dynamic process was formulated by Carter et al. assuming an arbitrary implantation probability function f(z') and an infinite medium[61]. This physical phenomenon can be accurately modeled through the implementation of a one-dimensional continuity equation of the following form:

$$\frac{\partial n(z',t)}{\partial t} = v_s \frac{\partial n}{\partial z'} + \frac{j}{e}\alpha f(z') \quad (7)$$

where n(z',t) is the concentration of implanted cesium ions and v_s is the speed at which the momentary implantation surface recedes in a fixed coordinate system. The third term, representing the primary ion source, is composed of the current density j, the ion charge e, an absorption coefficient α and the aforementioned implantation probability function. The spatial coordinate in Equation 7, z', is a time varying system with its zero fixed to the instantaneous sputter surface. In order to demonstrate the implications of Equation 7 a Gaussian shape for the implantation probability function is assumed:

$$f(z') = \frac{1}{\sqrt{2\pi}\Delta R_p} \exp\left(-\frac{\left(z' - R_p\right)^2}{2\Delta R_p^2}\right)$$

The variable ΔR_p is the standard deviation of the projected range. The spatial and temporal distribution of the implanted cesium ions can then be shown to assume the form:

$$n(z',t) = \frac{\alpha\left(\frac{j}{e}\right)}{2v_s}\left(\text{erf}\left(\frac{z' - R_p + tv_s}{\sqrt{2}\Delta R_p}\right) - \text{erf}\left(\frac{z' - R_p}{\sqrt{2}\Delta R_p}\right)\right) \quad \text{where} \quad \text{erf(x)} = \frac{2}{\sqrt{\pi}}\int_0^x \exp(-t^2)\,dt$$

With the purpose of illustrating the progressive establishment of an equilibrium cesium ion concentration within the sample, a normalized plot of n(z',t) at a series of discrete time steps is shown in Figure 9-13; the constant parameters are absorbed into the factor ϕ. The steady state distribution of cesium atoms within the sample is achieved at time t*. Consequently, for all t greater than or equal to t* the implantation profile remains constant.

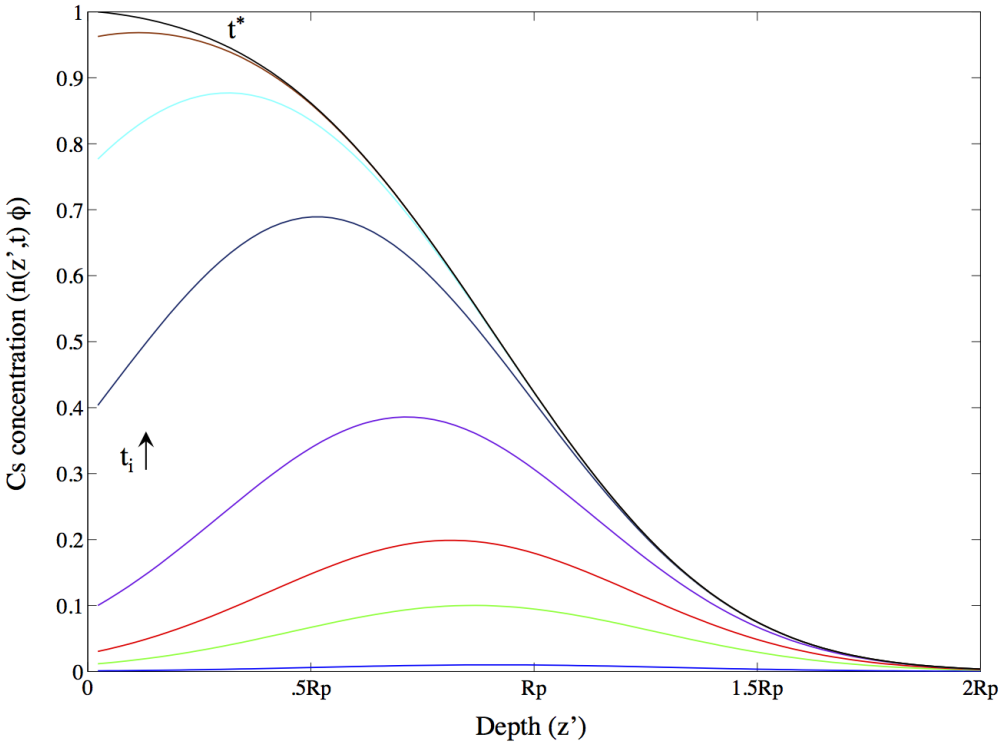

Figure 9-13: Normalized concentration of cesium atoms during NanoSIMS analysis. The depth coordinate fixed to the receding surface and is, therefore, time varying. An equilibrium level of cesium atoms is reached at a time t*.

Furthermore, if we make an assumption regarding the Gaussian implanted profile, namely, that the quantity $R_p/(\sqrt{2}\Delta R_p)$ is greater than approximately 1.6, and recall that equilibrium conditions are established at a point $t^* v_s = z^* = 2Rp$, a simple relation regarding the surface concentration of cesium ions at time t* can be formed:

$$n(0, t^*) \approx \frac{\alpha\left(\frac{j}{e}\right)}{v_s}$$

An additional parameter of interest is the stored ion fluence at saturation (F_s). Assessment of this quantity provides an indication of the level of cesium ions retained in the viral sample per area. F_s is formulated as follows:

$$F_s(t = t^*) \approx \int_0^{2R_p} n(z', t^*)dz' \approx \frac{\alpha\left(\frac{j}{e}\right)R_p}{v_s}$$

The physical implications of the equations developed above provide pertinent insight into the qualitative behavior of the data displayed in Figure 9-6. The overall shape of the curve can be attributed to the establishment of sputtering equilibrium. Region I is a non-equilibrium regime where the concentration of cesium atoms within the particle is steadily increasing until equilibrium conditions are reached. Region II is then entered and the rate of sputtering stabilizes to some value dependent on the physical characteristics of the analyzed medium. Regions I and II would, then, presumably correspond to times $t_i < t^*$ and $t_i > t^*$ in Figure 9-13, respectively. Upon entering region II the viral particle has reached the saturation point with regards to the implanted cesium ions. It is apparent that by this time, t*, the sputtered viral particle no longer exhibits its inherent molecular constitution; it is, effectively, a heterogeneous material composed of biological molecules and cesium atoms. The sputtering characteristics of this composite particle would naturally differ from those of the viral particle alone[62]; these characteristics do, however, remain relatively constant in region II due to the establishment of material composition equilibrium. Therefore, the change in effective sputter rate between the two regions can possibly be explained within this framework: the material sputtered in region I is primarily composed of biological components, exhibiting a rapid rate of erosion. In region II, however, the increased presence of alkali metal atoms within the viral particle results in a reduction in the apparent rate of sputtering.

In addition to accurately reflecting the qualitative aspects of the viral sputtering process, implementation of the model developed above provides the means to generate quantitative estimates of pertinent experimental parameters; these estimates, however, are predominately order of magnitude values. The lack of a well-defined quantitative

approach primarily stems from the absence of theoretical models and experimental data concerning the physical process of ion bombardment of biological materials. While numerous theories have been developed to model the sputtering process of inorganic substrates, including the aforementioned linear cascade theory, thermal spike models and hydrodynamic theories incorporating shock wave formation phenomenon, few studies have focused upon the systematic evaluation and modeling of the physical mechanisms governing the sputtering of heterogeneous biological materials. The work that has been done in this field, prompted by the desire to utilize ion beam bombardment to induce the transfer of exogenous macromolecules into cellular structures[63], has indicated a large discrepancy between experimentally determined parameters for cellular material and theoretical estimates, including an approximate seven-fold increase in the sputtering yield compared to theoretical predictions[64]. In addition, the aforementioned equations are based upon an infinite medium geometry and a Gaussian ion implantation profile. A quantitative approximation, then, is necessarily employed in extending this analysis to nanometer sized individual viral particles with variable geometry and composition, as well as an unspecified distribution of embedded cesium ions.

Insight into the latter consideration, namely, the distribution of deposited cesium atoms, can be gained through the examination of AFM images of NanoSIMS analyzed regions. At long analysis times large conglomerations of cesium are noted. In addition, virion piles exhibit dramatic changes in surface morphological characteristics, indicative, perhaps, of the presence of large surface concentrations of cesium. The AFM images in Figure 9-14 illustrate the effects of a 1.4 pA incident beam scanned over a 100 μm^2 raster area for approximately 4000 sec; Figure 9-14A, B are height and phase images, respectively. The NanoSIMS analyzed area is highlighted in red. Numerous cesium conglomerations are apparent in the image, representative examples of which are framed by the blue squares. In addition, there appears to be a substantial layer of cesium on the virion pile (blue arrow). As can be seen in the phase image, the surface characteristics of this layer are distinct from the underlying material. Furthermore, it is interesting to compare the AFM images in Figure 9-14 with those in Figure 9-3. The post NanoSIMS image in the latter figure lacks the presence of cesium aggregates, presumably due to the

significantly shorter analysis time. Based upon the experimental conditions, however, the equilibrium regime of cesium surface concentration had, theoretically, been reached. Therefore, no further accumulation of cesium would be expected during additional analysis. The results displayed in Figure 9-14, however, are indicative of a continuous accrual of implanted cesium atoms during the analysis time.

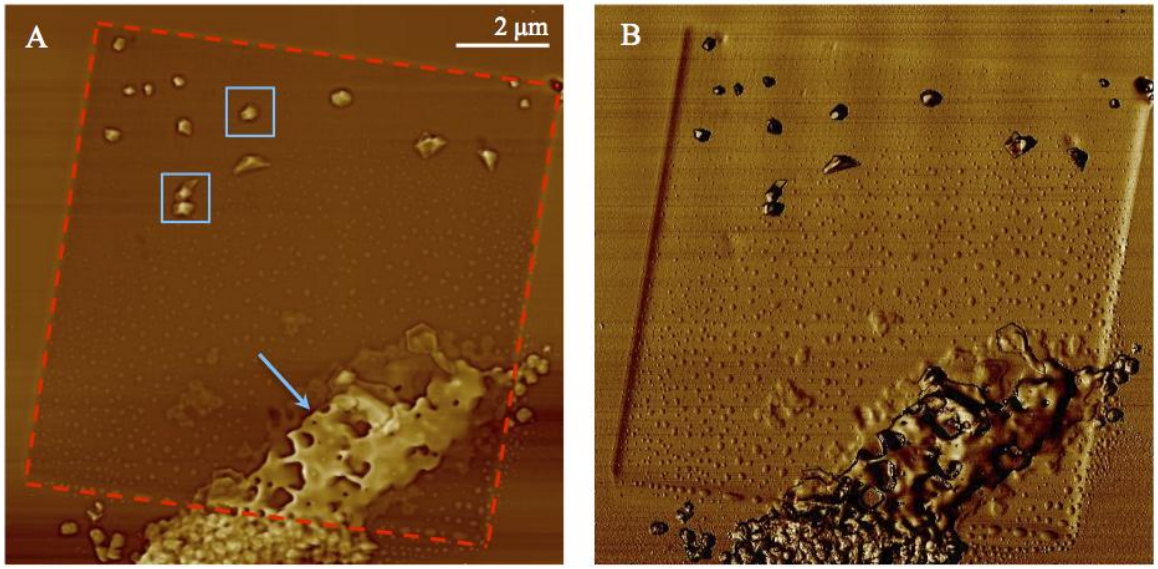

Figure 9-14: AFM height (A) and phase (B) image of a viral region analyzed with NanoSIMS (framed in red) illustrating the apparent presence of cesium conglomerations. These conglomerations, shown in blue, were observed during long analysis times of regions where virion piles were present.

While this phenomenon may be attributed to a multitude of factors, the presence of a large virion pile within the analysis region appears to play a prominent role. Numerous areas with similar virion conglomerations exhibited the same post analysis cesium structures. In addition, the possibility exists that the sputtering process may induce a phase change within the virion/cesium composite structure altering the sputtering characteristics and, possibly, the rate of cesium accumulation. While the sputtering induced thermodynamics of biological materials is a subject beyond the scope of the present research, it is possible that the high-energy ion bombardment causes local melting at the site of impact. Furthermore, the presence of chemical vapor deposition due

to sample outgassing is an additional complicating factor that can not be discounted. These results appear to bring into question two fundamental assumptions of the steady state cesium concentration model; the first being the relatively homogeneous distribution of cesium atoms in the analyzed region and the second being the establishment of an equilibrium level of implanted cesium atoms. Nonetheless, the model does appear to provide a convincing physical mechanism for the experimentally measured time varying sputter rate.

With these considerations in mind, then, a quantitative estimate of the average projected range of the implanted cesium atoms as well as the cesium atom surface concentration at the saturation time (n(0,t*)) is formulated. Within this theoretical construct the experimental data indicated that the average range, Rp, of the cesium atoms within the viral particle is approximately 35 nm. Assessment of this parameter entailed the inherent assumption that the demarcation point separating regions I and II in Figure 9-6 represents the transition from non-equilibrium to equilibrium conditions. In addition, the equilibrium cesium concentration was determined to be approximately 9.3×10^9 atoms/μm^3. Consequently, during equilibrium conditions approximately 15% of the viral particle surface atoms are cesium. The theoretically predicted progression of cesium accumulation within the sample is shown in Figure 9-15 along with the experimentally measured sputter rate variation. The data shown is for a 0.8 pA incident beam scanned over a raster area of 100 μm^2. The inverse behavior of the sputter rate and cesium atom surface concentration is readily apparent.

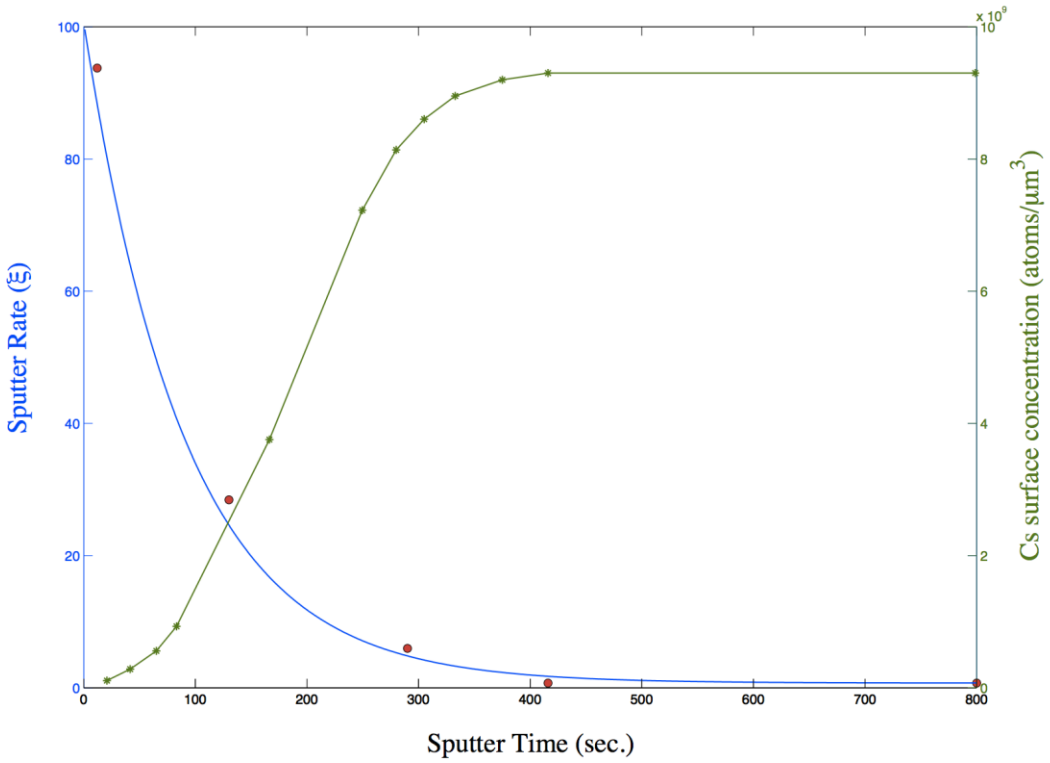

Figure 9-15: Comparison of sputter rate variation and cesium surface concentration for a 0.8 pA incident beam scanned over a 100 µm^2 area.

While a qualitative correspondence between these two variables is clearly present, the feasibility of a two order of magnitude change in the sputter rate due to the presence of implanted cesium atoms requires investigation. To this end, Equation 3 was employed to generate a theoretical prediction of the sputter yield (atoms ejected/Cs ion) for both the initial viral particle as well as for a particle implanted with the equilibrium concentration of cesium atoms. For calculation purposes, the chemical composition of vaccinia virus was assumed to be as previously reported[65]. Furthermore, values for the additional parameters in Equation 3 were calculated in the manner specified in Yamamura and Tawara[55]. Results indicated an approximate 30% reduction in the number of ejected atoms per incident cesium ion for the particle embedded with the equilibrium concentration of cesium atoms as compared to the initial viral particle. Conversion of

these quantities to the sputter rate formulation, however, indicated a negligible decrease in the rate of sputtering between the two compositionally distinct particles.

9.3.2 Monte Carlo simulations

A series of Monte Carlo computational studies was subsequently initiated in an attempt to more accurately model the dynamic sputtering characteristics of the viral particle. Calculations were performed utilizing the program SRIM, a computational tool that calculates the stopping and range of ions within matter based upon a quantum-mechanical modeling of the ion-atom collisional process[66]. Chemical composition models of the viral particle within both the non-equilibrium as well as the equilibrium sputtering regimes were constructed with SRIM. For modeling purposes, the implanted cesium was assumed to be uniformly distributed within the particle to a depth, R_p, corresponding to one half of the measured implantation front. In addition, the SRIM simulations were implemented using a 16 keV cesium ion beam at normal incidence. While the range of cesium implantation as well as the sputter yield is dependent upon surface curvature and roughness, the viral particle was modeled as a smooth flat surface. In addition, differential implantation and sputtering due to edge effects were neglected in the simulations. Utilizing the aforementioned assumptions, the range and trajectories of the implanted cesium ions as well as the resulting collisional cascade within the viral particle were calculated for each condition.

Initial computational studies were conducted to examine the range of the incident cesium ions within a simulated viral substrate composed of 68.75% carbon, 12% nitrogen, 10% oxygen, 8% hydrogen, .5% phosphorus and .75% sulfur; a chemical composition reflecting the viral state at the initiation of the non-equilibrium regime. Figure 9-16 details the calculated trajectories and range of 500 implanted cesium ions. Simulations conducted with 10,000 incident ions yielded an average penetration depth of 19 nm, a quantity approximately one half of the predicted value based upon the coupling of the non-equilibrium model with the experimentally measured data. In addition, the straggle, or standard deviation of the projected ion range was found to be 3 nm.

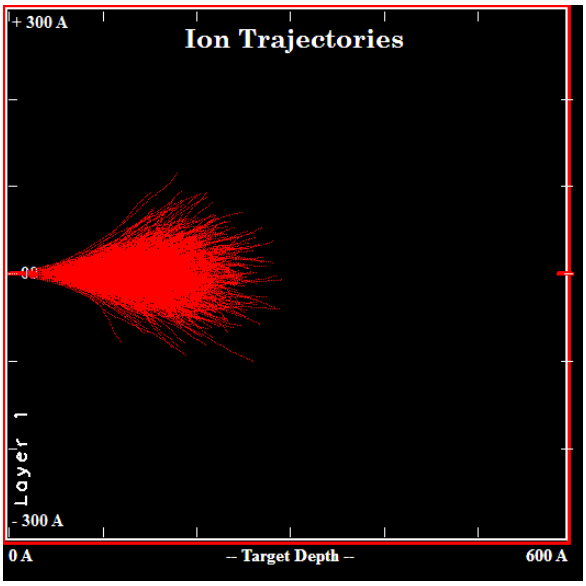

Figure 9-16: Cesium ion trajectories into a model substrate with an equivalent chemical composition as a vaccinia viral particle. The average penetration depth was observed to be 19 nm.

In order to assess the effect of an equilibrium amount of cesium atoms embedded within the sample, a simulated viral substrate composed of 15% cesium uniformly distributed to a specified depth, R_p, was constructed. Differential atomic sputtering was neglected, consequently, the remaining atomic composition was assumed to follow a suitably scaled form of the initial chemical distribution. For depths greater than R_p the material composition was assumed to be that of an unanalyzed viral particle. Furthermore, two models with distinct values of R_p were generated; the first with R_p set to 19 nm, the average projected range based upon the previous series of Monte Carlo simulations, and the second, set to the R_p value generated through the coupling of the experimental data and the time dependent cesium concentration model, namely 35 nm. In the former case the projected average ion range was found to be 24.4 nm with a straggle of 7.5 nm; simulations employing the latter value of R_p yielded range and straggle values of 26.1 nm and 10 nm, respectively. An approximate two-fold difference in the modeled depth of cesium deposition, then, appears to have only a slight effect on the substrate sputtering characteristics. Ion penetration depths and ion trajectories, however, are highly sensitive to the presence of cesium within the substrate. Figure 9-17 displays the

calculated trajectories of 500 cesium ions for the aforementioned simulation with R_p equal to 35 nm. As previously noted, the domain was divided into two regions with the equilibrium level of cesium atoms being confined within Layer 1. Readily apparent in Figure 9-17 is the increased ion penetration depth and range straggle as compared to Figure 9-16. In addition, the lateral distribution of implanted cesium ions varies significantly between the two simulation conditions. This physical phenomenon can be attributed to the increase in the effective average mass of the sputtered material due to the implantation of cesium atoms. As previously specified, sputtering collisions can be considered elastic; an assumption predicated upon the observation that the energies required for sputtering are typically much greater than vibrational or lattice bonding energies[49]. For elastic collisions maximum energy transfer occurs when the masses of the colliding atoms are equal; consequently, the trajectories of the implanted cesium ions within the virion/cesium composite material exhibit both a greater average penetration depth as well as a greater straggle value due to the increased average mass of the interrogated substrate.

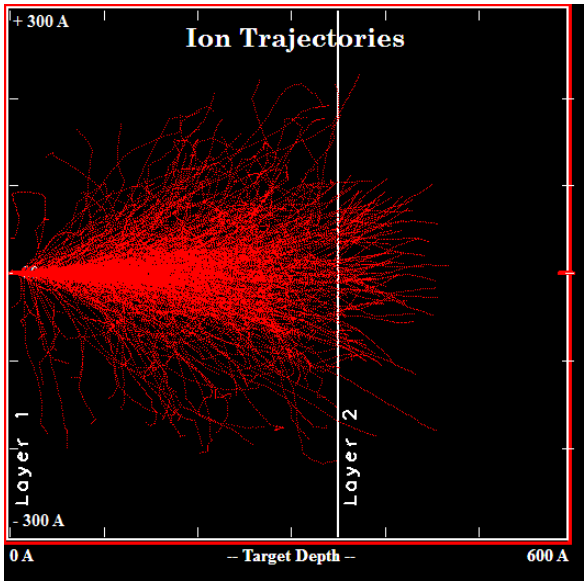

Figure 9-17: Cesium ion trajectories into a model substrate based upon the chemical composition of a vaccinia virion after an equilibrium level of cesium has been embedded within the sample. Layer 2 was constructed to reflect the original composition of the viral particle. The average penetration depth was observed to be 26 nm.

Further insight into the material dependent sputtering process can be ascertained by examining the damage cascades generated by the cesium bombardment event. Figures 9-18 and 9-19 detail the collision cascades for the viral particle model as well as for the viral particle model embedded with an equilibrium level of cesium ions, respectively. In order to generate distinguishable visual results the simulations were limited to 20 incident cesium atoms. The colored trajectories indicate the displacements of distinct atomic constituents induced by the cesium impact event; the most conspicuous are those for carbon (purple), oxygen (blue) and nitrogen (gold). As would be expected based upon the ion penetration depths displayed in Figures 9-16 and 9-17, the damage cascades induced in the virion/cesium composite substrate are more extensive than those for the viral particle alone. In addition, simulation results indicate that the average energy of a sputtered atom increases significantly with the inclusion of cesium within the viral particle. For example, the average energy of a sputtered carbon atom from a viral particle is 27 eV; after an equilibrium level of cesium has been implanted within the particle, however, the average value increases nearly threefold to 76 eV. The increase in sputtered atom energy is a result of the aforementioned observation concerning the relationship between energy transfer and mass difference of the sputtered material and bombarding species. The energy deposition process also plays an instrumental role in determining the sputter yield. In general, greater depths of ion penetration result in less energy transfer at the surface and more energy being deposited at subsurface locations. Consequently, all other factors being equal, the sputter yield is expected to decrease with increasing ion penetration depth. Simulations, however, indicate a 20% increase in the predicted sputter yield for the virion/cesium composite model versus the virion alone. This discrepancy may be attributed to the more efficient transfer of energy at the surface due to closer mass matching between target and projectile. While the quantitative sputter yields based upon Equation 3 and the Monte Carlo simulations differ, both models predict a 20-30% increase in the sputter yield when an equilibrium level of cesium has been established within the viral particle. These predictions are not consistent with the experimental measurements indicating a significant and continuous reduction in the quantity of atoms sputtered per ion with increasing cesium concentration.

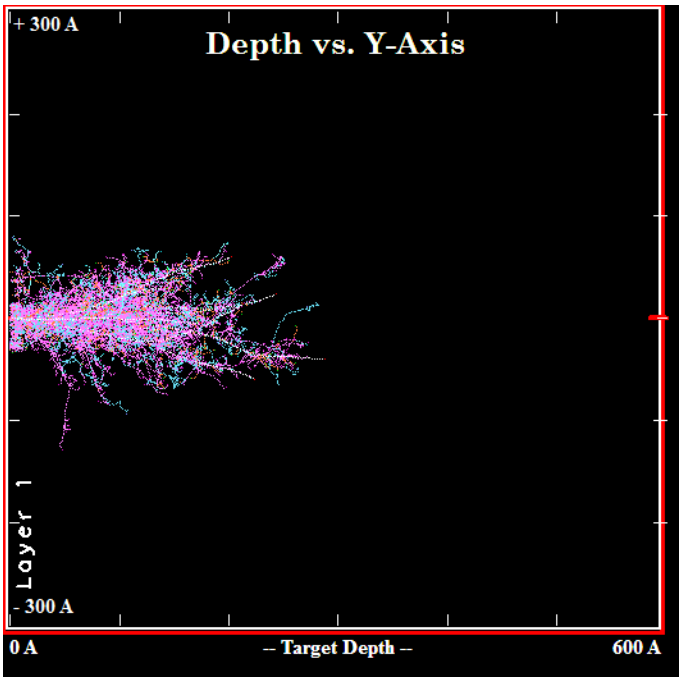

Figure 9-18: Damage cascades in the viral model substrate produced by cesium ion bombardment.

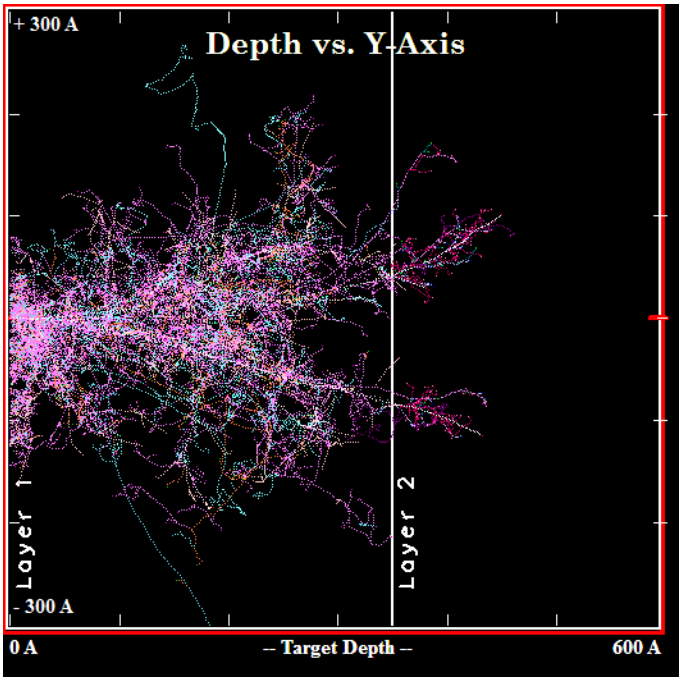

Figure 9-19: Damage cascades in the viral/cesium model substrate produced by cesium bombardment.

The discrepancy between simulation and experimental results can be ascribed to a multitude of factors. The most prominent of which is the extension of physical properties of homogeneous inorganic materials to a heterogeneous organic particle. Specifically, quantification of the sputtering process is highly dependent upon the surface binding energy (U_s) of the sputtered material. The theoretical/empirical calculations (Equation 3), as well as the Monte Carlo simulations, both employ surface binding energy values based either upon sputtering measurements of homogeneous constructed samples of the specific element or, where appropriate, the elemental heat of sublimation[55]. Substantial inaccuracies will presumably be present when modeling the surface binding energy of a heterogeneous composed viral particle with data obtained from homogeneous inorganic substrates. In addition, further uncertainties are present in quantifying the surface binding energy of a viral particle embedded with cesium atoms. The numerical methods previously detailed assume that the cesium is an integrally bonded, homogeneously distributed, constituent of the viral particle. Modeling of the implanted cesium in this manner is physically inaccurate; the assumption that the implanted cesium is bonded in any systematic manner within the virion is unfounded. Additionally, no sputtering data is available for cesium, consequently, the quantification of an effective surface binding energy value for the virion/cesium composite is an order of magnitude estimate.

Further complications regarding sputter rate quantification arise when considering the inherent geometric and compositional aspects of the viral particle sputtering process. Rates of sputtering have been shown to be highly sensitive to surface geometry[49]. Furthermore, the fact that the lateral dimensions of the viral particle are only 4-5 times larger than the 50 nm incident cesium ion beam may introduce sputtering complications not seen in previous studies. Specifically, rapid sputter rates may be the result of the close proximity of the particle edge to the cesium beam during a majority of the interrogation time. An additional consideration concerns the material construction of the viral particle. The level of porosity and material density may play an integral role in the rate of sputtering. An initially high level of porosity and low material density may result in extensive cesium implantation, leading to rapid initial particle degradation. The buildup of cesium within the sample may substantially reduce the sample porosity while

simultaneously increasing the surface density, leading, perhaps, to a reduction in the effective sputter rate. In addition, as previously alluded to, the thermodynamic aspects of the sputtering process may induce a phase change in the bombarded material. This process would be a time dependent phenomenon and the resulting variation in sputter rate characteristics would presumably be considerable.

9.3.3 Sputter rate variation: alternative possibilities and conclusions

Two final considerations regarding the apparent sputter rate variation warrant comment: the possibility of plastic deformation of the particle during ion bombardment as well as that of rate variation due to damage accumulation. In regards to the former issue, it has been forwarded that the dramatic initial change in viral particle height may not be due to the loss of material but instead be a result of virion collapse during NanoSIMS analysis. For this theory to be viable, a corresponding increase in the lateral dimensions of the particle should be observed; as is readily apparent in Figures 9-4 and 9-11, however, a substantial reduction in the planar dimensions of the viral particle is present. These results do not, however, preclude the possibility of apparent sputter rate variation due to ion-induced densification of the viral particle. Within this framework, the large initial dimensional change is attributed, not to the loss of viral material, but to the densification of the particle. While the experiments presented herein cannot necessarily preclude this possibility, the existence of a substantial lateral reduction in the viral particle dimensions is not consistent with this theory. Specifically, if the densification process were a dominant feature of the ion beam/viral particle interaction, one would expect low levels of dimensional change in planes parallel to the beam; a phenomenon not observed in the AFM images of analyzed particles. In contrast, the latter consideration, concerning the accrual of sample damage during the analysis, may play a prominent role in the sputtering process. It has been noted in TOF-SIMS studies that the sputtering of intact molecules rapidly declines with time due to the breaking of sub-surface bonds in the interrogated sample[67]. The same physical mechanism would presumably be at work in the present study. Therefore, large intact molecules may

comprise a substantial portion of the initially sputtered material resulting in a rapid volumetric loss and a high apparent sputter rate. With continued exposure to the ion beam, however, the molecular bonds would be destroyed, resulting in the sputtering of small molecular fragments or atoms and a corresponding decline in the rate of material loss.

The lack of consistent agreement between theoretical predictions and experimental results concerning the sputtering of sub-micron scale biological particles indicates the need for further study and the development of new conceptual models. Specifically, studies focused upon the examination of the initial non-equilibrium sputtering regime are warranted. The time dependence of the vaccinia virion sputter rate may depend on geometric and material considerations. The most intriguing relationship, however, is that between the dynamic accumulation of cesium atoms and sub-surface damage within the viral particle and the corresponding reduction in the sputter rate. While a definitive underlying physical mechanism for the experimentally measured sputter rate variation remains ambiguous, it is clear that small biological particles exhibit sputtering characteristics that deviate markedly from those predicted from traditional theoretical models.

Chapter 10 NanoSIMS analysis of vaccinia virus

The experimental methodology detailed in the previous chapter was implemented to analyze the architectural arrangement of isotopically labeled vaccinia viral particles. As an initial step, however, isotopic measurements of non-labeled virions were conducted to validate the ability of the technique to produce quantitatively accurate values. Subsequent experiments focused upon the examination of both ^{13}C lipid labeled and ^{15}N DNA labeled viral particles. Depth resolved profiles are presented and interpreted within the context of the prevailing architectural models regarding the localization and distribution of the vaccinia lipid membrane and genome. In addition, the possibility of NanoSIMS analysis of sub-viral constituents, specifically, isolated nucleoprotein structures, is explored.

10.1 Isotopic measurements of non-labeled viral particles

NanoSIMS experiments were conducted to quantify the level of ^{13}C and ^{15}N isotopes within unlabeled virions. These tests were implemented to provide both a baseline assessment of the amount of natural enrichment within the viral particles as well as to demonstrate the ability of the NanoSIMS to accurately measure isotopic ratios in nanometer scale biological systems. Due to the lack of information regarding the quantity of sputtered and ionized material per scan cycle, absolute isotopic species counts provide little information regarding the enrichment level of a sample. Consequently, ion count ratios were generated and compared to natural abundance levels to assess the extent of

isotopic enrichment. In order to quantify the natural levels of ^{13}C and ^{15}N isotopes within vaccinia virions the NanoSIMS instrument was aligned to detect the following molecular ions: $^{12}C_2^-$, $^{13}C^{12}C^-$, $^{14}N^{12}C^-$, $^{15}N^{12}C^-$ and $^{31}P^-$. An area of the vaccinia sample composed of individual viral particles was scanned for 200 cycles, resulting in the erosion of approximately 90% of the original virion height. A NanoSIMS secondary electron image of the analyzed area is shown in Figure 10-1. In addition, the accompanying chemical image illustrates the region of interest (ROI), highlighted in light blue. The ROI is a gating tool limiting the regions from which ion counts are obtained. Therefore, only ions originating from within the ROI will contribute to the total counts. The ROI containing the eight individual viral particles present in the analyzed region was generated based upon a 60% threshold of the $^{14}N^{12}C^-$ species counts.

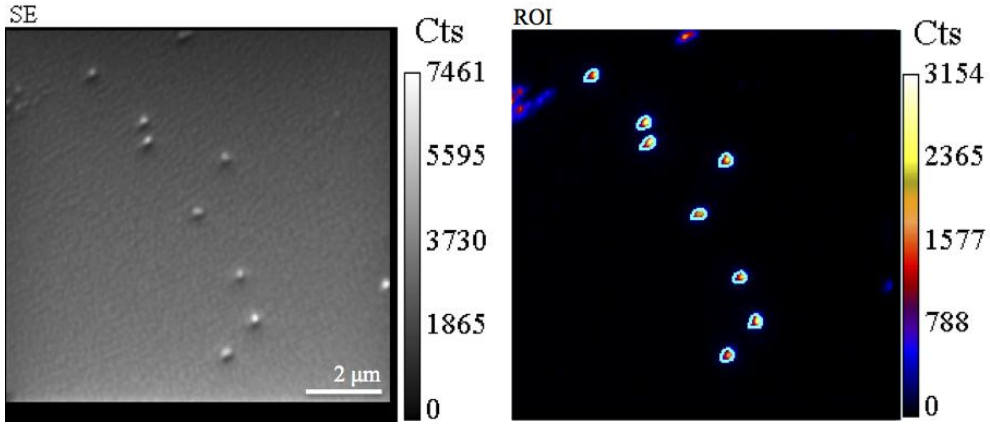

Figure 10-1: Secondary electron image (left) of the region analyzed to assess the natural abundance level of the ^{15}N and ^{13}C isotope within individual virions. The blue outlines surrounding the viral particles apparent in the chemical image (right) represent the region of interest (ROI). All species counts used for quantification purposes originated from within the ROI.

Chemical images detailing the spatial distribution and magnitude of the relevant species counts, as well as $^{13}C^{12}C^-/^{12}C_2^-$ and $^{15}N^{12}C^-/^{14}N^{12}C^-$ ratio images are shown in Figures 10-2 and 10-3, respectively. Furthermore, ion counts from the eight individual virions in the ROI were acquired as a function of scan cycle number; $^{13}C^{12}C^-/^{12}C_2^-$ and

$^{15}N^{12}C^{-}/^{14}N^{12}C^{-}$ ratios were subsequently generated and are shown in Figures 10-4 and 10-5, respectively.

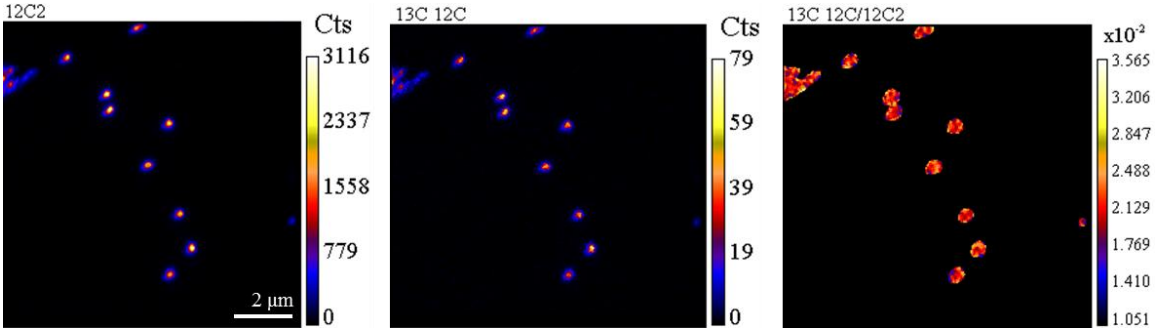

Figure 10-2: Chemical images detailing the distribution of $^{12}C_2^{-}$ (left) and $^{13}C^{12}C^{-}$ (middle) species counts as well as a $^{13}C^{12}C^{-}/^{12}C_2^{-}$ ratio image (right) generated from the ROI shown in Figure 10-1. Counts represent the summed quantity for the 200 analysis cycles.

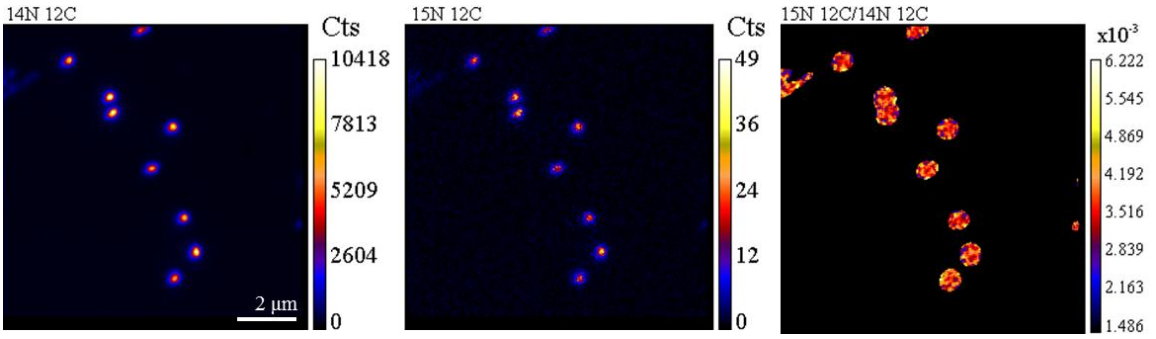

Figure 10-3: Chemical images detailing the distribution of $^{14}N^{12}C^{-}$ (left) and $^{15}N^{12}C^{-}$ (middle) species counts as well as a $^{15}N^{12}C^{-}/^{14}N^{12}C^{-}$ ratio image (right) generated from the ROI shown in Figure 10-1. Counts represent the summed quantity for the 200 analysis cycles.

For purposes of clarity, the ratio values in Figures 10-4 and 10-5 are plotted for every tenth analysis cycle. Error bars are derived from Poisson statistics and represent a 95% confidence interval based upon the cycle specific ion counts. Quantification of the average $^{13}C^{12}C^{-}/^{12}C_2^{-}$ and $^{15}N^{12}C^{-}/^{14}N^{12}C^{-}$ ratios for the 200 cycles yielded a result of $.0213 \pm 2.62*10^{-4}$ and $.00368 \pm 5.82*10^{-5}$, respectively; uncertainty values represent one standard error of the mean. These values correspond well to the natural abundance levels of .0214 for $^{13}C^{12}C^{-}/^{12}C_2^{-}$ and .00364 for $^{15}N^{12}C^{-}/^{14}N^{12}C^{-}$. The isotopic ratios were, as

expected, consistent throughout the virion depth. In addition, these data indicate that, despite the small volume of sputtered material, accurate isotopic ratios can be generated from individual viral particles.

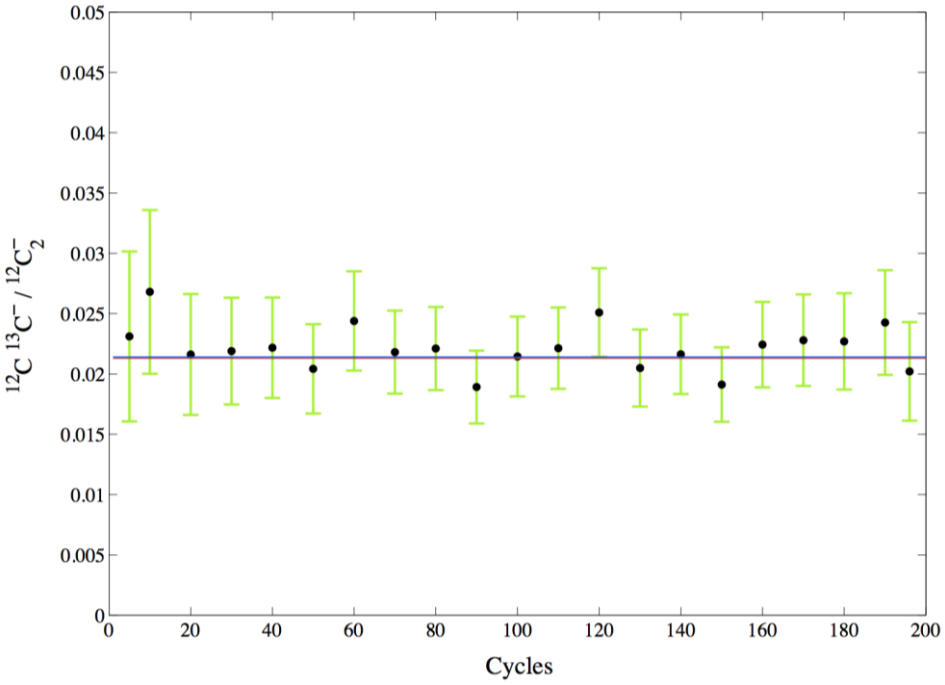

Figure 10-4: $^{12}C^{13}C^{-}/^{12}C_2^{-}$ ratio as a function of NanoSIMS scan cycle for the eight non-labeled viral particles shown in Figures 10-1 and 10-2. The average ratio value (.0213) is shown as the red line; the natural abundance level of .0214 is shown in blue.

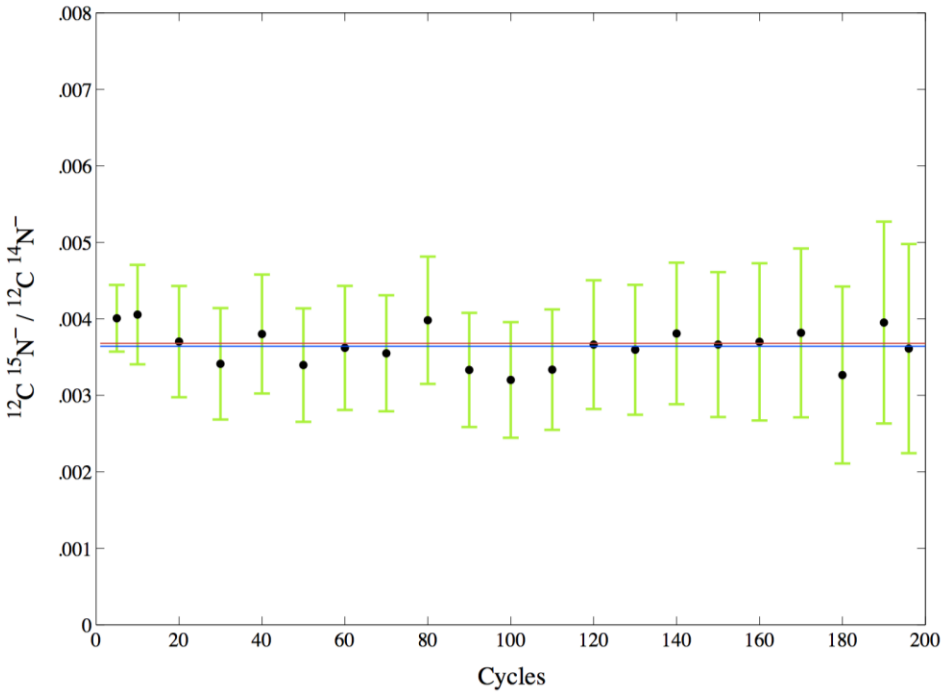

Figure 10-5: $^{12}C^{15}N^{-}/^{12}C^{14}N^{-}$ ratio as a function of NanoSIMS scan cycle for the eight non-labeled viral particles shown in Figures 10-1 and 10-3. The average ratio value (.00368) is shown as the red line; the natural abundance level of .00364 is shown in blue.

10.2 Isotopic label incorporation and heterogeneity

Vaccinia viral particles were grown in BSC-40 cells exposed to either ^{13}C labeled fatty acids or ^{15}N labeled thymidine. The production protocol for the generation of the isotopically labeled virions can be found in Appendix BVI.

Quantitative assessment of the extent of isotopic label incorporation and heterogeneity within the virion population was necessary for the accurate interpretation of chemical depth profiles. Evaluation of these quantities necessitated the examination of both the secondary ion counts as a function of cycle number as well as chemical images detailing the distribution of isotopic ratios. The former provided information regarding the level of incorporation of the isotopic label within individual virions. In addition, isotope count levels were pertinent for assessing the statistical reliability of the data. The

latter analysis method, namely, the construction of isotopic ratio images, provided information concerning the level of isotopic label heterogeneity present in the viral sample.

Secondary ion counts were tabulated for ^{13}C and ^{15}N isotopically labeled viral particles. Figure 10-6 depicts a representative example of ion counts as a function of cycle number for a single ^{13}C labeled virion; the red, blue and black curves signify the measured $^{12}C^{14}N^-$ and $^{13}C^{14}N^-$ counts and calculated natural abundance level of $^{13}C^{14}N^-$, respectively. Comparison of the measured and calculated $^{13}C^{14}N^-$ counts indicate that throughout the virion interior the isotopic label was incorporated to a level approximately three-fold above natural abundance. Due to the small volume of sputtered material, however, the emission of secondary ions was relatively low, resulting in the detection of 150-200 $^{13}C^{14}N^-$ ions per cycle; a count rate approximately 30 times less than that for the $^{12}C^{14}N^-$ ion. Based upon these count rates a $^{13}C^{14}N^-/^{12}C^{14}N^-$ measurement precision level of 8% was achieved.

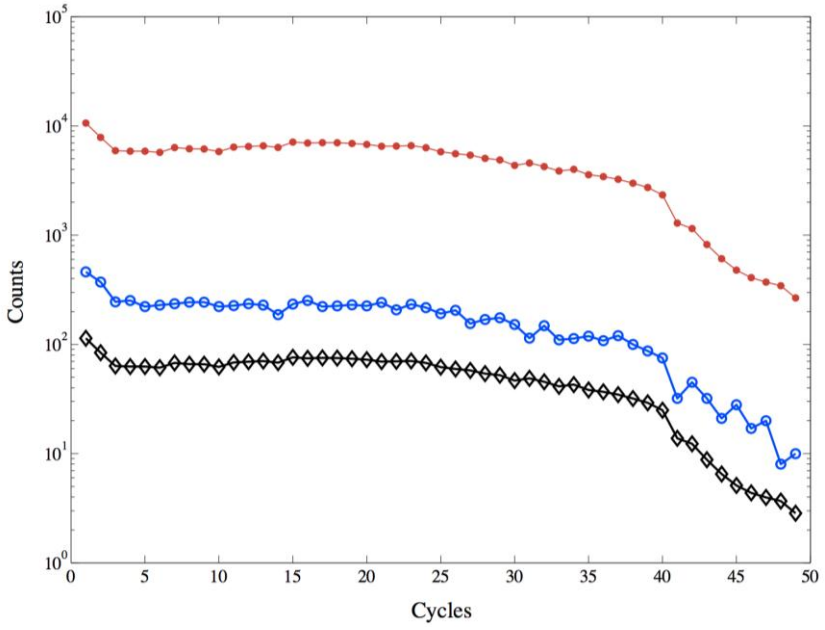

Figure 10-6: Measured species counts as a function of NanoSIMS scan cycle for an individual ^{13}C labeled viral particle: $^{12}C^{14}N^-$ (red), $^{13}C^{14}N^-$ (blue). The black curve is the calculated natural abundance level of $^{13}C^{14}N^-$ based upon the $^{12}C^{14}N^-$ counts. The ^{13}C tag was incorporated to a level approximately three times that of natural abundance.

A similar analysis was conducted for the ^{15}N labeled virions; ion counts as a function of cycle number for an individual virion are shown in Figure 10-7. The red, blue and black curves signify the measured $^{12}C^{14}N^-$ and $^{12}C^{15}N^-$ counts and calculated natural abundance level of $^{12}C^{15}N^-$, respectively. As with the isotopic carbon label, the ^{15}N tag was incorporated to a level approximately three times that of natural abundance. The $^{12}C^{15}N^-$ counts were, however, naturally lower than those for the $^{13}C^{14}N$ ion due to the disparate natural abundance levels of the respective species. Consequently, the precision of the $^{12}C^{15}N^-/^{12}C^{14}N^-$ measurement was approximately 10-15%.

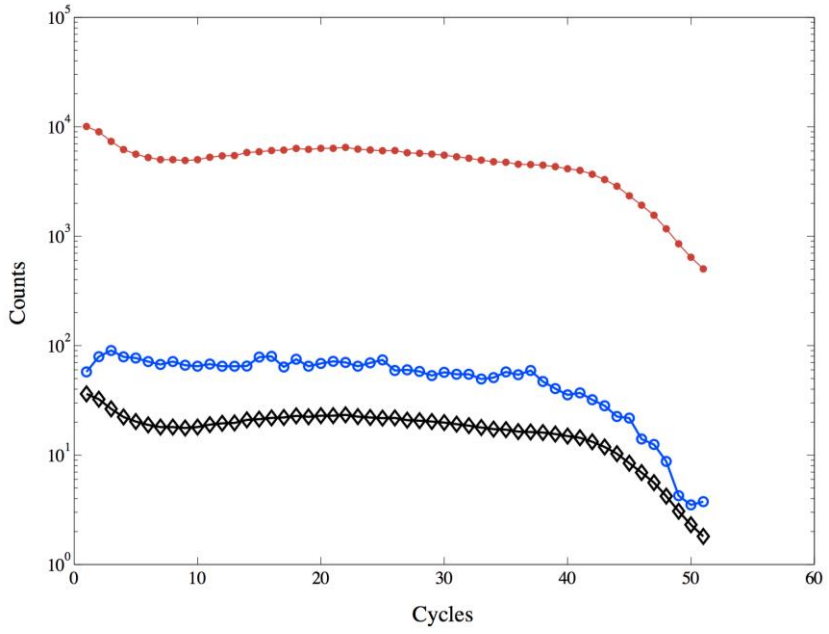

Figure 10-7: Measured species counts as a function of NanoSIMS scan cycle for an individual ^{15}N labeled viral particle: $^{12}C^{14}N^-$ (red), $^{12}C^{15}N^-$ (blue). The black curve is the calculated natural abundance level of $^{12}C^{15}N^-$ based upon the $^{12}C^{14}N^-$ counts. The ^{15}N tag was incorporated to a level approximately three times that of natural abundance.

The reproducibility of the depth profile data requires a relatively uniform incorporation of isotopic enrichment among the analyzed viral population. The level of isotopic label heterogeneity can be quantified by examining chemical images detailing the lateral and depth distribution of the isotopic ratio within individual scans. This analysis was done for both the ^{13}C lipid labeled virions as well as for the ^{15}N DNA

labeled viral prep. An analyzed region from the ^{13}C labeled viral sample is shown in Figure 10-8. The virion group displayed in the atomic force microscopy image in Figure 10-8 was exposed to a 0.78 pA cesium ion beam and was fully eroded at the completion of the scan; consequently, the chemical images and species counts provide information regarding the variation of the level of ^{13}C label incorporation between individual virions based upon a full depth analysis. The $^{14}N^{12}C^-$ and $^{14}N^{13}C^-$ counts were subsequently employed to generate a $^{14}N^{13}C^-/^{14}N^{12}C^-$ ratio image demonstrating the distribution of the isotopic label within the analyzed virions. The level of heterogeneity was quantified by constructing an error image displaying the absolute value of the number of standard errors of the mean for each pixel. As is readily apparent from Figure 10-9, viral incorporation of the isotopic tag was varied. Two of the virions, framed by red squares in the error image, were enriched to a level (.0336) approximately three times natural abundance. The most enriched virions, however, yielded a $^{14}N^{13}C^-/^{14}N^{12}C^-$ ratio of .0425, representing a 26% increase over the regions of least enrichment. The level of ^{13}C label incorporation naturally varied from region to region; therefore, in order to both generate an average level of enrichment and quantify the variation present, ten regions consisting of 35 virions were examined. An average enrichment level of .0378 with a standard deviation of .0021 was found. Consequently, while variations in isotopic label incorporation was observed, the level of ^{13}C enrichment was, on an aggregate level, relatively homogeneous.

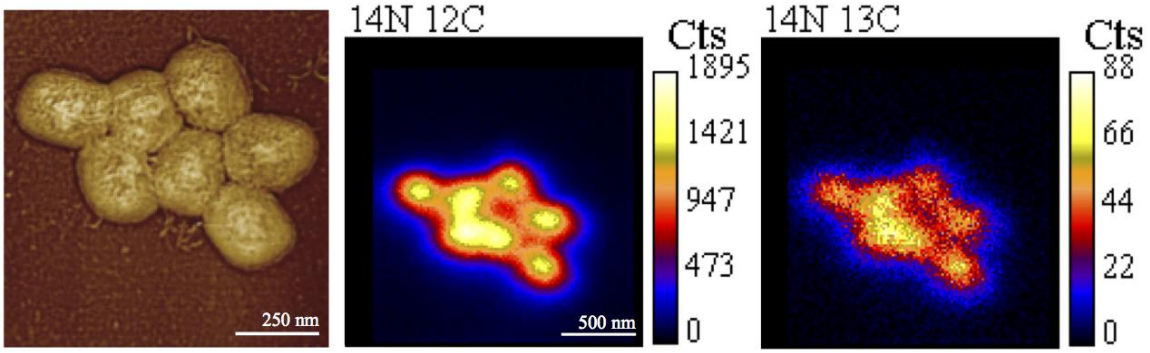

Figure 10-8: Correlated AFM (left)/NanoSIMS images of ^{13}C labeled viral particles. The $^{14}N^{12}C^-$ (middle) and $^{14}N^{13}C^-$ (right) counts are based upon a full depth analysis.

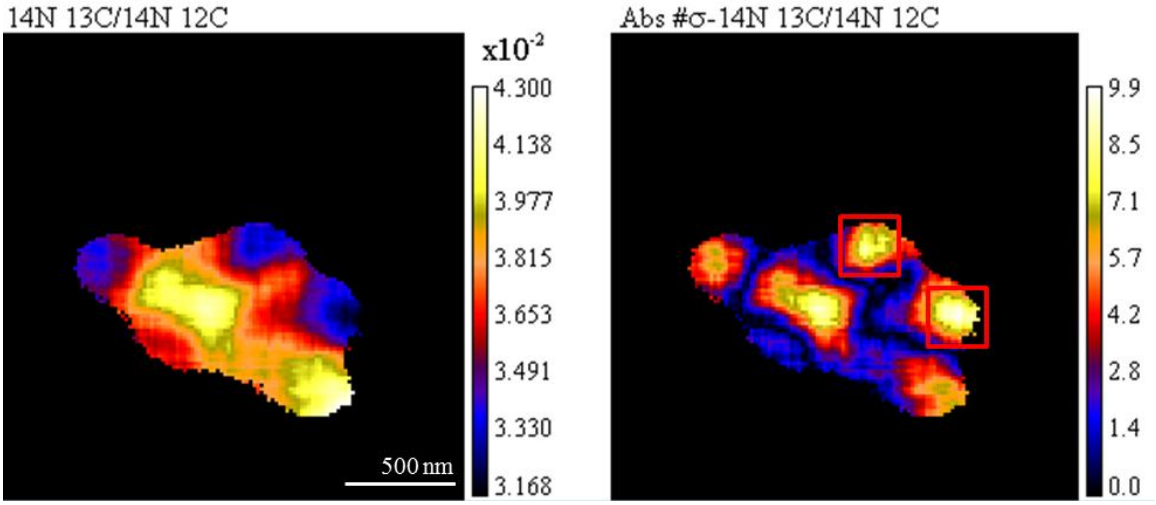

Figure 10-9: NanoSIMS ratio (left) and error (right) image illustrating the spatial distribution and heterogeneity of the ^{13}C label within the analyzed viral particles shown in Figure 10-8.

A similar analysis was undertaken to examine the level of label heterogeneity present within the ^{15}N labeled virion population. An atomic force microscopy image of a group of viral particles as well as the corresponding $^{12}C^{14}N^-$ and $^{12}C^{15}N^-$ chemical images is shown in Figure 10-10. The level of isotopic tag incorporation and secondary ion counts for individual virions was similar to that shown in Figure 10-7. An isotopic ratio image was subsequently generated to assess the distribution of the $^{12}C^{15}N^-/^{12}C^{14}N^-$ ratio after 99 analysis cycles with a .78 pA incident ion beam. Individual viral particles were fully eroded at the completion of data acquisition. An evaluation of the ratio image indicates that various levels of isotopic enrichment are present. Two viral particles, framed by red squares in the error image in Figure 10-11, were effectively not isotopically enriched; the average ratio for these two virions was measured to be approximately .00375. The viral particle framed by the white square was, however, enriched to a ratio of .0137, representing an approximately four - fold increase over natural abundance levels. The level of heterogeneity present in the scan displayed in Figure 10-11 is more pronounced than for the typical ^{15}N labeled virion sample area. This region was shown, however, to demonstrate the variation of isotopic label incorporation measured within the viral sample. To generate an average level of isotopic enrichment in

the virion population, eight regions composed of individual virions or monolayers were examined. Statistics generated from 65 distinct viral particles resulted in an average $^{12}C^{15}N^{-}/^{12}C^{14}N^{-}$ ratio of .00989 with a standard deviation of .00139. The expected isotopic ratio, assuming complete incorporation of the ^{15}N labeled thymidine nucleoside, was calculated to be approximately .0092. This value corresponds well with the average measured $^{12}C^{15}N^{-}/^{12}C^{14}N^{-}$ ratio. In addition, the standard deviation value is indicative of a relatively homogeneous level of isotopic enrichment within the viral population.

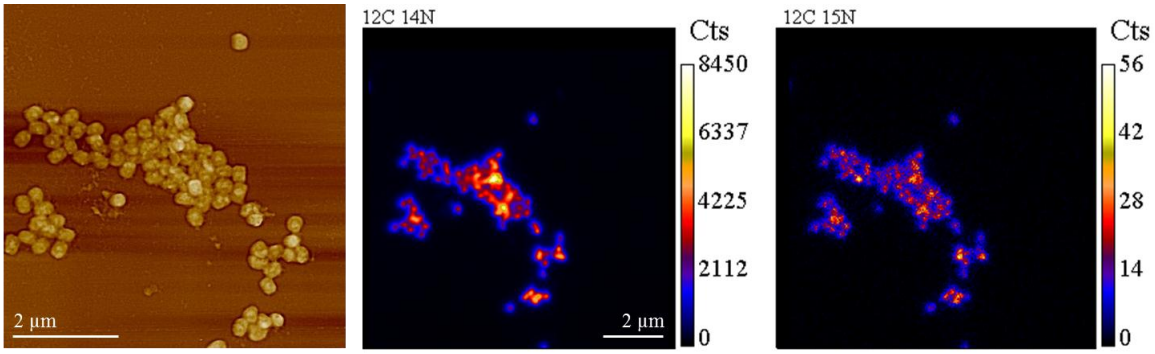

Figure 10-10: Correlated AFM/NanoSIMS analysis of ^{15}N labeled virions. The viral particles shown in the AFM image (left) were analyzed with the NanoSIMS and the resulting distribution and level of $^{12}C^{14}N^{-}$ (middle) and $^{12}C^{15}N^{-}$ (right) species counts are shown in the respective chemical images.

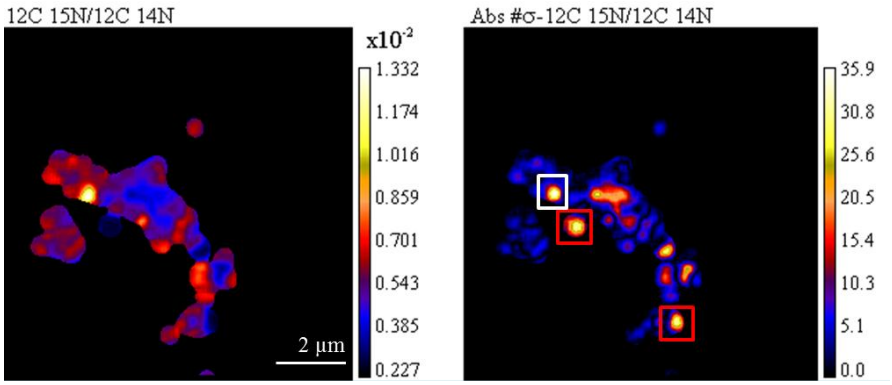

Figure 10-11: $^{12}C^{15}N^{-}/^{12}C^{14}N^{-}$ ratio (left) and error (right) image detailing the distribution of isotopic enrichment. The error image demonstrates the distribution of the absolute value of the number of standard errors from the mean. Virions framed in red were negligibly enriched. The particle framed in white was enriched to a level four-fold greater than natural abundance.

The relatively modest level of isotopic heterogeneity seen in both the ^{13}C and ^{15}N viral samples can be attributed to a multitude of factors. Perhaps the most prominent among these is the inherent biological heterogeneity of the viral population itself. As was examined in a previous section, the physical properties of the viral particles are not homogeneous; a range of virion dimensions and surface topological features were noted for the non-labeled viral samples. In addition, the biological mechanisms of metabolic labeling may have led to the breakdown of the isotopic tag resulting in incomplete viral incorporation. The latter consideration may account for the fact that the ^{13}C lipid tag was incorporated to a slightly higher and more homogeneous level than the ^{15}N DNA tag. This being stated, however, it is clear that the labeling procedure resulted in a consistent integration of both the ^{13}C and ^{15}N isotopic labels into the viral particles.

10.3 ^{13}C labeled viral particles

Modeling of the distribution and localization of lipid membranes in vaccinia virus is critical for understanding the mechanisms and processes of viral morphogenesis and cell infection. There exists, however, a degree of ambiguity regarding the spatial distribution and architectural arrangement of the lipid membrane within the vaccinia virion. Specifically, previous studies have resulted in conflicting conclusions regarding the presence of an interior membrane surrounding the core[9,12]. In order to address this issue, NanoSIMS experiments were conducted to map the depth distribution of ^{13}C labeled fatty acids incorporated into the lipid membrane of vaccinia viral particles. Depth resolved compositional information regarding the localization of the isotopic label is detailed and subsequently compared to the prevailing structural models concerning the arrangement and distribution of the virion lipid membrane.

The generation of quantitative information regarding the architectural conformation of the lipid membrane within the viral particle required the NanoSIMS instrument to be aligned to detect isotopic variations of the carbon-nitrogen ($^{13}C^{14}N^-$) and carbon dimer ($^{12}C^{13}C^-$) molecule. In addition, electronegative ions of $^{12}C^{14}N$, $^{12}C_2$ and ^{31}P were also detected. The generation of depth resolved data from two molecules containing

the ^{13}C isotopic label, namely, $^{13}C^{14}N^-$ and $^{12}C^{13}C^-$, enabled the formulation of complimentary data sets and provided a means to validate the fidelity of the measured values. In regards to the latter factor, depth profiles constructed from the $^{14}N^{13}C^-/^{14}N^{12}C^-$ and $^{12}C^{13}C^-/^{12}C_2^-$ data should display consistent qualitative behavior and differ numerically by a factor of two; the quantitative disparity is due to the difference in the respective levels of natural abundance (~.011 for $^{14}N^{13}C^-/^{14}N^{12}C^-$ and ~.022 for $^{12}C^{13}C^-/^{12}C_2^-$). Depth profiles deviating from these trends would be indicative of a detector misalignment. Therefore, before any further analysis was undertaken the corresponding $^{14}N^{13}C^-/^{14}N^{12}C^-$ and $^{12}C^{13}C^-/^{12}C_2^-$ depth profiles generated from a specific NanoSIMS scan were confirmed to be consistent with the aforementioned considerations.

Numerous virion sample areas of varying sizes were interrogated with the NanoSIMS and the species counts recorded as a function of scan cycle number. A sample $^{12}C^{13}C^-/^{12}C_2^-$ profile generated from an individual virion is depicted in Figure 10-12. The green line located at scan cycle 38 indicates the cycle at which the $^{12}C_2^-$ counts had been reduced to 30% of their maximum value. As previously detailed, this is the criterion employed to determine the final data value utilized in the construction of the depth resolved profile. The basis for this methodology can be readily ascertained by noting the presence of a rapid increase in the uncertainty values associated with the measured ratio for cycles greater than the critical cycle. As addressed in Chapter 9, the lack of reliable data for analysis cycles greater than the critical cycle is a result of the substantial reduction in sputtered volume at long analysis times.

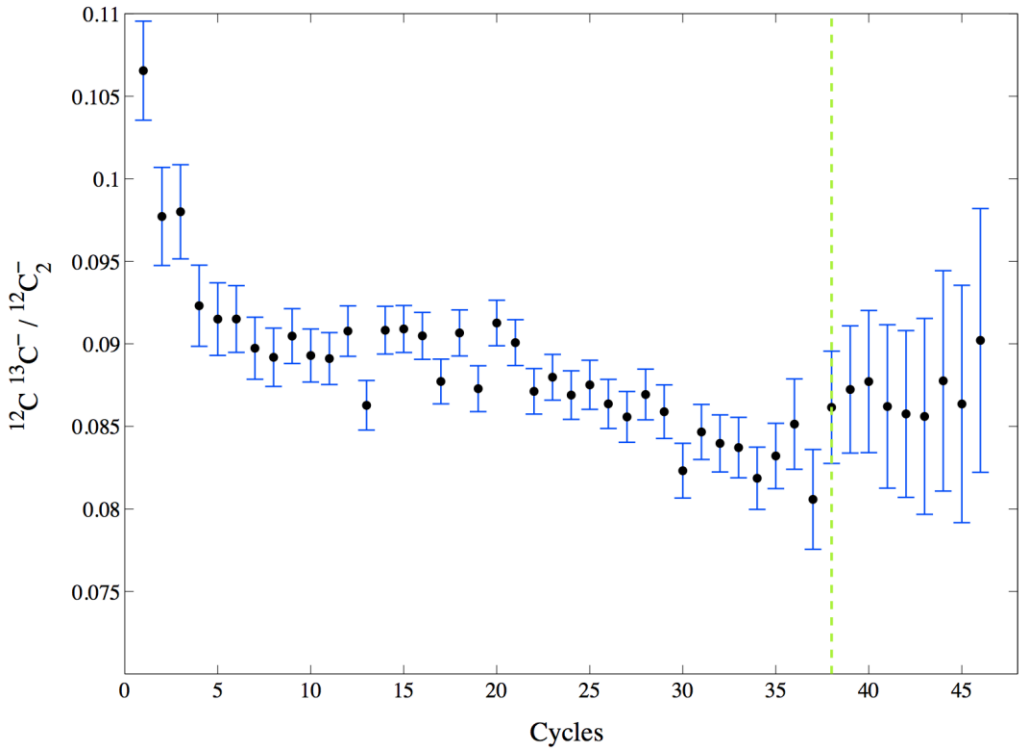

Figure 10-12: $^{12}C^{13}C^{-}/^{12}C_2^{-}$ variation as a function of cycle number for an individual viral particle within a 25 μm^2 area scanned with a 0.38 pA cesium ion beam.

10.3.1 ^{13}C depth profile analysis

Implementing the methodology detailed in Chapter 9, raw NanoSIMS data, such as that shown in Figure 10-12, was converted, through the employment of Equation 6, to depth resolved values in order to extract physically meaningful information regarding the distribution and localization of the ^{13}C label within the viral particle. The heterogeneous construction and size variability of the virions as well as the disparate levels of ^{13}C label incorporation resulted in a variety of distinct depth profiles. In addition, due to the relatively large variation in the measured sputter rates each set of scans was individually calibrated and the factors appearing in Equation 5 were adjusted accordingly. With these considerations in mind, a viral particle $^{14}N^{13}C^{-}/^{14}N^{12}C^{-}$ depth profiles from a 25 μm^2 area scanned with a 0.38 pA incident cesium beam is shown in Figure 10-13. The previously

addressed qualitative correspondence with the $^{12}C^{13}C^{-}/^{12}C_2^{-}$ profile (Figure 10-12) is readily apparent as is the approximate two-fold difference in ratio values. Due to the noisy nature of the NanoSIMS data (red line) a moving average filter was applied to the measured values and the subsequently generated curve is shown as the black line in Figure 10-13. For reasons of clarity the error bars on the NanoSIMS data have been suppressed; representative values, however, are as those shown in Figure 10-12.

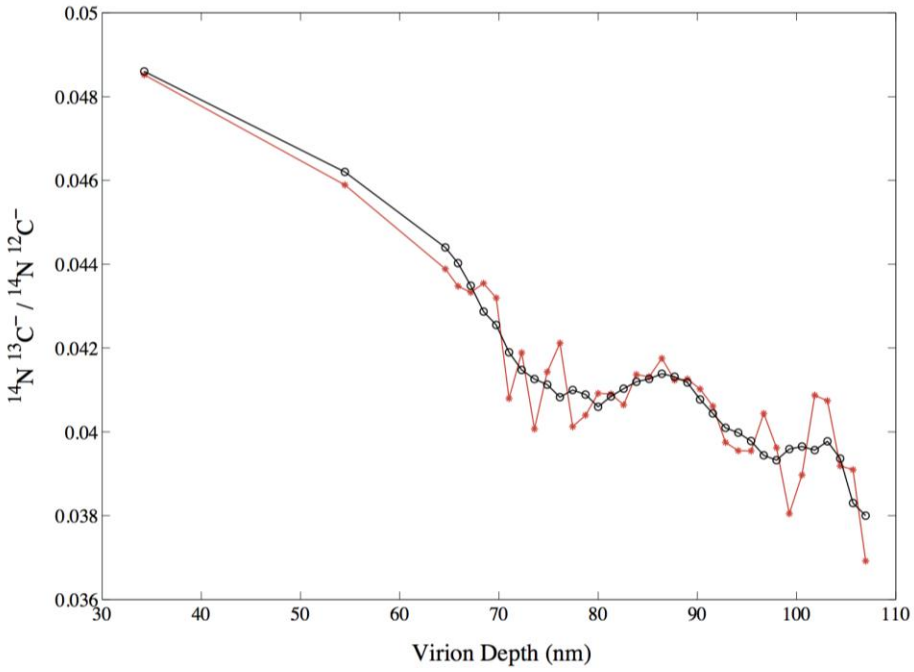

Figure 10-13: $^{14}N^{13}C^{-}/^{14}N^{12}C^{-}$ depth profile of an individual viral particle within a 25 μm^2 area scanned with a 0.38 pA cesium ion beam. The red line is the direct NanoSIMS values and the black line is the result of applying a moving average filter to the data.

The most relevant features of the isotopic carbon depth profile shown in the above figure is the distinct drop in the $^{14}N^{13}C^{-}/^{14}N^{12}C^{-}$ ratio over the initial portion of the profile and the establishment, over the latter profile section, of a stabilization regime where the $^{14}N^{13}C^{-}/^{14}N^{12}C^{-}$ ratio is at some relatively constant value significantly greater than the natural abundance value of approximately 0.011. The set of depth profiles displaying these qualitative characteristics, however, represented a minority of the NanoSIMS generated data. The majority of individual viral particle scans conducted with raster scan

areas less than 25 μm^2 yielded profiles lacking a discernible initial decrease in the $^{14}N^{13}C^-/^{14}N^{12}C^-$ ratio. The construction of a physically relevant interpretation of the isotopic carbon depth profiles, then, rests upon the development of a model explaining not only the distinct behavior of the two data sets, but, more importantly, how the measured data relates to the viral particle structure.

Prior to providing a physical interpretation of the measured isotopic carbon depth profiles, however, it is worthwhile to revisit the proposed architectural composition of the virion's lipid membrane and the implications of this arrangement within the context of NanoSIMS measurements. As previously specified, vaccinia virus is known to be a viral particle enveloped by an approximately 10 nm thick lipid membrane; additionally, numerous studies have indicated that a similarly constructed interior membrane may be present. Assuming that the ^{13}C label was solely incorporated within the lipid membrane, the former architectural model, proposing a single membrane composition, would imply a NanoSIMS depth profile displaying an initial rapid decrease in the $^{14}N^{13}C^-/^{14}N^{12}C^-$ ratio with subsequent ratio stabilization to a value near natural abundance throughout the viral particle interior. An enrichment value slightly greater than natural abundance would be expected throughout the particle depth due to the structural configuration of the lipid membrane; given that the exterior membrane envelops the interior viral components, an arbitrary depth cross section would necessarily entail exposure of the thin membrane cross section to the incident ion beam. In the latter model, postulating the existence of an interior membrane, two significant $^{14}N^{13}C^-/^{14}N^{12}C^-$ ratio peaks would be expected, one at the surface of the virion and another at a depth of approximately 25 nm; a depth corresponding to the inner membrane's proposed location surrounding the core. As a result of ion beam induced mixing, the second layer of the interior membrane would, in all likelihood, not display a $^{14}N^{13}C^-/^{14}N^{12}C^-$ enrichment level as high as the initial layer. Instead, a small peak in the depth profile would be expected near 100 nm. Additionally, a relatively high level of enrichment would be anticipated throughout the core region due to the aforementioned consideration regarding cross section membrane measurement.

Interpretation of the measured $^{14}N^{13}C^-/^{14}N^{12}C^-$ depth profile shown in Figure 10-13 within the framework of the one and two membrane models is ambiguous. The most

prominent issue concerns the lack of detailed information regarding the level of ^{13}C enrichment for viral particle depths less than 30 nm. The absence of measurements in this region is due to the rapid rate of non-equilibrium sputtering during the initial stages of NanoSIMS interrogation. It is interesting to note, however, that the first measured $^{14}N^{13}C^{-}/^{14}N^{12}C^{-}$ ratio value, corresponding to an approximate depth of 34 nm, represents the average enrichment value over that region of the virion. Consequently, structures exhibiting relatively high levels of ^{13}C enrichment are present within the initial 30 nm of the viral particle. With these measurements, however, no clear distinction can be made between the one and two lipid membrane model. The behavior exhibited in the latter half of the depth profiles is equally ambiguous. While a ^{13}C enrichment level greater than natural abundance would be expected throughout the entire virion depth, a level approximately three-fold greater cannot be attributed solely to the contribution from the membrane cross section. In addition, it is interesting to note the presence of small enrichment peaks in the 85-100 nm region; features that would be consistent with the two membrane model. Alternatively, however, these features may be measurement artifacts resulting from the rapid reduction in sputtered volume and the corresponding low levels of measured species counts.

In order to examine these issues two series of experiments were initiated. The first was designed to examine the ^{13}C enrichment at the virion surface and address the matter of virion depth profiles lacking the initial decline in the $^{14}N^{13}C^{-}/^{14}N^{12}C^{-}$ ratio value. The second experimental series, conducted using virion cores lacking an exterior lipid membrane, was implemented to examine the high levels of interior ^{13}C enrichment.

With the intention of assessing the surface ^{13}C enrichment of viral particles experimental parameters were varied to minimize the level of initial particle erosion. The non-equilibrium sputtering model developed in Chapter 9 indicates that a lower initial sputtered depth can be obtained by decreasing the incident ion beam current and increasing the size of the analyzed area. For instance, a 100 μm^2 area interrogated with a 0.38 pA beam would result in an initial eroded depth of approximately 10 nm. In addition, the second and third scan would result in NanoSIMS measurements at depths corresponding to the depth of the theorized inner membrane. Therefore, implementing

such a scan would provide data concerning the surface composition of the virion and would help resolve the issue concerning the number of lipid membranes within the viral particle. In addition, areas containing large conglomerations of virions were sought to increase the measured species counts and reduce data uncertainty.

A NanoSIMS generated secondary electron image of such a region along with the corresponding $^{14}N^{12}C^-$ and $^{14}N^{13}C^-$ chemical images are shown in Figure 10-14. In addition, a particle recognition algorithm within the image processing software LIMAGE was employed to generate a region of interest (ROI) composed of 765 individual viral particles. The particle outlines can be seen in light blue in the ROI image in Figure 10-14. The $^{14}N^{13}C^-/^{14}N^{12}C^-$ profile generated from the ROI is shown in Figure 10-15.

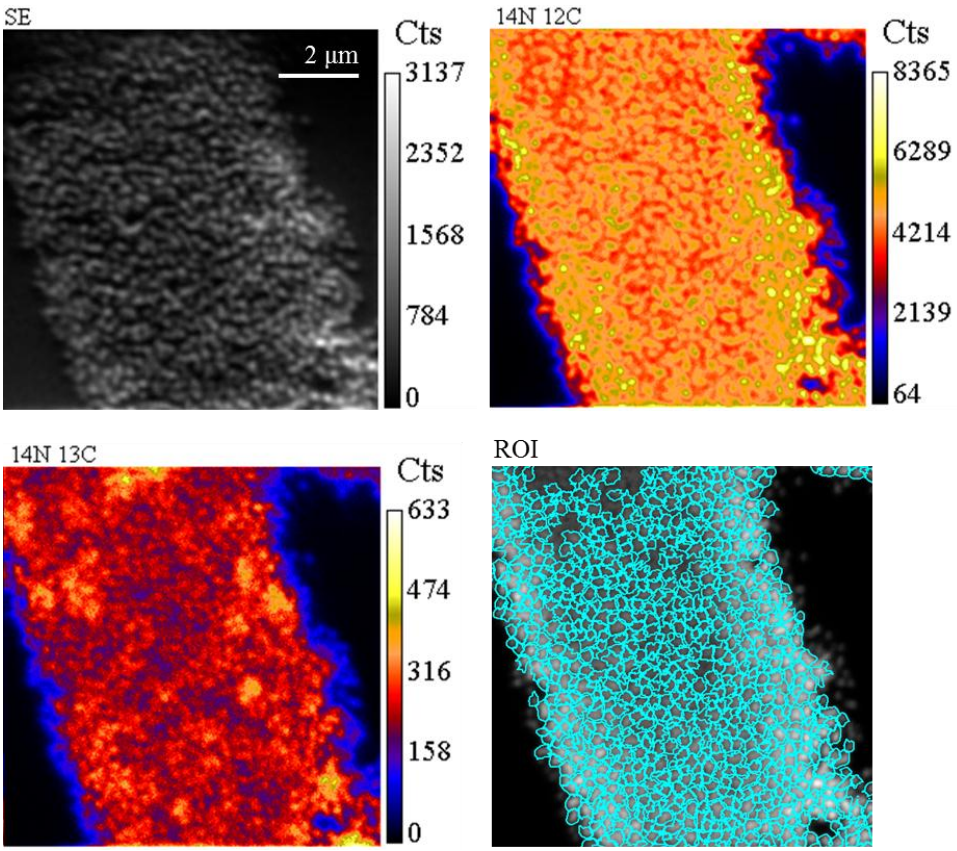

Figure 10-14: NanoSIMS generated secondary electron (SE) and chemical images of a large viral conglomeration. This area was scanned to determine the ^{13}C surface enrichment of the viral particles. The ROI was composed of 765 distinct viral particles.

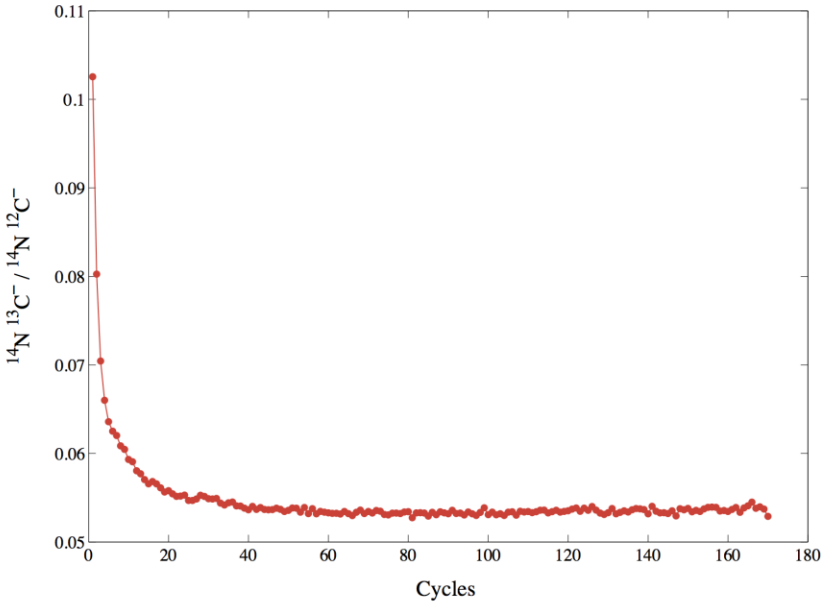

Figure 10-15: $^{14}N^{13}C^{-}/^{14}N^{12}C^{-}$ variation as a function of cycle number for the analyzed region shown in Figure 10-14. A high level of ^{13}C enrichment was observed at the surface.

Due to the nature of the analyzed region conversion of scan cycle number to virion depth does not provide physically relevant information; as the orientation and arrangement of the virions in the pile is not known, accurate attribution of cycle number to particle depth is precluded. What is clear, however, is that no matter the orientation of specific viral particles within the conglomeration, the initial data points will be indicative of the surface ^{13}C enrichment level. As is readily apparent in Figure 10-15, a significantly increased $^{14}N^{13}C^{-}/^{14}N^{12}C^{-}$ ratio value is obtained at the particle surface.

Prior to detailing the physical interpretation of the profile, however, it is necessary to examine the $^{13}C/^{12}C$ ratio distribution within the virion conglomeration. High levels of variation in the $^{13}C/^{12}C$ ratio may be indicative of the presence of ^{13}C labeled cellular structures within the analyzed area. If these structures are present, the quantitative values generated from the NanoSIMS scan would not accurately reflect the enrichment level of the viral particles. In order to assess the $^{13}C/^{12}C$ distribution a ratio image detailing the cycle averaged $^{13}C^{12}C/^{12}C_2^{-}$ levels throughout the virion assembly are shown in Figure 10-16. Clearly, there exist substantial levels of non-uniform isotopic enrichment within

the scanned region; the error image indicates that the highest enriched regions deviate by 68 standard errors from the average enrichment value.

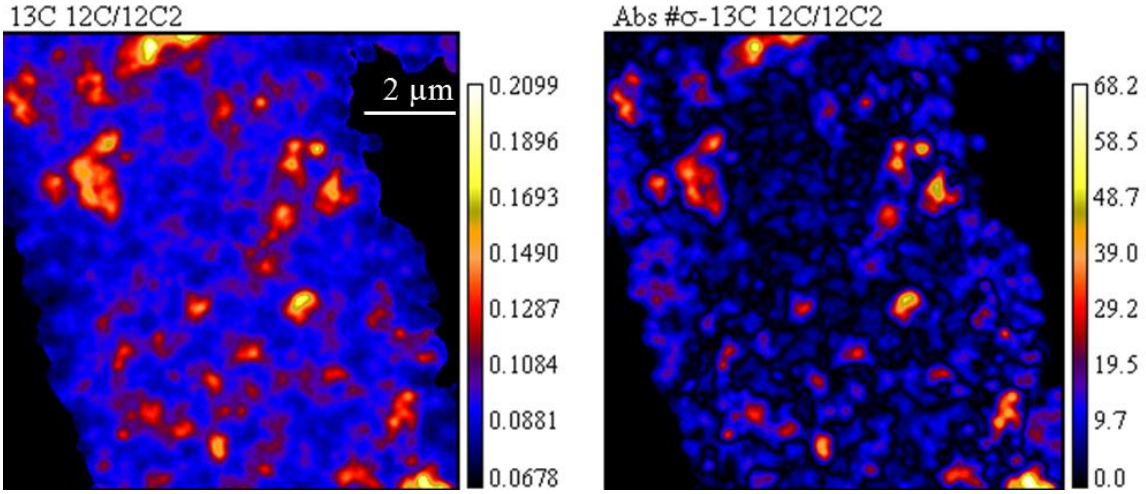

Figure 10-16: $^{13}C^{12}C^{-}/^{12}C_2^{-}$ ratio (left) and error (right) images detailing the distribution of the label within the viral conglomeration. The $^{13}C^{12}C^{-}/^{12}C_2^{-}$ distribution was chosen in order to demonstrate the quantitative agreement between the data obtained from either $^{14}N^{13}C^{-}/^{14}N^{12}C^{-}$ or $^{13}C^{12}C^{-}/^{12}C_2^{-}$ analysis.

For the present purposes, however, our interest lies in examining the depth location of the ratio variation. If the variation is at depth and not on the surface of the viral assembly than the initial $^{14}N^{13}C^{-}/^{14}N^{12}C^{-}$ ratio values can be reliably attributed to the viral particles and not the possible presence of cellular debris. To this end an ROI was generated based upon a 60% $^{14}N^{13}C^{-}/^{14}N^{12}C^{-}$ threshold; the regions of interest are outlined in white and presented in Figure 10-17. The $^{14}N^{13}C^{-}/^{14}N^{12}C^{-}$ profile from this region is shown as the red line in the adjacent plot in Figure 10-17. In addition, a $^{14}N^{13}C^{-}/^{14}N^{12}C^{-}$ profile from the regions of lower enrichment outside the ROI was generated and displayed as the blue line in the aforementioned plot. As is readily apparent, the levels of enrichment for the two distinct regions are relatively consistent for the initial scan cycles. The major quantitative discrepancy between the areas of high and low enrichment occurs at depth; the result, presumably, of the spatially non-uniform incorporation of ^{13}C labeled cellular debris within the viral assembly. In addition, the high equilibrium enrichment levels throughout the scan can, in part, be attributed to the inherent organization of the

viral assembly itself; intact virions and their ^{13}C labeled lipid membranes will be continuously present at sub-surface locations, providing a sustained level of high enrichment throughout the interrogated depth.

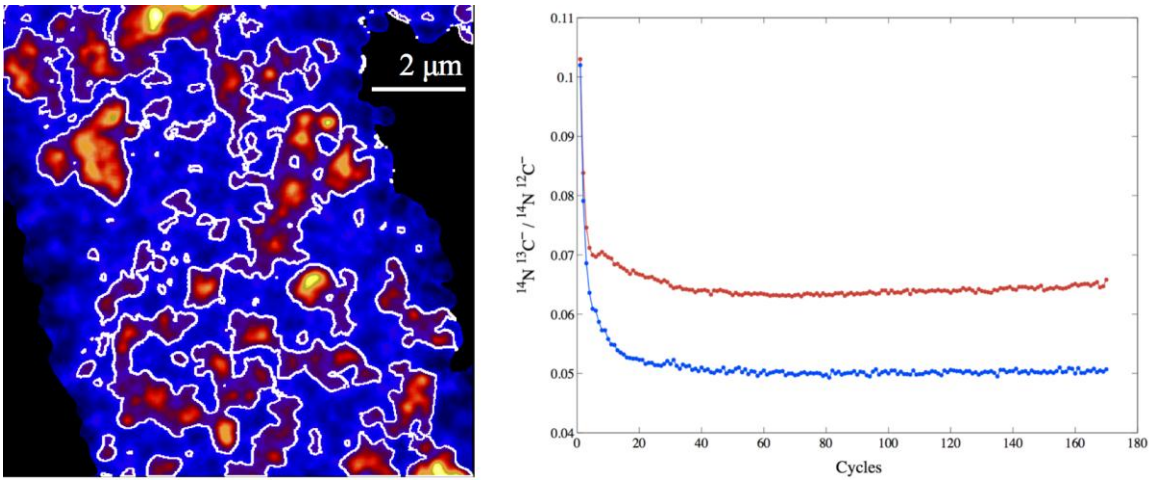

Figure 10-17: $^{14}N^{13}C^-/^{14}N^{12}C^-$ variation as a function of cycle number for the ROIs shown in the NanoSIMS image on the left. The red line was generated from the higher enriched areas shown in white. The blue line was generated from the areas of lower enrichment outside of the regions framed in white.

For the present purposes, however, we are primarily interested in the initial three $^{14}N^{13}C^-/^{14}N^{12}C^-$ ratio values. The first scan results in an interrogated depth of approximately 10 nm and would result in the full erosion of the exterior lipid membrane. The third scan, corresponding, as predicted by the non-equilibrium sputtering model, to a depth of roughly 24 nm would include the region of the theorized interior lipid membrane. If an inner lipid membrane was present we would expect to see a discernible increase in the level of isotopic enrichment in this region. Three conclusions, therefore, can be drawn from this data. The true ^{13}C enrichment level of the lipid membrane results in a $^{14}N^{13}C^-/^{14}N^{12}C^-$ ratio value of approximately 0.1. In addition, the continuous decrease in the isotopic enrichment values as a function of cycle number is indicative of a virion exhibiting a single exterior lipid membrane composition. The third implication of this data concerns the presence of two distinct ^{13}C enrichment depth profiles; those displaying

an initial decline in the $^{14}N^{13}C^{-}/^{14}N^{12}C^{-}$ ratio and those exhibiting a relatively stable ratio value over the full profile. Many of the depth profiles lacking the initial ratio decline were generated from data collected from small raster scan areas. In particular, numerous 1 μm^2 and 4 μm^2 areas were analyzed in an attempt to generate high resolution data regarding the lateral distribution of the isotopic label; such scans result in the initial erosion of between 50 -70 nm of material from the viral particle. The first $^{14}N^{13}C^{-}/^{14}N^{12}C^{-}$ data point, then, would represent the average ratio over a depth including a significant amount of proteinaceous and other non-lipid membrane related material. Therefore, the ^{13}C enrichment level would be severely reduced, exhibiting quantitatively similar values to those measured throughout the viral particle interior. Utilizing these conclusions and the data displayed in Figures 10-13 and 10-15, it is possible to reconstruct a single viral particle depth profile. Prior to detailing the results obtained from this reconstruction, however, it is necessary to address the relatively high levels of ^{13}C enrichment measured throughout the interior of individual viral particles.

10.3.2 Non-specific ^{13}C label incorporation and virion cores

Irrespective of the one or two lipid membrane composition within the viral particle, a $^{14}N^{13}C^{-}/^{14}N^{12}C^{-}$ ratio stabilization to levels near natural abundance would be expected over a distinct region of the depth profile. As displayed in Figure 10-13, however, the stabilization enrichment value throughout the virion interior was approximately three-fold greater than natural abundance. Due to material mixing during the NanoSIMS analysis, some level of ^{13}C enrichment would be expected to extend beyond the physical limits of the lipid membrane; a significant enrichment level, however, such as that shown in the aforementioned figure, can not be explained by this physical mechanism alone. The obvious implication of these measurements is that the ^{13}C isotopic label was incorporated, to some non-negligible level, into other biological components. In order to test this hypothesis, virion cores lacking the exterior membrane were generated in the manner outlined in Chapter 7 and Appendix BII. As our previous data is indicative of a single membrane construction, the analysis of the viral core

particles would be expected to yield no isotopic enrichment if the ^{13}C label had been segregated exclusively to the lipid membrane.

In order to assess the level of ^{13}C enrichment within the viral cores a series of NanoSIMS measurements was conducted. The instrument was aligned to detect the same species as previously specified and the customary isotopic enrichment information from the CN^- counts was generated. Furthermore, due to the chemical composition of the phospholipid membrane, the $^{31}P^-$ species counts from the intact and core particles were utilized to provide data validating the extent of lipid membrane removal. In regards to the latter consideration, virion core surface levels of $^{31}P^-$ were assessed and subsequently compared to values obtained from intact viral particles. A significant reduction in the $^{31}P^-$ counts (~20%) was noted for the virion cores. This physical phenomenon can be attributed to the absence of the lipid bilayer and the affiliated phosphate group. In addition, AFM measurements were implemented to confirm the theoretical height reduction due to the removal of the lipid membrane. Results indicated an approximate 12-15% reduction in viral particle height, a value consistent with the anticipated decrease in the vertical dimension. Having confirmed the successful production of virion cores, $^{14}N^{13}C^-/^{14}N^{12}C^-$ depth profiles for a variety of experimentally conditions were subsequently constructed and compared to those generated from intact viral particles.

Due to the aforementioned considerations regarding the absence of surface sensitivity for data generated from small area scans, NanoSIMS depth profile analysis of the virion core sample was implemented with scan sizes of 25 μm^2 and 100 μm^2. The former analysis area was employed to generate virion core depth profiles corresponding to those shown for intact virions in Figure 10-13. The latter analysis condition was utilized, as in previous experiments, to provide high surface sensitivity for large viral particle conglomerations. Virion core data produced from a 25 μm^2 area scanned with a 0.38 pA incident cesium beam is shown Figure 10-18; error bars are included to demonstrate the level of uncertainty associated with the measurements. Furthermore, for clarity every eighth data point is shown within the equilibrium sputtering regime and the average level of enrichment throughout the virion is shown as the blue dashed line. For comparison purposes, intact virion data reproduced from Figure 10-13 is shown. As

previously specified, the intact and viral core data were generated under identical experimental conditions. As is readily apparent, the enrichment of the virion core is significantly lower than that of the intact viral particle. In addition, the lack of an initial decline in the $^{14}N^{13}C^{-}/^{14}N^{12}C^{-}$ ratio is indicative of the absence of an exterior lipid membrane. Corroboration of this assertion was seen in the data produced from the 100 μm^2 NanoSIMS scans of virion core conglomerations. In contrast to the steep initial decline in the $^{14}N^{13}C^{-}/^{14}N^{12}C^{-}$ ratio measured for intact viral particles (Figure 10-15), analysis of assemblages composed of virion cores yielded constant ratio values consistent with those shown in Figure 10-18. The average enrichment of the virion core, however, was consistently measured to be approximately twice the natural abundance value of 0.011. Consequently, it is evident that the ^{13}C label was not exclusively incorporated into the virion lipid membrane.

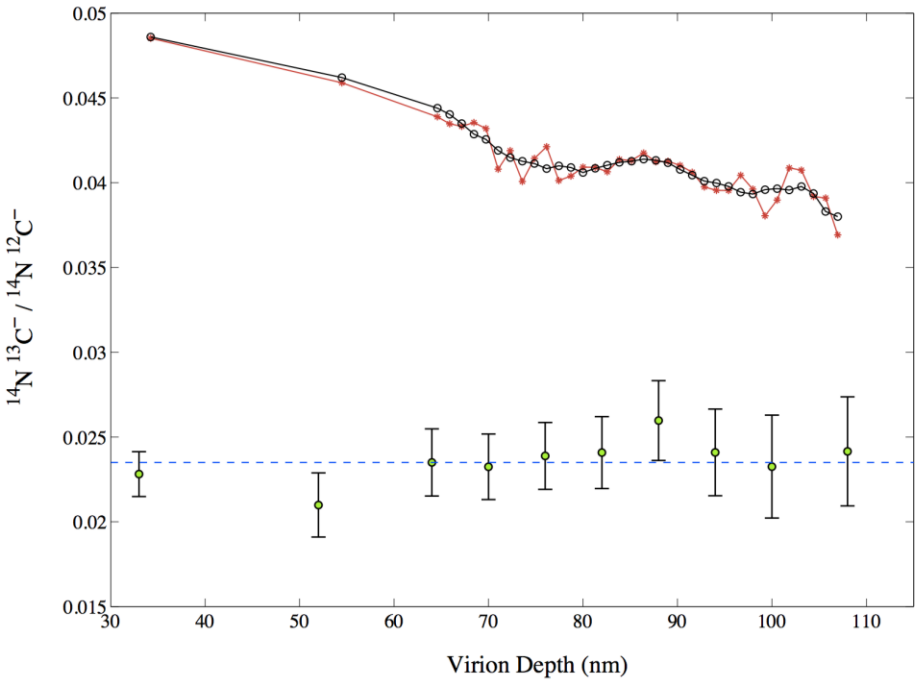

Figure 10-18: Depth resolved NanoSIMS data comparing the ^{13}C enrichment level of an intact particle (red, black) with that of a virion core lacking the exterior lipid membrane (blue). Both data sets were generated from a 25 μm^2 scan with a 0.38 pA cesium beam. The virion core was enriched to a level approximately twice that of natural abundance.

While this data brings into question the fidelity of the ^{13}C labeling procedure it is interesting to note that a number of studies have indicated that a multitude of phospholipids may be metabolized and associated with nuclear assemblages[68-70]. Specifically, it has been noted that sphingomyelin, a major cellular phospholipid, plays an instrumental role in the structural and regulatory mechanisms of chromatin assembly and dynamics[68]. In addition, evidence indicates that a variety of phospholipids may act as lipid mediators during nuclear processes such as DNA transcription, splicing and repair[69,70]. The cellular metabolism of lipids, then, may have resulted in the distribution of the ^{13}C label to an array of viral components during inter-cellular virion assembly. Therefore, the high level of ^{13}C enrichment measured throughout the virion particle may be a result of the labeling of lipids embedded within the interior of the virion and closely associated with the nucleoprotein complex. This hypothesis, while providing a plausible explanation for the elevated ^{13}C level throughout the virion interior, does not address the substantial discrepancy between the $^{14}N^{13}C^-/^{14}N^{12}C^-$ ratio stabilization level for the viral particle and the average enrichment of the virion core. One would expect a relatively consistent level of enrichment between the two particles after the physical region affected by the highly enriched exterior lipid membrane had been sputtered from the intact viral particle.

In order to address this issue, virion cores produced from unlabeled intact virions were exposed to the supernatant generated from the ^{13}C core procedure. The resulting supernatant solutions were, consequently, composed of isotopically labeled lipid membranes extracted from the ^{13}C labeled viral particles. Unlabeled virion cores were subsequently introduced into the supernatant solution and allowed to reach saturation. NanoSIMS analysis of the subsequent particles indicated substantial levels of ^{13}C enrichment throughout the originally unlabeled virion cores. These experiments demonstrate the high levels of porosity associated with the viral particles. In addition, these results indicate a physical mechanism to explain the aforementioned discrepancy in the level of interior enrichment between the ^{13}C labeled intact virions and the subsequently derived virion core particles: the chemical and enzymatic agents employed to remove the exterior lipid membrane would permeate the entire particle and result in the

breakdown of the ^{13}C lipids associated with interior viral structures. Consequently, the enrichment level within the equilibrium regime for the intact particle would be expected to be greater than the average virion core value.

10.3.3 Reconstructed ^{13}C depth profile and conclusions

The totality of the ^{13}C results previously detailed can be combined to generate and interpret a single particle $^{14}N^{13}C^{-}/^{14}N^{12}C^{-}$ depth profile. Specifically, the data obtained from the initial planes of the large area NanoSIMS scans (Figure 10-15) are utilized to reconstruct the depth profile regions inaccessible, due to the high rate of sputtering, during the high-resolution analysis of individual virions. These results are then combined with average individual depth profiles to predict the aggregate behavior of the $^{14}N^{13}C^{-}/^{14}N^{12}C^{-}$ ratio as a function of viral particle depth.

The procedure outlined above was implemented to construct a depth profile detailing the anticipated distribution of the ^{13}C lipid label throughout a single viral particle. Initial depth data points were generated from Figure 10-15 and Equation 6. For depths greater than approximately 15 nm, the depth profile was reproduced from average individual virion data; bearing in mind the fact that the initial enrichment value from such scans represented an effective average value over the preceding depth. The resulting $^{14}N^{13}C^{-}/^{14}N^{12}C^{-}$ ratio variation as a function of viral particle depth is shown in Figure 10-19. A qualitative interpretation of the depth profile provides pertinent information regarding the architectural arrangement of the lipids within the viral particle. The initial high level of isotopic enrichment indicates the presence of an exterior lipid membrane enveloping the viral core. After the initial region, approximately 8 nm, the $^{14}N^{13}C^{-}/^{14}N^{12}C^{-}$ ratio declines at a considerable rate due to the complete sputtering of the lipid membrane. Reduction in the ^{13}C signal in this region is, however, slowed by two factors; the first being the effect of material mixing caused by ion bombardment and the second being the presence of ^{13}C labeled lipid molecules associated with interior proteinaceous structures. After roughly 15 nm the effect of the former phenomenon is severely curtailed and the depth profile stabilizes to an enrichment value, approximately 3-4 times greater

than natural abundance, reflecting the contribution of the lipid/proteinaceous assemblages.

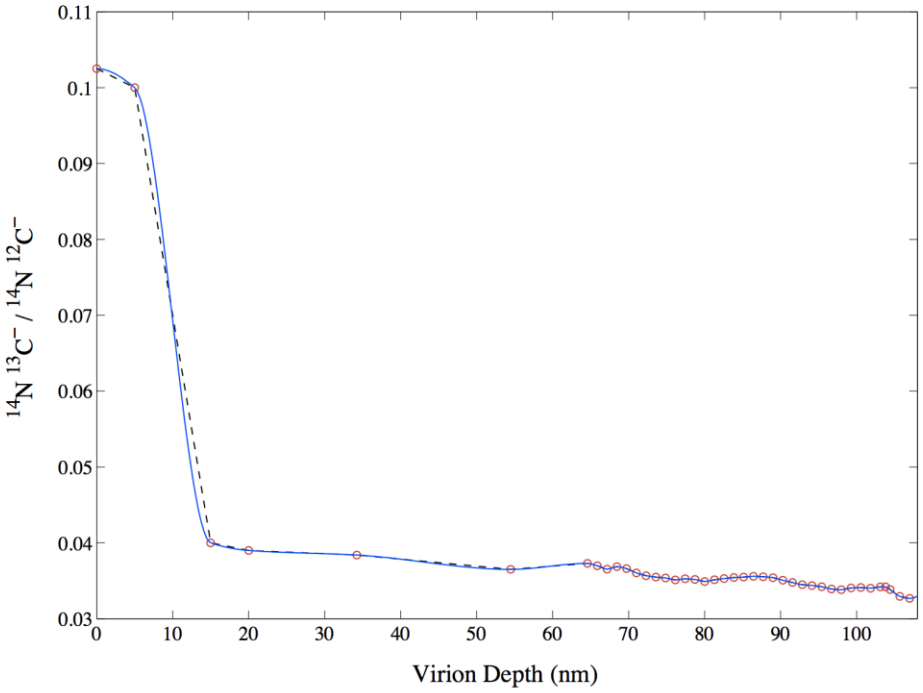

Figure 10-19: Reconstructed ^{13}C depth profile for a single viral particle. The presence of a single region displaying significantly enriched ^{13}C enrichment is indicative of a single exterior membrane.

The ^{13}C lipid label experiments, then, provide two critical sources of data, one regarding the feasible of examining nanometer-scale individual biological particles utilizing isotopic labels and NanoSIMS analysis and the other concerning the structural composition of the vaccinia viral particle. In regards to the former consideration, the experiments detailed herein indicate the possibility of generating depth resolved information regarding the distribution and localization of molecule specific isotopic tags within nanometer scale biological systems. This process, however, may require validation experiments focused upon the rate of sputtering of the specific biological system of interest as well as studies concerning the fidelity of the label incorporation procedure. In regards to the latter issue, these studies provide convincing evidence that the vaccinia viral particle is composed of a single exterior lipid membrane; the presence of a highly

enriched ^{13}C signal at the viral particle surface and the lack of a similar signal increase at 20-30 nm, the location of the hypothesized interior lipid membrane, is indicative of a single membrane construction. Furthermore, this conclusion corroborates recent biochemical research[12] and has significant implications for the modeling of the vaccinia viral infection and morphogenesis process.

10.4 ^{15}N labeled viral particles

Characterization of the viral nucleoprotein complex is critical for the development of anti-viral strategies. Specifically, elucidation of the structural relationship between the viral genome and its associated proteins is critical for the development and implementation of effective anti-viral therapies targeting specific nuclear assemblies and processes. A prevailing architectural model of the 190 kb vaccinia virion genome, supported by the AFM data detailed in Chapter 7, specifies a hierarchy of structures in which the DNA is coupled with proteins and the subsequent filament configuration is enclosed within 30-40 nm proteinaceous tubules. The tubules are, apparently, further condensed and encased within the virion core.

A series of NanoSIMS experiments was thereby implemented to examine the genome localization as well as the genome/protein compositional relationship within the vaccinia virion. As previously described, an isotopic tagged nucleoside, ^{15}N labeled thymidine, was incorporated into the viral genome. Spatially resolved data concerning the distribution of the isotopic label was then generated through NanoSIMS analysis and the resulting depth profiles assessed within the context of the proposed structural model. ^{15}N depth profiles, while providing data concerning the large-scale arrangement of the viral genome within the viral particle, do not offer high-resolution information regarding the structural composition of the proposed nucleoprotein assemblage. In order to generate data regarding the spatial distribution of DNA and proteinaceous structures within the nucleoprotein complex, the chemical and enzymatic protocols detailed in Chapter 7 were applied to intact ^{15}N viral particles. In this manner, systematic degradation of the virion was achieved and isolated nucleoprotein tubular elements were produced. NanoSIMS

analysis of the observed assemblages was subsequently conducted and the structural implications derived from the results assessed. Prior to explicating the conclusions drawn from the aforementioned experiments, however, a series of studies concerning the fidelity of the ^{15}N labeling procedure is detailed. Due to the widespread incorporation of the ^{13}C lipid label within the virion, a validation experiment was designed to assess the level of ^{15}N segregation within the viral genome. To this end, biochemical DNA, protein and lipid extraction techniques were implemented to generate viral constituent fractions. Each fraction was subsequently analyzed with the NanoSIMS, providing ^{15}N enrichment levels for each individual viral component. The NanoSIMS results concerning the exclusive DNA incorporation and spatial distribution of the ^{15}N isotopic label are subsequently synthesized and conclusions regarding the architectural arrangement of the viral genome are forwarded.

10.4.1 Fidelity of ^{15}N DNA labeling: fractionation experiments

In order to validate the fidelity of the ^{15}N labeling procedure intact viral particles were systematically decomposed into their constituent components, namely, lipids, proteins and DNA (see Appendix BVII). Assessment of the protein and DNA fractions indicated extraction levels of approximately 100 mg/ml and 4000 ng/μl, respectively. The purity of the DNA extraction was assessed by measuring the 260/280 nm absorbance ratio utilizing a spectrophotometer. Absorbance ratios of between 1.85 and 1.94 were measured; values indicative of a highly pure sample. In addition, atomic force microscopy was implemented to provide physical imaging of the structures within the DNA fraction suspension. A typical region, shown in Figure 10-20, contains features reminiscent of double stranded DNA. Furthermore, AFM measurements indicated that the height of the observed structures were approximately 3 nm. Previous studies have indicated that the width of double stranded DNA in solution varies between 2.2 and 2.6 nm[71], values which correspond fairly well to the height of the structures observed in the DNA fraction. Further inspection of Figure 10-20, however, makes clear the presence of residual proteinaceous structures associated with the DNA strands; numerous protein assemblages (blue arrows) can be discerned in the AFM image. Therefore, while the

260/280 nm absorbance ratio indicates a highly pure DNA sample there remains a perceptible level of proteins coupled with the nucleic acid structures.

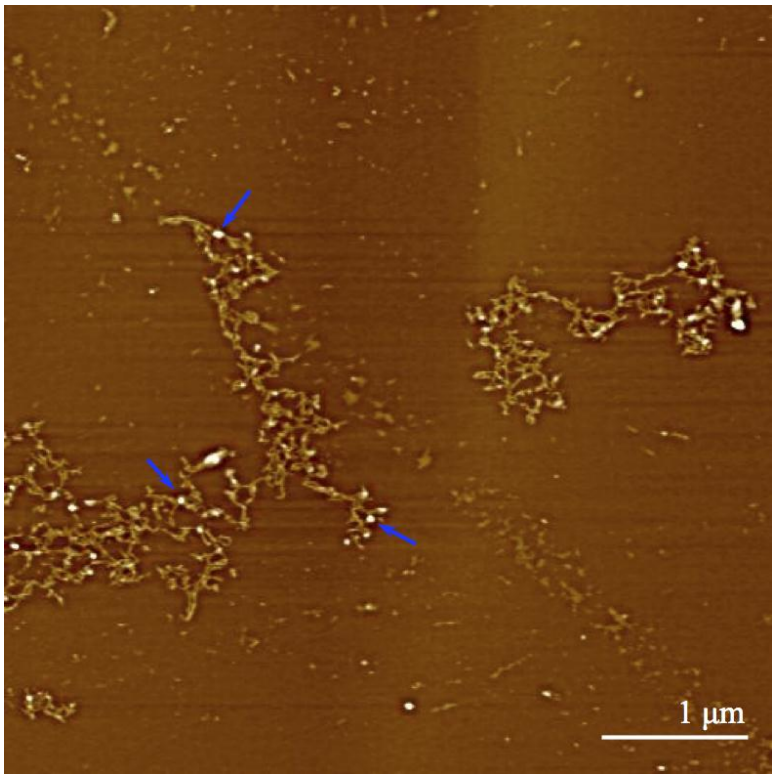

Figure 10-20: AFM image of ^{15}N DNA fraction. The presence of proteins attached to the DNA is indicated with blue arrows.

NanoSIMS analysis of the three constituent viral components was conducted, providing ^{15}N enrichment levels for each sample. Analysis results from a representative region of the lipid fraction are shown in Figure 10-21; the low levels of ^{15}N enrichment are readily apparent. Quantification of the $^{12}C^{15}N^{-}/^{12}C^{14}N^{-}$ ratio within the region of interest shown in Figure 10-21 yielded an average value of .0039, representing a negligible enrichment over the natural abundance level of .0036. Additional regions of the lipid fraction were analyzed and enrichment levels within 10% of natural abundance were obtained. NanoSIMS interrogation of the protein fraction yielded similar results; an average of five scanned regions resulted in a $^{12}C^{15}N^{-}/^{12}C^{14}N^{-}$ value of .0038. The lack of substantial ^{15}N enrichment within the lipid and protein fraction indicated that the isotopic label was almost completely segregated to the nucleic acid component of the viral

particle. This conclusion was confirmed by the NanoSIMS analysis of the DNA fraction; six individual regions were analyzed and $^{12}C^{15}N^{-}/^{12}C^{14}N^{-}$ ratio values between 0.006 and 0.01 were attained. It is evident, then, that the incorporation of the ^{15}N label resulted in viral particles containing isotopically labeled DNA. Furthermore, the additional virion constituents, namely the lipid membranes and proteinaceous structures, were shown to contain negligible levels of isotopic enrichment.

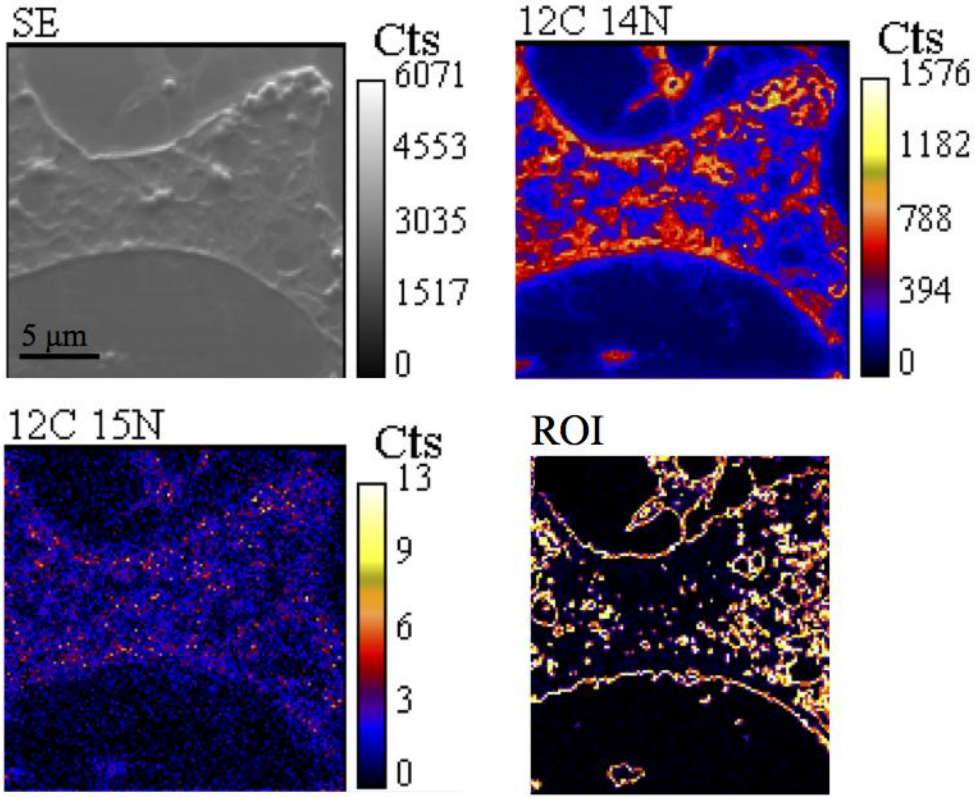

Figure 10-21: NanoSIMS generated secondary electron and chemical images of the ^{15}N lipid fraction. Near natural abundance levels of ^{15}N enrichment were observed.

The disparate levels of isotopic segregation observed between the two molecule specific labels, namely, ^{13}C and ^{15}N, can be attributed to the mechanism of cellular metabolism. As previously noted, the ^{13}C lipid membrane label was presumably metabolized by the host cells and distributed to non-specific molecules as well as lipid structures associated with nuclear assemblages. Conversely, the ^{15}N label, being associated with a chemical compound, thymidine, exclusively employed in the

construction of nucleic acids, would be expected to undergo minimal levels of metabolic activity; consequently, the isotopic nitrogen label would be expected to achieve a higher level of molecule specific isolation.

10.4.2 ^{15}N depth profile analysis

The generation of quantitative information regarding the architectural conformation of the nucleoprotein complex within the vaccinia virus required the depth profiling of individual particles. The NanoSIMS instrument was aligned to detect an isotopic variant, $^{12}C^{15}N^-$, of the carbon-nitrogen molecule. In addition, electronegative ions of $^{12}C^{14}N$, $^{12}C_2$, ^{12}C and ^{31}P were also detected. Viral sample areas of varying sizes were analyzed with the NanoSIMS and the lateral distribution of the species counts recorded for each scan cycle. The depth distribution and localization of the ^{15}N label was assessed by examining the variation of the $^{12}C^{15}N^-/^{12}C^{14}N^-$ ratio as a function of scan cycle number. A sample $^{12}C^{15}N^-/^{12}C^{14}N^-$ profile generated from an individual virion is displayed in Figure 10-22. As in Figure 10-12, the green dashed line at cycle 45 indicates the scan cycle at which the $^{12}C_2^-$ counts had been reduced to 30% of their maximum value; signifying the final data value to be used in the construction of the ^{15}N depth profile.

The qualitative aspects of the profile are consistent with the viral genome being confined within the interior of the core. An enrichment value close to the natural abundance level of .0036 is initially measured followed by a rapid rise in the $^{12}C^{15}N^-/^{12}C^{14}N^-$ ratio due to the sputtering of ^{15}N labeled nucleoprotein material. A sustained level of enrichment is subsequently measured throughout the interior of the virion as the nuclear structures are sputtered. A rapid decline in the $^{12}C^{15}N^-/^{12}C^{14}N^-$ ratio is then noted as the molecules associated with the unlabeled proteinaceous and lipid components are detected. The qualitative behavior of the ^{15}N signal is, then, consistent with the prevailing structural model regarding the localization of the genome within the viral particle. In order to generate physically relevant quantitative data concerning the spatial distribution of the ^{15}N label the non-equilibrium sputtering methodology detailed in Chapter 9 was implemented.

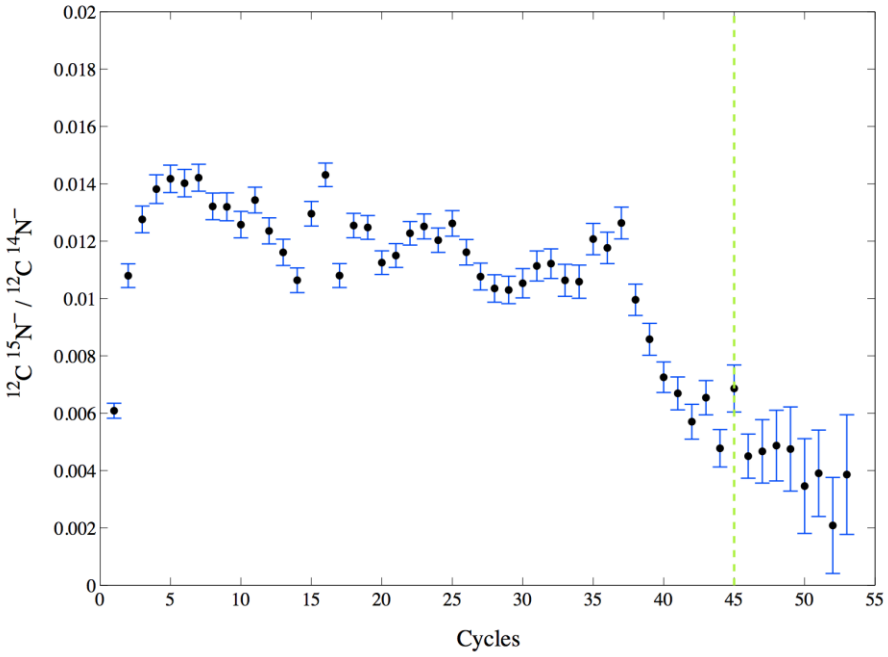

Figure 10-22: $^{12}C^{15}N^{-}/^{12}C^{14}N^{-}$ variation as a function of cycle number for an individual viral particle within a 25 µm^2 area scanned with a 0.8 pA cesium ion beam.

The raw NanoSIMS statistics detailing the $^{12}C^{15}N^{-}/^{12}C^{14}N^{-}$ ratio variation as a function of scan cycle number were converted, through the employment of Equation 6, to data indicating the variation of the ^{15}N signal as a function of viral particle depth. Due to the heterogeneous construction of the virions as well as the disparate levels of ^{15}N label incorporation, averaged $^{12}C^{15}N^{-}/^{12}C^{14}N^{-}$ depth profiles were generated. In addition, averaged data enabled subtle profile characteristics, ones that may otherwise have been lost in the noise of single particle depth profiles, to become more prominent. The averaging process involved constructing regions of interest (ROI) composed of multiple (10-40) individual viral particles; a composite single depth profile was then generated. Inherent in this methodology, however, is the assumption that the numerous individual virions in the analyzed region sputter in a synchronous manner. Additionally, variations in particle height are not reflected in the composite depth profile. Prior to implementing this methodology, then, a validation experiment was conducted to examine the level of

error introduced by the averaging procedure. Figure 10-23 details a depth profile constructed from a single composite measurement of 10 individual virions (blue curve) along with a profile (red curve) generated by combining the 10 individual particle depth profiles. Aside from the systematic deviation noted after a depth of approximately 100 nm, attributable to the increasingly low species counts, there exists a close correspondence between the two curves. These results, then, confirm that in a given scan individual viral particles sputter in a synchronous manner and indicate that accurate depth profiles can be constructed from high species count averaged statistics. Consequently, in an attempt to mitigate data variations arising from particle heterogeneity $^{12}C^{15}N^-/^{12}C^{14}N^-$ depth profiles were constructed from single ROIs composed of multiple ^{15}N labeled virions.

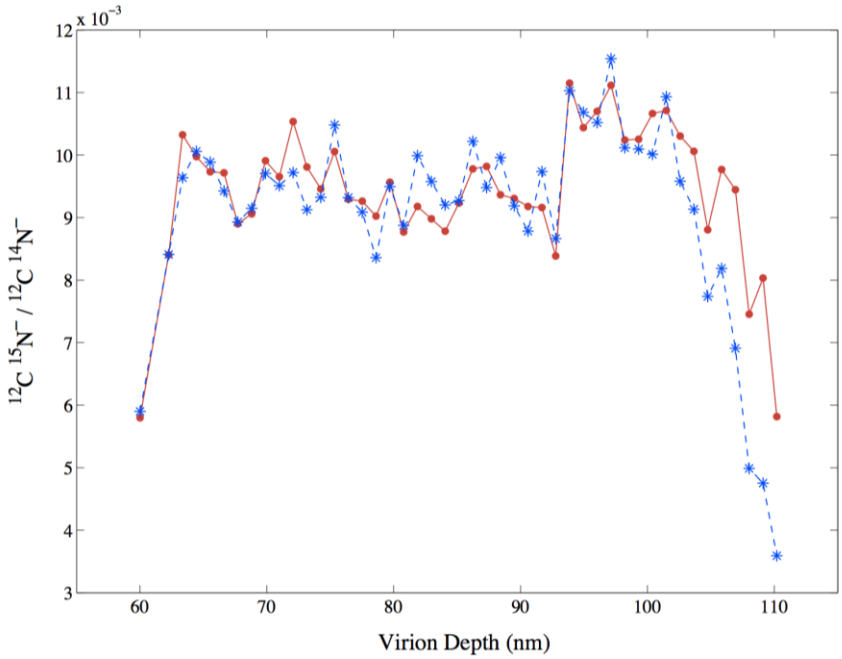

Figure 10-23: $^{12}C^{15}N^-/^{12}C^{14}N^-$ variation as a function of particle depth for a single ROI composed of 10 viral particles (blue) and an averaged measurement consisting of the 10 particles within their own ROI (red).

Implementation of the aforementioned methodology resulted in the construction of quantitative profiles detailing the localization and distribution of the ^{15}N label within the viral particle. Figure 10-24 illustrates a characteristic $^{12}C^{15}N^-/^{12}C^{14}N^-$ depth profile

generated from a 100 μm^2 scan with a 0.8 pA ion beam. An additional profile coupled with corresponding AFM images of viral particles at successive stages of the sputtering process is shown in Figure 10-25.

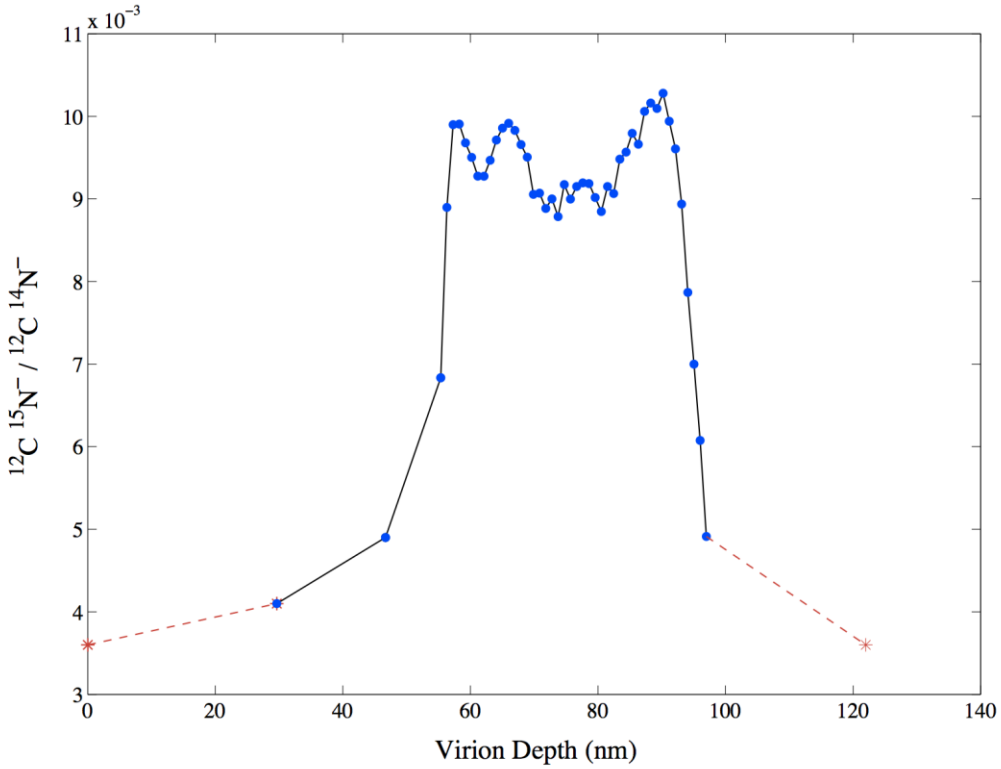

Figure 10-24: $^{12}C^{15}N^-/^{12}C^{14}N^-$ depth profile of an individual viral particle. The localization of the ^{15}N enriched region corresponds well to prevailing architectural theories regarding the arrangement of the genome within the viral particle.

As previously discussed, the rapid erosion characteristic of the non-equilibrium sputtering regime results in the initial data point occurring at a significant depth. In contrast to the ^{13}C data, however, surface sensitivity is of minor importance in the present case due to the localization of the genome within the interior of the viral particle. The two characteristics that warrant the most attention, then, are the depth distribution of the isotopic label, as well as the qualitative features of the ^{15}N enriched region. In regards to the former consideration, the physical extent of the region of enrichment, approximately 35-45 nm, corresponds well to the proposed dimensions of the nucleoprotein complex. In

addition, the localization of the enriched region within the depth profile, between 50-100 nm, is consistent with the prevailing architectural model.

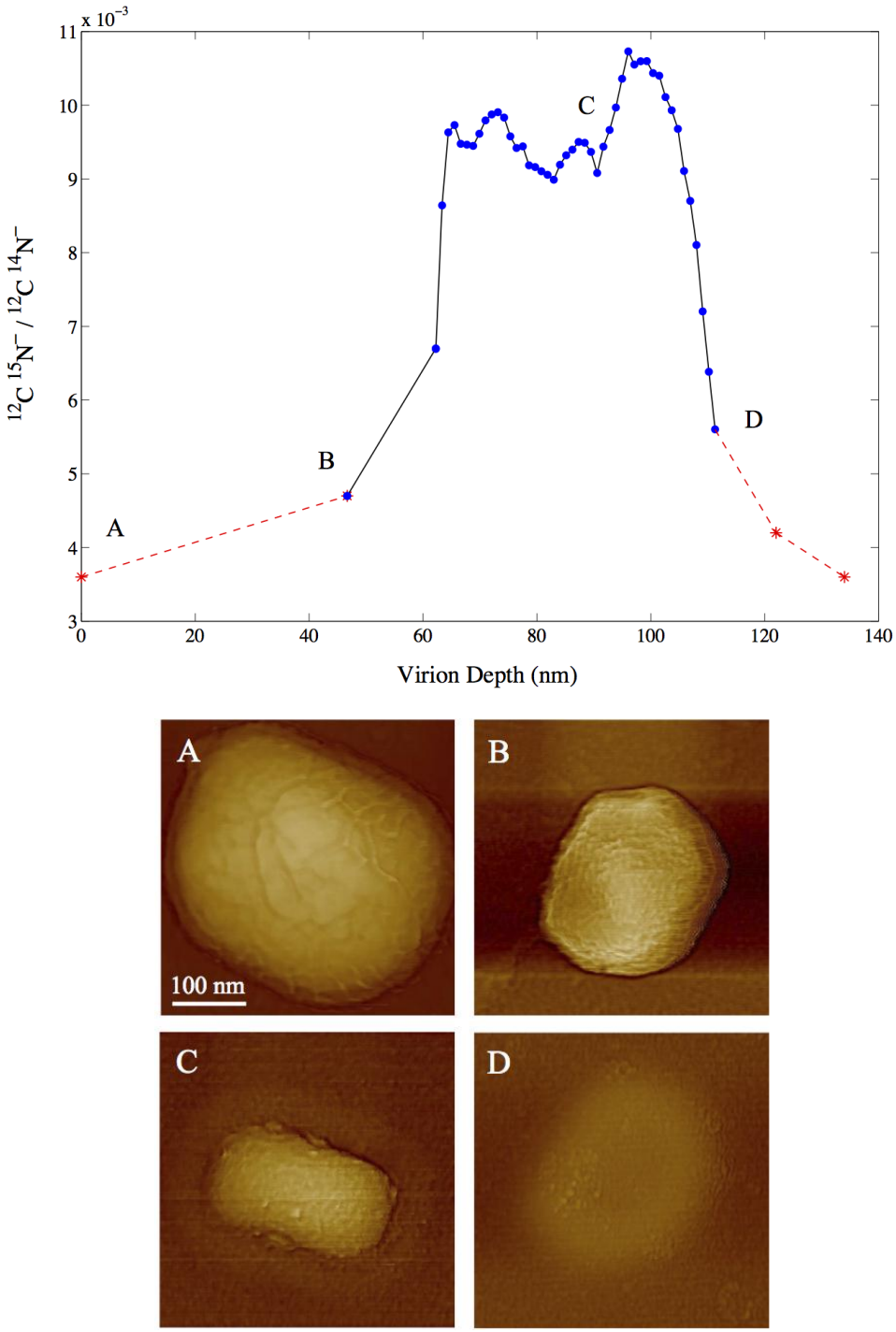

Figure 10-25: ^{15}N depth profile (upper) of an individual viral particle coupled with AFM images (A-D) at sequential points along the curve.

Insight into the ^{15}N depth profiles can be gained by comparing the results obtained with the NanoSIMS with those generated from electron microscopy. Figure 10-26 depicts an electron microscope cross section image of the vaccinia viral particle with the region theorized to contain the genome demarcated in red. The significant discrepancy in the virion height between Figure 10-26 and the depth profiles shown in Figures 10-24 and -25 can be attributed to the aforementioned effect of dimensional change due to virion dehydration. In addition, the presented depth profiles are constructed such that a depth of zero is at the top of the viral particle cross section in Figure 10-26. The qualitative correspondence between the depth profiles and the EM image is then readily apparent. A region containing lipid and proteinaceous material approximately 50 nm thick is first sputtered, yielding low levels of ^{15}N enrichment. The genomic region is subsequently entered generating high levels of isotopic enrichment for approximately 40 nm. A rapid decline in ^{15}N signal is then noted as the proteinaceous material of the core wall is sputtered. Interestingly, the genomic region of the viral particle does not seem to exhibit the extensive dimensional change due to the dehydration process.

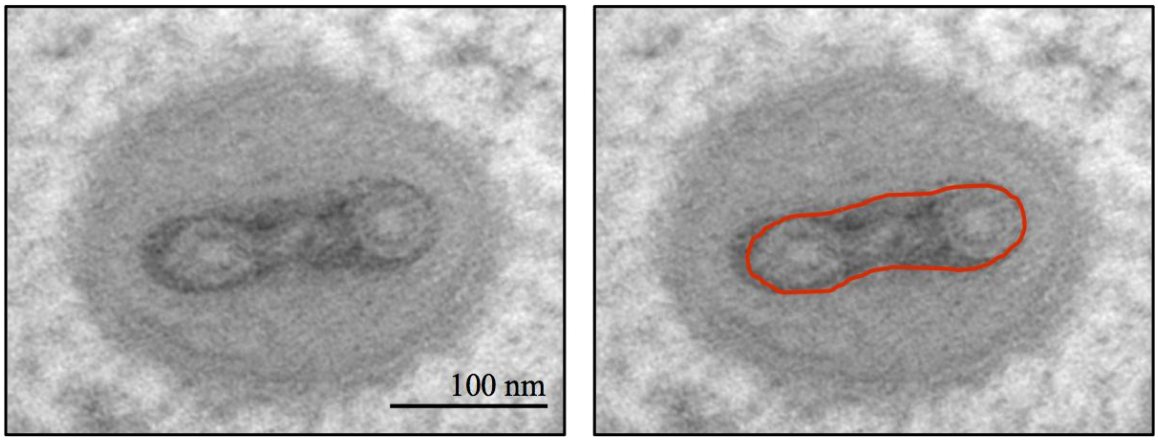

Figure 10-26: Electron microscopy cross-section of a vaccinia viral particle. The region encircled in red contains the presumed genomic structures. The presented depth profiles are constructed such that a depth of zero is at the top of the cross-section shown above. The current images were obtained from Prof. Condit at the University of Florida.

Further insight into the genomic arrangement can be gained by examining both the quantitative distribution as well as the qualitative variation of the ^{15}N signal within

the enriched region. The level of ^{15}N enrichment, approximately three-fold that of natural abundance, is the approximate level predicted assuming the ^{15}N labeled thymidine was completely and exclusively incorporated into the viral DNA. Furthermore, the qualitative behavior of the $^{12}C^{15}N^-/^{12}C^{14}N^-$ ratio within the enriched region is indicative of a repeating structural pattern composed of distinct areas of alternating high and low ^{15}N enrichment. Within the context of the architectural construction of the viral genome, this data supports a model of folded nucleoprotein substructures composed of ^{15}N labeled DNA encased within proteinaceous assemblages. The prominent $^{12}C^{15}N^-/^{12}C^{14}N^-$ peaks and valleys are, presumably, alternating regions of high DNA and protein content, respectively. The lack of a more pronounced disparity between the enrichment levels of the two regions can be attributed to the close association of the isotopically labeled nuclear structures with the nucleoproteins as well as the presence of material mixing during ion bombardment.

In addition to the depth resolved data previously presented, additional insight into the structural arrangement of the nucleoprotein complex can be generated by examining the chemical ratio images as well as the lateral distribution of the ^{15}N signal within individual viral particles. As an illustrative example, a NanoSIMS interrogated region composed of four virions is shown in Figure 10-27. In addition, a series of $^{12}C^{15}N^-/^{12}C^{14}N^-$ ratio images, generated at distinct particle depths within the region of ^{15}N enrichment, is presented in Figure 10-28. For a given depth, the ratio images indicate the pixel specific ratio generated by summing the species counts from all analysis planes; consequently, the ratio image constructed at a depth of 65 nm, for example, indicates the $^{12}C^{15}N^-/^{12}C^{14}N^-$ ratio distribution for the virion material comprising the first 65 nm of depth. In the first ratio image, detailing the $^{12}C^{15}N^-/^{12}C^{14}N^-$ distribution up to a depth of approximately 65 nm, regions of distinct ^{15}N enrichment are apparent in two of the four viral particles; those delineated by the lack of a square outline. After 85 nm of sputtered material, the region of enrichment for these two virions has expanded and, especially apparent for the lower left viral particle, the level of ^{15}N enrichment has increased. Following an erosion depth of 105 nm, little change in the distribution of the enriched regions is noted, save for a slight increase in ^{15}N signal in the uppermost viral particle.

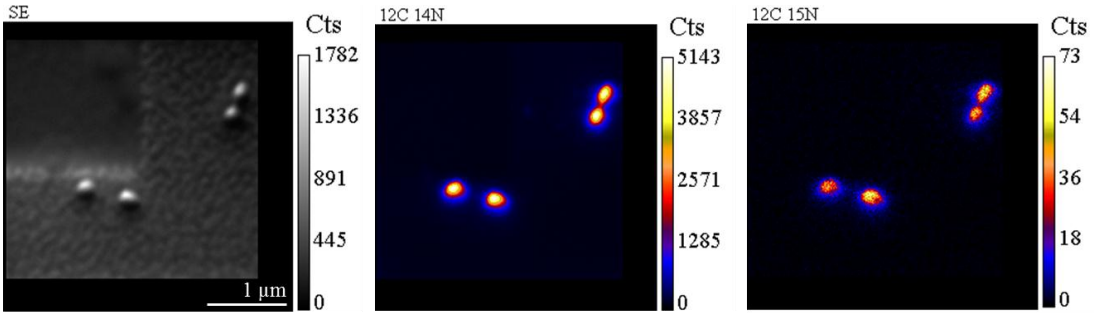

Figure 10-27: NanoSIMS analyzed region composed of four ^{15}N labeled viral particles. Area corresponds to the ratio and error images shown in Figure 10-28.

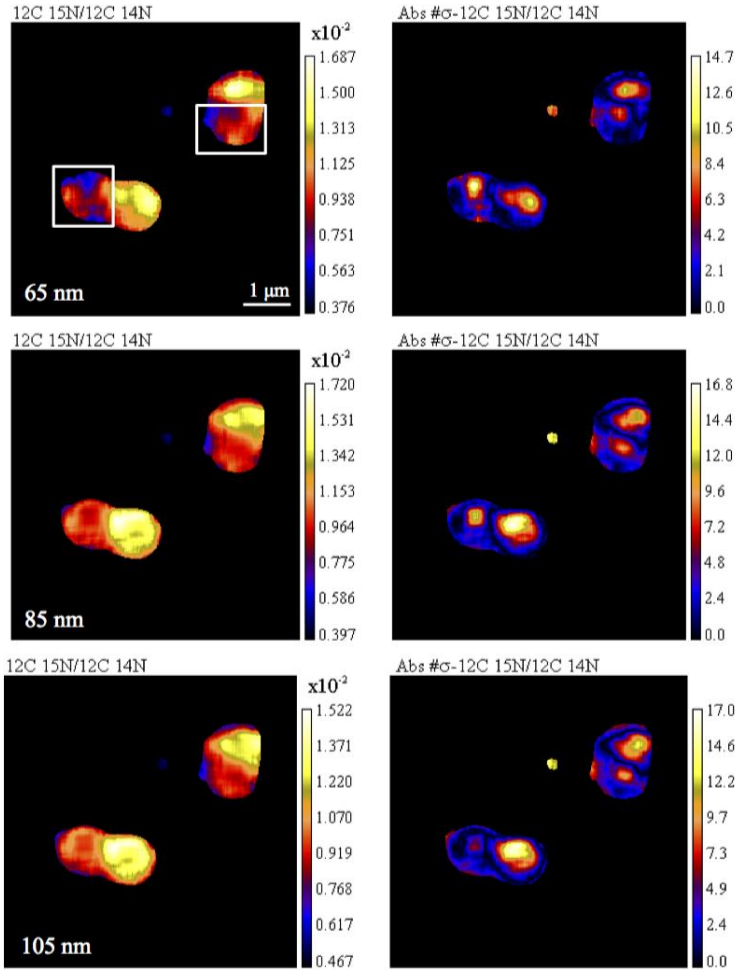

Figure 10-28: Lateral and depth distribution of ^{15}N label within individual virions. The variation noted in the isotopic label distribution is indicative of heterogeneously configured viral genomes.

This analysis, then, provides insight into the lateral arrangement of the nucleoprotein complex within the virion as a function of depth. As is apparent from the ratio images, the pattern of heterogeneity is relatively consistent throughout the virion depth; for the two virions under consideration the initial qualitative pattern of isotopic ratio distribution is maintained over the interrogated region. Therefore, it is clear that the viral genome is constructed in such a manner that its orientation and arrangement remains relatively constant throughout individual virions. There exist, however, substantial disparities between the distributions of the genome within different viral particles. The ^{15}N labeled region of the lower virion is extensively distributed throughout the particle while the genome within the upper particle appears less diffuse. While discrepancies such as this may indicate non-uniformity with regards to isotopic label incorporation, an additional and more likely explanation concerns the orientation and arrangement of the labeled structures within the virion. Specifically, due to the heterogeneous nature of the viral structure, the lateral distribution of the genome within individual particles would presumably exhibit a myriad of configurations.

Further evidence of this can be seen in the two virions demarcated in Figure 10-28 by the white squares. As is readily apparent in the first ratio image, the two virions framed in white exhibit substantially less enrichment after 65 nm than the other two viral particles. While this characteristic is present throughout the interrogated depth, a significant increase in the level of ^{15}N enrichment is noted for both particles after 85 and 105 nm. Comparatively speaking, then, the genomes of the viral particles framed in white appear to be less enriched and configured in such a way that the majority of the labeled nuclear structures occur at a greater depth. As would be expected, the depth profiles of the two groups of viral particles reflect these differences; for the virions framed in white, the region of high ^{15}N enrichment begins at a depth near 65 nm, approximately 15 nm deeper than was noted for the other two particles. Furthermore, the lateral distribution of the $^{12}C^{15}N^{-}/^{12}C^{14}N^{-}$ ratio within the two particles indicates a diffuse genome configuration surrounding a core region of low ^{15}N enrichment. This is especially apparent in the framed virion on the lower left; an area of high ^{15}N label incorporation is observed surrounding a rectangular region exhibiting relatively low enrichment. Presumably, the

interior region, demonstrating a lowered $^{12}C^{15}N^{-}/^{12}C^{14}N^{-}$ ratio, is composed of a comparatively high level of proteinaceous material.

NanoSIMS analysis of ^{15}N labeled viral particles yielded data concerning the depth as well as the lateral distribution of the viral nucleoprotein complex. Quantitative depth profiles indicated the confinement of the nuclear material to depths between approximately 50-90 nm. In addition, the repetitive pattern of the ^{15}N signal within the enriched region corroborates the theory of a hierarchical substructure composed of folded nuclear and proteinaceous assemblies. Examination of the lateral distribution of the viral genome indicated a variety of configurations; particles were observed displaying ^{15}N enrichment evenly distributed throughout planes of constant depth, other particles, however, consisted of genomes confined to comparatively small regions or surrounding areas composed of high levels of proteinaceous material. The aforementioned experiments, then, provide data regarding the architectural arrangement of the nucleoprotein structure within intact viral particles. In order to examine the composition of the nucleoprotein assemblage itself a series of studies implementing systematic viral particle degradation techniques coupled with NanoSIMS analysis was initiated.

10.4.3 NanoSIMS analysis of ^{15}N labeled nucleoprotein structures

Elucidating the architectural composition of the nuclear material and proteinaceous assemblages within the viral nucleoprotein complex is of central importance for the design of anti-viral strategies. Modeling of the DNA configuration within the nucleoprotein complex itself, however, requires high-resolution data specifying the orientation and structural coupling of the nuclear and proteinaceous material. In an attempt to explore this relationship, the viral particle degradation techniques detailed in Chapter 7 were implemented to produce isolated isotopically labeled nucleoprotein assemblages. Discrete levels of the protein digesting enzyme proteinase K were utilized to generate a spectrum of nucleoprotein structures; the sub-viral assemblages were thereafter physically and chemically imaged with AFM and NanoSIMS, respectively. Viral suspensions composed of ^{15}N labeled virion cores were initially exposed to 0.2 mg/ml proteinase K and incubated for one hour at 37 ºC. Sample

imaging with atomic force microscopy resulted in the observation of regions composed of small conglomerations of nucleoprotein material consistent with the structures displayed in Figure 7-4. AFM measurements indicated that the heights of the observed assemblages varied between 25-40 nm. NanoSIMS analysis of the AFM imaged regions was subsequently implemented to access the level and distribution of the ^{15}N label. A typical analyzed area is shown in Figure 10-29; the AFM image corresponds to the region framed by white in the $^{14}N^{12}C^-$ NanoSIMS image. In addition, the distribution of the isotopic label throughout the imaged region is detailed in the $^{15}N^{12}C^-$ NanoSIMS figure. Due to the exceptionally small volume of sputtered material the detected species counts per scan cycle were associated with high levels of uncertainty. Large disparities in the qualitative aspects of the data were therefore detected. Consequently, no discernible systematic variation in the ^{15}N signal within the nucleoprotein structures was observed. Due to this consideration, then, the possibility of generating high-resolution depth resolved structural information regarding the architectural arrangement of the DNA and proteinaceous assemblages was precluded. By examining the ratio images, however, pertinent data concerning the large-scale association of the isotopic label with the isolated nucleoprotein complex was generated.

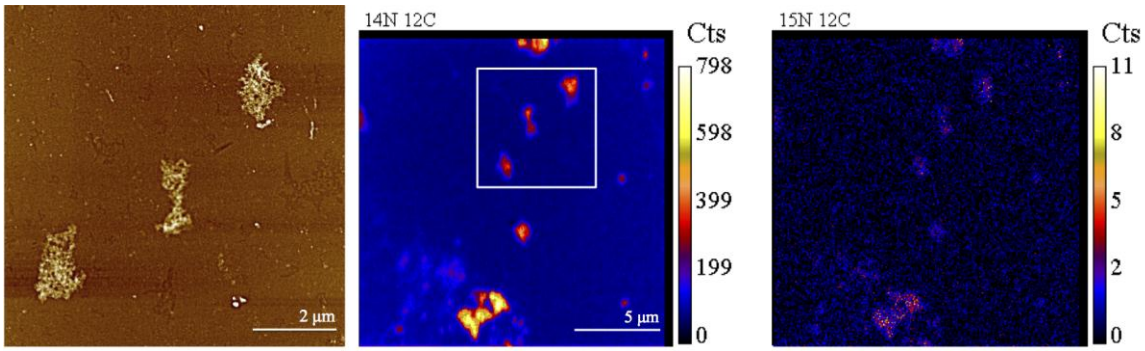

Figure 10-29: Correlated AFM/NanoSIMS analysis of isolated nucleoprotein structures. The AFM imaged region (left) corresponds to the area framed in white in the $^{14}N^{12}C^-$ NanoSIMS image (middle).

The magnitude and distribution of the $^{15}N^{12}C^-/^{14}N^{12}C^-$ ratio for the region under consideration is shown in Figure 10-30. While a significant portion of the region was enriched to a level approximately twice that of natural abundance (~0.0065), numerous

areas displayed negligible isotopic enrichment. Interestingly, the nucleoprotein conglomerations did not exhibit a higher level of ^{15}N enrichment than the majority of the background. It appears then, that small fragments of the nucleoprotein structure, ones similar in composition to the large complexes shown in Figure 10-29, covered large regions of the analyzed area. Furthermore, based upon the moderate ^{15}N levels associated with these structures it is clear that a substantial amount of non-enriched proteinaceous material was present within the analyzed region.

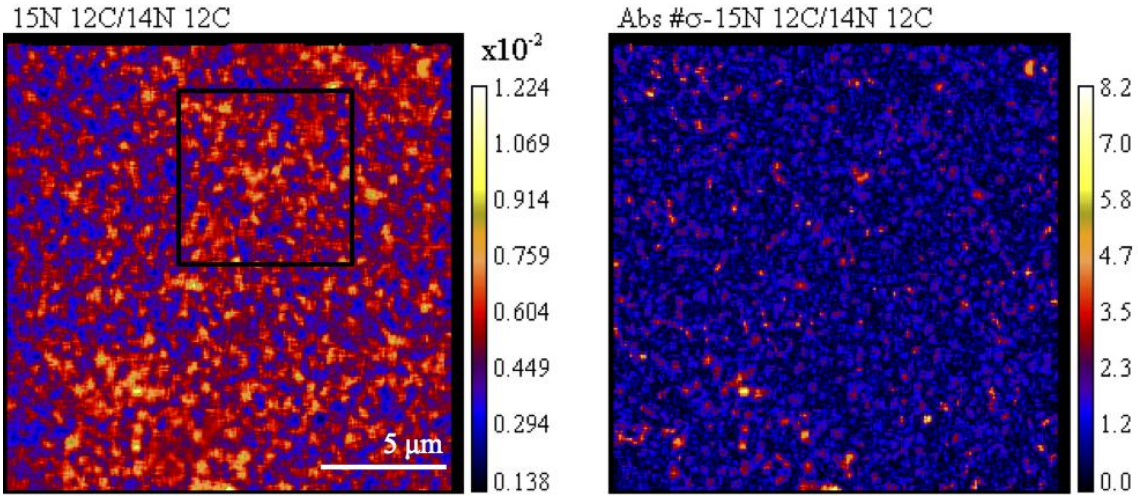

Figure 10-30: Distribution of the $^{15}N^{12}C^{-}/^{14}N^{12}C^{-}$ ratio (left) and error (right) for the area shown in Figure 10-29. The region framed in black corresponds to the AFM image in Figure 10-29. The nucleoprotein structures were enriched to a level consistent with the background.

In order to quantitatively examine the dynamic process of nucleoprotein degradation, viral core suspensions exposed to an increased concentration of proteinase K were analyzed for ^{15}N enrichment. The subsequently elevated levels of protein deterioration would presumably result in increased breakdown of the nucleoprotein complex accompanied by a corresponding rise in the presence of naked DNA. As a result, the $^{15}N^{12}C^{-}/^{14}N^{12}C^{-}$ ratio assessed throughout the region should exhibit a marked increase over that measured at the lower proteinase K concentration. In order to evaluate this hypothesis sample regions composed of nucleoprotein structures generated from exposure to 0.5 mg/ml proteinase K for one hour at 37 ºC were analyzed; a characteristic

area is shown in Figure 10-31, the region framed in red in the AFM image corresponds to the NanoSIMS analyzed area.

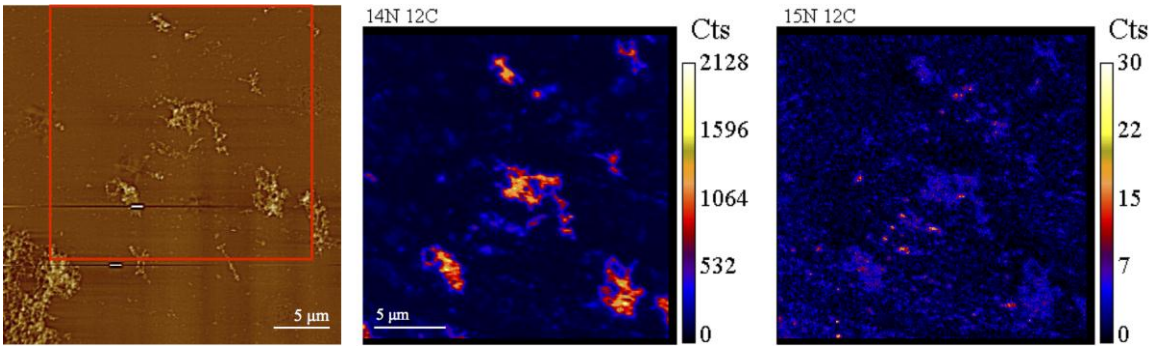

Figure 10-31: Correlated AFM/NanoSIMS analysis of isolated nucleoprotein structures. The AFM imaged region (left) framed in red corresponds to the $^{14}N^{12}C^-$ NanoSIMS image (middle). This sample was exposed to a higher level of proteinase K treatment than that shown in Figure 10-29.

As before, significant insight can be gained by examining the spatial distribution of the $^{15}N^{12}C^-/^{14}N^{12}C^-$ ratio throughout the interrogated region. These data, illustrated in Figure 10-32, display substantial discrepancies from the $^{15}N^{12}C^-/^{14}N^{12}C^-$ ratio image, generated at the lower proteinase K concentration, shown in Figure 10-30. Specifically, for the viral sample exposed to high concentrations of proteinase K, the nucleoprotein structures demonstrate significantly less enrichment with respect to the background than was noted for the low proteinase K concentration sample. This characteristic is readily apparent in the ratio and standard error images in Figure 10-32; the nucleoprotein structures exhibit an average $^{15}N^{12}C^-/^{14}N^{12}C^-$ ratio of .00576 while the enriched background regions indicate an isotopic ratio value of .0255. Therefore, an approximate 4.5 fold difference was present between the enrichment level of the nucleoprotein structures and the sample background. As previously addressed, at the lower concentrations of proteinase K treatment the nuclear/proteinaceous assemblages demonstrated an approximately equivalent level of ^{15}N enrichment as the surrounding environment. This differential phenomenon can be attributed to the increased breakdown of proteinaceous material at elevated levels of enzymatic concentration. The viral sample exposed to 0.5 mg/ml proteinase K experienced substantial degradation of the protein

elements within the nucleoprotein structure, leaving background regions of naked DNA. The quantitative level of background enrichment corroborates this conclusion; DNA composed of ^{15}N thymidine would be expected to exhibit a $^{15}N^{12}C^{-}/^{14}N^{12}C^{-}$ ratio within 15% of that measured in the sample background. Parenthetically, the widespread presence of nuclear/proteinaceous material within the sample exposed to the elevated level of proteinase K provides evidence of the high degree of biologically heterogeneity. In addition, it is indicative of the lack of uniform exposure of the viral sample to the proteinase K enzyme.

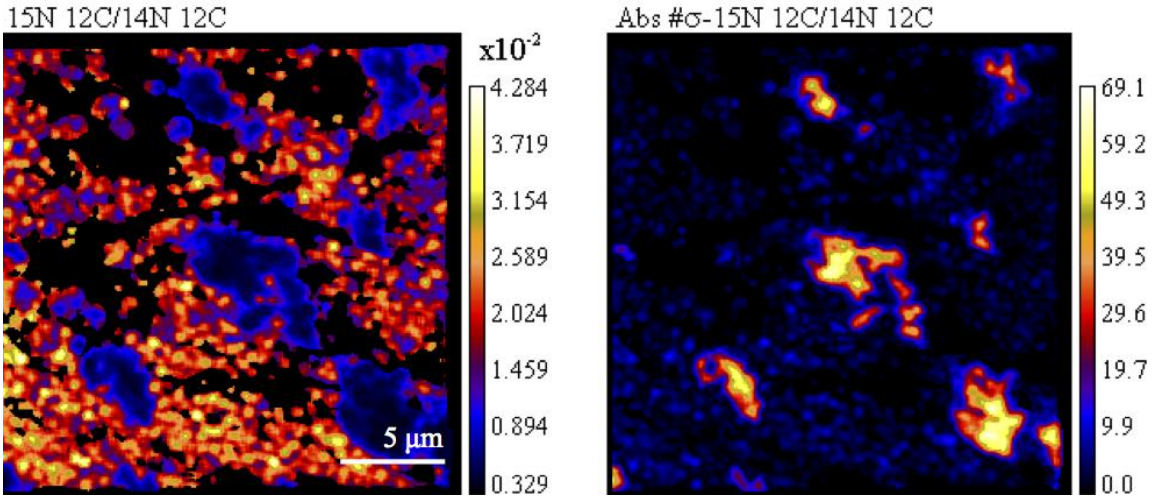

Figure 10-32: Distribution of the $^{15}N^{12}C^{-}/^{14}N^{12}C^{-}$ ratio (left) and error (right) for the area shown in Figure 10-31. The nucleoprotein structures were less enriched than the background, indicating the presence of nuclear material not extensively associated with proteinaceous material.

The aforementioned experiments, then, resulted in data concerning the spatial distribution of the ^{15}N label within regions composed of nucleoprotein structures. Due to the small volume of the nuclear/proteinaceous assemblages themselves, however, detailed depth resolved information concerning the architectural relationship of the constituent elements was excluded. Nevertheless, the NanoSIMS data indicating that the nucleoprotein structures are isotopically enriched confirms that the viral DNA is associated with these assemblages. This data corroborates and provides an independent confirmation of the AFM DNase experiments detailed in Chapter 7. Furthermore, the

correlated increase in aggregate isotopic enrichment at elevated proteinase K concentrations is consistent with the breakdown of natural abundance proteinaceous material and the subsequent exposure of naked isotopically labeled DNA. These results, then, provide substantial support to the theory that the viral genome is heavily associated with proteinaceous material and that the consequent assemblage displays a tubular architecture with individual elements approximately 30 nm in diameter.

Chapter 11 Conclusion and future work

11.1 Conclusion

The experiments presented herein demonstrate the application of a correlated AFM/NanoSIMS to the study of the architectural composition of vaccinia virus. Physical imaging was performed with atomic force microscopy and the subsequent results were combined with depth resolved chemical information generated with nano-scale secondary ion mass spectrometry. These data enabled the formulation of structural models for the localization and arrangement of the viral particles' lipid membrane and nucleoprotein complex.

A series of atomic force microscopy experiments were conducted utilizing intact virions as well as a variety of chemically and enzymatically derived viral sub-structures. Experimental results generated by exposing viral cores to proteinase K resulted in the decomposition of the core wall and the release of extensive networks of nuclear/proteinaceous assemblies. These tubule filaments varied in height from approximately 10-40 nm; tubule height being closely correlated to the concentration of, and exposure time to, the reducing agent. Subsequent exposure of the structures to DNase, an enzyme that catalyzes the hydrolytic cleavage of covalent bonds in the DNA backbone, resulted in substantial degradation of the filaments, indicating that nuclear material was an integral component of the structure. The AFM results, then, support the structural theory forwarded by others, namely, that the viral genome is condensed or folded within the core region and is closely coupled with a variety of proteinaceous

material. Furthermore, the results indicate that the nucleoprotein complex exhibits a tubule structure and may be constructed in a hierarchy manner, with smaller filamentous elements encased within the larger tubules.

Generation of spatial data concerning the arrangement of specific constituents within the vaccinia virion, namely, the lipid membrane and nucleoprotein complex, required the implementation of isotopic labeling procedures and nano-scale secondary ion mass spectrometry. Isotopically labeled molecules, ^{13}C fatty acids and ^{15}N thymidine, were incorporated into the viral particles' lipid membrane and DNA, respectively; the lateral and depth distribution of the isotopic tags was subsequently measured with the NanoSIMS, providing quantitative compositional information regarding the structure of the vaccinia virion.

The extension of NanoSIMS analysis to biological entities on the nanometer scale was first validated through natural abundance measurements of unlabeled viral particles; the ability to produce quantitatively accurate $^{13}C/^{12}C$ and $^{15}N/^{14}N$ chemical measurements for individual virions was subsequently confirmed. The possibility of extending this methodology to produce spatial maps of specific isotopically labeled components of the viral particle required the investigation of two critical capabilities: 1) the ability to introduce isotopic labels into the viral particles and ensure their exclusive incorporation into the specific molecules of interest and 2) the ability to quantitatively correlate the raw NanoSIMS data with a physical depth dimension. In regards to the former consideration, isotopic measurements indicated a high level of incorporation of both the ^{13}C lipid membrane label as well as the ^{15}N thymidine DNA label. The ability to achieve exclusive segregation of the ^{13}C label to the lipid membrane was, however, hindered by the metabolic activity of the host cell and the labeling of lipid molecules throughout the virion interior. Fractionation experiments coupled with NanoSIMS analysis validated the fidelity of the ^{15}N labeling procedure. The second consideration, namely, the formation of quantitative methodology to produce accurate depth resolved isotope enrichment maps, required the implementation of a variety of sputtering experiments. The subsequent results demonstrated that the sputter rate of the viral particle is a highly non-linear function of the sputter time. The measured sputter rate curve is composed of a non-

equilibrium regime characterized by a rapid decline followed by an equilibrium region where the sputtering process has stabilized; the curve is well approximated by a decaying exponential. These data indicate that the initial transitory period, where non-equilibrium conditions exist, displays highly distinct sputtering characteristics. The physical mechanism responsible for this phenomenon is ambiguous, however, a correspondence between the time variation of the sputter rate and the dynamic process of cesium implantation and sub-surface damage accumulation was observed. Theoretical considerations aside, these experiments enabled the generation of a family of sputter rate curves for a range of experimental conditions and provided a quantitative methodology for the accurate production of chemical depth profiles.

The non-equilibrium sputter rate model was subsequently implemented to generate ^{13}C and ^{15}N depth profiles of isotopically labeled virions. Data for the former indicated the presence of one exterior lipid membrane surrounding the viral particle. This conclusion corroborates the latest studies and lends considerable support to the theory that the vaccinia virion lacks a structured interior lipid membrane. The ^{15}N data indicated, as expected, the confinement of the viral genome within the core interior. Furthermore, the distinct periodic behavior of the ^{15}N signal within the enriched region supports the architectural model of the genome being constructed from folded tubules composed of proteinaceous and nuclear material.

Additional experiments were then implemented to further elucidate the nature of the structural configuration between the proteinaceous and nuclear material within the nucleoprotein complex. Isolated nucleoprotein structures were generated from chemical and enzymatic treatment of ^{15}N labeled virions and analyzed with the NanoSIMS. While results indicated clear isotopic enrichment of the sub-viral structures, the small volume of sputtered material, coupled with the lack of sufficient depth resolution, precluded the possibility of forming any definite conclusions regarding the distribution of the DNA within the tubule structures.

The totality of the results presented herein demonstrates the development and application of a novel orthogonal physical and chemical imaging methodology for the field of structural virology. We have demonstrated the ability to accurately introduce

molecule specific isotopic labels into individual virions and quantitatively map their distribution with secondary ion mass spectrometry. Implementation of this methodology resulted in the construction of nanometer scale depth resolved maps detailing the architectural localization and arrangement of the lipid membrane and viral genome within the vaccinia virion. In addition, we have extended this capability to the nucleoprotein complex, demonstrating the ability to combine high-resolution physical and chemical imaging for the determination of the structure-function relationship of specific sub-viral structures.

11.2 Future work

In order to extend the methodology presented in the present work, two specific areas of future study have been identified. The first focuses upon the analysis of both the sputtering of heterogeneous biological materials as well as the non-equilibrium sputter rate phenomenon. The second area of proposed future work entails the examination of utilizing multiple molecule specific isotopic labels for the structural determination of sub-viral elements.

The ability to accurately predict and quantify the sputtering behavior of heterogeneous constructed biological entities is predicated upon the formulation of theoretical models and the generation of experimental data. Due to the relatively recent application of secondary ion mass spectrometry to biological structures, however, there exists a lack of research in both of the aforementioned areas. The identification in the present work of a time dependent sputter rate for the vaccinia viral particle does not conform to the sputtering theories developed for inorganic homogeneous substrates. Consequently, further investigation into this phenomenon is warranted. Additional sputtering experiments utilizing a variety of diverse nanometer/micrometer biological particles are recommended. These studies would help identify the specific physical properties that contribute to the sputter rate variation and the establishment of equilibrium conditions. Experimentally examining sputter rate variations due to particle geometry, physical constitution, porosity and density would provide valuable insight into the

underlying physical mechanism governing the sputtering of heterogeneously constructed biological materials. Furthermore, a detailed investigation of the dynamic process of ion implantation and its effects on the sputtering characteristics of the biological particle would be a worthwhile endeavor. The generation of experimental data in this vein, coupled with new theoretical models, would contribute to the development of predictive computational schemes that would more accurately reflect the behavior of small biological particles under ion bombardment.

The other field of proposed future work concerns the development of schemes focused upon the generation of high-resolution isotopic information on the scale of sub-viral structures. The ability to extract structural data from the isolated nucleoprotein complexes was hindered both by the small scale of the analyzed elements as well as the lack of conclusive variation in the ^{15}N signal. While the first issue is an inherent physical constraint, incorporating an additional isotopic label into the proteinaceous material of the nucleoprotein complex may mitigate the second. To ensure exclusive incorporation of the isotopic labels into the molecules of interest labeling would be performed with an elemental isotope unique to each molecule. A radioactive isotope of phosphorous (^{32}P) could be employed as the DNA label - phosphorous not being present in amino acids - and ^{35}S, a radioactive isotope of sulfur could, for similar reasons, be incorporated into the proteinaceous material. In this manner, two corresponding isotopic signals would be generated: one indicating the presence of nuclear material and the other proteinaceous material. Consequently, significant trends in the variation of the isotopic signals would be more easily discerned, enabling the construction of detailed models regarding the architectural relationship between the DNA and proteins within the nucleoprotein complex.

Appendix A: Part I: bio-aerosol protocols and considerations

AI. *B. atrophaeus* and *B. subtilis* endospore production

Initial endospore production and cultivation was conducted at SRI International and was performed using an agar plate method. While this technique yielded a highly pure and concentrated prep the resulting suspension volume was prohibitively small for our experimental program. To produce accurate, statistically reliable results endospore suspensions on the order of tens of milliliters at a concentration of 10^9 endospores/ml were needed. In an effort to expand our production method we worked with Dr. Burkholder in the Biology department at Stanford University on a large - scale broth protocol. Utilizing this technique we were able to increase our endospore yields substantially while retaining the highly pure suspension quality characteristic of the SRI plating method. Sporulation of both the *Bacillus atrophaeus* bacterial strain obtained from SRI and the *Bacillus subtilis* strain obtained from Dr. Peter Setlow of the University of Connecticut was induced utilizing the broth production method. To prepare the endospore suspensions we first induced the sporulation of the bacterial strain by growth to exhaustion in Difco sporulation medium (DSM) at 37 ºC[47]. The endospore suspension was thereafter purified through ddH_2O washing. Subsequent incubation with lysozyme for one hour at 37 ºC and the addition of SDS for 20 minutes was implemented to eliminate vegetative cell debris[47]. The resulting suspension was once again washed with ddH_2O until only phase-bright endospores were observed utilizing phase-contrast microscopy. Figure AppA-1 illustrates a typical endospore sample prepared using the large scale broth method. Aqueous endospore suspensions were subsequently concentrated to 10^9 spores/ml. Additional details regarding this procedure are shown below.

DSM liquid growth method

1. Inoculate the desired strain into 5 ml LB; grow overnight.

2. Inoculate the overnight starter culture into 1 L DSM media (see below); grow for 24-28 hours at 37 ºC.
3. Spin down the culture in a centrifuge; 4500 xg for 10 minutes.
4. Wash the cell suspension twice with sterile dH_20. Centrifuge 4500 xg for 10 minutes after each wash.
5. Re-suspend pellet in 30 ml of sterile dH_20. Add 30 mg lysozyme and incubate with shaking at 37 ºC for 1 hour.
6. Add 6 ml 10% SDS and incubate with shaking for 20 minutes.
7. Centrifuge 4500 xg for 10 minutes.
8. Wash with sterile dH_20 until washes are clear and the endospore prep is sufficiently pure.
9. Store endospore suspension at 4 ºC.

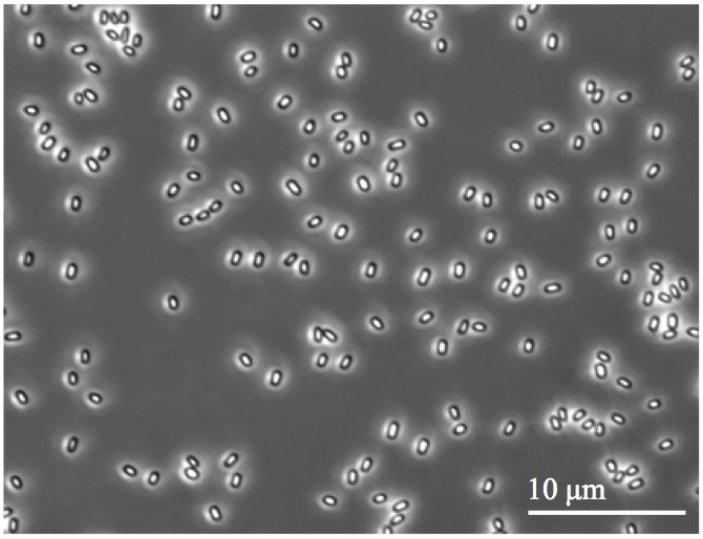

Figure AppA-1: Light microscope image of phase bright endospores grown with the DSM liquid growth method.

DSM Media:

1. To 996 ml dH_20 add:
    a. 8g BD/Difco Nutrient Broth
    b. 2.7 ml 2.5M KCl
    c. 0.5 ml 1M $MgSO_4$

d. 0.5 ml 1M NaOH

2. Stir until nutrient broth is dissolved
3. Autoclave
4. Add the following sterile salt solution
    a. 1 ml 1M $Ca[NO_3]_4$
    b. 1 ml 0.1M $MnCl_2$
    c. 1 ml 1mM $FeSO_4$

AII. Fundamental Spectroscopy

The theory of the laser diagnostic method employed in the current study is predicated upon the time varying absorption and scattering of incident laser light by the bio-aerosol. Quantitatively interpreting the laser signals required the implementation of spectroscopic models; the following section briefly surveys these models and their underlying assumptions.

The interaction of spectrally narrow radiation at frequency ν and incident intensity I_o with a uniform gas medium of path length L results in a reduced transmitted laser intensity I. The spectroscopic methods employed in this study result in path – averaged measurements; inherent in this construct, then, is the assumption of a spatially uniform absorbing and scattering medium. Within this framework the incident and transmitted laser intensities can be related through the Beer-Lambert Law:

$$\left(\frac{I}{I_o}\right)_v = exp(-k_v L), \text{ and, upon rearranging: } -ln\left(\frac{I}{I_0}\right)_v = k_v L$$

The quantity k_vL is the spectral absorbance or extinction and k_v (cm^{-1}) is the spectral absorption coefficient. For the temperature diagnostic we were concerned with two specific transitions, therefore, we employed k_v as follows:

$$k_v = P x_{abs} S_i(T) \phi_v,$$

P is the static pressure, x_{abs} is the mole fraction of the absorbing species, S_i (cm^{-2} atm^{-1}) is the transition line strength at the specified temperature T (K) and ϕ_v (cm) is the line-shape function. The line-shape function is approximated using a Voigt profile; a constructed

profile consisting of the convolution of a Lorentz distribution for collisional broadening effects and a Gaussian distribution for Doppler broadening effects.

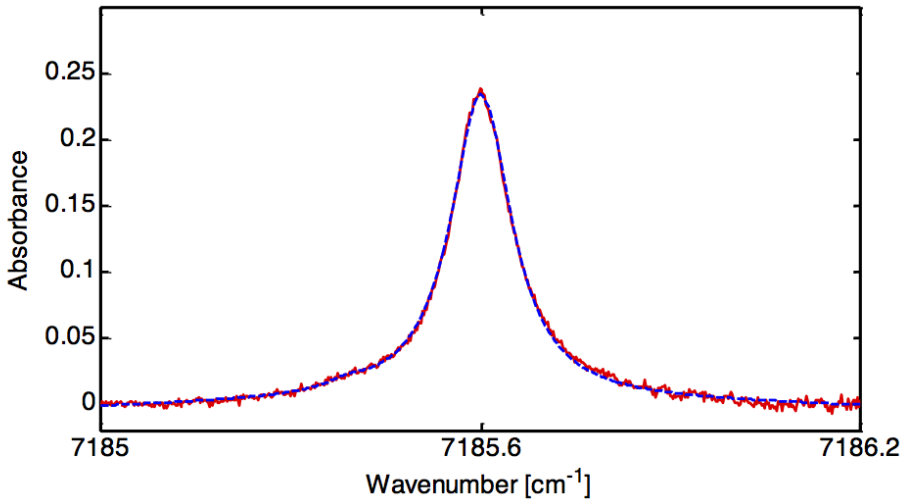

Figure AppA-2: Wavelength scan of the 1391.7 nm laser over the H_2O absorption feature. The measured data (red) is fit with a Voigt lineshape (blue) to ascertain the gas temperature as well as the H_2O concentration.

The line shape function is constructed such that $\int \phi_v \, dv \stackrel{\text{def}}{=} 1$, consequently the integrated absorbance, A_i (cm^{-1}), of the absorption feature can be expressed in the following manner:

$$A_i = -\int ln\left(\frac{I}{I_o}\right)_v \, dv = \int k_v L \, dv = P x_{abs} S_i(T) L \qquad (1)$$

The Voigt fit allows for the accurate quantification of the integrated absorbance area, thereby, enabling determination of the absorbing species mole fraction as well as temperature. The former measurement can be conducted utilizing a single transition at a known temperature T; the latter, however, requires implementation of a two-line thermometry method. This technique is predicated upon the evaluation of the ratio of integrated absorbance for two absorption features: by forming the ratio of A_i for the two transitions we are, in effect, constructing the ratio of line strengths, the other three

variables, namely, P, x_{abs} and L being constant. The line strength, a function of temperature alone, can be evaluated at an arbitrary temperature T through the following relation:

$$S(T) = S(T_o)\frac{Q(T_o)}{Q(T)}\left(\frac{T_o}{T}\right)exp\left[-\frac{hcE''}{k}\left(\frac{1}{T}-\frac{1}{T_o}\right)\right],$$

T_o is a reference temperature where the line strengths are known, $Q(T_o)$ and $Q(T)$ are the species specific rovibronic partition function at reference temperature T_o and experimental temperature T, respectively, h is the Planck constant, c is the speed of light and k is the Boltzmann constant. The ratio of transition line strengths at temperature T can thus be related to known quantities:

$$R = \left(\frac{S_1}{S_2}\right)_T = \left(\frac{S_1}{S_2}\right)_{T_o} exp\left[-\frac{hc(E_2'' - E_1'')}{k}\left(\frac{1}{T}-\frac{1}{T_o}\right)\right],$$

The unknown temperature can then be expressed as follows:

$$T = \frac{\frac{hc}{k}(E_2'' - E_1'')}{ln\,R + ln\frac{S_2(T_o)}{S_1(T_o)} + \frac{hc}{k}\frac{(E_2'' - E_1'')}{T_o}}$$

In addition to the temperature measurement, the water diagnostic was also employed to determine the initial water mole fraction of the bio-aerosol. Rearranging Equation 1 readily yields the following expression:

$$x_{abs} = \frac{1}{P\,S_i(T)\,L}\int -ln\left(\frac{I}{I_o}\right)_v dv$$

As was specified in Chapter 2 the initial water mole fraction during our experiments varied between approximately 3 and 7 percent.

AIII. Determination of laser absorption model coefficients

Determination of the cross section coefficients in Equation 4 and 5 of Part I required the implementation of a series of shock tube experiments. For the 665 nm laser this entailed a sequence of two shock wave tests. A high temperature test was conducted with an initial aerosol loading pressure P*; due to the complete morphological breakdown of endospores at high temperatures, the sustained scattering signal at 665 nm was attributed solely to the scatter from the SiO_2 beads. Utilizing the known visible Mie scattering coefficient, the SiO_2 bead number density for the specific loading conditions was then determined. To quantify the variables related to the intact endospore, a low temperature shock experiment was next conducted with the same loading pressure as the previous experiment, namely, P*. Performing experiments with the same loading pressure ensured that the particle number density was consistent and was critical for the accurate determination of the cross section values. Due to the equality of initial pressures, post-shock temperature was tailored through the variation of diaphragm thickness. Low temperature shock conditions do not induce the breakdown of endospore morphology, therefore, the resulting 665 nm signal includes scattering from both set of particles. For the specific loading condition P*, the silica bead density was known from the high temperature test; employing the known ratio of silica beads to endspores in the suspension the endospore number density value was then determined. Consequently, there reamined one unknown quantity in Equation 4, $\sigma_{Intact\ Spores}$; this coefficient was then calculated from the stable extinction value from the low temperature experiment.

Calculation of the 266 nm coefficients was inherently more complicated due to the presence of the additional term in Equation 5 accounting for laser absorption due to the release of UV active biochemicals. Therefore, to quantitatively assess the cross section values in Equation 5 a series of three experiments was conducted. Due to the fact that endospore lysate absorbs at 266 nm, a high temperature shock would be insufficient for quantifying the silica bead number density. Consequently, a pure SiO_2 suspension was prepared at the same particle concentration as the endospore/SiO_2 test suspension. The former was then aerosolized and introduced into the shock tube to a pressure P*. Extinction data coupled with the calculated Mie scattering coefficient was then used to

establish the number density value. In a similar manner as the 665 nm test, a low temperature shock was then preformed, where the breakdown of endospores was precluded, to determine the parameters relating to the intact endospores. Having established the number density and cross section coefficients for the silica beads and the intact endospores, a third, high temperature shock, resulting in complete endospore breakdown, enabled quantification of the final unknown parameter, namely, $\sigma_{Aromatics}$. As previously stated, all tests were conducted at initial loading pressure P* to ensure consistent particle loading densities.

This series of experiments was systematically designed to produce homogeneous post-shock aerosols (i.e. solely intact endospores, solely destroyed endospores), eliminating specific quantities in the exponential of Equation 4 and 5 and allowing for the quantification of the cross section parameters. Most shock conditions, however, resulted in a bio-aerosol composed of a mixture of intact and ruptured endospores; additionally, varied loading pressures resulted in an experiment specific particle count. Therefore, for each experiment the aforementioned equations were solved for the unknown values of n_i. Noting that the coefficients σ_i have been established, Equation 4 and 5, coupled with the known ratio relating the SiO_2 count to the endospore count, represent three equations for the three unknown number density quantities. Due to the inherent heterogenity of biological samples and the variety of endospore strains employed in our study, endospore suspensions were homogenized after each test and extinction coefficients were recalibrated for each set of experiments.

AIV. Scanning electron microscopy

The scanning electron microscope employed in this study, Hitachi model S-3400N VP, consists of a large analytical chamber with a 5-axis, computer eucentric stage and can be operated in the variable vacuum conditions needed for the analysis of aqueous endospore suspensions. Portions (50 µl) of the impinger samples were filtered through a 0.22 µm cellulose medium, air-dried, and mounted on double-sided carbon tape on aluminum stubs. Additionally, 1 ml of the sample was centrifuged (5,000 rpm for 5 min) to concentrate the collected material, and 50 µl sub-samples were extracted and mounted

as previously detailed. All stubs were thereafter sputter-coated with a 100 Å layer of gold-palladium in a Denton Vacuum Desk II unit. Samples were then visualized with secondary electron detection utilizing the SEM operated under high vacuum at 10 and 15 kV at a working distance of 8-9 mm. Images were captured with a CCD camera.

AV. *B. thuringiensis*-Al Hakam endospore production

Endospores of *B. thuringiensis* Al Hakam were prepared in 0.8% nutrient broth amended with CCY salts. Sterile-filtered, refined olive oil was added as a non-toxic anti-foam to a final concentration of 5%. Sporulation was performed in 333 ml of pre-aerated broth and incubated in shaker/incubators at 34°C, 300 rev min^{-1} for 72 hours. Endospores were pelleted at 2,000 g, 4 ºC for 10 min. Pellets were re-suspended and washed 4 times with sterile-filtered 5% Tween 80, suspended in 33.3 mL of 0.1% Tween 80, and frozen at -80 ºC. Samples were removed at various times after sporulation and heat-treated at 65°C for 30 min to determine viable endospore titers. Samples were serially diluted in 0.1% Tween 80, pH 7, and dilutions were used to inoculate Tryptic Soy Agar (TSA) plates. Plates were incubated for 16 hours at 37 ºC prior to colony counting. Heat-resistant titers for independent endospore preparations ranged from 2.3 - $8.9x10^9$ spores per ml after cold storage. Light microscopy showed 80-95% phase-bright endospores with the remainder being dead, decaying vegetative cells.

This protocol was obtained from Dr. Tony Buhr at the Naval Surface Warfare Center – Dahlgren.

Appendix B: Part II: AFM/NanoSIMS protocols and considerations

BI. Atomic force microscopy

1 µl droplets of vaccinia virus suspension, or chemically and enzymatically treated samples thereof, were deposited onto glass substrates and allowed to air dry. The sample surface was subsequently rinsed with double-distilled water and dried with a stream of nitrogen gas. To ensure viral adhesion the glass substrates were treated with polylysine prior to viral plating. AFM images were collected with a Digital Instruments Multimode Nanoscope IV atomic force microscope (Veeco Instruments, Santa Barbara, CA.) operated in tapping mode. Silicon AFM probes with a force constant of 10 – 130 N/m were employed at tapping frequencies of 200 – 500 kHz for high-resolution image acquisition. For large scale scans, greater than approximately 20 µm x 20 µm, low resolution tips with a force constant of 1-5 N/m were employed at tapping frequencies of 150-250 kHz. Other AFM experimental procedures and operating parameters were as described in Plomp et al[20].

BII. Vaccinia virus: Growth procedures and viral degradation protocols

Vaccinia virus growth and purification

The vaccinia viral suspensions employed in the current study were obtained from the laboratory of Dr. Richard Condit at the University of Florida. The virus was grown in BSC-40 cells, an African green monkey kidney cell line. Cells were maintained at 37 ^{o}C in 5% CO_2 in the presence of Dulbecco's Modified Eagle's medium containing 10% fetal bovine serum, 0.12 mg/ml penicillin, 0.2 mg/ml streptomycin and 250 mg/l fungizone[72]. Vaccinia virus strain WR was maintained as described previously[72].

Virus purification was done as described previously[73]. Infected cells were harvested by centrifugation at 3,000 x g at 4 ºC, re-suspended in 3 ml of 10 mM Tris-

HCl, pH 8.0, and frozen at -80 ºC. All subsequent steps were carried out at 4 ºC in a buffer containing 10 mM Tris HCl, pH 8.0. The cell suspension was thawed, then disrupted by Dounce homogenization and the nuclear fraction was separated by centrifugation at 900 x g for 10 min. The post nuclear supernatant was saved and the nuclear pellet re-suspended in 3 ml, re-extracted by Dounce homogenization and centrifuged as described above. The supernatant was removed, combined with the previous supernatant, layered on a 6 ml cushion of 36% sucrose, and centrifuged in a Beckman SW41 rotor at 19,000 rpm for 80 min. The pellet was re-suspended in 1 ml, sonicated 3 times for 30 seconds each time, layered on a 10.5 ml 24–40% sucrose gradient, and centrifuged in an SW41 rotor at 14,000 rpm for 40 min. A visible band in the middle of the tube was collected in a volume of approximately 4 ml, diluted to 12 ml and centrifuged in an SW41 rotor at 16,000 rpm for 60 min. Virus pellets were re-suspended in 300 µl and virus concentrations determined by measuring light scattering at $OD_{260\ nm}$ (1 U $OD_{260\ nm}$ = $1.2x10^{10}$ particles/ml). In some preparations the virus pellet was washed 3 times by re-suspending the pellet in 750 µl of water, centrifuging at 14,000 x g for 10 min. in an Eppendorf microfuge and finally re-suspended in 300 µl of water.

The vaccinia virus growth and purification protocol was obtained from Dr. Nissin Moussatche at the University of Florida.

Protocols for the systematic degradation of the viral particle

The initial stage of the virion degradation process required the removal of the exterior lipid membrane and the generation of viral cores. This process was done by exposing the viral suspension to a multitude of chemical and enzymatic agents in the following manner:

1. Produce 5x core buffer with final concentrations:
    a. Tris HCl pH 8.0 – 250 mM
    b. Dithiothreitol (DTT) – 250 mM
    c. Tergitol-type NP-40 – 2.5%
2. Add 5x core buffer to viral suspension to achieve final concentrations of:

a. Tris HCl pH 8.0 – 50 mM
b. Dithiothreitol (DTT) – 50 mM
c. Tergitol-type NP-40 – .5%

4. Incubate subsequent suspension for one hour at 37ºC. Vortex suspension every 10 minutes.
5. Centrifuge suspension for 5 min. at maximum speed in an Eppendorf centrifuge.
6. Remove supernatant.
7. Re-suspend virion pellet in 10mM Tris HCl or ddH_2O.

Continued viral particle degradation was done through the exposure of the virion core suspension to varying levels of proteinase K. To achieve the targeted final enzyme concentration appropriate quantities of stock solutions of proteinase K were added directly to the core suspension and allowed to incubate. Various proteinase K concentrations and incubation time durations were employed throughout this work; specific quantities are detailed in the text. After treatment with proteinase K the resulting suspension was directly plated for AFM imaging.

DNase treatment

Exposure of viral sub-structures to the DNase enzyme required direct application of the reagent to the imaging surface. The protocol implemented for these experiments was as follows:

1. Produce 1x buffer by mixing 1 µl of 10x DNase buffer with 9 µl ddH_2O.
2. Conduct control experiment - Expose viral sample to 2 µl of 1x buffer and incubate for 20 minutes at 37 ºC. Wash sample with ddH_2O and image region to confirm nucleoprotein structures have not been affected.
3. Produce DNase solution with the desired final concentration by mixing enzyme solution with buffer solution.
4. Expose viral sample to reagent and incubate for 20 minutes at 37 ºC. Wash sample with ddH_2O.
5. Expose region to 1 µl of 30 mM EDTA and incubate for 20 minutes at 37 ºC. Wash sample with ddH_2O.

6. Image with AFM.

As with the proteinase K treatment, a variety of DNase concentrations were implemented during the course of this work. The specific concentrations utilized are detailed in the relevant sections of the text.

Chemical Fixation

Chemical fixation of the vaccinia virus particles was achieved by exposing a virion suspension to a solution of McDowell Trumps Fixative. The fixative solution contained: 10% Formalin (37%), 4% Glutaraldehyde, 1.16% NaH_2PO_4, 0.27% NaOH and was diluted to 1:20 (final concentration) for the experiments detailed herein. The resulting suspension was incubated for 20 minutes at 37 ºC and plated as previously specified for AFM imaging.

BIII. NanoSIMS: experimental parameters and considerations

Viral samples were plated on 5 mm x 5 mm silicon wafers etched with identifying markers for AFM/NanoSIMS mapping purposes. SIMS analysis was performed using the NanoSIMS 50 (Cameca Instruments, Geneviers, France) operated in simultaneous secondary ion measurement mode. The cesium ions were accelerated to an energy of 16 keV and focused with ion optics for sample analysis. Analysis was conducted with a 0.3 – 2.98 pA Cs+ primary ion beam scanned over the sample in a 256 x 256 or 512 x 512 pixel raster configuration. Ion beam dwell time was .5 ms/pixel or 1 ms/pixel and raster sizes varied from 1 μm^2 to 100 μm^2. Samples were evacuated to ultra-high vacuum conditions prior to analysis (1 x 10^{-10} torr). Quantitative image data was generated using custom software (LIMAGE, L.R. Nittler) and were corrected for image shift during analysis as well as detector dead time.

Prior to analysis some viral samples were sputter coated with a conductive film of iridium to minimize surface charging and non-equilibrium sputtering. Experiments conducted with coated and non-coated virions, however, indicated analogous qualitative and quantitative sputtering profiles. Furthermore, the addition of the metallic coating

complicated depth profile analysis due to the re-deposition of the iridium during or after the sputtering process. An example of this phenomenon can be seen in the following figure.

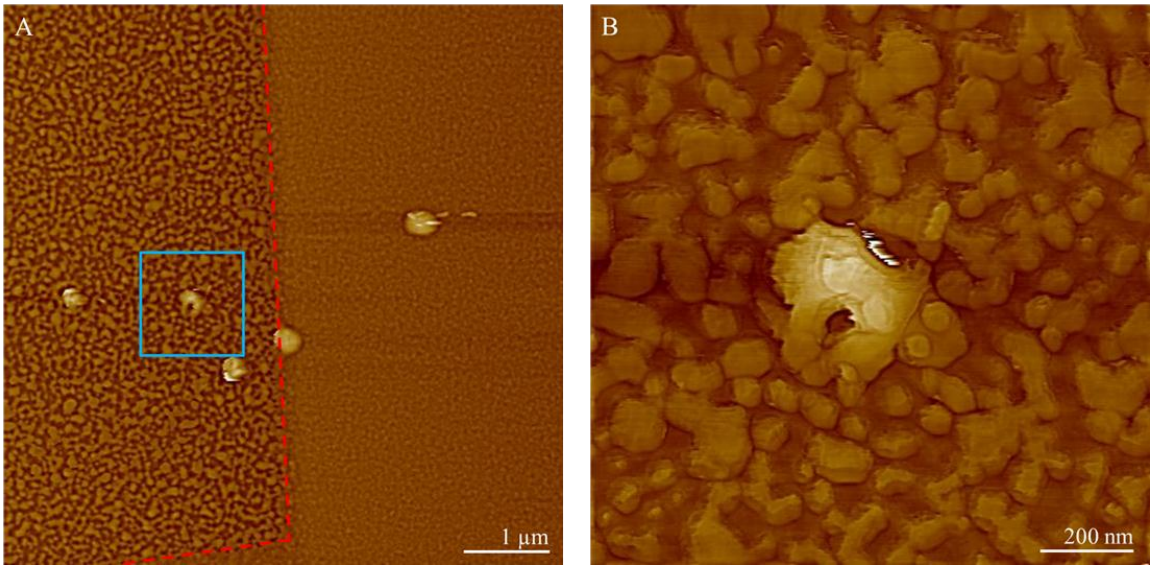

Figure AppB-1: AFM images of a NanoSIMS analyzed region from a viral sample sputter coated with iridium. The region exposed to the cesium ion beam is on the left of the red dashed line in image A. Image B is a high resolution scan of the region framed by the blue square in image A. The presence of iridium conglomerations on the surface is readily apparent. In addition, the iridium appears to have been re-deposited on the viral particle itself.

The formation of extensive iridium surface features was observed after NanoSIMS analysis and can be clearly seen in the region to the left of the dashed line in Figure AppB-1A. Furthermore, the iridium re-deposition process was not secluded to surface regions, viral particles within the analyzed region were observed to be closely associated with the conglomerations (Figure AppB-1B). Numerous virions displayed increases in height after sputtering analysis due to the iridium deposition process. Consequently, accurate quantification of the rate of particle sputtering was precluded within this experimental framework. Sputter rate analysis was, therefore, conducted with non-coated viral samples. The difference in surface morphology after NanoSIMS analysis

between the coated and non-coated samples can be seen by comparing the AFM images in the figure above with those in Figures 9-3 and 9-4 in the main body of the text.

An additional experimental issue that was observed during the course of this work was the development of ion beam induced surface damage outside the specified region of analysis. This phenomenon can be observed in the following light microscope image of a NanoSIMS analyzed area (Figure AppB-2). The blue squares denote regions used for ion beam tuning and were, therefore, exposed to the cesium beam for short times (~100 seconds). The majority of the regions framed in red, however, were analyzed for significantly longer periods. The presence of lighter regions surrounding the analyzed areas is indicative of ion damage caused by surface bombardment. Even with a highly focused ion beam then, residual damage to the surrounding region outside of the specified analysis area was incurred. Consequently, viral particles near a previously analyzed region would have been exposed to a non-negligible level of erosion due to cesium bombardment. Interrogated regions were therefore selected at a sufficient distance from each other to minimize extraneous particle damage due to ion beam divergence.

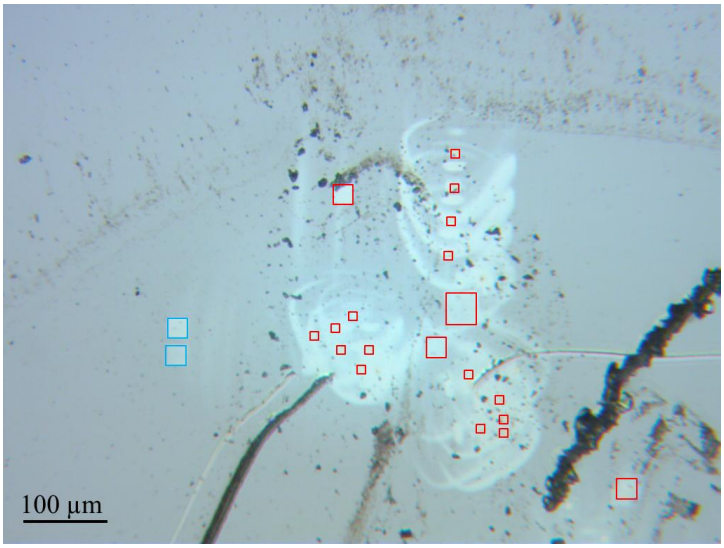

Figure AppB-2: Light microscope image of NanoSIMS analyzed region. Blue squares denote regions used for tuning. Red squares indicate areas used for depth profile analysis. The presence of lighter regions surrounding the analyzed areas is indicative of ion damage. The large abrasions apparent in the silicon surface are the aforementioned etchings used for AFM and NanoSIMS mapping purposes.

BIV. AFM viral particle profiles

The images displayed below are AFM generated viral particle profiles illustrating specific stages in the sputtering process. The profiles correspond to the AFM images shown in Figure 9-11 of the text.

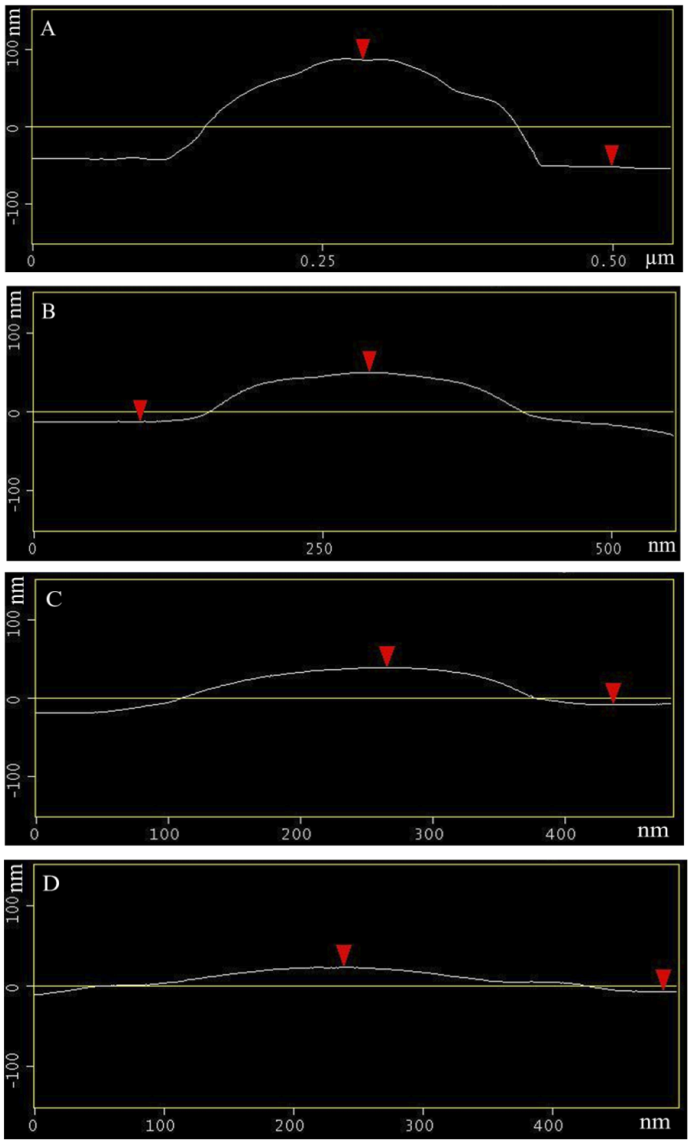

Figure AppB-3: Viral particle profiles at sequential stages of the sputtering process. Heights were measured as followed 130 nm (A), 71 nm (B), 52 nm (C) and 32 nm (D). Due to substrate erosion during the analysis height measurements were referenced to non-scanned sample regions. The profiles correspond to the AFM images shown in Figure 9-11.

BV. Sputtering of chemically fixed viral particles

A series of sputtering experiments was conducted with chemically fixed virions in order to assess the change in viral particle height as a function of sputter time. The viral sample was analyzed with both the NanoSIMS and the FIB and quantitative height measurements were subsequently generated with atomic force microscopy. The results are shown in Figure AppB-4.

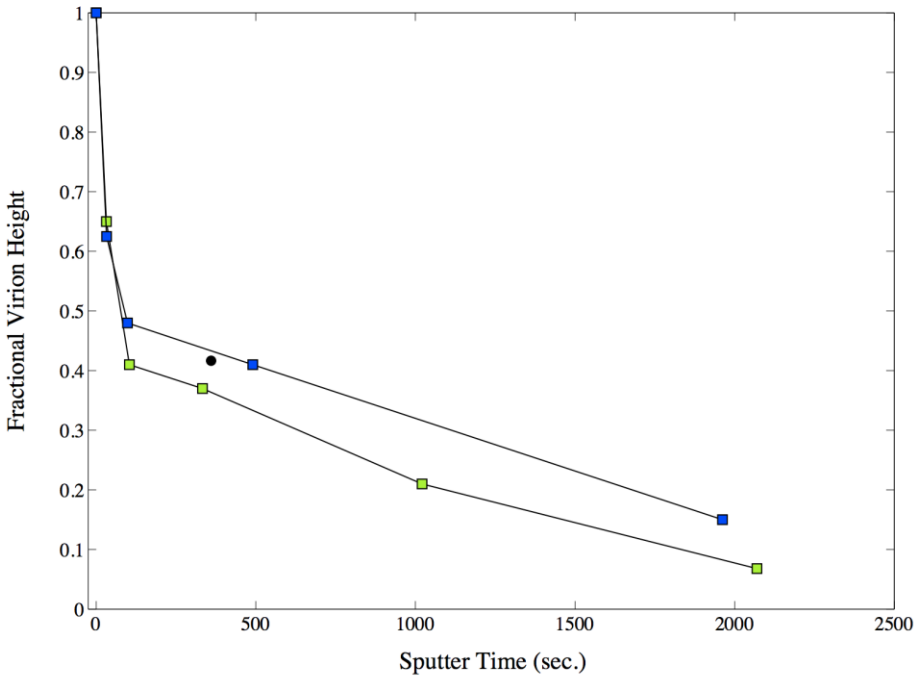

Figure AppB-4: Viral particle height change as a function of sputter time. Blue squares indicate fixed virions exposed to a 2.6 pA cesium beam. Green squares indicate non-fixed virions exposed to 2.98 pA cesium beam. Black dot is a data point from the FIB analysis of fixed virions with a 3.4 pA gallium beam.

Three sets of data are illustrated: non-fixed virions analyzed with a 2.98 pA cesium incident beam (green squares), fixed virions analyzed with a 2.6 pA cesium incident beam (blue squares) and fixed virions analyzed with a 3.4 pA gallium incident beam (black dot). The former two experiments were conducted with the NanoSIMS; the latter with the FIB. As detailed in the body of the current manuscript, the results indicate

a consistent demarcation of the data into two distinct sputtering regions: an initial non-equilibrium regime characterized by rapid time dependent erosion and an equilibrium region exhibiting a significantly slower rate of constant erosion. In addition, the quantitative aspects of the data, namely, the fact that analysis with the 2.98 pA cesium beam results in reduced particle heights as compared to the 2.6 pA cesium beam, are consistent. Therefore, the fixation process does not appear to affect the viral particle sputtering process.

BVI. ^{13}C and ^{15}N isotopic labeling procedure

^{13}C fatty acid labeling

Three confluent monolayers of BSC-40 cells in 100 mm dishes were sub-cultured into six 150 mm dishes and grown for 3 days to near confluency in ^{13}C labeling medium (9% lipid reduced fetal bovine serum), 1% fetal bovine serum, and 215 µM ^{13}C fatty acid mixture (4:1:28 mass ratio UL-^{13}C- algal fatty acids/^{13}C-stearic acid/fatty acid-free BSA). The ^{13}C fatty acid mixture was replenished twice at 24 and 48 hr. after sub-culturing. To infect the cells, the medium was removed and 4 ml of virus inoculum was added per dish to achieve a multiplicity of infection of 1. After a 45 min adsorption period, the inoculum was removed and fresh ^{13}C labeling medium was added. Infected cells were incubated for 48 hr. at which time complete cytopathic effect was observed.

^{15}N thymidine labeling

Six 150 mm confluent monolayers of BSC-40 cells were infected with virus at a multiplicity of infection of 1 and incubated in medium supplemented with 30 ug/ml ^{15}N labeled thymidine for 48 hr. at which time complete cytopathic effect was observed.

The vaccinia virus ^{13}C and ^{15}N labeling protocol was obtained from Dr. Nissin Moussatche at the University of Florida.

BVII. Extraction method for vaccinia virus components

Liquid-liquid extraction was used to separate virus proteins, nucleic acids, and lipids. Virus stocks of known concentrations were suspended in a minimum volume of 200 µL of TE buffer, pH 8.0 and an equal volume of 1% (w/v) SDS. The vaccinia virus was then heat-inactivated at 100 °C for 10 minutes. After cooling, 200 µL of 1:1 (v/v) phenol:chloroform was added to the inactivated virus, and the mixture was vortex mixed for 10 seconds followed by centrifugation for 5 minutes at room temperature at maximum speed in a benchtop microcentrifuge. The upper, aqueous phase containing DNA was carefully removed and transferred to a fresh tube, after which the aqueous phase was re-extracted with an equal volume of 1:1 phenol:chloroform. The extract was centrifuged, and the aqueous phase was again collected and transferred to a fresh tube and the organic phases from both extractions were pooled. The pooled organic phase was extracted with 100 µL of TE buffer, pH 8.0, and the aqueous phase was collected and pooled with the previous aqueous phase.

DNA extraction was performed by addition of 1:10 volume of 3 M sodium acetate, pH 5.2, to the pooled aqueous phases. The mixture was vortexed briefly, followed by addition of 2 volumes of ice-cold 100% ethanol. Mixing was performed by gentle inversion, after which tubes were incubated in a -70 °C freezer for 15 minutes. Tubes were then centrifuged for 5 minutes at maximum speed, after which the supernatant was carefully removed, leaving a DNA pellet. DNA pellets were washed with 1 mL of room-temperature 70% ethanol followed by centrifugation. After removal of the supernatant, pellets were air-dried for 10 minutes and re-suspended in water.

Protein and lipid extractions were accomplished by addition of 200 µL chloroform to the pooled organic phase, which was then vortex-mixed for 30 seconds and centrifuged at maximum speed for 5 minutes. The protein fraction formed a disc at the top of the organic phase, and lipids partitioned to the organic phase. The lower organic phase was carefully removed from the protein disc, and transferred to a fresh tube. Solvent was removed from protein and lipid fractions by rotary vacuum extraction. SDS was removed from protein fractions by re-extracting three times with 400 µL water and passing through a 10 kDa molecular weight centrifugal filter. The filter was then washed

and protein was re-suspended in water. The lipid-containing organic extract was extracted three times with water to remove residual SDS. Lipid was then re-suspended in 100% ethanol. Protein and DNA quantitation was performed using a NanoDrop ND-1000 spectrophotometer (NanoDrop Products, Wilmington, DE), and DNA purity was assessed using the 260/280 absorbance ratio.

The vaccinia virus component extraction protocol was obtained from Dr. Benjamin Stewart at Lawrence Livermore National Laboratory.

Bibliography

Part I

1. Errington, J. (2003) Regulation of endospore formation in Bacillus subtilis. Nature Rev. Microbiol. 1: 117-126.

2. Nicholson, W.L., and Setlow, P. (1990) Sporulation, germination, and outgrowth, p. 391-450. In Molecular biological methods for Bacillus, (ed.) Harwood, C.R., and Cutting, S.M. John Wiley and Sons, Sussex, England.

3. Nicholson, W. L., Munakata, N., Horneck, G., Melosh, H. J., and Setlow, P. (2000) Resistance of Bacillus endospores to extreme terrestrial and extraterrestrial environments. Microbiol. Mol. Biol. Rev. 64: 548-572.

4. Setlow, B., Loshon C.A., Genest, P.C., Cowan A.E., Setlow C. and Setlow P. (2002) Mechanisms of killing of spores of Bacillus subtilis by acid, alkali and ethanol. J. of Appl. Microbiol. 92: 362-375.

5. Setlow, P. (2006) Spores of Bacillus subtilis: their resistance to and killing by radiation, heat and chemicals. J. of Appl. Microbiol. 101: 514-525.

6. Melly, E., Cowan A.E., and Setlow P. (2002) Studies on the mechanism of killing of Bacillus subtilis spores by hydrogen peroxide. J. of Appl. Microbiol. 93: 316-325.

7. Coleman, W.H., Chen, D., Li, Y.Q., Cowan A.E. and Setlow, P. (2007) How moist heat kills spores of Bacillus subtilis. J. of Bacteriol. 189: 8458-8466.

8. Atrih, A., and Foster, S. J. (2001) Analysis of the role of bacterial endospore cortex structure in resistance properties and demonstration of its conservation amongst species. J. Appl. Microbiol. 91: 364-372.

9. Setlow, B., and Setlow, P. (1995) Small, acid-soluble spore proteins bound to DNA protect Bacillus subtilis spores from killing by dry heat. Appl. Environ. Microbiol. 61: 2787-2790.

10. Setlow, P. (1995) Mechanisms for the prevention of damage to DNA in spores of Bacillus species. Ann. Rev. Microbiol. 49: 29-54.

11. Sliemandagger, TA., and Nicholson, WL. (2001) Role of dipicolinic acid in survival of Bacillus subtilis spores exposed to artificial and solar UV radiation. Appl. Environ. Microbiol. 67: 1274-1279.

12. Gaydon, A.G., and Hurle, I.R. (1963) The Shock Tube in High Temperature Chemical Physics. Chapman and Hall, London.

13. Bradley, J. (1962) Shock Waves in Chemistry and Physics. Chapman and Hall, London.

14. Davidson, D.F., Haylett D.R., and Hanson R.K. (2008) Development of an aerosol shock tube for kinetic studies of low-vapor-pressure fuels. Combust. Flame 155: 108-117.

15. Vasudevan, V., Davidson, D. F., & Hanson, R. K. (2005) Shock tube measurements of toluene ignition times and OH concentration time histories. P. Combust. Inst. 30: 1155-1163.

16. Herbon, J. T., Hanson, R. K., Golden, D. M., and Bowman, C. T. (2002) A shock tube study of the enthalpy of formation of OH. P. Combust. Inst. 29: 1201-1208.

17. Liepmann, H.W., and Roshko A. (1957) Elements of Gasdynamics. John Wiley, New York.

18. Emanuel, G. (2001) Shock Waves in Gases. In Handbook of Shock Waves: Volume 1, (ed.) Ben-Dor, G., Igra, O. and Elperin, T. Academic Press, San Diego, Ca.

19. Farooq, A., Jeffries, J. B., and Hanson, R. K. (2009) Sensitive detection of temperature behind reflected shock waves using wavelength modulation spectroscopy of CO_2 near 2.7 μm. Appl. Phys. B 96: 161-173.

20. Marble, F. E. (1970) Dynamics of dusty gases. Annu. Rev. Fluid Mech. 2: 397-446.

21. Prabhu, N. V., and Sharp, K. A. (2005) Heat capacity in proteins. Annu. Rev. Phys. Chem. 56: 521-548.

22. Landau, L. D., and Lifshitz, E. M. (1963) Course of Theoretical Physics: Vol.: 6: Fluid Mechanics. Pergamon Press, Tarrytown, New York.

23. McCartt, A. D., Gates, S., Lappas, P., Jeffries, J. B., and Hanson, R. K. (2012) In situ optical measurements of bacterial endospore breakdown in a shock tube. Appl. Phys. B 106: 769-774.

24. Hanson, R.K. (2011) Applications of quantitative laser sensors to kinetics, propulsion and practical energy systems. P. Combust. Instit. 33: 1-40.

25. Davidson, D.F. and Hanson R.K., (2001) Spectroscopic Diagnostics. In Handbook of Shock Waves: Volume 1, (ed.) Ben-Dor, G., Igra, O. and Elperin, T. Academic Press, San Diego, Ca.

26. Baer, D.S., Nagali, V., Furlong, E.R., Hanson R.K. and Newfield, M.E. (1996) Scanned- and fixed-wavelength absorption diagnostics for combustion measurements using multiplexed diode-laser sensor system. AIAA J. 34: 489-493.

27. Campbell, M.F., Haylett, D.R., Davidson D.R. and Hanson, R.K. AEROFROSH: A chemically frozen ideal gas shock condition calculator for aerosol-laden flows. Unpublished manuscript.

28. Mallidis, C. G., & Scholefield, J. (2008) The release of dipicolinic acid during heating and its relation to the heat destruction of Bacillus stearothermophilus spores. J. Appl. Microbiol. 5: 479-486.

29. Tuminello, P. S., Arakawa, E. T., Khare, B. N., Wrobel, J. M., Querry, M. R., and Milham, M. E. (1997) Optical properties of Bacillus subtilis spores from 0.2 to 2.5 μm. Appl. Opt. 36: 2818-2824.

30. Goodacre, R., et al. (2000) Detection of the dipicolinic acid biomarker in Bacillus spores using Curie-point pyrolysis mass spectrometry and Fourier transform infrared spectroscopy. Anal. Chem. 72: 119-127.

31. Nicoletti, I., Migliorati, G., Pagliacci, M. C., Grignani, F., and Riccardi, C. (1991) A rapid and simple method for measuring thymocyte apoptosis by propidium iodide staining and flow cytometry. J. Immun. Methods 139: 271-279.

32. Lyons, A. B., and Parish, C. R. (1994) Determination of lymphocyte division by flow cytometry. J. Immun. Methods 171: 131-137.

33. Hedley, D. W., Friedlander, M. L., Taylor, I. W., Rugg, C. A., and Musgrove, E. A. (1983) Method for analysis of cellular DNA content of paraffin-embedded

pathological material using flow cytometry. J. Histochem. Cytochem., 31: 1333-1335.

34. Riccardi, C., and Nicoletti, I. (2006) Analysis of apoptosis by propidium iodide staining and flow cytometry. Nat. Protoc. 1: 1458-1461.

35. Suzuki, T., Fujikura, K., Higashiyama, T., and Takata, K. (1997) DNA staining for fluorescence and laser confocal microscopy. J. Histochem. Cytochem. 45: 49-53.

36. Klobutcher, L.A., Ragkousi, K. and Setlow, P. (2006) The Bacillus subtilis spore coat provides "eat resistance" during phagosomal predation by the protozoan Tetrahymena thermophila. Proc. Natl. Acad. Sci. USA 103: 165-170.

37. Sislian, P.R., Zhang, X., Li, M., Pham, D., Madler, L. and Christofides, P.D., (2009) Bacterial aerosol neutralization by aerodynamic shocks using a novel impactor system: design and computation. Chem. Engin. Sci. 64: 1953-1967.

38. Moeller, R., Horneck, G., Rabbow, E., Reitz, G., Meyer, C., Hornemann, U., and Stöffler, D. (2008) Resistance of Bacillus subtilis spores to ultra-high shock pressures simulating hypervelocity impacts: role of DNA protection and repair. Appl. Environ. Microbiol. 74: 6682-6689.

39. Margosch, D., Gänzle, M. G., Ehrmann, M. A., and Vogel, R. F. (2004) Pressure inactivation of Bacillus endospores. Appl. Environ. Microbiol. 70: 7321-7328.

40. Gates, S. D., McCartt, A. D., Jeffries, J. B., Hanson, R. K., Hokama, L. A., and Mortelmans, K. E. (2011) Extension of Bacillus endospore gas dynamic heating studies to multiple species and test conditions. J. Appl. Microbiol. 111: 925-931.

41. Han, C.S. et al. (2006) The pathogenomic sequence analysis of Bacillus cereus and Bacillus thuringiensis isolates closely related to Bacillus anthracis. J. Bacteriol. 188: 3382-3390.

42. Hoffmaster, A.R., K.K. Hill, J.E. Gee, C.K. Marston, B.K. De, T. Popovic, D. Sue, P.P. Wilkins, S.B. Avashia, R. Drumgoole, C.H. Helma, L.O. Ticknor, R.T. Okinaka, and P.J. Jackson (2006) Characterization of Bacillus cereus isolates associated with fatal pneumonias: strains are closely related to Bacillus anthracis and harbor B. anthracis virulence genes. J. Clin. Microbiol. 44: 3352-3360.

43. Plomp, M., Leighton, T. J., Wheeler, K. E., and Malkin, A. J. (2005) Architecture and high-resolution structure of Bacillus thuringiensis and Bacillus cereus spore coat surfaces. Langmuir 21: 7892-7898.

44. McCartt, A. D., Gates, S. D., Jeffries, J. B., Hanson, R. K., Joubert, L. M., and Buhr, T. L. (2011) Response of Bacillus thuringiensis Al Hakam endospores to gas dynamic heating in a shock tube. Z. Phys. Chem. 225: 1367-1377.

45. Buhr, T., McPherson, D.C., and Gutting, B.W. (2008) Analysis of broth-cultured Bacillus atrophaeus and Bacillus cereus spores. J. Appl. Microbiol. 105: 1604-1613.

46. Haylett, D. R., Davidson, D. F., and Hanson, R. K. (2012) Second-generation aerosol shock tube: an improved design. Shock Waves 22: 483-493.

47. Harwood, C.R. and Cutting S.M., (ed.) (1990) Molecular biological methods for Bacillus. Chichester: John Wiley & Sons.

Part II

1. Moss, B. (2001) Poxviridae and their replication, p. 2849-2883. Fields virology, 4th ed., vol. 2., (ed.) Knipe, D.M., and Howley, P.M., Lippincott Williams and Wilkins, Philadelphia, Pa.

2. Moss, B. (1991) Vaccinia virus: a tool for research and vaccine development. Science 252:1662-1667.

3. Kieny, M.P., Lathe, R., Drillien, R., et al. (1984) Expression of rabies virus glycoprotein from a recombinant vaccinia virus. Nature 312:163-166.

4. Smith, G.L., Mackett, M. and Moss, B. (1983) Infectious vaccinia virus recombinants that express hepatitis B virus surface antigen. Nature 302:490-495.

5. Smith, G.L., Murphy, B.R., Moss, B. (1983) Construction and characterization of an infectious vaccinia virus recombinant that expresses the influenza hemagglutinin gene and induces resistance to influenza virus infection in hamsters. Proc. Natl. Acad. Sci. USA 80: 7155-7159.

6. Harrison, S.C. et al. (2004) Discovery of antivirals against smallpox. Proc. Natl. Acad. Sci. USA 101: 11178-11192.

7. Mercer, J., and Helenius, A. (2009) Virus entry by macropinocytosis. Nat. Cell Biol. 11: 510-520.

8. Mercer, J., Helenius, A. (2008) Vaccinia virus uses macropinocytosis and apoptotic mimicry to enter host cells. Science 320:531-535.

9. Cyrklaff, M. et al. (2005) Cyro-electron tomography of vaccinia virus. Proc. Natl. Acad. Sci. USA 102: 2772-2777.

10. Griffiths, G., Roos, N., Schleich, S., and Krijne-Locker, J. (2001) Structure and assembly of intracellular mature vaccinia virus: thin-section analysis. J. Virol. 75: 11056-11070.

11. Griffiths, G., Wepf, R., Wendt, R., Krijnse-Locker, J., Cyrklaff, M. and Roos, N. (2001) Structure and assembly of intracellular mature vaccinia virus: isolated-particle analysis. J. Virol. 75:11034-11055.

12. Chlanda P., Carbajal, M.A., Cyrklaff M., Griffiths G., Krijnse-Locker J. (2009) Membrane rupture generates single open membrane sheets during vaccinia virus assembly. Cell Host Microbe 6:81-90.

13. Condit, R.C., Moussatche, N., Traktman, P. (2006) In a nutshell: structure and assembly of the vaccinia virion. Adv. Virus Res. 66:31-124.

14. Dubochet, J., M. Adrian, K. Richter, J. Garces, and R. Wittek. (1994) Structure of intracellular mature vaccinia virus observed by cryoelectron microscopy. J. Virol. 68:1935-1941.

15. Easterbrook, K.B. (1966) Controlled degradation of vaccinia virions in vitro: an electron microscopy study. J. Ultrastruct. Res. 14:484-496.

16. Medzon, E. L., and Bauer, H. (1970) Structural features of vaccinia virus revealed by negative staining, sectioning, and freeze-etching. Virology 40:860-867.

17. Baker, T.S., N.H. Olson, and S.D. Fuller. (1999) Adding the third dimension to virus life cycles: three-dimensional reconstruction of icosahedral viruses from cyro-electron micrographs. Microbol. Mol. Biol. Rev. 63:862-922.

18. Kuznetsov, Y., Gershon P.D., and McPherson A. (2008) Atomic force microscopy investigation of vaccinia virus structure. J. Virol. 82:7551-7566.

19. Malkin, A.J., McPherson A., and Gershon P.D. (2003) Structure of intracellular mature vaccinia virus visualized by in situ atomic force microscopy. J. Virol. 77:6332-6340.

20. Plomp, M., Rice M.K., Wagner E.A., McPherson A., and Malkin A.J. (2002) Rapid visualization at high resolution of pathogens by atomic force microscopy: structural studies of herpes simplex virus-1. Am. J. Pathol. 160:1959-1966.

21. Mallardo, M., Schleich, S., and Locker, J. K. (2001) Microtubule-dependent organization of vaccinia virus core–derived early mRNAs into distinct cytoplasmic structures. Mol. Biol. Cell 12: 3875-3891.

22. Kates, J., and Beeson, J. (1970) Ribonucleic acid synthesis in vaccinia virus: I. The mechanism of synthesis and release of RNA in vaccinia cores. J. Mol. Biol. 50: 1-18.

23. Fenner, F., Wittek, R., and Dumbell, K.R. (1989) The orthopoxviruses. Academic Press, Inc., New York, N.Y.

24. Soloski, M. J., Cabrera, C. V., Estevan, M., and Holowczak, J. A. (1979) Studies concerning the structure and organization of the vaccinia virus nucleoid: I. Isolation and characterization of subviral particles prepared by treating virions with guanidine-HCI, nonidet-P40, and 2-mercaptoethanol. Virology 99: 209-217.

25. Holowczak, J. A. (1982) Poxvirus DNA. Curr. Top. Microbial. Immunol. 97: 27-79.

26. Sekiguchi, J., Seeman, N. C., and Shuman, S. (1996) Resolution of Holliday junctions by eukaryotic DNA topoisomerase I. Proc. Natl. Acad. Sci. USA 93: 785-789.

27. Shuman, S., and Moss, B. (1987) Identification of a vaccinia virus gene encoding a type I DNA topoisomerase. Proc. Natl. Acad. of Sci. USA 84: 7478-7482.

28. Shuman, S., Golder, M., and Moss, B. (1989) Insertional mutagenesis of the vaccinia virus gene encoding a type I DNA topoisomerase: evidence that the gene is essential for virus growth. Virology 170: 302-306.

29. Hollinshead, M., Vanderplasschen, A., Smith, G. L., and Vaux, D. J., (1999) Vaccinia virus intracellular mature virions contain only one lipid membrane. J.Virol. 73: 1503-1517.

30. Boxer, S.G., Kraft, M.L., and Weber, P.K. (2009) Advances in imaging secondary ion mass spectrometry for biological samples. Annu. Rev. Biophys. 38:53-74.

31. Audinot J.N., Guignard C., Migeon H.N., and Hoffmann L. (2006) Study of the mechanism of diatom cell division by means of Si-29 isotope tracing. Appl. Surf. Sci. 252:6813–15.

32. Behrens S., Losekann T., Pett-Ridge J., Weber P.K., Ng W.O., et al. (2008) Linking microbial phylogeny to metabolic activity at the single-cell level by using enhanced element labeling-catalyzed reporter deposition fluorescence in situ hybridization (EL-FISH) and NanoSIMS. Appl. Environ. Microbiol. 74:3143–50.

33. Li T, Wu TD, Mazeas L, Toffin L, Guerquin-Kern JL, et al. (2008) Simultaneous analysis of microbial identity and function using NanoSIMS. Environ. Microbiol. 10:580–88.

34. Musat N, Halm H,Winterholler B, Hoppe P, Peduzzi S, et al. (2008) A single-cell view on the ecophysiology of anaerobic phototrophic bacteria. Proc. Natl. Acad. Sci. USA 105:17861–66.

35. Orphan V.J., House C.H., Hinrichs K.U., McKeegan K.D., and DeLong E.F. (2001) Methane-consuming Archaea revealed by directly coupled isotopic and phylogenetic analysis. Science 293:484–87.

36. Kleinfeld A.M., Kampf J.P., Lechene C. (2004) Transport of 13C-oleate in adipocytes measured using multi imaging mass spectrometry. J. Am. Soc. Mass Spectrom. 15:1572–80.

37. Lechene C.P., Luyten Y., McMahon G., Distel D.L. (2007) Quantitative imaging of nitrogen fixation within animal cells. Science 317:1563–66.

38. Lechene C., Hillion F., McMahon G., Benson D., Kleinfeld A.M., et al. (2006) High-resolution quantitative imaging of mammalian and bacterial cells using stable isotope mass spectrometry. J. Biol. 5:20.1–20.30.

39. Kraft M.L.,Weber P.K., Longo M.L., Hutcheon I.D., and Boxer S.G. (2006) Phase-separation of lipid membranes analyzed with high-resolution secondary ion mass spectrometry. Science 313:1948–51.

40. Fletcher, J. S., Lockyer, N. P., Vaidyanathan, S., and Vickerman, J. C. (2007) TOF-SIMS 3D biomolecular imaging of Xenopus laevis oocytes using buckminsterfullerene (C60) primary ions. Anal. Chem. 79: 2199-2206.

41. Ghosal S., Fallon S.J., Leighton T., Wheeler K.E., Hutcheon I.D., and Weber P.K. (2008) Imaging and 3D elemental characterization of intact bacterial spores with high-resolution secondary ion mass spectrometry (NanoSIMS) depth profile analysis. Anal. Chem. 80: 5986–92.

42. Hillion F., Daigne B., Girard F., and Slodzian G. (1993) A new high performance instrument: the CAMECA NanoSIMS 50. In Secondary Ion Mass Spectrometry: SIMS IX, (ed.) A Benninghoven, Y Nihei, R Shimizu, HW Werner, pp. 254–57. New York: Wiley.

43. Yu, M.L. (1978) Work-function dependence of negative-ion production during sputtering. Phys. Rev. Lett. 40:574-577.

44. Slodzian G., Daigne B., Girard F., Hillion F. (1993) Ion optics for a high resolution scanning ion microscope and spectrometer: transmission evaluations. In Secondary Ion Mass Spectrometry: SIMS IX, ed. A Benninghoven, Y Nihei, R Shimizu, HW Werner, pp. 294–97. New York:Wiley.

45. Guerquin-Kern J.L.,Wu T.D., Quintana C., and Croisy A. (2005) Progress in analytical imaging of the cell by dynamic secondary ion mass spectrometry (SIMS microscopy). Biochim. Biophys. Acta 1724: 228–38.

46. Cheng J., Wucher A., and Winograd N. (2006) Molecular depth profiling with cluster ion beams. J. Phys. Chem. B 110:8329-8336.

47. Sigmund P. (1969) Theory of sputtering. I. Sputtering yield of amorphous and polycrystalline targets. Phys. Rev. 184:383-416.

48. Sigmund P. (1972) Collision theory of displacement damage, ion ranges, and sputtering. Rev. Roum. Phys. 17:823-870.

49. Benninghoven A., Rudenauer F.G., and Werner H.W. (1987) Secondary ion mass spectrometry: basic concepts, instrumental aspects, applications and trends. New York: Wiley Interscience.

50. Lindhard J., Scharff M., and Schiott H.E. (1963) Integral equations governing radiation effects. Kgl. Danske Videnskab., Selskab. Mat. Fys. Medd. 33:1-42.

51. Sigmund P. (1974) Energy density and time constant of heavy-ion-induced elastic-collision spikes in solids. Appl. Phys. Lett. 25:169-171.

52. Vineyard, G.H. (1976) Thermal spikes and activated processes. Radiat. Eff. 29: 245-248.

53. Sigmund, P., and Claussen, C. (1981) Sputtering from elastic-collision spikes in heavy-ion-bombarded metals. J. Appl. Phys. 52: 990-993.

54. Jakas, M. M., E. M. Bringa, and R. E. Johnson (2002) Fluid dynamics calculation of sputtering from a cylindrical thermal spike. Phys. Rev. B 65: 165425.

55. Yamamura, Y., and Tawara, H. (1996) Energy dependence of ion-induced sputtering yields from monatomic solids at normal incidence. Atom. Data Nucl. Data 62: 149-253.

56. Krohn, V. E. (1962) Emission of negative ions from metal surfaces bombarded by positive cesium ions. J. Appl. Phys. 33: 3523-3525.

57. Nørskov, J. K., and Lundqvist, B. I. (1979) Secondary-ion emission probability in sputtering. Phys. Rev. B 19: 5661.

58. Williams, P. (1979) The sputtering process and sputtered ion emission. Surf. Sci. 90: 588-634.

59. Vaz, A. R., Da Silva, M. M., Leon, J., Moshkalev, S. A., and Swart, J. W. (2008) Platinum thin films deposited on silicon oxide by focused ion beam: characterization and application. J. Mater. Sci. 43: 3429-3434.

60. Tsai, J., and Morabito, J. (1974) The mechanism of simultaneous implantation and sputtering by high energy oxygen ions during secondary ion mass spectrometry (SIMS) analysis. Surf. Sci. 44: 247-252.

61. Carter G., Colligon J.S., and Leck, J.H. (1962) Ion sorption in the presence of sputtering. Proc. Phys. Soc. 79: 299-309.

62. Werner, H. W., and Warmoltz, N. (1976) The influence of selective sputtering on surface composition. Surf. Sci. 57: 706-714.

63. Anuntalabhochai, S., Chandej, R., Phanchaisri, B., Yu, L. D., Vilaithong, T., and Brown, I. G. (2001) Ion-beam-induced deoxyribose nucleic acid transfer. App. Phys. Lett. 78: 2393-2395.

64. Yu, L. D., Vilaithong, T., Phanchaisri, B., Apavatjrut, P., Anuntalabhochai, S., Evans, P., and Brown, I. G. (2003) Ion penetration depth in the plant cell wall. Nucl. Instrum. Meth. B 206: 586-590.

65. Zwartouw, H. T. (1964) The chemical composition of vaccinia virus. J. Gen. Microbiol. 34: 115-123.

66. Ziegler, J. F., Ziegler, M. D., and Biersack, J. P. (2010) SRIM–The stopping and range of ions in matter. Nucl. Instrum. Meth. B 268: 1818-1823.

67. Postawa, Z., Czerwinski, B., Szewczyk, M., Smiley, E. J., Winograd, N., and Garrison, B. J. (2003). Enhancement of sputtering yields due to C_{60} versus Ga bombardment of Ag {111} as explored by molecular dynamics simulations. Anal. Chem. 75: 4402-4407.

68. Scassellati, Catia, et al. (2010) Intranuclear sphingomyelin is associated with transcriptionally active chromatin and plays a role in nuclear integrity. Biol. Cell 102: 361-375.

69. Albi, E., and Magni, M.P. (2003) Chromatin associated sphingomyelin: metabolism in relation to cell function. Cell Biochem. Funct. 21: 211-215.

70. Lucki, N. C., and Sewer, M.B. (2012) Nuclear sphingolipid metabolism. Annu. Rev. Physiol. 74: 131-151.

71. Mandelkern, M., Elias, J. G., Eden, D., and Crothers, D. M. (1981) The dimensions of DNA in solution. J. Mol. Biol. 152: 153-161.

72. Condit, R.C., and Motyczka, A. (1981) Isolation and preliminary characterization of temperature-sensitive mutants of vaccinia virus. Virology 113: 224-241.

73. McFadden, B.D., Moussatche, N., Kelley, K., Kang, B.H., and Condit, R.C. (2012) vaccinia virions deficient in transcription enzymes lack a nucleocapsid. Virology 434: 50-58.